KATHOLIEKE UNIVERSITEIT LEUVEN
FACULTEIT DER TOEGEPASTE WETENSCHAPPEN
DEPARTEMENT WERKTUIGKUNDE
AFDELING PRODUCTIETECHNIEKEN
MACHINEBOUW EN AUTOMATISATIE
Celestijnenlaan 300B − B-3001 Leuven (Heverlee), Belgium

Vibration-Based Methods for the Identification of the Elastic Properties of Layered Materials

Promotoren:
Prof. Dr. Ir. W. Heylen
Prof. Dr. Ir. O. Van Der Biest

Proefschrift voorgedragen tot
het behalen van het doctoraat
in de toegepaste wetenschappen

door

Tom LAUWAGIE

2005D06 October 2005

KATHOLIEKE UNIVERSITEIT LEUVEN
FACULTEIT DER TOEGEPASTE WETENSCHAPPEN
DEPARTEMENT WERKTUIGKUNDE
AFDELING PRODUCTIETECHNIEKEN
MACHINEBOUW EN AUTOMATISATIE
Celestijnenlaan 300B − B-3001 Leuven (Heverlee), Belgium

Vibration-Based Methods for the Identification of the Elastic Properties of Layered Materials

Jury:
Prof. Dr. Ir. Arch. H. Neuckermans, voorzitter
Prof. Dr. Ir. W. Heylen, promotor
Prof. Dr. Ir. O. Van Der Biest, promotor
Prof. Dr. Ir. D. Vandepitte
Prof. Dr. Ir. J. Van Humbeek
Prof. Dr. Ir. H. Sol (Vrije Universiteit Brussel)
Dr. Ir. G. Roebben (Inst. for Reference Materials and Measurements)
B.Eng. M.Sc. Ph.D S. Patsias (University of Sheffield)

Proefschrift voorgedragen tot
het behalen van het doctoraat
in de toegepaste wetenschappen

door

Tom LAUWAGIE

U.D.C. 539.3 620.179

October 2005

© Katholieke Universiteit Leuven – Faculteit Toegepaste Wetenschappen
Arenbergkasteel, B-3001 Heverlee (Belgium)

Alle rechten voorbehouden. Niets uit deze uitgave mag worden vermenigvuldigd en/of openbaar gemaakt worden door middel van druk, fotocopie, microfilm, elektronisch of op welke andere wijze ook zonder voorafgaande schriftelijke toestemming van de uitgever.
All rights reserved. No part of the publication may be reproduced in any form by print, photoprint, microfilm or any other means without written permission from the publisher.

D/2005/7515/80
ISBN 90-5682-646-8

Met wiskundige formules kun je niet spelen zolang je de functies niet begrijpt. Het kost dan ook jaren om iets te verstaan van wat je doet of maakt, omdat die abstracte puzzels op zichzelf lastiger zijn dan de projecten.
Wanneer het uiteindelijk lukt de boel te kraken ontstaat er iets, inzichtelijk en waardevol, over de werking van de dingen, een grenzeloos heelal van wonderlijke variatie.

Panamarenko

Acknowledgements

I would like to thank and acknowledge the contributions of the following persons and organisations:

My promoters Prof. Ward Heylen and Prof. Omer Van Der Biest. I would especially like to thank Prof. Heylen for providing a prosperous working environment for me at PMA. I truly appreciate the opportunity you gave me for investing in myself and I am looking forward to continue our collaboration.

Dr. Gert Roebben for all the help you offered me during my doctoral training. I would like to thank you explicitly for motivating me to develop the uncertainty analysis routine. Without your encouragement chapter 7 would most likely not have existed.

Prof. Hugo Sol for informing me about the GRAMATIC project and bringing me into contact with Prof. Heylen. I would also like to thank you for introducing me in the field of mixed numerical-experimental techniques. I enjoyed the scientific discussions we had in the beginning of my doctoral training and I appreciated the useful comments you gave me on many of the articles I wrote.

The members of the jury for the interesting discussion we had during the preliminary defence of my thesis and for all the constructive comments I received that helped improve the quality of this text. I would explicitly like to thank Prof. Dirk Vandepitte for correcting my thesis so carefully and Prof. Jan Van Humbeeck for the interesting remarks you made on the material science aspects of my text.

Hilde De Gersem for proof reading a major part of my text. I really appreciate the effort you have made.

Joop Van Deursen and Jean Claude Drohé for their assistance with the preparation of the test samples.

Dr. Sophoclis Patsias and Nicola Tassini of the University of Sheffield for providing the air plasma sprayed coatings.

Dr. Marion Bratsch and Iulian Mirceau of the Deutsches Zentrum für Luft- und Raumfart for providing the electron beam – physical vapour deposited coatings.

The research on which my thesis is based was performed in the framework of the

STWW project GRAMATIC. I would like to acknowledge the financial support of the IWT (Instituut voor de aanmoediging van innovatie door Wetenschap & Technologie in Vlaanderen) to the GRAMATIC project in general and to my research in particular. I would also like to thank Dynamic Design Solutions, Integrated Material Control Engineering, and LMS International for the software and/or support they provided me in the framework of this project.

And last but not least, I would like to thank Konstantza for the microstructural characterisation of the ceramic coatings, the SEM pictures, the excellent job you did with proof reading my thesis, but most of all for supporting in any possible way during the period I was writing my thesis, you have earned my eternal gratitude ... σε λατρεύω.

Tom Lauwagie
Brugge, September 2005

Abstract

This thesis develops a vibration-based identification technique to determine the elastic properties of the constituent layers of layered materials. The presented mixed numerical-experimental technique (MNET) derives the layer properties from the resonant frequencies of rectangular beam- or plate-shaped specimens, and is able to identify the in-plane elastic properties of both isotropic and orthotropic materials. An optional post-processing step allows the estimation of the uncertainty of the identified elastic parameters.
The thesis comprises three main parts. The first part, chapters 1 to 4, introduces the mathematical tools that are required to construct an MNET procedure. The second part, chapters 5 to 7, uses these mathematical tools to build a series of vibration-based identification procedures for the identification of the elastic properties of layered materials. The last part, chapters 8 and 9, provides an experimental validation together with a number of applications of the developed identification routines.

x

Preface

The principal goal of this thesis is to finalise my doctoral training at the Katholieke Universiteit Leuven. However, the ambition of this text reaches further than just being a report of the research that was performed during my doctoral training.

Goal

Besides developing identification routines for layered materials, this text presents a detailed discussion on the vibration-based identification of in-plane elastic material properties. Furthermore, it also aims at providing a sound theoretical foundation on how to develop mixed numerical-experimental techniques (MNET) for material identification purposes.
A serious effort was made to present the content as comprehensible as possible. Although this text contains a substantial amount of theory, is does not give any theoretical overview with the sole purpose of providing an overview. All the presented theory is strictly necessary to develop MNET identification routines. Moreover, this thesis does not present an extensive literature review. The main reason for this is the lack of interesting articles on the identification of the elastic properties of layered materials. Most articles dealing with MNET-based material identification are written by researchers that focus on optimisation theory. Usually, the material identification problem is used as a 'simple' example to illustrate the use of a novel optimisation technique. Although these articles are very interesting from an optimisation point of view, they are usually quite disappointing from a material identification point of view.

Audience

This thesis addresses two different audiences: (a) engineers who want to develop mixed numerical-experimental techniques for the identification of material parameters, and (b) scientists who are interested in determining elastic material properties using vibration-based identification techniques.
To use this text as a guide to develop an MNET, a basic knowledge of the theory behind the finite element method is required. Chapters 3, 4, and 6 provide the information to develop MNET routines. If one wishes to add an uncertainty analysis procedure to the MNET, chapter 7 is essential.
If one wants to use the text to learn more about vibration-based identification techniques for in-plane elastic properties, chapters 1, 6, and 8 are important.

The study of these chapters only requires an understanding of the fundamental concepts of mechanical vibrations, like the phenomenon of resonance.

Nederlandstalige Samenvatting

Trillingsgebaseerde Methodes voor de Identificatie van de Elastische Eigenschappen van Gelaagde Materialen

Dit hoofdstuk bevat een Nederlandstalige samenvatting van de thesis. Deze samenvatting heeft dezelfde structuur als de thesis; elke sectie van de samenvatting stemt overeen met een hoofdstuk van de thesis.

Inleiding

Materiaal Identificatie

Numerieke simulaties zijn een onmisbaar hulpmiddel geworden in het ontwikkelingsproces van een technische structuur. Een zinvolle simulatie vereist een nauwkeurige kennis van de materiaaleigenschappen van het numerieke model. Deze parameters kunnen echter enkel op een experimentele wijze bepaald worden.
Gelaagde materialen zijn een klasse van nieuwe materialen die steeds belangrijker wordt voor de productie van hoog performante mechanische componenten. Hun stijfheidseigenschappen zijn van fundamenteel belang voor de berekening van spanningsvelden. Er bestaan reeds verschillende technieken voor de bepaling van de stijfheidseigenschappen van materialen, maar in het geval van gelaagde materialen leveren deze technieken enkel de 'gemiddelde' stijfheid van het volledige materiaal. Deze thesis spits zich toe op de ontwikkeling van identificatieprocedures voor de bepaling van de elastische eigenschappen van de individuele lagen van een gelaagd materiaal.

Trillingsgebaseerde Identificatietechnieken

Elastische eigenschappen worden traditioneel opgemeten met quasi-statische proeven zoals uni-axiale trektesten of vierpuntsbuigingsproeven. De trillings-

gebaseerde technieken bieden hier echter een zinvol alternatief. Met trillingsgebaseerde testen kunnen de elastische eigenschappen op een contactloze wijze bepaald worden, wat een belangrijk voordeel is in het geval van kleine monsters of brosse materialen.
De trillingsgebaseerde aanpak steunt op het verband tussen het trillingsgedrag en de elastische eigenschappen van een structuur. De trillingsgebaseerde aanpak werd voor het eerste toegepast door Förster [1] in 1937. Förster gebruikte de balk theorie van Euler om de elasticiteitsmodulus van een materiaal te bepalen uit de resonantiefrequentie van de fundamentele buigingsmode van een balkvormig monster. Försters methode werd door o.a. Pickett [2], Spinner en Teft [3] verfijnd. Het werk van de laatste twee auteurs leverde de basis voor een ASTM norm [4]. Deze norm standaardiseerde de trillingsgebaseerde identificatie van de elastische eigenschappen van isotrope materialen.
De belangrijkste hinderpaal voor de verdere uitbreiding van de trillingsgebaseerde methodes was het gebruik van analytische formules voor de beschrijving van het trillingsgedrag van de monsters. In 1986 toonde Sol [5] aan dat de analytische formules kunnen vervangen worden door eindige elementen modellen. Deze doorbraak opende de weg voor de identificatie van de elastische parameters van complexere materialen zoals gelaagde materialen.

Gemengde Numeriek-Experimentele Technieken

Sommige fysische eigenschappen kunnen zeer moeilijk of zelfs onmogelijke rechtstreeks opgemeten worden. In zo'n situatie moet de fysische eigenschap op een indirecte manier bepaald worden. Dit kan door de fysische eigenschap af te leiden van een aantal gerelateerde grootheden die wel opgemeten kunnen worden. Indien het verband tussen de fysische eigenschap en de opgemeten grootheden te complex wordt om analytische uit te drukken moet dit verband gelegd worden met een numeriek model, en moeten de fysische grootheden bepaald worden met een gemengde numeriek-experimentele techniek (GNET). Figuur 1 schets het algemeen concept van de gemengde numeriek-experimentele aanpak.

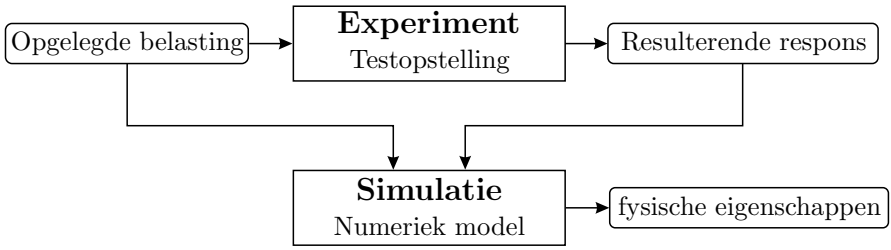

Figuur 1: *Het algemeen concept van gemengde numeriek-experimentele technieken.*

Numerieke modellen zijn meestal geformuleerd om respons van een systeem te berekenen aan de hand van de systeem parameters (het directe probleem). Maar in een GNET moeten een aantal systeem parameters bepaald worden aan de hand van de respons van het systeem (het inverse probleem). De meeste numerieke modellen kunnen echter niet op een adequate manier geherformuleerd

worden zoals vereist voor het oplossen van het inverse probleem. De oplossing van het inverse probleem kan dan enkel op een iteratieve manier gevonden worden door de systeemparameters van het numerieke model 'af te regelen' totdat de respons van het model overeenstemt met de opgemeten respons. Figuur 2 geeft de flowchart van een gemengde numeriek-experimentele techniek voor de identificatie van materiaal parameters.

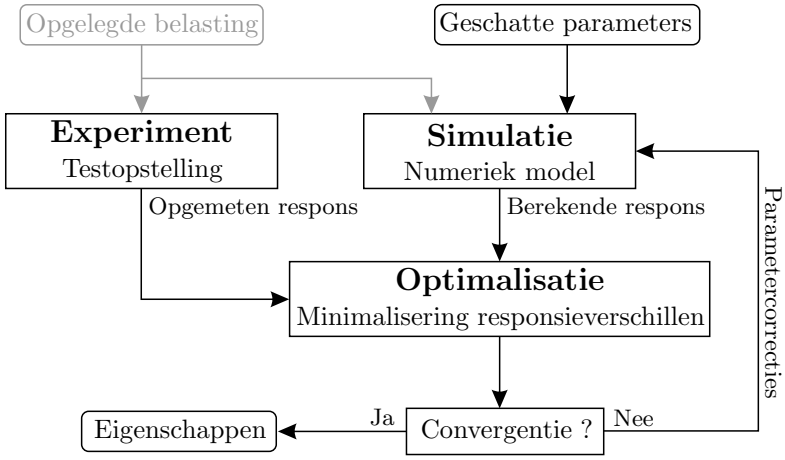

Figuur 2: *De flowchart van een gemengde numeriek-experimentele techniek (GNET) voor materiaalidentificatie.*

In een eerste fase wordt een experiment uitgevoerd en wordt de opgelegde belasting en resulterend respons opgemeten. Vervolgens wordt het uitgevoerde experiment met een numeriek model gesimuleerd. De respons wordt berekend met behulp van een ruwe schatting van de waarden van de ongekende modelparameters. De respons van de simulatie wordt vergeleken met de opgemeten respons en een set van parametercorrecties wordt geschat door middel van een minimalisatie van de responsieverschillen. De gecorrigeerde modelparameters worden in het numerieke model ingevoerd, en daarna wordt er een nieuwe iteratiecyclus gestart. Eenmaal de parametercorrecties kleiner zijn dan een wel bepaalde limiet wordt de iteratielus afgebroken.
In het geval van trillingsgebaseerde materiaalidentificatie worden resonantiefrequenties gebruikt als responsies. Voor lineair elastische materialen zijn de resonantiefrequenties onafhankelijk van de opgelegde belasting. Hierdoor hoeft de opgelegde belasting niet opgemeten te worden bij trillingsgebaseerde GNETs.

Lineaire Elasticiteit

In het geval van lineair elastische materialen wordt de spannings-rek relatie gegeven door de wet van Hook. In het meest algemene geval bevat deze uitdrukking 21 onafhankelijke stijfheidscoëfficiënten. Voor dunne, orthotrope materialen reduceert het aantal onafhankelijke stijheidscoëfficiënten zich tot vier: E_1, E_2, G_{12}, en ν_{12}. In het geval van een isotroop materiaal zijn er slechts twee onafhankelijke stijfheidscoëfficiënten: E en ν. Voor beide materialen zijn

de mogelijke waardes die deze parameters kunnen aannemen begrensd. De grenzen zijn gebaseerd op de wetten van de thermodynamica, en bepalen het geldigheidsdomein van de oplossing van het materiaalidentificatie probleem.

Eindige Elementen Methode & Gevoeligheidsanalyse

De Eindige Elementen Methode

De eindige elementen methode (EEM) is een numerieke techniek die courant gebruikt wordt bij de analyse van mechanische structuren, en is in het bijzonder interessant voor de berekening van het trillingsgedrag van een structuur. Door zijn veelzijdigheid is de eindige elementen methode uiterste geschikt voor de ontwikkeling van krachtige GNET-gebaseerde technieken voor materiaalidentificatie.

Bij het gebruik van de EEM in trillingsgebaseerde GNETs is het aan te raden om de monsters te modelleren met driedimensionale elementen met kwadratische vormfuncties. De densiteit van het elementen grid wordt het best bepaald aan de hand van een convergentie test.

Gevoeligheidsanalyse

Gevoeligheidsanalyse bestudeert de invloed van de inputparameters van een bepaald model op de respons. In het geval van locale gevoeligheidsanalyse wordt de invloed van een welbepaalde inputparameter op de respons bestudeerd in een enkel punt van de inputparameterruimte. Een locale gevoeligheidsanalyse levert een aantal gevoeligheidscoëfficiënten op. Elke gevoeligheidscoëfficiënt geeft aan in welke mate een welbepaalde respons veranderd in functie van een wijziging van de beschouwde inputparameter. Deze gevoeligheidscoëfficiënten zijn dus een ideaal hulpmiddel bij de bepaling van de parametercorrecties die noodzakelijke om de gewenste wijziging van de respons te verwezenlijken.

De gevoeligheidscoëfficiënten van de resonantiefrequenties ten opzichte van de materiaalparameters (elastische eigenschappen en densiteit) worden best bepaald door de sommatie van de gevoeligheden van de elementen van het model, berekend met een semi-analytische differentiaal formulatie. De gevoeligheden van de monsterparameters (lengte, breedte, laagdiktes) worden bij voorkeur met een eindige differentie aanpak bepaald.

Correlatieanalyse

Trillingsgebaseerde materiaalidentificatie vereist een routine die in staat is het type (buigingsmode, torsiemode, etc.) van de berekende modevormen automatische te herkennen. Een automatische herkenning van de modevormen kan gerealiseerd worden door de berekende modes te vergelijken met de modevormen van een referentiedatabase aan de hand van het 'modal assurance criterion' (MAC).

Optimalisatietheorie

Inleiding

Optimalisatietheorie is van primordiaal belang voor gemengde numeriek-experimentele technieken. GNETs bepalen de waardes van een aantal fysische grootheden door een dataset die opgemeten werd tijdens een experiment te vergelijken met een dataset die berekend werd met een simulatiemodel. De resultaten van de simulatie worden gecontroleerd door een aantal ongekende maar 'afstelbare' parameters. Er wordt verondersteld dat de correcte waardes van de fysische parameters overeenstemmen met de waardes van de modelparameters die resulteren in een optimale overeenstemming tussen de opgemeten en berekende dataset. Een GNET vereist dus een oplossing van een optimalisatieprobleem.

Optimalisatietechnieken

Nulde-Orde Methodes

Nulde-orde technieken gebruiken enkel waardes van de kostfunctie om het optimalisatieprobleem op te lossen, ze gebruiken geen afgeleiden. In het geval van GNETs hebben de nulde-orde technieken het voordeel dat ze geen toegang tot de code van de eindige elementen software vereisen. Een evaluatie van drie verschillende nulde-orde technieken (de simplex methode, genetische algoritmes en neurale netwerken) toonde echter aan dat de nulde-orde technieken een zeer groot aantal kostfunctieëvaluaties nodig hebben voor de bepaling van het optimum. Aangezien de evaluatie van de kostfunctie van een trillingsgebaseerde GNET een oplossing van één of meerdere eindige elementen modelen omvat, is de beperking van het aantal kostfunctieëvaluaties van primair belang. Nulde-orde technieken zijn dus niet geschikt voor de oplossing van de trillingsgebaseerde GNETs wegens inefficiënt.

Daalmethodes

Daalmethodes (descent methods) zijn numerieke algoritmes die het minimum van de kostfunctie op een iteratieve wijze bepalen. Elke iteratiestap omvat twee acties: 1) het bepalen van een optimale daalrichting, 2) het verkleining van de waarde van de kostfunctie door een stap te nemen in de optimale daalrichting. Eerste-orde methodes zijn daalmethodes die enkel gradiëntinformatie gebruiken voor de bepaling van de ideale daalrichting, tweede-orde methodes gebruiken hiervoor zowel gradiënt- als Hessiaaninformatie. In het geval van tweede-orde methodes levert de berekening van de ideale daalrichting meteen ook een optimale stap op. Uiteindelijke bleken de tweede-orde methodes zeer geschikt te zijn voor het oplossen van de trillingsgebaseerde GNETs.

Trillingsgedrag van Gelaagde Materialen

Door middel van de klassieke laminaattheorie kan er aangetoond worden dat het trillingsgedrag van gelaagde materialen bepaald wordt door totale stijfheid van het materiaal en niet door de stijfheid van de individuele lagen. Dit heeft als gevolg dat de laageigenschappen niet geïdentificeerd kunnen worden aan de hand van het trillingsgedrag van één enkel monster.

De laagstijfheden kunnen enkel bepaald worden aan de hand van het trillingsgedrag van een set van testmonsters die elk een verschillende laagconfiguratie hebben. Twee laagconfiguraties verschillen van elkaar door verschillende laagdiktes of laagsequenties. De uniciteit van de oplossing van de GNET is enkel gegarandeerd indien het aantal gebruikte laagconfiguratie groter dan of gelijk is aan het aantal materialen dat geïdentificeerd moeten worden.

Identificatieroutines

De Vorm van de Monsters

Aan de hand van een gevoeligheidsanalyse werd de invloed van de vorm van het monster op de informatieïnhoud van de resonantiefrequenties geëvalueerd.

Balkvormige Monsters

De resonantiefrequenties van balkvormige monsters blijken enkel informatie te bevatten over de elasticiteitseigenschappen in de richting van de langs-as van het monster. De buigingsfrequenties over de elasticiteitsmodulus, de torsiefrequenties leveren informatie over de glijdingsmodulus. Alle buigings- en torsiefrequenties blijken dezelfde informatie te bevatten, het gebruik van meerdere buigings- of torsiefrequenties van eenzelfde monster levert dus geen extra informatie op.

Plaatvormige Monsters

De resonantiefrequenties van plaatvormige monsters leveren informatie over de vier orthotrope materiaalparameters. De informatieïnhoud is sterk afhankelijk van de lengte/breedte verhouding van de plaat. Een optimale informatieïnhoud wordt bekomen voor een plaat met een lengte/breedte verhouding die voldoet aan uitdrukking (6.1).

Identificatieroutines

De identificatieroutine vereist een set monsters met een voldoende aantal laagconfiguraties zodat de uniciteit van de oplossing gegarandeerd is. In de experimentele fase worden de resonantiefreqeunties van de verschillende monsters opgemeten. De identificatie van de elastische eigenschappen start met het modelleren van alle monster met behulp van de eindige elementen methode. De resonantiefrequenties van alle monsters worden berekend met hulp van een set geschatte waarden van de ongekende elastische parameters. De berekende frequenties worden vergeleken met de gemeten frequenties, en een set van parametercorrecties wordt geschat uit de minimalisatie van de frequentieverschillen. De elastische parameters worden aangepast en er wordt een nieuwe iteratie cyclus gestart. Het iteratieproces loopt tot de parametercorrecties kleiner zijn dan de convergentielimiet. In het totaal worden drie varianten van deze procedure geïntroduceerd.

Balkvormige Monsters

Mono-Oriëntatie Routines — De mono-oriëntatie routine gebruikt een set van balkvormige monsters die allen uitgesneden zijn in dezelfde materiaalrichting. In deze routine worden E en ν van de verschillende materiaallagen bepaald aan de hand van de fundamentele buigings- en torsiefrequenties van de verschillende test monsters. De glijdingsmodulus wordt bepaald in een post-processing stap aan de hand van uitdrukking (2.31). Hoewel de mono-oriëntatie routine in theorie enkel geschikt is voor de identificatie van isotrope materialen is het toch mogelijk om de elasticiteits- en glijdingsmodulus van licht anisotrope materialen te bepalen. In dit geval kan de correctheid van het geïdentificeerde Poisson getal echter niet gegarandeerde worden.

Multi-Oriëntatie Routines — De multi-oriëntatie routine gebruikt een set van balkvorimige monsters die allen uitgesneden zijn in een verschillende materiaalrichting. Met deze routine kunnen de vier orthotrope materiaalparameters van de verschillende materiaallagen, E_1, E_2, G_{12}, en ν_{12}, bepaald aan de hand van de fundamentele buigings- en torsiefrequenties van de verschillende test monsters.

Plaatvormige Monsters

Deze routine gebruikt een set van een set van plaatvormige monsters die allen een optimale lengte/breedte verhouding hebben. Deze routine bepaalt de vier orthotrope materiaalparameters van de verschillende materiaal lagen, E_1, E_2, G_{12}, en ν_{12}, aan de hand van de resonantiefrequenties van de eerste vijf trillingsmodes van de verschillende test monsters.

Onzerkerheidsanalyse

Inleiding

Een opgemeten waarde van een fysische parameter is niet zinvol als ze niet vergezeld is van een verklaring over haar betrouwbaarheid. Zo'n betrouwbaarheidsverklaring moet gebaseerd zijn op objectieve feiten en wetenschappelijke onderbouwd zijn. Maar aangezien het over een oordeel gaat, zal een betrouwbaarheidsverklaring steeds, in zekere mate, subjectief zijn. De betrouwbaarheidsverklaring kan enkel aanvaard worden indien het duidelijk is hoe ze bekomen werd.

Bronnen van Onzekerheid

Een belangrijke bron van onzekerheid is de onzekerheid op de gemeten grootheden: lengte, breedte, dikte, massa, en resonantiefrequenties van de test monsters. Als een gevolg van benaderingen die gemaakt werden bij het opstellen van de eindige elementen modellen van de test monsters, is er ook een onzekerheid op de berekende frequenties. Uit een evaluatiestudie blijkt dat: a) de onzekerheid afkomstig van het beperkte meetbereik van de meetapparatuur belangrijker is dan de stochastische variatie van de opgemeten waardes, b) de onzekerheid afkomstig van de modelleringsfouten is verwaarloosbaar zijn ten opzichte van de onzekerheid op de gemeten grootheden, c) de discretisatiefout

van het eindige elementen model levert wel een significante onzekerheid op.

Onzekerheidsroutines

Het onzekerheidsprobleem wordt zowel op een probabilistische als een niet-probabilistische manier opgelost. De onzekerheidsroutines worden geformuleerd als een post-processing stap die kan uitgevoerd worden nadat de materiaalparameters geïdentificeerd zijn. Om de rekentijd te beperken worden de GNET vergelijking vervangen door een eerst-orde benadering die bekomen wordt aan de hand van een Taylor expansie in het werkingspunt van de laatste iteratiestap.

Probabilistische Aanpak

Bij de probabilistische aanpak wordt de onzekerheid op de materiaalparameters bepaald aan de hand van een Monte Carlo simulatie. De onzekerheden van de inputparameters worden voorgesteld door een distributies met een uniforme waarschijnlijkheid tussen een boven en ondergrens. De gesamplede inputdistributies worden aan de hand van de gelineariseerde GNET vergelijking omgezet in outputdistributies. De onzekerheden van de materiaalparameters kunnen dan geschat worden aan de hand van de bekomen outputdistributies.

Niet-Probabilistische Aanpak

Bij de probabilistische aanpak wordt de onzekerheid op de grootheden voorgesteld met onzekerheidsintervallen. Elke onzekerheidsinterval bepaald de onder en boven grens van de beschouwde grootheid. De onzekerheidsintervallen van de materiaalparameters worden bepaald uit de onzekerheidsintervallen van de inputparameters aan de hand van intervalrekenkunde.

Probabilistische versus Niet-Probabilistische Aanpak

De probabilistische en niet-Probabilistische aanpak zijn complementair en hebben beiden een specifiek toepassingsgebied. De probabilistische aanpak is optimaal om de onzekerheid te bepalen van een set van opgemeten materiaalparameters, terwijl de niet-probabilistische aanpak ideaal is om de betrouwbaarheid of nauwkeurigheid van verschillende testconfiguraties te vergelijken.

Validatie

Een zinvolle validatie van een meettechniek kan alleen op een experimentele manier uitgevoerd worden. Om de identificatieroutines voor gelaagde materialen te valideren werden ze toegepast op twee referentiematerialen waarvan de stijfheden van de lagen gekend waren. Het eerste referentiemateriaal was een messing-staal bi-metaal, het tweede referentiemateriaal was een met koolstofvezel versterkte kunststof. De validatietesten resulteerden in de volgende conclusies: 1) de trillingsgebaseerde GNETs zijn in staat om de elastische eigenschappen van de lagen correct identificeren, 2) de mono-oriëntatie routine resulteerde in een hoge spreiding op de waardes van de geïdentificeerde materiaalparameters, 3) de multi-oriëntatie routine is de gebruiksvriendelijkste en betrouwbaarste GNET, en 4) het gebruik van plaatvorimge monsters is mogelijk maar resulteert meestal in een aantal praktische problemen.

Toepassingen

De trillingsgebaseerde GNETs werden gebruikt voor de identificatie van een 'air plasma sprayed' en een 'electrom beam – physical vapour deposited' coating. Beide coatings bestonden uit twee lagen: a) een metalische verbindingslaag, en b) een ceramische toplaag. In beide gevallen kon de GNET de eigenschappen van de twee lagen identificeren. De bekomen resultaten waren in overeenstemming met de microstructurele karakteristieken van de coatings.

Conclusies

Het is mogelijke om de elastische eigenschappen van de verschillende lagen van een gelaagd materiaal te identificeren aan de hand van een trillingsgebaseerde gemengde numeriek-experimentele procedure. De ontwikkelde procedures kunnen zowel de eigenschappen van isotrope als van orthotrope materialen bepalen. Door de trillingsgebaseerde aanpak kunnen de metingen contactloos uitgevoerd worden wat het testen van kleine monsters en/of brosse materialen toelaat. De GNET aanpak zorgt tevens voor een grote flexibiliteit wat het gebruik van verschillende monstertypes toelaat: balkvormige monsters, plaatvormige monsters, cilindrische monsters, gedeeltelijk gecoate monsters, etc.

List of Symbols

General Conventions

$\mathbb{R}$	Real numbers
$\lvert \diamond \rvert$	Absolute value
$\ln \diamond$	Natural logarithm
$\mathbb{R}^n$	Real n-vectors ($n \times 1$ matrices)
$\{\diamond\}$	Vector
$\lVert \diamond \rVert$	Euclidean norm of a vector
$\mathbb{R}^{n \times m}$	Real $n \times m$ matrices
$[\diamond]$	Matrix
$[\diamond]^{\mathrm{T}}$	Transpose of a matrix
$[\diamond]^{-1}$	Inverse of a matrix
$[\diamond]^{\dagger}$	Moore-Penrose pseudo inverse of a matrix
$[\diamond]^{\dagger w}$	Weighted pseudo inverse of a matrix
$\Delta \diamond$	Variation
$\mathrm{d} \diamond$	Differential
$\partial \diamond$	Partial differential
$\mathrm{dom}\, \diamond$	Domain of a function
$\nabla \diamond$	Gradient of a function
$\nabla^2 \diamond$	Hessian of a function
$\sum$	Summation
∞	Infinity
$\approx$	Approximately
$\hat{\diamond}$	Approximation of
$\diamond^{\star}$	Optimal value
$\forall$	For all
$\diamond^{\circ}$	Degrees

Theory of Elasticity

$\overline{\diamond}$	Quantity expressed in the local coordinate system
$\diamond^0$	Quantity related to the middle surface
A_{ij}	Extensional stiffness coefficients
B_{ij}	Coupling stiffness coefficients
$[C]$	Stiffness matrix
C_{ij}	Stiffness coefficient
D_{ij}	Bending stiffness coefficients

E	Elastic modulus of an isotropic material
E_i	Elastic modulus in the i-direction of an orthotropic material
E_1, E_2, E_3	Principal elastic moduli of an orthotropic material
E_x, E_y, E_z	Apparent elastic moduli of an orthotropic material
E_l	E-modulus in the fibre direction of an UD-composite
E_t	E-modulus in the transverse direction of an UD-composite
$\{\varepsilon\}$	The strain vector
ε_i	The strain in the i-direction
ε_x, ε_y, ε_z	The strain expressed in the local coordinate system
ε_1, ε_2, ε_3	The strain expressed in the global coordinate system
ε_x^0, ε_y^0, ε_z^0	The strain of the middle surface
γ_{ij}	The shear strain in the ij-plane
γ_{12}, γ_{31}, γ_{23}	Principal shear moduli of an orthotropic material
γ_{xy}, γ_{zx}, γ_{yz}	Apparent shear moduli of an orthotropic material
k	Index of the layers
κ_x^0, κ_y^0, κ_{xy}^0	The curvature of the middle surface
M_x, M_y	Bending moments
M_{xy}	Twisting moment
n_l	Number of layers
N_x, N_y	In-plane normal forces
N_{xy}	In-plane shear force
ν	Poisson's ratio of an isotropic material
ν_{ij}	Poisson's ratio for transverse strain in the j-direction when stressed in the i-direction, orthotropic materials
ν_{12}, …, ν_{23}	Principal Poisson's ratios of an orthotropic material
ν_{xy}, …, ν_{yz}	Apparent Poisson's ratios of an orthotropic material
Q_{ij}	Reduced stiffness coefficient
Q_x, Q_y	Transverse shear forces
$[R]$	Reuter matrix
$[S]$	Compliance matrix
S_{ij}	Compliance coefficient
$\{\sigma\}$	The stress vector
σ_i	The stress in the i-direction
σ_x, σ_y, σ_z	The stress expressed in the local coordinate system
σ_1, σ_2, σ_3	The stress expressed in the global coordinate system
$[T]$	Rotation matrix
θ	Material orientation
u	Displacement in the x-direction
$\{u\}$	Displacement vector
u^0, v^0, w^0	Displacement of the middle surface
v	Displacement in the y-direction
w	Displacement in the z-direction

Finite Element Modelling & Sensitivty Analysis

$\tilde{\diamond}$	Virtual quantity, according to the principle of virtual work
$\diamond_e$	Indicates that the considered properties is related to a finite element

f_i	Resonant frequency of the i$^{\text{th}}$ mode
$[K]$	Global stiffness matrix
$[K_e]$	Element stiffness matrix
λ	Eigenvalue
λ_i	Eigenvalue of the i$^{\text{th}}$ mode
$[\Lambda]$	Eigenvalue matrix
$[M]$	Global mass matrix
$[M_e]$	Element mass matrix
N_i	Shape function associated with node i
$[N_e]$	Shape function matrix of finite element
p	Material parameter
$\{\phi\}$	Mode shape vector
$\{\phi\}_i$	Mode shape vector of the i$^{\text{th}}$ mode
$\{\phi_e\}$	Element mode shape vector
$[\Psi]$	Mode shape matrix
r	Response
ρ	Mass density
s_{ij}	Sensitivity coefficient, relative normalised unless mentioned otherwise
$[S]$	Sensitivity matrix
ϑ	Higher order term
u	Continuous displacement field
$\{u\}$	Displacement vector of one particular point
$\ddot{u}$	Continuous acceleration field
$\{\ddot{u}\}$	Acceleration vector of one particular point
$\{U\}$	Global nodal displacement vector
$\{\ddot{U}\}$	Global nodal acceleration vector

Optimisation Theory

$[A]$	Coefficient matrix of a least-squares problem
$\{b\}$	Constants vector of a least-squares problem
ϵ	Residual
η_i	Lagrange multiplier of the i$^{\text{th}}$ equality constraint
$f_0(x)$	Cost-function
$f_i(x)$	Inequality constraints
$h_i(x)$	Equality constraints
$\mathcal{L}(\diamond)$	Lagrange function
λ_i	Lagrange multiplier of the i$^{\text{th}}$ inequality constraint
n	Number of optimisation variables
N	Norm of the Euclidean norm
N_a	Matrix that groups the gradients of the active constraints
P_a	Orthogonal projection matrix
r	Number of inequality constraints
s	Number of equality constraints
t	Step size
$\bar{t}$	Upper limit of the step size
v	Search direction

v_p	Projected search direction
v_{nt}	Newton step
w_i	Weighting factor of the i$^{\text{th}}$ optimisation variable
$[W]$	Weighting matrix of a weighted least-squares problem

Vibration-Based Identification Routines

$\diamond^{exp}$, $\diamond_{exp}$	Experimental quantity
$\diamond^{num}$, $\diamond_{num}$	Numerical quantity
$\overline{\delta}$	Convergence limit for the finite element model
f_{brea}	Resonant frequency of the breathing mode of a plate-shaped specimen
f_f	Resonant frequency of the fundamental out-of-plane flexural mode of a beam-shaped specimen
f_{sadd}	Resonant frequency of the saddle mode of a plate-shaped specimen
f_t	Resonant frequency of the fundamental torsional mode of a beam-shaped specimen
f_{tf-x}	Resonant frequency of the torsional-flexural mode in the x-direction of a plate-shaped specimen
f_{tf-y}	Resonant frequency of the torsional-flexural mode in the y-direction of a plate-shaped specimen
f_{tors}	Resonant frequency of the torsional mode of a plate-shaped specimen
l	Sample length
m	Sample mass
n_e	Number of elements of a finite element model
n_r	Number of elements of responses
n_l	Number of layers
n_s	Number of elements of samples
n_c	Number of layer configurations
n_p	Number of parameters
n_m	Number of different materials
n_f	Number of frequencies
t	Sample thickness
w	Sample width

Uncertainty Analysis

$\overline{\diamond}$	Upper bound
$\underline{\diamond}$	Lower bound
$[\chi]$	Coefficient matrix of the linearised MNET equations
f_{p_i}	The function that relates p_i to the output parameters
k	Coverage factor
max $\diamond$	Maximum
min $\diamond$	Minimum
μ	The mean
n_{in}	Number of input parameters

n_{out}	Number of output parameters
p_i	The i^{th} output parameter
P	Probability
q_i	The i^{th} input parameter
$[S_p]$	Sensitivity matrix of the resonant frequencies with respect to the material parameters
$[S_s]$	Sensitivity matrix of the resonant frequencies with respect to the sample properties
σ	The standard deviation
$u(\diamond)$	The uncertainty
$u_c(\diamond)$	The combined standard uncertainty
$u_e(\diamond)$	The expanded uncertainty
$u_s(\diamond)$	The standard uncertainty

List of Abbreviations

APS	Air Plasma Sprayed
ASTM	American Society for Testing and Materials
BC	Bond Coat
BD	Bi-Directional
BSE	Backscattered Electron
CCD	Charge Coupled Device
CLT	Classical Lamination Theory
CoP	Code of Practice
CPU	Central Processing Unit
EB-PVD	Electron Beam – Physical Vapour Deposition
FEM	Finite Element Method
FE-model	Finite Element model
FGM	Functionally Graded Material
GA	Genetic Algorithm
GUM	ISO guide to the expression of Uncertainty in Measurement
IP	In-plane
ISO	International Organisation for Standardisation
KKT	Karush-Kuhn-Tucker
LS	Least-Squares
MAC	Model Assurance Criterion
MC	Monte Carlo
MNET	Mixed Numerical-Experimental Technique
NN	Neural Network
MO	Multi-Orientation MNET identification routine
OOP	Out-of-plane
PS	MNET identification routine using Plate-Shaped specimens
SEM	Scanning Electron Microscope
SO	Single-Orientation MNET identification routine
TBC	Thermal Barrier Coating
TC	Top Coat
UD	Uni-Directional
WLS	Weighted Least-Squares

Contents

Acknowledgements vii

Abstract ix

Preface xi

Nederlandstalige Samenvatting xiii

List of Symbols xxiii

Contents xxix

1 Introduction 1
- 1.1 Material Identification . . . 2
  - 1.1.1 Vibration-Based Material Identification . . . 2
  - 1.1.2 Layered Material Identification . . . 3
  - 1.1.3 Conclusions . . . 6
- 1.2 Mixed Numerical-Experimental Techniques . . . 7
  - 1.2.1 Introduction . . . 7
  - 1.2.2 The MNET Approach . . . 8
  - 1.2.3 MNETs versus Finite Element Model-Updating . . . 10
- 1.3 Focus of the Thesis . . . 12
- 1.4 Structure of the Thesis . . . 12

2 Linear Elasticity 15
- 2.1 The Generalized Hooke's Law . . . 16
- 2.2 Orthotropic Materials . . . 18
  - 2.2.1 Engineering Constants . . . 18
  - 2.2.2 Elastic Properties for an Arbitrary Orientation . . . 19
- 2.3 Isotropic Materials . . . 21
- 2.4 Two-Dimensional Stress Analysis . . . 22
  - 2.4.1 Orthotropic Materials . . . 22
  - 2.4.2 Isotropic Materials . . . 25
- 2.5 Restrictions on the Engineering Constants . . . 26
  - 2.5.1 Orthotropic Materials . . . 26
  - 2.5.2 Isotropic Materials . . . 27

2.6 Summary . . . 28

3 The Finite Element Method & Sensitivity Analysis 29
3.1 The Finite Element Method . . . 30
3.1.1 Theoretical Background . . . 30
3.1.2 Finite Element Modelling in Material Identification . . . 33
3.1.3 Conclusions . . . 39
3.2 Sensitivity Analysis . . . 39
3.2.1 Finite Difference versus Differential Sensitivities . . . 39
3.2.2 The Direct versus the Adjoint Approach . . . 41
3.2.3 Sensitivity Coefficients of Vibrating Structures . . . 42
3.2.4 The Sensitivity Matrix . . . 52
3.2.5 Conclusions . . . 55
3.3 Correlation Analysis . . . 55
3.3.1 The Modal Assurance Criterion . . . 55
3.3.2 Automatic Mode Recognition . . . 56
3.3.3 Conclusions . . . 57
3.4 Summary . . . 57

4 Optimisation Theory 59
4.1 Introduction . . . 60
4.1.1 Global and Local Minima . . . 60
4.1.2 MNETs and Optimisation . . . 61
4.1.3 Overview of the Optimisation Techniques . . . 62
4.2 Zero-Order Methods . . . 63
4.2.1 Simplex Methods . . . 63
4.2.2 Genetic Algorithms . . . 64
4.2.3 Neural Networks . . . 66
4.2.4 Conclusions . . . 67
4.3 Basic Concepts of Convex Optimisation . . . 68
4.3.1 Convex Sets . . . 69
4.3.2 Convexity . . . 69
4.3.3 Optimality Condition . . . 70
4.4 Unconstrained Optimisation . . . 70
4.4.1 Optimality Condition . . . 70
4.4.2 Analytical Solutions . . . 71
4.4.3 Descent Methods . . . 74
4.5 Constrained Optimisation . . . 79
4.5.1 Optimality Conditions . . . 79
4.5.2 Solving the Equality-Constrained Problem . . . 81
4.5.3 Solving the Inequality-Constrained Problem . . . 82
4.6 Solving the MNET Optimisation Problem . . . 87
4.6.1 Introduction . . . 87
4.6.2 Sequential Quadratic Optimisation . . . 87
4.6.3 The MNET Cost-Function . . . 88
4.6.4 The Constraints . . . 90
4.6.5 The MNET Optimisation Routine . . . 96

4.7 Summary . . . 96

5 Vibratory Behaviour of Layered Materials 97
5.1 Classical Lamination Theory . . . 98
5.1.1 Introduction . . . 98
5.1.2 The Strain Field under the Kirchhoff Assumptions . . . 99
5.1.3 The Stress-strain Relation in a Layered Material . . . 100
5.1.4 Extensional, Coupling and Bending Stiffnesses . . . 101
5.2 Vibratory Behaviour of a Layered Material . . . 104
5.2.1 Equations of Motion . . . 104
5.2.2 Discussion . . . 106
5.2.3 Numerical Example . . . 106
5.3 Identifying the Layer Properties . . . 109
5.4 Summary . . . 110

6 Identification Routines 111
6.1 The Specimen Shape . . . 112
6.1.1 Beam-Shaped Specimens . . . 112
6.1.2 Plate-Shaped Specimens . . . 114
6.2 Identification Routines for Non-Layered Materials . . . 119
6.2.1 Using Beam-Shaped Specimens . . . 119
6.2.2 Using Plate-Shaped Specimens . . . 127
6.3 Layered Materials . . . 128
6.3.1 The Required Test Specimens . . . 128
6.3.2 The Identification Routines . . . 129
6.4 The General Vibration-Based MNET Framework . . . 130
6.4.1 The Identification Routine . . . 130
6.4.2 The Global Sensitivity Matrix . . . 132
6.4.3 Constrained and Weighted Least-Squares . . . 133
6.5 Numerical Validation . . . 134
6.6 Discussion, Conclusions and Overview . . . 136
6.7 Summary . . . 139

7 Uncertainty Analysis 141
7.1 Essentials of Expressing Measurement Uncertainty . . . 142
7.1.1 Basic Definitions . . . 142
7.1.2 Step 1: Specifying the Measurands . . . 142
7.1.3 Step 2: Identifying the Uncertainty Sources . . . 143
7.1.4 Step 3: Quantifying the Uncertainty Components . . . 143
7.1.5 Step 4: Calculating the Combined Uncertainty . . . 143
7.1.6 Expanded Uncertainty . . . 143
7.2 The Uncertainty Sources . . . 144
7.2.1 Measurement Errors . . . 144
7.2.2 Modelling Errors . . . 145
7.2.3 Conclusions . . . 145
7.3 First-Order Approximation of the MNET Equations . . . 146
7.3.1 Single-Model Routines . . . 146
7.3.2 Multi-Model Routines . . . 147

7.3.3 Extending the Measurement Equations 148
7.4 The Probabilistic Approach 148
7.4.1 Verification of the Analytical Approach 148
7.4.2 Estimation of the Confidence Intervals 150
7.5 The Non-Probabilistic Approach 152
7.5.1 Uncertainty Intervals 152
7.5.2 Interval Calculations 153
7.5.3 Computing the Uncertainty Intervals 155
7.6 Examples 157
7.6.1 Comparison of the Probabilistic and Non-Probabilistic Approach 157
7.6.2 Validation of the Linear MNET Approximation 160
7.6.3 Optimal Sample Orientations for the MO Routine . . . 160
7.7 Summary 162

8 Validation Tests **165**
8.1 Introduction 166
8.2 Brass-Steel Bi-Metal 166
8.2.1 Introduction 166
8.2.2 Homogeneous Brass Samples 168
8.2.3 Homogeneous Stainless Steel Samples 170
8.2.4 Brass-Steel Bi-Metal Samples 172
8.3 Carbon-Epoxy Composite 182
8.3.1 Introduction 182
8.3.2 Equivalent Thickness of the Material 183
8.3.3 The Test Specimens 185
8.3.4 Identification of the Layer Properties 188
8.3.5 Conclusions 191
8.4 Summary 191

9 Applications **193**
9.1 Introduction 194
9.2 Air Plasma Sprayed Coatings 194
9.2.1 Introduction 194
9.2.2 The Initial Samples 196
9.2.3 The Beam-Shaped Specimens 198
9.2.4 Conclusions 210
9.3 Electron Beam – Physical Vapour Deposited Coatings 211
9.3.1 Introduction 211
9.3.2 The Test Samples 212
9.3.3 The Identification Routine 213
9.3.4 The Identified Properties 213
9.3.5 Analytical Identification Approach 216
9.3.6 Conclusion 217
9.4 Summary 217

10 Conclusions **219**
10.1 Conclusions . . . 220
10.1.1 The MNET Identification Routines . . . 220
10.1.2 Comparison to the State-of-the-Art . . . 220
10.1.3 Comments on the Use of the MNET Techniques . . . 221
10.2 Recommendations for Future Research . . . 222

A The ASTM Standard on Resonant Beam Testing **225**
A.1 Introduction . . . 226
A.2 Calculating the Elastic Properties . . . 226

B Experimental Set-up & Measurement Procedures **229**
B.1 Measuring the Resonant Frequencies . . . 230
B.1.1 The Measurement Set-up . . . 230
B.1.2 Sample Suspension . . . 231
B.2 Measuring the Sample Properties . . . 232

C The Influence of an Out-of-Plane Sample Deformation **235**
C.1 Introduction . . . 236
C.2 Beam-Shaped Specimens . . . 237
C.2.1 Curved Beams . . . 237
C.2.2 Twisted Beams . . . 238
C.3 Plate-Shaped Samples . . . 239
C.3.1 Curved in One Direction . . . 239
C.3.2 Curved in Both Directions . . . 240
C.3.3 Twisted Plates . . . 241
C.4 Conclusions . . . 241

D The Analytical Approach for Layered Cylinders **243**
D.1 Identification Formulas for Cylindrical Specimens . . . 244
D.1.1 Homogenenous Specimens . . . 244
D.1.2 Layered Specimens . . . 244
D.2 Evaluation of the Identification Approach . . . 245
D.2.1 Comparison of the ASTM Formula with FEM . . . 245
D.2.2 Verification of the Identification Approach of [6] . . . 245
D.3 Conclusions . . . 247

E Experimental Results **249**
E.1 Brass-Steel Bi-metal . . . 250
E.1.1 The Homogeneous Brass Samples . . . 250
E.1.2 The Homogeneous Steel Samples . . . 254
E.1.3 The Brass-Steel Bi-Metal Samples . . . 258
E.1.4 The Glass Samples . . . 269
E.2 Carbon-Epoxy Composite . . . 272
E.2.1 The Carbon-Epoxy Specimens . . . 272
E.2.2 Glass Specimens . . . 274
E.3 Air Plasma Sprayed Coatings . . . 275
E.3.1 The Initial Plate-Shaped Specimens . . . 275

E.3.2 The Beam-Shaped Specimens 276
E.3.3 Sample Description 276
E.4 Electron Beam – Physical Vapour Deposited Coatings 285

Bibliography **287**

Curriculum Vitae **297**

Publications **299**

1
Introduction

This chapter introduces the thesis by situating the subject, highlighting the personal contributions and clarifying the structure of the text.

1.1. Material Identification

Numerical simulations have become an indispensable tool in the process that leads to the development of an engineering structure. Although these simulations have replaced a substantial amount of experimental tests, they have not rendered testing obsolete. A successful simulation requires an accurate knowledge of the material parameters that are used in the numerical model. These parameters can only be obtained with an actual experiment.

To improve the performance, durability or efficiency of mechanical equipment, material scientists are continuously developing new materials. Unfortunately, the mechanical behaviour of these novel materials is becoming increasingly more complex. The description of their behaviour thus requires more elaborate models that use a larger number of model parameters. All these material parameters have to be measured in order to use the simulation models in a reliable way. However, the knowledge of these parameters is not only important for mechanical simulations. Since these material parameters represent the true behaviour of the material, they can also be used by material scientists to evaluate and possibly improve the performance of newly developed materials.

Layered materials is one class of new materials that is becoming increasingly important for the production of high performance components. During design calculations, their stiffness properties are crucial for the assessment of stress fields. Numerous analysis techniques to identify the elastic properties of materials exist, however in the case of layered materials, these techniques usually yield properties that are 'homogenised' over the thickness of the material. This thesis focuses on the development of identification procedures to identify the elastic parameters of the constituent layers of a layered material.

1.1.1. Vibration-Based Material Identification

Traditionally, elastic material parameters are measured with quasi static tests such as tensile tests or four point bending tests. Alternatively, elastic material parameters can also be determined with vibration-based methods. With the vibration-based approach, the elastic properties can be determined in a contactless way, which is a major advantage for small test samples or brittle materials. Other advantages of the vibration-based approach are the accuracy, the simplicity and affordability of the test set-up, the short time required to perform a measurement, etc.

The vibration-based approach is founded on the fundamental relation that exists between the elastic material properties of a structure and its vibratory behaviour. The first application of the vibration-based approach was reported by Förster [1] in 1937. Förster used the Euler beam theory to link the sample's elastic modulus to the eigenfrequency of the fundamental flexural mode. In 1945 Pickett [2] used Goens' [7] approximate solution of the Timoshenko beam equations [8] to establish a more accurate relation between the elastic modulus and the fundamental transverse flexural frequency of a vibrating prism or cylinder. In 1961, Spinner and Teft [3] extended Pickett's work with torsional frequencies, enabling the identification of the shear modulus. The work of Spinner and Teft formed the base of the ASTM resonant beam test pro-

cedure [4], which standardised material testing based on analytical vibration models. However, the use of analytical formulas to describe the vibratory behaviour of test specimens is a major obstacle for extending the vibration-based methods to more complex materials.

1.1.2. Layered Material Identification

There is an extensive amount of literature on the identification of the elastic properties of layered materials. Unfortunately, almost all the articles present procedures that either identify the 'homogenised' properties of the laminate, or consider relations between the properties of the various layers, reducing the problem to the identification of the properties of a single material. The following four articles, discussing a genuine layered identification technique, were found.

Article 1: "Young's modulus of bioactive glass coated oral implants: porosity corrected bulk modulus versus resonance frequency analysis" [6] — In this article the properties of a bioactive glass (BAG) coating are identified from a set of cylindrical specimens. In the considered article, the coating properties were identified using a pure substrate and a coated specimen.

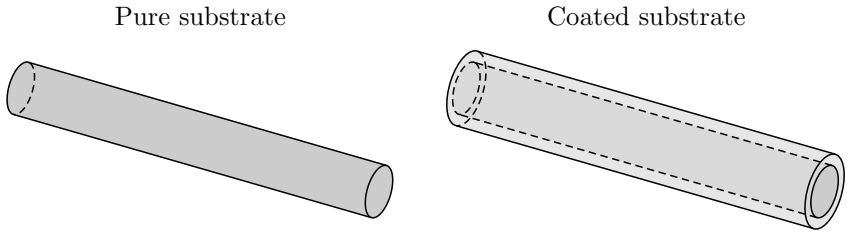

Figure 1.1: *The specimens used to identify the Young's modulus of the BAG coating.*

The elastic properties of the BAG coating were measured using the following approach. A number of BAG coated cylindrical test specimens were produced. These rods were regarded as composite cylindrical beams, made up of homogeneous, isotropic materials. The overall Young's modulus of these bars was identified from the resonant frequency of the fundamental flexural vibration mode using the ASTM [4] standard[1]. The Young's modulus of the substrate was identified in an identical way from the fundamental flexural frequency of the same specimen after removing the coating. The coating layer was removed by stressing the rotating sample with a point load. In this way the coating totally cracked up and subsequently spalled of the substrate without changing the properties of the substrate.
Eventually, the elastic modulus of the BAG coating was calculated from the overall stiffness of the coated specimen and the elastic modulus of the substrate material. The overall stiffness of the coated specimen was decomposed by stating that the bending stiffness of the coated beam can be expressed as the

[1] Appendix D provides the identification formulas.

sum of the bending stiffness of the substrate and the bending stiffness of the coating. Since the bending stiffness of the substrate and coated rod are known, this relation provides the bending stiffness of the coating. Finally, the Young's modulus of the coating material is found by dividing the bending stiffness of the coating by its moment of inertia.
The presented procedure is a genuine multi-layered identification technique and has the following qualities:

- It is a vibration-based identification procedure that can identify the elastic modulus of layered materials with isotropic layers.
- The procedure has been successfully applied to identify the Young's modulus of a coating.
- Although the method is presented for cylindrical rods, the procedure can easily be adapted to estimate the elastic properties of beam-shaped samples with a rectangular cross-section.

Article 2: "An inverse method for determining material parameters of a multi-layer medium by boundary element method" [9] — This article presents a mixed numerical-experimental approach[2] to determine the elastic moduli of the layers using indentation measurements. In the experimental phase, a disc-shaped sample of the layered material is indented with an axisymmetric indenter, while the applied force and resulting deformation are measured. The experiment is modelled with a boundary element model that considers the layers to be elastically isotropic and to have a uniform thickness. The procedure identifies the elastic modulus of the layers together with the layer thicknesses. In theory, there is no limit on the number of layers that can be identified. Also note that this procedure is able to identify the properties of layers with a thickness of a few micrometers.

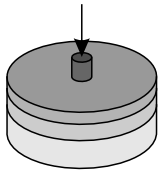

Figure 1.2: *A sample of a three-layer material indented by a cylindrical body.*

The article presents two theoretical examples, it does not present any actual test cases. In these theoretical examples, the indentation experiments are simulated with a boundary element model. The simulation results are used as experimental data to identify the layer properties. The first example considers a material with two layers, the second example considers a material with four layers. In both cases, there is an difference between the correct and identified properties. For the first and second example, an average difference of 2.0 % and 2.6 % respectively is observed. The authors explain the difference by indicating that the identification problem is ill-conditioned. Another consequence of

[2] A general introduction about mixed numerical-experimental techniques is presented in section 1.2.

this ill-conditioning is that the procedure does not yield a unique solution; the obtained solution depends on the starting values. The authors indicate that the 'correct' solution is only found, if the starting values were close enough to the correct values, and if the search space of the identification procedure was restricted by a set of constraints.

Article 3: "Measurement of coatings' elastic properties by mechanical methods: Part 1. Considerations on experimental errors" [10] — The authors present a four point bending technique to measure the elastic properties of isotropic coatings. They introduce two analytical models to describe a pure bending phenomenon in layered beam- and plate-shaped samples. From these model equations, they derive a set of analytical formulas to calculate the elastic modulus and Poisson's ratio of the outermost coating layer. With these equations, the layer properties can be derived from a sample set that comprises specimens with an increasing number of layers, i.e. a test is performed after every layer deposition. The properties of the last deposited layer can be deduced on the basis of the results gained with the previous tests that were performed on samples with fewer layers. The presented technique considers all the layer materials to be isotropic. An estimate of the elastic modulus is obtained from beam-shaped samples, an estimate of the Poisson's ratio is obtained from plate-shaped samples.
Figure 1.3 presents the four variations of the four point bending test considered in the article; in each plot, only the measured quantities are indicated. Method 1 uses the strain on the surface of both the substrate (ε_s) and the coating (ε_c), method 2 uses the applied load (P) and the strain on the coating surface, method 3 uses the applied load and the strain on the substrate surface, and method 4 uses the applied load and the resulting displacement of the midsection of the specimen (w). Note that only methods 2 and 4 can be applied with symmetrically coated specimens.

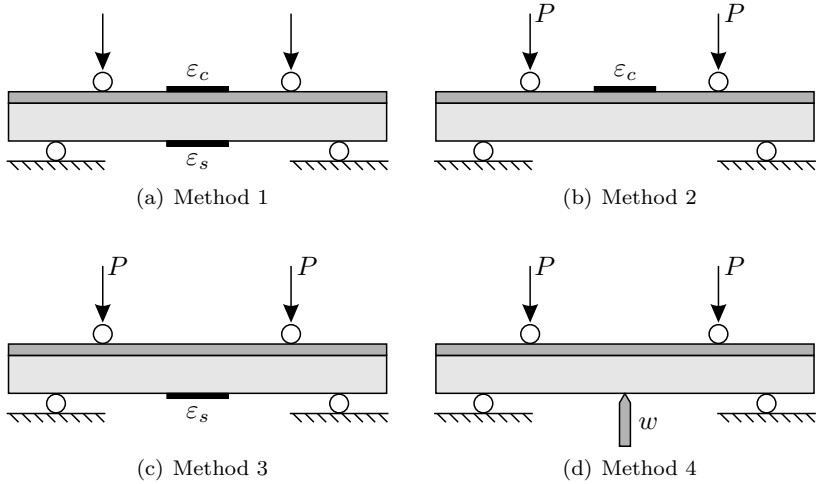

(a) Method 1 (b) Method 2

(c) Method 3 (d) Method 4

Figure 1.3: *The four methods presented by [10].*

Article 4: "Measurement of coatings' elastic properties by mechanical methods: Part 2. Application to thermal barrier coatings" [11] — In this article, the methods that were introduced in part one [10] are applied to identify the properties of thermal barrier coatings (TBCs)[3] consisting of two separate layers: a metallic bond coat (BC) and a ceramic top coat (TC). The properties are identified using five different samples types: pure substrate samples, samples coated with BC on one side, samples coated with BC both sides, samples coated with BC and TC on one side, samples coated with BC and TC on both sides. To enable the identification of the elastic modulus and Poisson's ratio of the coatings, both beam-shaped and plate-shaped samples were tested.

With this sample set, methods 1, 2 and 4 can be evaluated and compared. All the approaches managed to identify the elastic properties of both the bond coat and the top coat. This procedure is thus a genuine multi-layered identification technique and has the following qualities:

- The procedure can identify the elastic modulus and Poisson's ratio of layered materials with isotropic layers.
- Method 1 does not derive the layer stiffness from the overall bending stiffness of the beam. Through this, method 1 is less sensitive to errors on the layer thicknesses than methods 2, 3 and 4.
- It is possible to measure the applied load and the resulting midsection displacement in a furnace. Therefore, it is possible to identify the layer properties as a function of temperature with method 4. The feasibility of high temperature testing is proven in [11].

1.1.3. Conclusions

The procedures presented in [6, 10] are genuine layered identification procedures, that have proven to work under testing conditions. Although these techniques worked fine for the considered applications, they have a number of important limitations:

- Both techniques are limited to isotropic materials, it is impossible to identify the elastic properties of orthotropic materials.
- The technique of [10] is limited to beam- and plate-shaped samples. The use of cylindrical or disc-shaped samples would require the derivation of a new set of analytical equations. The approach of [6] is limited to cylindrical and beam-shaped specimens.
- Both techniques require a particular set of test samples: a sample set that comprises specimens that have an increasing number of layers. It is not possible to identify the layer properties with a single specimen.
- The approach of [6] is only applicable with samples that have a symmetric layer configuration.
- It is not possible to identify the properties of specimens that are partially coated.
- The procedure of [10] not contactless. Porous materials might be crushed in the vicinity of the support or load points, brittle materials might crack.

[3] The introduction of the third test-case discussed in chapter 9 provides some background information about thermal barrier coatings.

Note that nearly all the limitations are related to the use of analytical formulas to describe the mechanical behaviour of the sample. These limitations could easily be overcome by using finite element models. A contactless, non-destructive procedure can be obtained by using a vibration-based approach. So, the vibration-based mixed numerical-experimental approach appears to be the most promising concept for the development of powerful identification techniques for layered materials.

1.2. Mixed Numerical-Experimental Techniques

1.2.1. Introduction

Mixed numerical-experimental techniques (MNETs) were introduced about two decades ago. In those twenty years MNETs have proven to be very versatile and flexible tools for the identification of material parameters. MNET-based identification routines have been introduced in a wide range of disciplines to estimate a broad variety of material parameters, e.g. in civil engineering to estimate the permeability [12] or elasticity [13] of soil, in electrical engineering to identify the piezoelectric properties of materials [14], in material engineering to quantify the porosity [15] or to determine the permeability of textiles for fibre reinforced plastics [16], in mechanical engineering to identify the thermal conductivity [17], acoustic [18], damping [19, 20] and plastic [21, 22] properties of materials, and in biomedical engineering to estimate the mechanical properties of skin [23] or liver tissue [24]. In those fields MNETs have been applied to identify material properties using specimens ranging from 50 µm thick structures [25] to real sized flood-control dams [26].

In the field of mechanical engineering, several authors have presented techniques to identify the elastic properties of materials. For this purpose, MNETs have been proposed to characterise materials using tensile tests [27], bending tests [28], shear tests [29], compression tests [30], indentation tests [31], elastic waves [32,33], stress waves [34], and resonant frequencies [35–37]. However, this thesis will only consider the resonant-based approach, since it is a very attractive option from both an experimental and a numerical point of view.

Resonant based testing is standardised by an ASTM standard [4] which presents a number of analytical formulas to estimate the elastic material properties of homogeneous, isotropic materials. The use of analytical formulas to describe the vibratory behaviour of test specimens is, however, the main obstacle for extending the vibration-based methods to more complex materials. In 1986, Sol [5] showed that it is possible to replace the analytical formulas by special purpose finite element models. The MNET he presented identifies the four in-plane engineering constants of an orthotropic material, i.e. E_1, E_2, G_{12} and ν_{12}, from the resonant frequencies of the fundamental flexural modes of two beam-shaped specimens, and the first three resonant frequencies of a plate-shaped specimen. Meanwhile, several authors introduced related approaches for the identification of elastic constants of orthotropic materials using thin plate specimens, [38–42], or have extended the technique to thick plates [43,44].

In the last decade several researchers have developed MNET-based procedures to identify the elastic properties of layered materials. In 1993 Soares [45] intro-

duced a vibration-based MNET to identify the elastic properties of laminated composites from a number of resonant frequencies of a plate-shaped specimen. In 1997 Cunha [46, 47] proposed a similar technique to identify the stiffness coefficients of laminated composite plates. In 2000 he extended this procedure for the characterisation of the elastic properties of laminated composite tubes. In 2004 Cugnoni [48, 49] presented a vibration-based MNET to identify the overall elastic properties of thick sandwich panels. In [50] Rikards presented an interesting overview of MNET-based routines for the characterisation of layered materials. His overview clearly indicates that the routines that have been introduced so far have one major limitation: they only identify the average properties of the material, they do not provide any information about the properties of the individual layers.

1.2.2. The MNET Approach

Some physical properties are difficult or even impossible to measure in a direct way. Sometimes, the physical property can be measured with an indirect measurement procedure. Instead of measuring the property of interest, indirect procedures measure a number of related quantities and derive the unknown property from the experimental values of these quantities.
Traditional indirect measurement techniques use analytical expressions to relate the physical property of interest to the measured quantities. This approach can only be used when there is a simple relation between the measured quantities and the physical property of interest. If this relation becomes too complex to be expressed analytically, the physical properties of interest have to be related to the measured quantities by means of a numerical model, and the properties of interest have to be identified by a mixed numerical-experimental technique. Figure 1.4 illustrates the general concept of the mixed numerical-experimental approach.

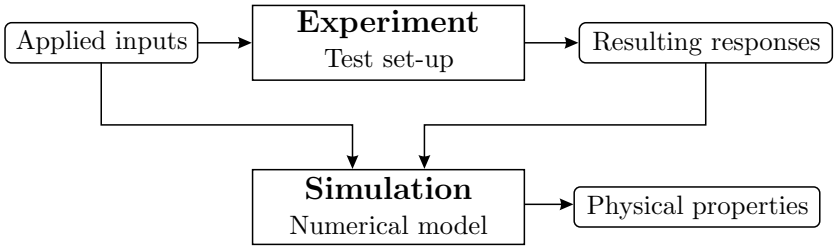

Figure 1.4: *The general concept of mixed numerical-experimental techniques.*

Numerical models are usually formulated in such a way that they compute the response of a system using the applied inputs and system properties. The problem of determining the response from the input and system properties is called the direct problem and is illustrated in figure 1.5.
However, the direct problem is not the problem that has to be solved in a mixed numerical-experimental technique – figure 1.4. In an MNET, a number of model parameters have to be derived from the system's response to a particular input.

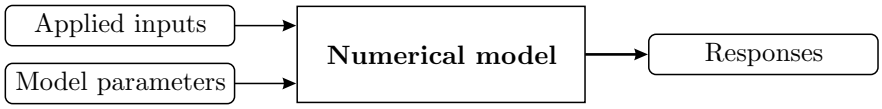

Figure 1.5: *The direct problem.*

This problem is called the inverse problem and is sketched in figure 1.6. Most numerical models can not be reformulated in the form that complies with the inverse problem. The solution of the inverse problem has to be found in an iterative way by 'fine-tuning' the model parameters in such a way that the obtained response equals the measured response.

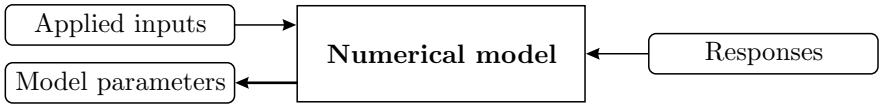

Figure 1.6: *The inverse problem.*

Incorporating the concept of inverse problems into the scheme of figure 1.4 provides the general MNET flowchart of figure 1.7. In the first phase, an experiment is performed and the applied inputs and resulting responses are recorded. In a second phase, a numerical model of this experiment is constructed. The responses are computed with this simulation model using a set of trial values of the unknown model parameters, i.e. the physical properties that have to be identified. The simulation responses are compared with the experimental responses and an improved set of model parameters is obtained by minimising the response differences. The improved model parameters are

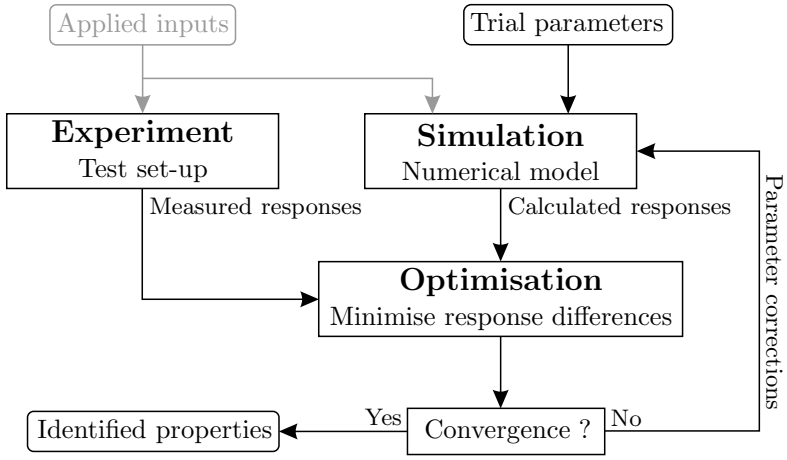

Figure 1.7: *The general flowchart of a mixed numerical-experimental technique (MNET).*

inserted into the numerical model and a new iteration cycle is performed. The iterative procedure is aborted once the solution has converged, and the model parameters can be extracted from the database of the numerical model. Note that vibration-based identification routines use resonant frequencies and mode shapes as response quantities. For linear elastic material behaviour, resonant frequencies and mode shapes do not depend on the excitation, which implies that vibration-based MNETs do not require to record the applied input[4].

The MNET approach might look like a quite complicated concept to measure physical parameters. However, if looked at from a modelling point of view, it is actually a very logical approach. For mechanical engineering applications, the identified material parameters will eventually be used in numerical simulations. An MNET routine will use this simulation code to identify the unknown values of the model parameters. It therefore creates a perfect synergy between the worlds of modelling and testing, since the numerical simulation code is used to both determine the values of the model parameters and predict the behaviour of a real structure. Note that the MNET approach is a generic concept allowing the identification of any parameter that is used in a numerical simulation code.

MNETs also have a number of other interesting advantages over traditional measurement techniques. For example, it is possible to extract more than one physical parameter from a single experiment or to extract a set of parameters from a combination of different experiments. Unlike conventional measurement approaches, MNETs can also handle more complex types of experimental data and this might become an important issue in the future. Due to recent technological advances, optical measurement devices like scanning laser vibrometers and CCD cameras are becoming more and more affordable. Although these systems provide a wealth of information, the information is only becoming useful when there are techniques to process the measured data in an efficient way. MNETs could play an important role in this process.

1.2.3. MNETs versus Finite Element Model-Updating

The reader with a background in mechanical engineering might have the impression that mixed numerical-experimental techniques is just another name for finite element model-updating. Both techniques are based on the same mathematical tools: numerical modelling, correlation analysis, sensitivity analysis and optimisation theory. Despite these important similarities, there is a significant difference: the two methods differentiate themselves from each other based on their main goal. To be more precise, model-updating focuses on the mathematical model, while MNETs focus on the model parameters. All other differences between model-updating and MNETs are a consequence of this fundamental difference.

The quality of a numerical model is of course determined by its capability to predict the responses of the real structure. However, every mathematical model is based on a number of assumptions and has therefore a limited accuracy. In the case of finite element models, the inaccuracy of the model can be caused by

[4] As long as the characteristics of the input spectrum are known and allow the estimation of the relevant resonant frequencies and/or mode shapes.

approximating the geometry of the considered structure with a limited number of elements, the type of elements and element formulation, uncertainties on the material properties or any other simplification made during the construction of the numerical model. Because of these assumptions and simplifications, the results of the numerical model will not exactly match the experimental responses of the real structure. Model-updating aims to improve the reliability of a mathematical model by fine-tuning a number of model parameters, in order to obtain an optimal correlation between the numerical results and a set of experimental data.

An MNET aims to identify the values of a set of physical parameters by minimising the differences between a data set measured during an experiment and the results of a numerical simulation of this experiment. Like model-updating routines, MNETs minimise the differences between experimental and numerical results by fine-tuning a set of model parameters. However, the goal of MNETs is not to compensate the shortcomings of the model, but to measure a set of physical properties. This leads to the following practical differences between model-updating and MNETs:

Accuracy of the model — In model-updating, the model parameters are fine-tuned to improve the reliability of the model. In some cases, the simulation model was even deliberately simplified, e.g. to obtain a shorter computation time. This is not a serious problem, since the optimised parameter values can compensate the inaccuracies of the model. However, the optimised parameter values will only compensate the inaccuracies of that particular model. The optimised parameters are thus model-dependent and meaningless, if they are not used in combination with the associated model. MNETs aim at identifying the values of physical parameters, which are by definition model-independent. The inaccuracy of the simulation model of a certain MNET will have a negative effect on the quality of the identified parameters. Therefore, the mathematical model of any MNET should be as accurate as possible. This can only be achieved by combining a rather simple experiment with a detailed simulation model.

The choice of the parameters — The proper selection of the updating parameters is a key step for the successful updating of a finite element model. If the selected model parameters are indeed the ones with incorrect values, the procedure should converge and yield an updated model that is reliable. On the contrary, if the model parameters with incorrect values are not selected, the updating process might not converge or might yield a model that is not very reliable and/or contains parameters with unrealistic values [51]. Usually, the selection of the proper updating parameters is a difficult process, however in the case of an MNET this process is very straightforward. The updating parameters are simply the ones that represent the physical quantities that have to be identified.

The uniqueness of the solution — Updating problems can have multiple solutions that result in an equivalent correlation between model and experiment. In the case of model-updating, this is not a problem since the goal is to have – at least one – reliable model. On the contrary, in the case of an MNET, multiple solutions pose a serious problem. MNETs identify physical properties, which

of course have a unique value. If there are multiple solutions that result in an equivalent correlation, it is impossible to determine which solution represents the correct physical values. So, if an MNET results in multiple solutions, it has to be redesigned in such a way that it provides only one solution.

1.3. Focus of the Thesis

The main objective of this thesis was to develop a vibration-based identification procedure to determine the elastic properties of the individual layers of layered materials. In order to achieve this objective, a lot of intermediate steps had to be taken, some of which provided better insight in vibration-based material identification or resulted in new identification procedures for non-layered materials. More specifically, the original contributions of this thesis are:

- The identification procedure that was introduced in [5] is a vibration-based MNET that can identify the elastic properties of orthotropic materials. It requires the resonant frequencies of the fundamental flexural vibration mode of two beam-shaped specimens and the resonant frequencies of the three lowest vibration modes of a plate-shaped specimen. The procedure was modified in such a way that the elastic properties can now be identified from the resonant frequencies of the first five vibrations modes of the plate-shaped specimen. The two beam-shaped specimens are no longer required.
- The development of a new MNET procedure that can identify the elastic properties of orthotropic materials from the resonant frequencies of the fundamental flexural and torsional vibration modes of a set of beam-shaped specimens each of which represents a different material orientation. Since this technique only requires beam-shaped specimens, it allows the characterisation of orthotropic materials at high temperatures, in a furnace.
- The introduction of three vibration-based MNETs for the identification of the elastic properties of layered materials. The developed techniques can identify the elastic properties of both isotropic and orthotropic layers.
- The text presents a comparison of the various vibration-based identification techniques for both homogeneous and layered materials. All these techniques are critically evaluated using a number of numerical and experimental validation tests.
- The introduction of a probabilistic and a non-probabilistic approach to handle the uncertainties in vibration-based MNETs. The presented uncertainty analysis algorithms estimate the uncertainty on the identified elastic parameters from the uncertainties on the experimentally measured quantities in a computationally efficient way.

1.4. Structure of the Thesis

This thesis comprises three main parts. The first part introduces a number of mathematical tools, the second part uses these mathematical tools to build a series of identification procedures, and the last part provides an experimental validation together with a number of applications of the presented identification routines. The text is organised in nine chapters.

Chapter 1 — Introduces the thesis by situating the subject, highlighting the personal contributions and clarifying the structure of the text.

Chapter 2 — Discusses the basics of the theory of linear elasticity. It introduces the isotropic and orthotropic material model and presents the thermodynamic restrictions on the parameters of these two models.

Chapter 3 — The first part of this chapter discusses the basics of the finite element method for normal modes analysis. The second part of this chapter introduces sensitivity analysis and gives a detailed discussion on its use in vibration-based material identification routines.

Chapter 4 — Presents an overview of the use of optimisation theory in MNETs together with the general framework to solve the optimisation problem of a vibration-based MNET.

Chapter 5 — Introduces the classical lamination theory and discusses the vibratory behaviour of layered materials.

Chapter 6 — Presents and discusses the vibration-based identification routines for both homogeneous and layered materials.

Chapter 7 — This chapter introduces the concept of measurement uncertainty and presents a probabilistic and a non-probabilistic approach to handle uncertainty with MNET-based identification routines.

Chapter 8 — Presents the validation tests performed on two different reference materials in order to validate the MNET-based procedures of chapter 6 in an experimental way.

Chapter 9 — Presents a number of applications of layered material identification, using the MNET-based procedures introduced in chapter 6, to identify the elastic properties of different types of ceramic coatings.

Chapter 10 — Summarises the conclusions and provides some suggestions for future research.

2
Linear Elasticity

This chapter provides a general overview of the theory of linear elasticity and presents a detailed discussion of both the isotropic and orthotropic material model. The text of this chapter is based on the material presented in references [52] and [53].

2.1. The Generalized Hooke's Law

When linear elastic behaviour is assumed, the stress-strain relation of a material is given by the generalized Hooke's law. In matrix form, Hooke's law is expressed as

$$\{\sigma\} = [C]\{\varepsilon\} \tag{2.1}$$

in which the vectors $\{\sigma\}$ and $\{\varepsilon\}$ group the stress and strain components, respectively. Since both $\{\sigma\}$ and $\{\varepsilon\}$ are elements of $\mathbb{R}^6$, the stiffness matrix $[C]$ has to be an element of $\mathbb{R}^{6\times 6}$. This means that 36 parameters are needed to describe a material's stress-strain relation. However, it can be shown that the stiffness matrix has to be symmetric [52], reducing the number of independent constants to 21. The most general expression within the framework of linear elasticity is thus given by

$$\begin{Bmatrix} \sigma_1 \\ \sigma_2 \\ \sigma_3 \\ \tau_{23} \\ \tau_{31} \\ \tau_{12} \end{Bmatrix} = \begin{bmatrix} C_{11}\, C_{12}\, C_{13}\, C_{14}\, C_{15}\, C_{16} \\ C_{12}\, C_{22}\, C_{23}\, C_{24}\, C_{25}\, C_{26} \\ C_{13}\, C_{23}\, C_{33}\, C_{34}\, C_{35}\, C_{36} \\ C_{14}\, C_{24}\, C_{34}\, C_{44}\, C_{45}\, C_{46} \\ C_{15}\, C_{25}\, C_{35}\, C_{45}\, C_{55}\, C_{56} \\ C_{16}\, C_{26}\, C_{36}\, C_{46}\, C_{56}\, C_{66} \end{bmatrix} \begin{Bmatrix} \varepsilon_1 \\ \varepsilon_2 \\ \varepsilon_3 \\ \gamma_{23} \\ \gamma_{31} \\ \gamma_{12} \end{Bmatrix} \tag{2.2}$$

in which σ_i and ε_i are the normal stress and strain component in the i-direction, while τ_{ij} and γ_{ij} are the shear stress and shear strain in the ij-plane. Under the assumption of small deformations, the strain vector $\{\varepsilon\}$ is related to the displacement vector $\{u\}$ as

$$\{\varepsilon\} = [\partial]\{u\} \tag{2.3}$$

or

$$\begin{Bmatrix} \varepsilon_1 \\ \varepsilon_2 \\ \varepsilon_3 \\ \gamma_{23} \\ \gamma_{31} \\ \gamma_{12} \end{Bmatrix} = \begin{bmatrix} \dfrac{\partial}{\partial x} & 0 & 0 & 0 & \dfrac{\partial}{\partial z} & \dfrac{\partial}{\partial y} \\ 0 & \dfrac{\partial}{\partial y} & 0 & \dfrac{\partial}{\partial z} & 0 & \dfrac{\partial}{\partial x} \\ 0 & 0 & \dfrac{\partial}{\partial z} & \dfrac{\partial}{\partial y} & \dfrac{\partial}{\partial x} & 0 \end{bmatrix}^{\mathrm{T}} \begin{Bmatrix} u \\ v \\ w \end{Bmatrix} \tag{2.4}$$

where u, v, and w are the displacement components in the x-, y-, and z-direction, respectively.

Equation (2.2) models an anisotropic material which has no planes of symmetry for its material properties. Such a material is called a triclinic material. If any material symmetry exists, the number of independent properties decreases further, since the material symmetry induces relations between the various stiffness coefficients. For a material with a single symmetry plane, the stress-strain relation reduces to

$$\begin{Bmatrix} \sigma_1 \\ \sigma_2 \\ \sigma_3 \\ \tau_{23} \\ \tau_{31} \\ \tau_{12} \end{Bmatrix} = \begin{bmatrix} C_{11} & C_{12} & C_{13} & 0 & 0 & C_{16} \\ C_{12} & C_{22} & C_{23} & 0 & 0 & C_{26} \\ C_{13} & C_{23} & C_{33} & 0 & 0 & C_{36} \\ 0 & 0 & 0 & C_{44} & C_{45} & 0 \\ 0 & 0 & 0 & C_{45} & C_{55} & 0 \\ C_{16} & C_{26} & C_{36} & 0 & 0 & C_{66} \end{bmatrix} \begin{Bmatrix} \varepsilon_1 \\ \varepsilon_2 \\ \varepsilon_3 \\ \gamma_{23} \\ \gamma_{31} \\ \gamma_{12} \end{Bmatrix} \tag{2.5}$$

in case the *12*-plane is the symmetry plane. Materials with one symmetry plane are called monoclinic and can be described with 13 independent elastic constants. Note that the structure of the stiffness matrix will only comply with the structure presented in (2.5), when the coordinate system used to define the stress and strain vectors is aligned with the symmetry plane of the material properties. When an arbitrary coordinate system is chosen, the stiffness matrix will contain 36 non-zero elements, of which only 13 are independent.

The existence of two orthogonal symmetry planes in a material automatically implies the presence of a third symmetry plane, orthogonal to the first two [53]. A material with three orthogonal symmetry planes is called orthotropic. If the used coordinate system is aligned with the principal material directions, i.e. the directions parallel to the intersections of the three orthogonal symmetry planes, the stress-strain relation becomes

$$\begin{Bmatrix} \sigma_1 \\ \sigma_2 \\ \sigma_3 \\ \tau_{23} \\ \tau_{31} \\ \tau_{12} \end{Bmatrix} = \begin{bmatrix} C_{11} & C_{12} & C_{13} & 0 & 0 & 0 \\ C_{12} & C_{22} & C_{23} & 0 & 0 & 0 \\ C_{13} & C_{23} & C_{33} & 0 & 0 & 0 \\ 0 & 0 & 0 & C_{44} & 0 & 0 \\ 0 & 0 & 0 & 0 & C_{55} & 0 \\ 0 & 0 & 0 & 0 & 0 & C_{66} \end{bmatrix} \begin{Bmatrix} \varepsilon_1 \\ \varepsilon_2 \\ \varepsilon_3 \\ \gamma_{23} \\ \gamma_{31} \\ \gamma_{12} \end{Bmatrix} \tag{2.6}$$

The elastic behaviour of an orthotropic material can be described with 9 independent constants. Equation (2.6) shows that there is no interaction between the normal stresses and the shear strains, between the shear stresses and normal strains, and between the shear stresses and shear strains in different planes. Also note that these interactions do exist, when the coordinate system is not aligned parallel to the symmetry planes. In this situation, the stiffness matrix will once again have 36 non-zero coefficients.

If the material has an infinite number of symmetry planes, the material is said to be isotropic. In the case of an isotropic material, the stress-strain relation simplifies to

$$\begin{Bmatrix} \sigma_1 \\ \sigma_2 \\ \sigma_3 \\ \tau_{23} \\ \tau_{31} \\ \tau_{12} \end{Bmatrix} = \begin{bmatrix} C_{11} & C_{12} & C_{12} & 0 & 0 & 0 \\ C_{12} & C_{11} & C_{12} & 0 & 0 & 0 \\ C_{12} & C_{12} & C_{11} & 0 & 0 & 0 \\ 0 & 0 & 0 & \dfrac{C_{11}-C_{12}}{2} & 0 & 0 \\ 0 & 0 & 0 & 0 & \dfrac{C_{11}-C_{12}}{2} & 0 \\ 0 & 0 & 0 & 0 & 0 & \dfrac{C_{11}-C_{12}}{2} \end{bmatrix} \begin{Bmatrix} \varepsilon_1 \\ \varepsilon_2 \\ \varepsilon_3 \\ \gamma_{23} \\ \gamma_{31} \\ \gamma_{12} \end{Bmatrix} \tag{2.7}$$

Equation (2.7) indicates that an isotropic material is defined by only 2 inde-

pendent constants. Since any arbitrary plane is a symmetry plane, the choice of the coordinate system does not change the values of the stiffness constants, nor the number of non-zero elements of the stiffness matrix.

The generalized Hooke's law can also be written in terms of compliances, relating the strains to the stresses as

$$\{\varepsilon\} = [S]\{\sigma\} \quad \text{with} \quad [S] = [C]^{-1} \tag{2.8}$$

The matrix $[S]$ is called the compliance matrix. It can be shown that the compliance matrix has the same structure as the stiffness matrix [53]. The compliance matrices of triclinic, monoclinic, orthotropic, and isotropic materials can thus be obtained by replacing C_{ij} with S_{ij} in equations (2.2) and (2.5–2.7).

To conclude, it must be emphasised that the number of independent constants is a very important quantity from an identification point of view, since it determines the number of parameters that will have to be identified in order to fully describe the constitutive behaviour of the material. Also note that the behaviour of a material is controlled by the number of non-zero coefficients and not as much by the number of independent constants. For example: an on-axis orthotropic material and an isotropic material will qualitatively behave the same, since both materials have 12 non-zero stiffness coefficients. Table 2.1 summarizes the properties of the different material classes.

Table 2.1: *Summary of the material symmetries [53].*

Symmetry type	Independent constants	Non-zero constants	
		On-axis	Off-axis
Triclinic	21	36	36
Monoclinic	13	20	36
Orthotropic	9	12	36
Isotropic	2	12	12

2.2. Orthotropic Materials

2.2.1. Engineering Constants

In practice, elastic material properties are usually characterized with a set of engineering constants like generalized Young's moduli, shear moduli and Poisson's ratios. For an orthotropic material, there are twelve engineering constants. The Young's modulus in the i-direction is defined as

$$E_i = \frac{\sigma_i}{\varepsilon_i}, \qquad i = 1, 2, 3 \tag{2.9}$$

considering a stress state where σ_i is the only non-zero stress component.

The shear modulus in the ij-plane is defined as

$$G_{ij} = \frac{\tau_{ij}}{\gamma_{ij}}, \qquad ij = 12, 23, 31 \tag{2.10}$$

considering a stress state where τ_{ij} is the only non-zero stress component.
The Poisson's ratio for transverse strain in the j-direction when the material is stressed in the i-direction is defined as

$$\nu_{ij} = -\frac{\varepsilon_j}{\varepsilon_i}, \qquad ij = 12, 13, 21, 23, 31, 32 \tag{2.11}$$

considering a stress state where σ_i is the only non-zero stress component.
The definitions of the engineering constants originate from the traditional test methods used to characterise the elastic behaviour of materials such as uni-axial tension or pure shear tests [52]. These traditional tests are usually performed with a controlled strain or displacement, while the required force is measured. This obviously explains the choice of uni-axial stress conditions in the definitions of the engineering constants.
Since the engineering constants are defined for uni-axial stress conditions, it is much easier to express them in terms of compliances than in terms of stiffnesses. The combination of the definitions in (2.9–2.11) with the strain-stress relations of an orthotropic material result in the expressions of (2.12–2.14), which relate the engineering constants to the compliances. Remember that the compliance matrix of an orthotropic material has the same structure as the stiffness matrix of (2.6).

$$E_1 = \frac{1}{S_{11}} \qquad E_2 = \frac{1}{S_{22}} \qquad E_3 = \frac{1}{S_{33}} \tag{2.12}$$

$$G_{23} = \frac{1}{S_{44}} \qquad G_{31} = \frac{1}{S_{55}} \qquad G_{12} = \frac{1}{S_{66}} \tag{2.13}$$

$$\begin{aligned} \nu_{12} &= -\frac{S_{12}}{S_{11}} & \nu_{23} &= -\frac{S_{23}}{S_{22}} & \nu_{31} &= -\frac{S_{13}}{S_{33}} \\ \nu_{21} &= -\frac{S_{12}}{S_{22}} & \nu_{32} &= -\frac{S_{23}}{S_{33}} & \nu_{13} &= -\frac{S_{13}}{S_{11}} \end{aligned} \tag{2.14}$$

The expressions of equation (2.14) show that

$$\frac{\nu_{ij}}{S_{jj}} = \frac{\nu_{ji}}{S_{ii}} \tag{2.15}$$

which means that there are only three independent Poisson's ratios. In terms of engineering constants, the Poisson's ratios are related as follows

$$\frac{\nu_{ij}}{E_i} = \frac{\nu_{ji}}{E_j} \tag{2.16}$$

2.2.2. Elastic Properties for an Arbitrary Orientation

The properties discussed in the previous section are defined in the directions of the principal material axes. These on-axis properties describe the behaviour of the material when subjected to a stress field that is aligned with the principal

material axes. But as already mentioned, the behaviour of a material can vary with the orientation of the considered load. The off-axis properties describe the material behaviour when subjected to a stress field with an arbitrary orientation. The goal of this section is to establish the link between the on- and off-axis properties.

Consider a load with an arbitrary orientation and a local axis system x-y-z which is aligned to the principal directions of this load. In this local axis system, the stress-strain relation can be expressed as

$$\{\overline{\varepsilon}\} = [\overline{S}]\{\overline{\sigma}\} \tag{2.17}$$

where the overline indicates that the quantities are expressed in local coordinates. The transformed compliance matrix $[\overline{S}]$ contains the off-axis properties. The local coordinate system can be obtained from the global system, i.e. the *1-2-3* system, by applying three successive rotations. These rotations are mathematically represented by the transformation matrix

$$[T] = \left[\begin{array}{c|c} T_{11} & T_{12} \\ \hline T_{21} & T_{22} \end{array}\right] \tag{2.18}$$

where

$$[T_{11}] = \begin{bmatrix} a_{11}^2 & a_{12}^2 & a_{13}^2 \\ a_{21}^2 & a_{22}^2 & a_{23}^2 \\ a_{31}^2 & a_{32}^2 & a_{33}^2 \end{bmatrix}$$

$$[T_{12}] = \begin{bmatrix} 2a_{11}a_{12} & 2a_{12}a_{13} & 2a_{13}a_{11} \\ 2a_{21}a_{22} & 2a_{22}a_{23} & 2a_{23}a_{21} \\ 2a_{31}a_{32} & 2a_{32}a_{33} & 2a_{33}a_{31} \end{bmatrix}$$

$$[T_{21}] = \begin{bmatrix} a_{11}a_{21} & a_{12}a_{22} & a_{13}a_{23} \\ a_{21}a_{31} & a_{22}a_{32} & a_{23}a_{33} \\ a_{31}a_{11} & a_{32}a_{12} & a_{33}a_{13} \end{bmatrix}$$

$$[T_{22}] = \begin{bmatrix} a_{11}a_{22} + a_{12}a_{21} & a_{12}a_{23} + a_{13}a_{22} & a_{13}a_{21} + a_{11}a_{23} \\ a_{21}a_{32} + a_{22}a_{31} & a_{22}a_{33} + a_{23}a_{32} & a_{23}a_{31} + a_{21}a_{33} \\ a_{31}a_{12} + a_{32}a_{11} & a_{32}a_{13} + a_{33}a_{12} & a_{33}a_{11} + a_{31}a_{13} \end{bmatrix}$$

in which a_{ij} represents the cosine of the angle between the final position of the i-axis, and the initial position of the j-axis. The on- and off-axis stress vectors are thus related as

$$\begin{Bmatrix} \sigma_x \\ \sigma_y \\ \sigma_z \\ \tau_{yz} \\ \tau_{zx} \\ \tau_{xy} \end{Bmatrix} = [T] \begin{Bmatrix} \sigma_1 \\ \sigma_2 \\ \sigma_3 \\ \tau_{23} \\ \tau_{31} \\ \tau_{12} \end{Bmatrix} \tag{2.19}$$

or in contracted notation

$$\{\overline{\sigma}\} = [T]\{\sigma\} \tag{2.20}$$

The on-axis and off-axis strains are related as

$$\begin{Bmatrix} \varepsilon_x \\ \varepsilon_y \\ \varepsilon_z \\ \frac{1}{2}\gamma_{yz} \\ \frac{1}{2}\gamma_{zx} \\ \frac{1}{2}\gamma_{xy} \end{Bmatrix} = [T] \begin{Bmatrix} \varepsilon_1 \\ \varepsilon_2 \\ \varepsilon_3 \\ \frac{1}{2}\gamma_{23} \\ \frac{1}{2}\gamma_{31} \\ \frac{1}{2}\gamma_{12} \end{Bmatrix} \tag{2.21}$$

In order to express this relation in terms of 'classical' strain vectors as in (2.2), Reuter [54] introduced a weighting matrix $[R]$.

$$[R] = \begin{bmatrix} 1 & 0 & 0 & 0 & 0 & 0 \\ 0 & 1 & 0 & 0 & 0 & 0 \\ 0 & 0 & 1 & 0 & 0 & 0 \\ 0 & 0 & 0 & 2 & 0 & 0 \\ 0 & 0 & 0 & 0 & 2 & 0 \\ 0 & 0 & 0 & 0 & 0 & 2 \end{bmatrix} \tag{2.22}$$

By using the Reuter matrix, the strain relation (2.21) can be contracted as

$$\{\overline{\varepsilon}\} = [R][T][R]^{-1}\{\varepsilon\} \tag{2.23}$$

In the global axis system, the strain and stress vectors are related as (2.8).

$$\{\varepsilon\} = [S]\{\sigma\} \tag{2.24}$$

This on-axis strain-stress relation can be expressed in term of off-axis strain and stress components by means of the transformation expressions (2.20) and (2.23).

$$\{\overline{\varepsilon}\} = [R][T][R]^{-1}[S][T]^{-1}\{\overline{\sigma}\} \tag{2.25}$$

Equation (2.25) expresses the off-axis strain-stress relation (2.17). The on- and off-axis compliances are thus related as

$$[\overline{S}] = [R][T][R]^{-1}[S][T]^{-1} \tag{2.26}$$

Note that the elaboration of the right-hand side of (2.26) will show that the off-axis compliance matrix is symmetrical.

2.3. Isotropic Materials

In case of isotropic material behaviour, the engineering constants are related to the compliances as

$$E_1 = \quad E_2 = \quad E_3 = \frac{1}{S_{11}} \tag{2.27}$$

$$G_{12} = \quad G_{23} = \quad G_{13} = \frac{1}{2(S_{11} - S_{12})} \tag{2.28}$$

$$\begin{aligned} \nu_{12} &= \quad \nu_{23} = \quad \nu_{31} = -\frac{S_{12}}{S_{11}} \\ \nu_{21} &= \quad \nu_{32} = \quad \nu_{13} = -\frac{S_{12}}{S_{11}} \end{aligned} \tag{2.29}$$

or simplified

$$E = \frac{1}{S_{11}}, \qquad G = \frac{1}{2(S_{11} - S_{12})}, \qquad \nu = -\frac{S_{12}}{S_{11}} \tag{2.30}$$

Elimination of the compliances S_{11} and S_{12} from the equations of (2.30) provides the following relation between the three engineering constants of an isotropic material

$$G = \frac{E}{2(1+\nu)} \tag{2.31}$$

Note that for isotropic materials, every plane is a plane of symmetry. Therefore, the properties of isotropic materials cannot vary in function of the material orientation.

2.4. Two-Dimensional Stress Analysis

For plate-like structures, the stress analysis is usually carried out under the Kirchhoff assumptions[1]. For a structure parallel to the *12*-plane, the Kirchhoff assumptions result in plane stress state where

$$\sigma_3 = 0, \qquad \tau_{23} = 0, \qquad \tau_{31} = 0 \tag{2.32}$$

Furthermore, in the case of plate-like objects, the normal strain in the transverse direction, ε_3, is sufficiently small so that it can be ignored.

2.4.1. Orthotropic Materials

Accepting the Kirchhoff assumptions, the general strain-stress relation for orthotropic materials reduces to the following in-plane strain-stress relation

$$\begin{Bmatrix} \varepsilon_1 \\ \varepsilon_2 \\ \gamma_{12} \end{Bmatrix} = \begin{bmatrix} S_{11} & S_{12} & 0 \\ S_{12} & S_{22} & 0 \\ 0 & 0 & S_{66} \end{bmatrix} \begin{Bmatrix} \sigma_1 \\ \sigma_2 \\ \tau_{12} \end{Bmatrix} \tag{2.33}$$

The in-plane stress-strain relation (2.34) is obtained by inverting the reduced strain-stress relation (2.33)

$$\begin{Bmatrix} \sigma_1 \\ \sigma_2 \\ \tau_{12} \end{Bmatrix} = \begin{bmatrix} Q_{11} & Q_{12} & 0 \\ Q_{12} & Q_{22} & 0 \\ 0 & 0 & Q_{66} \end{bmatrix} \begin{Bmatrix} \varepsilon_1 \\ \varepsilon_2 \\ \gamma_{12} \end{Bmatrix} \tag{2.34}$$

[1] More information on the Kirchhoff assumptions can be found in chapter 5.

The reduced stiffness coefficients Q_{ij} are related to the compliances as follows

$$\begin{aligned} Q_{11} &= \frac{S_{22}}{S_{11}S_{22} - S_{12}^2}, \qquad Q_{12} = -\frac{S_{12}}{S_{11}S_{22} - S_{12}^2}, \\ Q_{22} &= \frac{S_{11}}{S_{11}S_{22} - S_{12}^2}, \qquad S_{66} = \frac{1}{S_{66}} \end{aligned} \tag{2.35}$$

or to the engineering constants as

$$\begin{aligned} Q_{11} &= \frac{E_1}{1 - \nu_{12}\nu_{21}}, \qquad Q_{12} = \frac{\nu_{12}E_2}{1 - \nu_{12}\nu_{21}}, \\ Q_{22} &= \frac{E_2}{1 - \nu_{12}\nu_{21}}, \qquad Q_{66} = G_{12} \end{aligned} \tag{2.36}$$

Remember that, according to equation (2.16)

$$\frac{\nu_{12}}{E_1} = \frac{\nu_{21}}{E_2} \tag{2.37}$$

which implies that, under the Kirchhoff assumptions, the elastic behaviour of an orthotropic material can be fully described by four instead of nine independent engineering constants, i.e. E_1, E_2, G_{12} and ν_{12}. The off-axis properties are still obtained with (2.26), but the rotation matrix (2.18) and Reuter matrix (2.22) reduce to

$$[T] = \begin{bmatrix} \cos^2\theta & \sin^2\theta & -2\sin\theta\cos\theta \\ \sin^2\theta & \cos^2\theta & 2\sin\theta\cos\theta \\ \sin\theta\cos\theta & -\sin\theta\cos\theta & \cos^2\theta - \sin^2\theta \end{bmatrix}, \quad [R] = \begin{bmatrix} 1 & 0 & 0 \\ 0 & 1 & 0 \\ 0 & 0 & 2 \end{bmatrix} \tag{2.38}$$

where θ is the angle between the x- and 1-axis, as shown in figure 2.1.

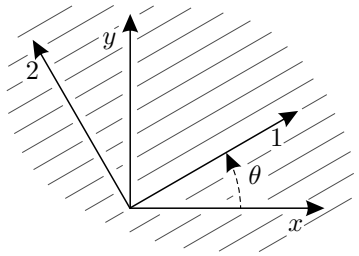

Figure 2.1: *The definition of the orientation angle θ.*

Elaboration of the right-hand side of (2.26) after the introduction of the two expressions of (2.38) yields the following relations between the on- and off-axis in-plane compliances.

$$
\begin{aligned}
\overline{S}_{11} &= S_{11}\cos^4\theta + (2S_{12}+S_{66})\sin^2\theta\ \cos^2\theta + S_{22}\sin^4\theta \\
\overline{S}_{12} &= S_{12}\left(\sin^4\theta+\cos^4\theta\right) + (S_{11}+S_{22}-S_{66})\sin^2\theta\ \cos^2\theta \\
\overline{S}_{22} &= S_{11}\sin^4\theta + (2S_{12}+S_{66})\sin^2\theta\ \cos^2\theta + S_{22}\cos^4\theta \\
\overline{S}_{16} &= (2S_{11}-2S_{12}-S_{66})\sin\theta\ \cos^3\theta - (2S_{22}-2S_{12}-S_{66})\sin^3\theta\ \cos\theta \\
\overline{S}_{26} &= (2S_{11}-2S_{12}-S_{66})\sin^3\theta\ \cos\theta - (2S_{22}-2S_{12}-S_{66})\sin\theta\ \cos^3\theta \\
\overline{S}_{66} &= 2\,(2S_{11}+2S_{22}-4S_{12}-S_{66})\sin^2\theta\ \cos^2\theta + S_{66}\left(\sin^4\theta+\cos^4\theta\right)
\end{aligned}
\tag{2.39}
$$

Since the transformed compliance matrix is symmetrical, the six coefficients of (2.39) are sufficient to construct the complete $[\overline{S}]$ matrix. Note that, for an arbitrary value of the orientation angle θ, the transformed compliance matrix has nine non-zero elements. However, the elastic behaviour is still fully characterised by only four independent material constants. By considering the relations of (2.12–2.14), the on- and off-axis compliance relations can be transformed into the following relations between the engineering constants [52]

$$\frac{1}{E_x} = \frac{1}{E_1}\cos^4\theta + \left(\frac{1}{G_{12}} - \frac{2\nu_{12}}{E_1}\right)\sin^2\theta\ \cos^2\theta + \frac{1}{E_2}\sin^4\theta \tag{2.40}$$

$$\frac{1}{E_y} = \frac{1}{E_1}\sin^4\theta + \left(\frac{1}{G_{12}} - \frac{2\nu_{12}}{E_1}\right)\sin^2\theta\ \cos^2\theta + \frac{1}{E_2}\cos^4\theta \tag{2.41}$$

$$\frac{1}{G_{xy}} = 2\left(\frac{2}{E_1}+\frac{2}{E_2}+\frac{4\nu_{12}}{E_1}-\frac{1}{G_{12}}\right)\sin^2\theta\ \cos^2\theta + \frac{1}{G_{12}}\left(\sin^4\theta+\cos^4\theta\right) \tag{2.42}$$

$$\nu_{xy} = E_x\left[\frac{\nu_{12}}{E_1}\left(\sin^4\theta+\cos^4\theta\right) - \left(\frac{1}{E_1}+\frac{1}{E_2}-\frac{1}{G_{12}}\right)\sin^2\theta\ \cos^2\theta\right] \tag{2.43}$$

The constants E_x, E_y, G_{xy}, and ν_{xy} are the apparent elastic properties and represent the values of the engineering constants in the directions defined by the local axis system. Unlike the principal engineering constants E_1, E_2, G_{12}, and ν_{12}, the apparent properties are not independent and do not, therefore, provide enough information to fully describe the material behaviour. The description of the material behaviour in the local axis system also requires the values of the two coefficients of mutual influence. The coefficient of mutual influence of the first kind characterises the stretching in the i-direction caused by a shear deformation in the ij-plane. The coefficient of mutual influence of the second kind characterises the shearing in the ij-plane caused by a normal deformation in the i-direction. Both coefficients of mutual influence are zero in the on-axis directions. More details about these coefficients can be found in [55].

The equations (2.40–2.43) allow to plot the apparent elastic properties in function of the material orientation. To illustrate this, consider a unidirectionally reinforced carbon-epoxy material with the following elastic properties: $E_1 = 100\,\text{GPa}$, $E_2 = 10\,\text{GPa}$, $G_{12} = 5\,\text{GPa}$, and $\nu_{12} = 0.25$. Figure 2.2 presents the orientational variation of the elastic properties. These plots illustrate that orthotropic materials have two orthogonal symmetry axes in the *12*-plane. One quarter of the plots of figure 2.2 provides all the available information. The vari-

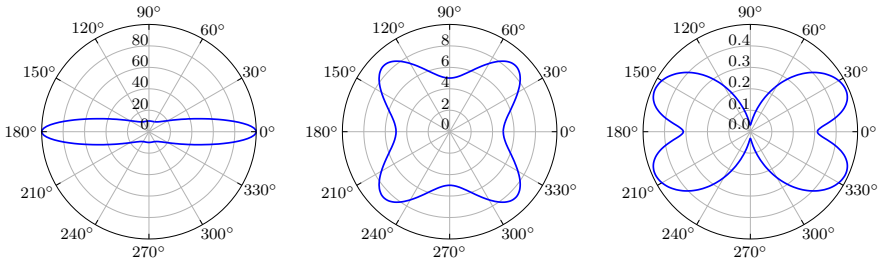

(a) E_x-modulus [GPa] (b) G_{xy}-modulus [GPa] (c) Poisson's ratio ν_{xy} [–]

Figure 2.2: *The variation of the elastic properties in function of the orientation in a polar coordinate system of the considered carbon-epoxy.*

ation of the material properties can therefore be fully represented by plotting the properties for the range $[0°, 90°]$. Figure 2.3 shows the elastic properties in this range using a Cartesian coordinate system. The relations between the principal and apparent elastic properties (2.40–2.43) and the Cartesian representation of the variation of the apparent properties will be extensively used in the identification routines that are developed in chapter 6.

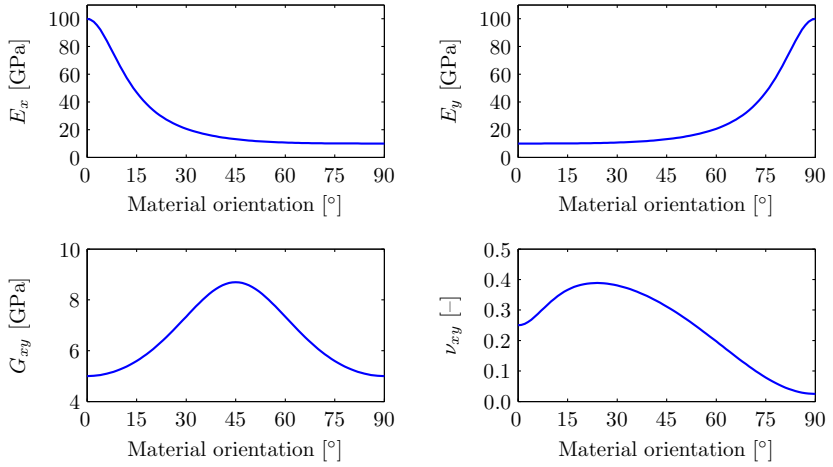

Figure 2.3: *The variation of the elastic properties in function of the orientation in a Cartesian coordinate system.*

2.4.2. Isotropic Materials

Under the Kirchhoff assumptions, the strain-stress relation of an isotropic material becomes

$$\begin{Bmatrix} \varepsilon_1 \\ \varepsilon_2 \\ \gamma_{12} \end{Bmatrix} = \begin{bmatrix} S_{11} & S_{12} & 0 \\ S_{12} & S_{11} & 0 \\ 0 & 0 & 2(S_{11} - S_{12}) \end{bmatrix} \begin{Bmatrix} \sigma_1 \\ \sigma_2 \\ \tau_{12} \end{Bmatrix} \tag{2.44}$$

in which

$$S_{11} = \frac{1}{E} \qquad S_{12} = -\frac{\nu}{E} \tag{2.45}$$

The in-plane stress-strain relation (2.46) is obtained by inverting the strain-stress relation (2.44)

$$\begin{Bmatrix} \sigma_1 \\ \sigma_2 \\ \tau_{12} \end{Bmatrix} = \begin{bmatrix} Q_{11} & Q_{12} & 0 \\ Q_{12} & Q_{22} & 0 \\ 0 & 0 & Q_{66} \end{bmatrix} \begin{Bmatrix} \varepsilon_1 \\ \varepsilon_2 \\ \gamma_{12} \end{Bmatrix} \tag{2.46}$$

in which the reduced stiffnesses Q_{ij} are related to the engineering constants as

$$Q_{11} = \frac{E}{1-\nu^2} \qquad Q_{12} = \frac{\nu E}{1-\nu^2} \qquad Q_{66} = \frac{E}{2\,(1+\nu)} \tag{2.47}$$

Unlike the case of orthotropic materials, the Kirchhoff assumptions do not reduce the number of independent parameters needed to describe the linear elastic behaviour of isotropic materials.

2.5. Restrictions on the Engineering Constants

The elastic material parameters cannot just take any value, they are restricted by a number of physical limits [52]. In the case of material identification applications, these limits can be used to check the validity of the obtained material parameters.

2.5.1. Orthotropic Materials

The considered restrictions are the so-called thermodynamic constraints which are based on the principle that the total work done by all the stress components must be positive in order to avoid the creation of energy [56]. The work done by a stress component is given by the product of the stress component with the corresponding strain component. The work of the stress components will only be positive, if the stiffness and compliance matrices are positive-definite [56]. Besides this mathematical approach, the restrictions on the engineering constants can also be derived in a more physical way. Consider a stress field where only the i^{th} stress component is non-zero. The work done by the stress field now equals the square of the stress component multiplied by S_{ii}. Since the work must be strictly positive, the diagonal elements of the compliance matrix must also be strictly positive. Under the Kirchhoff assumptions, this means that

$$S_{11}, S_{22}, S_{66} > 0 \tag{2.48}$$

which implies that

$$E_1 > 0 \qquad E_2 > 0 \qquad G_{12} > 0 \tag{2.49}$$

In the same way, by considering a strain field where there is only one non-zero strain component, one can prove that the diagonal elements of the reduced

stiffness matrix are strictly positive

$$Q_{11}, Q_{22}, Q_{66} > 0 \tag{2.50}$$

Considering the equations of (2.36), this implies that

$$1 - \nu_{12}\nu_{21} > 0 \tag{2.51}$$

By substituting (2.37) into (2.51), this inequality can be rewritten as

$$|\nu_{12}| < \sqrt{\frac{E_1}{E_2}} \qquad \text{or} \qquad |\nu_{21}| < \sqrt{\frac{E_2}{E_1}} \tag{2.52}$$

2.5.2. Isotropic Materials

The restrictions on the isotropic material parameters can be established using the same thermodynamic considerations as in the previous section. Once again, the diagonal elements of the compliance and reduced stiffness matrix must be strictly positive. Therefore,

$$S_{11} > 0 \qquad \text{and} \qquad Q_{11} > 0 \tag{2.53}$$

The first inequality shows that

$$E > 0 \tag{2.54}$$

In combination with (2.47) and (2.54), the second inequality implies that

$$1 - \nu^2 > 0 \tag{2.55}$$

or that

$$|\nu| < 1 \tag{2.56}$$

Note that the restriction of (2.56) complies with the restrictions found for orthotropic materials (2.52). However, in the case of isotropic materials the upper limit on Poisson's ratio can be improved. Consider a brick shaped solid body, made out of an isotropic material, which is subjected to a hydrostatic pressure p. If this brick shaped body has a unit volume V_0, then the volumetric strain [57] is defined as

$$\varepsilon_{vol} = \frac{\Delta V}{V_0} = \frac{V - V_0}{V_0} = (1 + \varepsilon_1)(1 + \varepsilon_2)(1 + \varepsilon_3) - 1 \approx \varepsilon_1 + \varepsilon_2 + \varepsilon_3 \tag{2.57}$$

By using the three-dimensional strain-stress relations for isotropic materials, i.e. the inverse of (2.7), the expression of the volumetric strain can be rewritten as

$$\varepsilon_{vol} = 3\,(S_{11} + 2S_{12})\,(-p) = 3\left(\frac{1}{E} - \frac{2\nu}{E}\right)(-p) \tag{2.58}$$

Note that the hydrostatic pressure p induces a stress $\sigma = -p$. The hydrostatic

pressure will compress the body, which means that the volumetric strain ε_{vol} must be negative. This implies that

$$\frac{1}{E} - \frac{2\nu}{E} > 0 \tag{2.59}$$

or that

$$\nu < \frac{1}{2} \tag{2.60}$$

The Poisson's ratio of an isotropic material is thus restricted to the range

$$-1 < \nu < \frac{1}{2} \tag{2.61}$$

2.6. Summary

This chapter discussed the linear elastic model for both isotropic and orthotropic materials. It also presented the principal material parameters that are required to model the elastic behaviour of a material, the relations between the material parameters in an on- and off-axis coordinate system, and the restrictions on the values of the material parameters which define the feasible domain of the identification problem.

3

The Finite Element Method & Sensitivity Analysis

The MNET procedures considered in this text require a mathematical model to compute the resonant frequencies of the test specimens. There is variety of available techniques of which the finite element method appears to be the optimal choice. The finite element method is not only the most popular technique to perform a numerical modal analysis, in the case of MNET procedures it has the advantage that it can provide the response gradients in a computationally efficient way. The second part of this chapter focuses on the computation of the necessary gradient information by means of sensitivity analysis.

3.1. The Finite Element Method

3.1.1. Theoretical Background

The finite element (FE) method is a commonly used technique in the analysis of mechanical structures, and is particularly useful to compute the vibratory behaviour of a structure. The versatility of the finite element method makes it an excellent technique for the development of powerful MNET-based material identification routines. This section aims at giving a short introduction on the finite element method, and at defining the notations that will be used in the remainder of the text. A detailed treatment of the finite element method can be found in [58, 59] or on-line on [60]. Figure 3.1 presents the three key steps of the finite element method: idealisation, discretisation and solution.

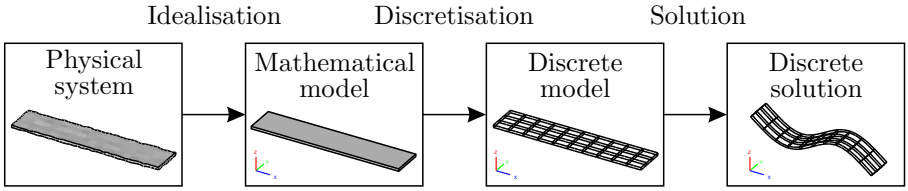

Figure 3.1: *Solving a physical problem with the finite element method.*

Idealisation

The first step consists of transforming the studied physical system into a mathematical model. This step is called idealisation, because the mathematical model is necessarily an abstraction of the physical reality. Even to build a model of a relatively simple system like a layered material sample, a substantial number of assumptions and simplifications have to be made. In this text, all samples will be modelled with:

- linear material behaviour
- purely elastic material behaviour, i.e. ignoring the influence of damping
- a uniform sample length, width and (layer) thickness
- homogeneous layers
- a perfect bonding of the different layers

The studied physical system is a vibrating material specimen. The mathematical model can be obtained by expressing the equilibrium of the specimen using the principle of virtual displacements [58]. According to this principle, the equilibrium of a body requires that, for any small virtual displacement imposed onto the body, the total internal virtual work equals the total external virtual work

$$\int_V \sigma^{\mathrm{T}} \tilde{\varepsilon} \, \mathrm{d}V = \int_V \tilde{u}^{\mathrm{T}} f_b \, \mathrm{d}V + \int_S \tilde{u}^{\mathrm{T}} f_s \, \mathrm{d}S + \sum \tilde{u}^{\mathrm{T}} f_c \tag{3.1}$$

in which u denotes the continuous displacement field, the overscript $\tilde{\diamond}$ marks the virtual quantities. The left-hand side of (3.1) represents the internal virtual work, which is a function of the displacement field u since $\{\sigma\} = [C]\{\varepsilon\}$ (2.1)

and $\{\varepsilon\} = [\partial]\,\{u\}$ (2.3) in every point of the volume V. The right-hand side quantifies the external virtual work of the body forces (f_b), the surface forces (f_s) and the concentrated forces (f_c). Since we are studying the free vibrations of undamped systems, the body forces are the inertial forces and there are no concentrated or surface forces, i.e.

$$f_b = -\rho\,\ddot{u}, \qquad f_s = 0, \qquad f_c = 0 \tag{3.2}$$

Substituting (3.2) into (3.1) provides the mathematical model of a freely vibrating, undamped material specimen as a set of partial differential equations

$$\int_V \tilde{u}^{\mathrm{T}} \rho \ddot{u}\,\mathrm{d}V + \int_V \sigma^{\mathrm{T}} \tilde{\varepsilon}\,\mathrm{d}V = 0 \tag{3.3}$$

Discretisation

The finite element method solves the partial differential equations of (3.3) by discretising the mathematical model in space, i.e. the continuous model is reduced to a discrete model with a finite number of degrees of freedom. This is done by dividing the volume of the specimen into a number of elements. Figure 3.2 presents a 20 node 3D element; further on in this chapter it will be shown that this is the optimal element for vibration-based MNETs.

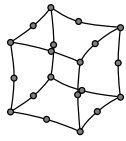

Figure 3.2: *A 20-node 3D finite element.*

In the case of 3D elements, the unknowns are the values of the displacement field u at the nodes of the elements. The displacements of the points between the nodes are obtained from the nodal displacements by interpolation. In finite element terminology, the interpolation functions are called shape functions and will be denoted as N_i. By grouping the shape functions of all the degrees of freedom i of one element into a shape function matrix $[N_e]$, the continuous displacement field can be related to the nodal displacement vector $\{u_e\}$ as

$$u_e = [N_e]\{u_e\} \tag{3.4}$$

where u_e is the continuous displacement field limited to the volume enclosed by the considered element. By inserting (3.4) into (2.3), the continuous strain field can be related to the nodal displacements as[1]

$$\varepsilon_e = [\partial][N_e]\{u_e\} = [B_e]\{u_e\} \tag{3.5}$$

Usually, the acceleration field $\ddot{u}_e$ is related to the nodal accelerations $\{\ddot{u}_e\}$ with the same shape functions, so

$$\ddot{u}_e = [N_e]\{\ddot{u}_e\} \tag{3.6}$$

[1]The structure of the $[B_e]$ matrix obtained from (2.4) is only valid for three-dimensional elements.

For the discretised model, the integrals of the system equations (3.3) can be expressed as a sum of integrals over the elements. In combination with equations (3.4–3.6), this provides

$$\sum_e \int_{V_e} \{\tilde{u}_e\}^{\mathrm{T}} [N_e]^{\mathrm{T}} \rho_e [N_e] \{\ddot{u}_e\} \, \mathrm{d}V_e + \sum_e \int_{V_e} \{\tilde{u}_e\}^{\mathrm{T}} [B_e]^{\mathrm{T}} [C_e] [B_e] \{u_e\} \, \mathrm{d}V_e = 0 \quad (3.7)$$

where V_e represents the volume enclosed by the element, ρ_e and $[C_e]$ respectively describe the mass density and the elastic properties of the material represented by the considered element. By grouping the nodal displacements of the whole model into one global nodal displacement vector $\{U\}$, equation (3.7) can be rewritten as

$$\{\tilde{U}\}^{\mathrm{T}} \left[\left(\sum_e \int_{V_e} [N_e]^{\mathrm{T}} \rho_e [N_e] \, \mathrm{d}V_e \right) \{\ddot{U}\} + \left(\sum_e \int_{V_e} [B_e]^{\mathrm{T}} [C_e] [B_e] \, \mathrm{d}V_e \right) \{U\} \right] = 0 \quad (3.8)$$

Since equation (3.8) must hold for any possible virtual displacement, the expression between the square brackets has to be equal to zero. Finally, the discretised model equations can be expressed as

$$[M]\{\ddot{U}(t)\} + [K]\{U(t)\} = \{0\} \quad (3.9)$$

where $[M]$ and $[K]$ are the global mass and stiffness matrices which are defined as

$$[M] = \sum_e [M_e] \qquad [K] = \sum_e [K_e] \quad (3.10)$$

where

$$[M_e] = \int_{V_e} [N_e]^{\mathrm{T}} \rho_e [N_e] \, \mathrm{d}V_e \quad (3.11)$$

$$[K_e] = \int_{V_e} [B_e]^{\mathrm{T}} [C_e] [B_e] \, \mathrm{d}V_e \quad (3.12)$$

The matrices $[M_e]$ and $[K_e]$ are called the element mass and stiffness matrices. Note that the finite element approach results in a symmetric global mass and stiffness matrix [58].

Solution

The material identification methods discussed in this text use the finite element models to compute the resonant frequencies of the test specimens. The resonant frequencies of the considered sample can be computed from (3.9) by assuming that the nodal displacements can be expressed as harmonic functions

$$\{U(t)\} = \{\psi\} \, \sin \omega t \quad (3.13)$$

in which ω represents the circular frequency and the vector $\{\psi\}$ describes the amplitude of the nodal displacements. By introducing (3.13) into (3.9), the time dependent factor can be segregated and eliminated. This leaves the following algebraic condition

$$\left([K] - \omega^2[M]\right)\{\psi\} = \{0\} \tag{3.14}$$

Equation (3.14) has the form of a generalised eigenvalue problem, where the eigenvalues $\lambda_i = \omega_i^2$ are the squared circular resonant frequencies while the eigenvectors $\{\psi\}_i$ represent the corresponding mode shapes[2]. By defining a diagonal matrix $[\Lambda]$ that groups all the eigenvalues, and by combining all the eigenvectors in one mode shape matrix $[\Psi] = [\{\psi\}_1\ \{\psi\}_2\ \ldots\ \{\psi\}_n]$, the eigenvalue problem (3.14) can be written as

$$[K][\Psi] - [M][\Psi][\Lambda] = [0] \tag{3.15}$$

There is a whole range of numerical techniques to solve the eigenvalue problem of (3.15), with the block-Lanczos algorithm being the most popular one [61].
To conclude, note that the eigenvectors are only defined upon a constant factor α, i.e. both $\{\psi\}$ and $\alpha\{\psi\}$ comply with (3.14). To obtain a unique solution, the mode shapes are usually scaled in such a way so as to satisfy the following condition

$$\{\psi\}^{\mathrm{T}}[M]\{\psi\} = \{1\} \tag{3.16}$$

Mode shapes scaled according to (3.16) are said to be mass normalised.

Error Sources

Every simulation step introduces a source of error, therefore one has to deal with modelling, discretisation and solution errors. The modelling errors result from the assumptions and simplifications that are made during the idealisation step. In engineering applications, the modelling errors are by far the most important ones, but they are very difficult to quantify [60]. Next in order of importance are the discretisation errors. Even if the solution errors are ignored – and usually they can be ignored – the solution of the discrete model is in general only an approximation of the exact solution of the mathematical model. The corresponding error, the discretisation error, decreases with an increasing number of degrees of freedom.

3.1.2. Finite Element Modelling in Material Identification

While the previous section dealt with the general theory behind the finite element method, this section focuses on the practical use of FE-modelling in the field of material identification. It addresses three important choices that have to be made to build a finite element model of a test specimen, i.e. the element type, the order of the shape functions, and the density of the mesh.

[2] A mode shape represents the relative displacement of all points on a structure at a particular resonant frequency.

The Element Type

The first choice regards the dimension of the elements, i.e. whether the elements are one-dimensional, two-dimensional or three-dimensional. Figure 3.3 presents these three classes of elements.

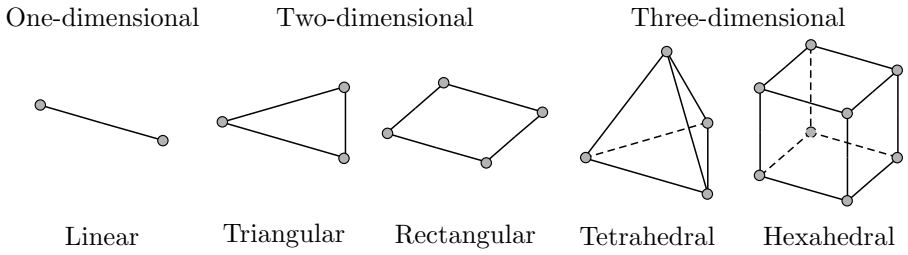

Figure 3.3: *A number of commonly used element types.*

One-dimensional elements cannot be used to model layered materials, since they are limited to homogeneous isotropic materials[3]. Therefore, one-dimensional elements will not be considered in the remainder of this text.
In theory, both two- and three-dimensional elements can be used to model layered beam- and plate-shaped samples. Two- and three-dimensional elements are available in different shapes, e.g. triangular, rectangular, tetrahedral, and hexahedral. The triangular and tetrahedral elements are only useful to model complex shapes. The rectangular and hexahedral elements are better suited to model rectangular beam- and plate-shaped specimens. Three-dimensional elements can be used for any type of structure and application, their use being only restricted by the high computational cost. Two-dimensional elements are computationally more efficient than three-dimensional elements, but their use in vibration-based MNETS is restricted by a number of limitations on the element formulation.
To verify whether two-dimensional elements are suitable to model the vibratory behaviour of the test samples, the three reference beams of figure 3.4 were modelled with both two- and three-dimensional elements. Table 3.1 summarises the properties of these three beams, table 3.2 presents the resonant frequencies that were obtained[4] for the fundamental flexural (f_f) and fundamental torsional mode (f_t).

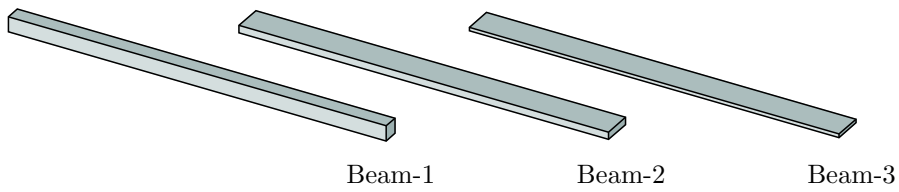

Figure 3.4: *The three reference beams.*

[3] In theory, it is possible to develop a one-dimensional element for layered materials. However, such an element is not available in commercial software packages as Nastran, Ansys, Patran, Marc, FEMtools etc.

[4] All the FE-calculation presented in this text were performed with the FEMtools software.

Table 3.1: *The properties of the three reference beams.*

Material		
E	[GPa]	70.0
ν	[–]	0.34
ρ	[kg/m^3]	2700

Sample	l [mm]	w [mm]	t [mm]
Beam-1	100.00	4.00	4.00
Beam-2	100.00	8.00	2.00
Beam-3	100.00	8.00	1.00

Table 3.2: *The resonant frequencies of the three reference beams.*

	Beam-1		Beam-2		Beam-3	
	$f_f[Hz]$	$f_t[Hz]$	$f_f[Hz]$	$f_t[Hz]$	$f_f[Hz]$	$f_t[Hz]$
2D	2095.10	30368.07	1047.97	7742.80	523.99	3878.05
3D	2081.65	14284.31	1046.05	6933.29	523.99	3710.38
Diff.	0.65%	112.60%	0.18%	11.68%	0.00%	4.52%

The results show an acceptable agreement between the resonant frequencies of the flexural mode, but reveal a significant difference for the frequency of the fundamental torsional mode. To verify if the results of the three-dimensional model are in fact more accurate than those of the two-dimensional model, the elastic material properties were identified from the resonant frequencies using the standardised ASTM identification formulas[5]. Table 3.3 presents the identified properties, and the differences between these properties and the properties of the finite element models.

Table 3.3: *The properties identified with the ASTM formulas.*

			Beam-1		Beam-2		Beam-3	
			Value	Diff.	Value	Diff.	Value	Diff.
2D-model	E	[GPa]	70.93	1.3%	70.37	0.5%	70.22	0.3%
	G	[GPa]	118.02	351.8%	32.33	23.8%	28.19	7.9%
3D-model	E	[GPa]	70.03	0.0%	70.11	0.2%	70.22	0.3%
	G	[GPa]	26.11	0.0%	25.92	−0.8%	25.81	−1.2%

If the frequencies are correct, they should result in the properties of the finite element model. Table 3.3 clearly indicates that the resonant frequencies of the three-dimensional model are more accurate than those of the two-dimensional model. Note that the ASTM formulas were derived for samples with a square cross-section and that an empirical correction factor is applied for samples with

[5]The ASTM standard [4] presents a set of analytical formulas that can identify the elastic and shear modulus of homogeneous and isotropic beam-shaped samples from the resonant frequencies of the fundamental flexural and torsional modes. The ASTM formulas are discussed in appendix A.

a rectangular cross-section. Therefore, the accuracy of the ASTM formulas decreases with the aspect-ratio of the cross-section. This explains why the difference is zero for beam-1 and increases from beam-2 to beam-3, in the case of the three-dimensional model. This evaluation demonstrates that material identification applications require three-dimensional finite element models.

The Order of the Shape Functions

The second choice that has to be made in order to build an FE-model regards the order of the shape functions of the elements. As explained in section 3.1.1, the finite element method calculates the modal displacements only in the nodes. The displacements of the other points are derived from the nodal displacements by means of shape functions. Standard finite element softwares usually provide elements with linear and quadratic shape functions. Using elements with quadratic shape functions results in a faster convergence of the resonant frequencies[6] with respect to the mesh density in the length, width, and thickness direction. To illustrate this, the fundamental out-of-plane flexural frequency of an aluminium beam was computed with a three-dimensional finite element model using both linear or quadratic shape functions. The mesh density in the length direction of the beam was gradually increased. Figure 3.5 presents the obtained resonant frequency as a function of the degrees of freedom of the finite element model. It is clear that the use of quadratic shape functions requires much less degrees of freedom than the use of linear shape functions, and will therefore result in a shorter computation time.

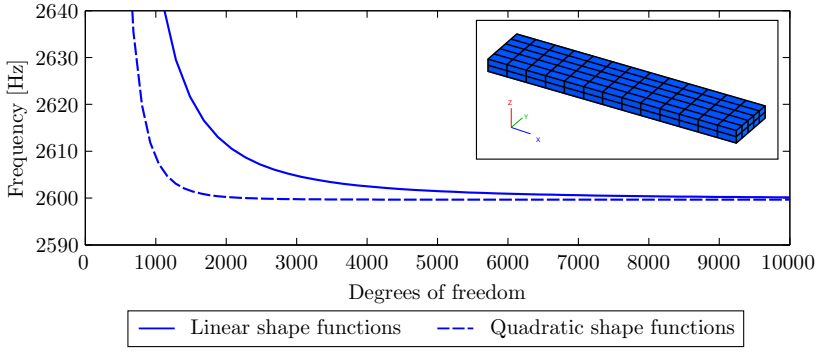

Figure 3.5: *Comparison of the resonant frequency of the fundamental flexural mode computed with the linear and quadratic shape functions.*

The Mesh Density

The last model parameter that has to be chosen is the mesh density. Section 3.1.1 explains that the finite element method uses a discretised version of the

[6]Finite element models with 3D elements are solved in terms of nodal displacements. The convergence criterion should thus be expressed in terms of displacements instead of in terms of resonant frequencies. However, the considered test samples have a rectangular shape and a structured mesh. Therefore, it is acceptable to express the convergence criterion in terms of resonant frequencies.

initial model to approximate the solution. The finer the discretisation, the better the FE-solution will approximate the correct solution. However, the finer the discretisation, the longer it takes to solve the system equations. The choice of the mesh density is therefore always a trade-off between accuracy and computation time. Since in material identification both accuracy and computation time[7] are important, the mesh density should be chosen in a well-considered manner.

Due to the fact that the correct solution to the problem is unknown, it is impossible to estimate the accuracy of the discretised solution in absolute terms. Consider two finite element models of which one has a mesh density of n_e elements along a particular sample side, while the other model has a mesh density of n_e+1 elements along the same side. The relative difference between the frequencies of one particular mode of these two models (δ) can be expressed as

$$\delta = \frac{f^{(n_e)} - f^{(n_e+1)}}{f^{(n_e)}} \tag{3.17}$$

Because the finite element solution converges with a refinement of the discretisation, the relative frequency difference will decrease with an increasing mesh density. Once δ is smaller than a predefined limit $\overline{\delta}$, the solution can be considered to have converged and the mesh density n_e should be used to model the test sample. A threshold $\overline{\delta} = 0.01\,\%$ was found to be a good compromise between speed and accuracy, and will be kept throughout this text.

Consider a 100×25×2 mm aluminium beam with the material properties of table 3.1. The resonant frequencies of the first four vibration modes were computed for an increasing mesh density along the length, width and thickness direction. Figure 3.6 presents the mode shapes of the first four vibration modes: two out-of-plane flexural (OOP) and two torsional (Tors) modes. Figures 3.7 to 3.9 present the relative frequency difference δ in function of the number of elements along a particular sample direction. These plots show that the higher order modes converge slower than the lower order modes, e.g. the first flexural mode requires 19 elements in the length direction, while the second flexural mode needs 25 elements. From a computational point of view, it is thus not advisable to include the higher order modes in the identification routines, if this is not strictly necessary. According to this convergence study, the computation of the fundamental flexural and torsional mode requires a finite element model with a 19×16×3 element mesh. Although the considered sample is much longer than wide, i.e. a length/width ratio of 4, the convergence criterion requires more or less the same number of elements in the length and the width direction. This shows that it is very difficult to determine a correct mesh density intuitively. It

[7] Accuracy — The material identification routines described in this text use simple beam- or plate-shaped specimens that are carefully machined out of a uniform material sample. The modelling error is therefore much lower than for finite element models of conventional engineering structures like car bodies or jet engines. Unlike in conventional finite element models, the discretisation error of a material sample model cannot be ignored.
Computation time — Solving the finite element model(s) is a part of every iteration step of the identification routine. A small reduction in the computation time of one model can thus result in a significant reduction of the total computation time.

Mode-1: OOP-1 Mode-2: Tors-1 Mode-3: OOP-2 Mode-4: Tors-2

Figure 3.6: *The first four vibration modes of the beam model.*

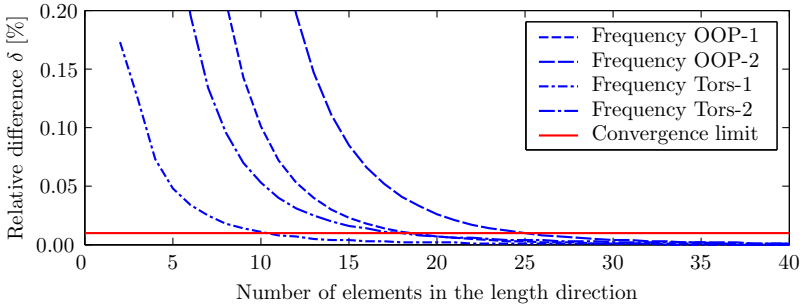

Figure 3.7: *The convergence plot in the length direction.*

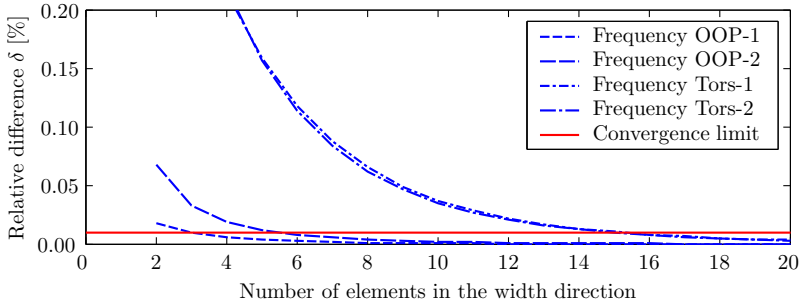

Figure 3.8: *The convergence plot in the width direction.*

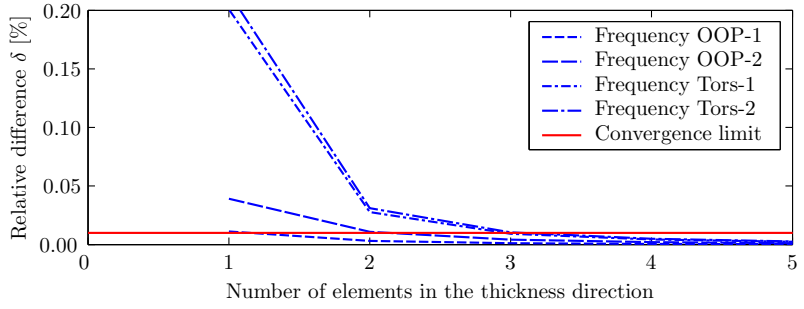

Figure 3.9: *The convergence plot in the thickness direction.*

is strictly necessary to perform a convergence study for every sample geometry used in the identification procedure.

3.1.3. Conclusions

Vibration-based material identification requires finite element models made of three-dimensional elements with quadratic shape functions. To limit the computation time to an acceptable level, it is advisable to use only the lower order modes, and to determine the optimal mesh density with a convergence study.

3.2. Sensitivity Analysis

The aim of sensitivity analysis is to quantify the influence of the input parameters of a particular model on the values of the output quantities. In this definition, the term model should be interpreted in a very broad sense. The model can be any type of mathematical relation between a set of input parameters and a set of output quantities. In sensitivity analysis, there are two important approaches: global sensitivity analysis and local sensitivity analysis. Global sensitivity analysis tools are statistical methods that aim at estimating the importance of the input parameters of a particular model, considering a well-defined region in the input parameter space. There is of course no absolute definition for the term 'important', but it generally relates to how much and/or what kind of influence each input has on the outputs of interest [62]. Global sensitivity analysis attempts to comprehend the general behaviour of the model in a large region of the parameter space. It can be used to study the overall input-output relations of complex models, to identify the principal input parameters or to reduce the dimensionality of the input space of the model by fixing the values of the least important input parameters. An introduction to global sensitivity analysis can be found in [63], a full overview of the theory and applications of global sensitivity analysis is presented in [64].
Local sensitivity analysis aims at estimating the influence of the input parameters on the output quantities in one particular point of the input parameter space. Local sensitivity analysis techniques result in a number of sensitivity coefficients. Each sensitivity coefficient represents the rate of change of a particular model response caused by a change of a specific input parameter. These sensitivity coefficients can relate a step taken from a particular point in the input parameter space to the corresponding step in the output parameter space. Therefore, local sensitivity analysis is an excellent tool to predict the modification needed to achieve a desired change of the behaviour of a system [65]. Since this is exactly what is needed to solve inverse problems, only local sensitivity analysis techniques will be considered in the remainder of this text. For reasons of convenience, the term 'local sensitivity analysis' will be shortened into sensitivity analysis.

3.2.1. Finite Difference versus Differential Sensitivities

The finite difference approach [66, 67] is the oldest and most commonly used method to calculate sensitivity coefficients. With the finite difference approach

the partial derivative of the model response is numerically approximated from the responses calculated with a set of slightly modified parameters. The centred finite difference approach approximates the sensitivity coefficients as

$$\frac{\partial r_i(p)}{\partial p} \approx \frac{r_i(p+\Delta p) - r_i(p-\Delta p)}{2\Delta p} \tag{3.18}$$

where $r_i(p)$ is the i^{th} response of the FE-model for the parameter value p, and Δp is the considered parameter perturbation. While this is an accurate approximation, it has the major disadvantage that two perturbed FE-models have to be solved. Two computationally more efficient approximation schemes are the forward and backward finite difference approaches, where the sensitivity coefficients are defined by (3.19) and (3.20), respectively.

$$\frac{\partial r_i(p)}{\partial p} \approx \frac{r_i(p+\Delta p) - r_i(p)}{\Delta p} \tag{3.19}$$

$$\frac{\partial r_i(p)}{\partial p} \approx \frac{r_i(p) - r_i(p-\Delta p)}{\Delta p} \tag{3.20}$$

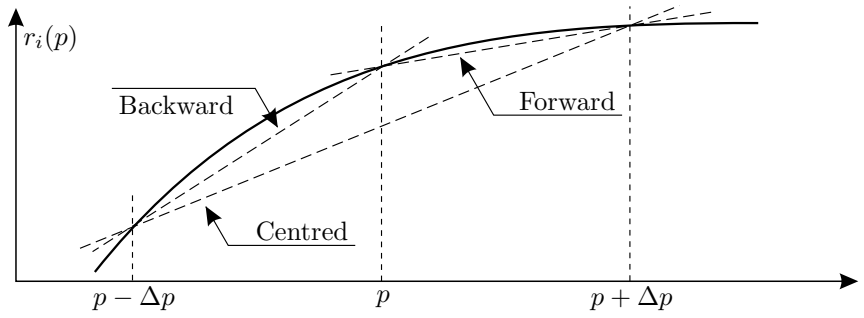

Figure 3.10: *Comparison of the centred, forward, and backward approximation schemes.*

Since the response $r_i(p)$ is already known from the FE-analysis, the calculation of a sensitivity coefficient with (3.19) or (3.20) only requires one additional FE-analysis. For small values of the perturbation Δp, the differences between the centred and the forward or backward approach will be minimal, which means that the forward or backward approach should be preferred over the centred approach. But even by adopting a forward or backward approximation scheme, the finite difference approach remains highly inefficient from a computational point of view. The main advantage of the global finite difference approach is the simplicity of its implementation. Note that it is not even necessary to have access to the finite element code to implement this type of sensitivity analysis. On the other hand, differential sensitivity calculation is based on explicit expressions of the partial derivatives of the FE-responses. This approach has the main advantage that it results in a severe reduction of the computational cost in comparison with the finite difference approach. The major drawback

of the differential approach is that every model parameter requires a dedicated sensitivity expression, which has to be derived from the model equations. The application of the differential approach also requires interaction with the finite element code, which makes this approach more difficult to implement. Note that all the drawbacks of the differential approach are situated in the implementation phase; once implemented, the user will definitely benefit from the reduced computational cost of the differential approach.

3.2.2. The Direct versus the Adjoint Approach

In differential sensitivity calculation, there are two major approaches to derive the sensitivity expressions from the model equations: the direct and the adjoint approach [68, 69]. With the finite element method, the governing differential equations are discretised and transformed to a set of algebraic equations. In the residual form, these algebraic equations can be expressed as

$$\mathcal{M}\big(u(p), p\big) = 0 \tag{3.21}$$

where p represents the set of model parameters and $u(p)$ represents the direct output of the finite element model. In general, the response of interest is not always a direct output quantity of the finite element model; in fact, the output of a structural finite element model is given in terms of displacements, while the user, for example, might be interested in stresses. The response of interest r_j is thus a function of both the input parameters p and output quantities $u(p)$. This relation can be written as

$$r_j = \mathcal{R}\big(u(p), p\big) \tag{3.22}$$

An expression for the sensitivity coefficient of the output quantity r_j with respect to a particular model parameter p_i can be obtained by derivation of equation (3.22).

$$\frac{\mathrm{d}r_j}{\mathrm{d}p_i} = \frac{\partial \mathcal{R}}{\partial u}\frac{\partial u}{\partial p_i} + \frac{\partial \mathcal{R}}{\partial p_i} \tag{3.23}$$

In this expression, the terms $\frac{\partial \mathcal{R}}{\partial u}$ and $\frac{\partial \mathcal{R}}{\partial p_i}$ can easily be obtained by deriving the explicit relation of (3.22), e.g. the displacement-stress relation. The main challenge of the sensitivity computation lies in the evaluation of the term $\frac{\partial u}{\partial p_i}$. With the direct approach [68], the term $\frac{\partial u}{\partial p_i}$ is determined by the direct differentiation of expression (3.21).

$$\frac{\mathrm{d}\mathcal{M}}{\mathrm{d}p_i} = \frac{\partial \mathcal{M}}{\partial u}\frac{\partial u}{\partial p_i} + \frac{\partial \mathcal{M}}{\partial p_i} = 0 \tag{3.24}$$

or

$$\frac{\partial \mathcal{M}}{\partial u}\frac{\partial u}{\partial p_i} = -\frac{\partial \mathcal{M}}{\partial p_i} \tag{3.25}$$

The direct approach thus requires a solution of the set of equations defined by (3.25) with respect to $\frac{\partial u}{\partial p_i}$. This set of equations has to be solved for each

considered model parameter p_i, which means that the computational cost of the direct approach is proportional to the number of considered model parameters. The adjoint approach [67] aims at reducing the computational cost by considering the following Lagrange functional

$$\tilde{r}_j = \mathcal{R}\big(u(p), p\big) - \lambda^{\mathrm{T}} \mathcal{M}\big(u(p), p\big) \tag{3.26}$$

Note that $\tilde{r}_j = r_j$ and $\frac{\mathrm{d}\tilde{r}_j}{\mathrm{d}p_i} = \frac{\mathrm{d}r_j}{\mathrm{d}p_i}$ for any value of λ since $\mathcal{M}\big(u(p), p\big) = 0$. Differentiation of equation (3.26) provides

$$\frac{\mathrm{d}\tilde{r}_j}{\mathrm{d}p_i} = \frac{\mathrm{d}r_j}{\mathrm{d}p_i} = \frac{\partial \mathcal{R}}{\partial u}\frac{\partial u}{\partial p_i} + \frac{\partial \mathcal{R}}{\partial p_i} - \lambda^{\mathrm{T}} \left(\frac{\partial \mathcal{M}}{\partial u}\frac{\partial u}{\partial p_i} + \frac{\partial \mathcal{M}}{\partial p_i} \right) \tag{3.27}$$

By grouping the terms that contain direct output derivatives, expression (3.27) can be rewritten as

$$\frac{\mathrm{d}r_j}{\mathrm{d}p_i} = \left(\frac{\partial \mathcal{R}}{\partial u} - \lambda^{\mathrm{T}} \frac{\partial \mathcal{M}}{\partial u} \right) \frac{\partial u}{\partial p_i} + \frac{\partial \mathcal{R}}{\partial p_i} - \lambda^{\mathrm{T}} \frac{\partial \mathcal{M}}{\partial p_i} \tag{3.28}$$

By choosing the Lagrange multipliers λ in such a way that

$$\lambda^{\mathrm{T}} \frac{\partial \mathcal{M}}{\partial u} = \frac{\partial \mathcal{R}}{\partial u} \tag{3.29}$$

the direct output derivatives $\frac{\partial u}{\partial p_i}$ can be eliminated from the sensitivity equations and expression (3.28) simplifies to

$$\frac{\mathrm{d}r_j}{\mathrm{d}p_i} = \frac{\partial \mathcal{R}}{\partial p_i} - \lambda^{\mathrm{T}} \frac{\partial \mathcal{M}}{\partial p_i} \tag{3.30}$$

The application of the adjoint approach requires a solution for the adjoint problem defined by the set of equations (3.29). The adjoint problem has to be solved for each different functional $\mathcal{R}$, which means that the computation cost is proportional to the number of considered output quantities r_j.
To summarize, the computational cost of the direct approach is determined by the number of considered model parameters, while the computational cost of the adjoint approach is determined by the number of considered output quantities. To guarantee the uniqueness of an inverse problem, the number of unknown model parameters, i.e. the parameters used in the sensitivity analysis, must be smaller than the number of considered output quantities. This implies that, in the case of inverse problems, the direct approach will always be more efficient than the adjoint approach.

3.2.3. Sensitivity Coefficients of Vibrating Structures

The Expression for the Frequency Sensitivities

This section presents the differential computation of the resonant frequency sensitivity coefficients using the direct approach. The following derivation was introduced by Fox and Kapoor [70], and is based on the direct derivation of the discretised differential equations of an undamped vibrating structure. As

shown in section 3.1.1, the discretised differential equations are given by the set of algebraic equations of (3.15).

$$[K][\Psi] - [M][\Psi][\Lambda] = [0]$$

Pre-multiplication of the i^{th} equation of expression (3.15) with the transpose of the i^{th} eigenvector gives

$$\{\Psi\}_i^{\mathrm{T}} \left([K] - \lambda_i[M]\right) \{\Psi\}_i = \{0\} \tag{3.31}$$

Differentiating expression (3.31) with respect to the model parameter p yields

$$\begin{aligned} \frac{\partial \{\Psi\}_i^{\mathrm{T}}}{\partial p} \left([K] - \lambda_i[M]\right) \{\Psi\}_i + \{\Psi\}_i^{\mathrm{T}} \frac{\partial \left([K] - \lambda_i[M]\right)}{\partial p} \{\Psi\}_i + \\ \{\Psi\}_i^{\mathrm{T}} \left([K] - \lambda_i[M]\right) \frac{\partial \{\Psi\}_i}{\partial p} = \{0\} \end{aligned} \tag{3.32}$$

Since the finite element method generates symmetrical stiffness and mass matrices, expression (3.32) can be rewritten as

$$2 \frac{\partial \{\Psi\}_i^{\mathrm{T}}}{\partial p} \left([K] - \lambda_i[M]\right) \{\Psi\}_i + \{\Psi\}_i^{\mathrm{T}} \frac{\partial \left([K] - \lambda_i[M]\right)}{\partial p} \{\Psi\}_i = \{0\} \tag{3.33}$$

The i^{th} equation of (3.31) shows that the first term of (3.33) equals zero, expression (3.33) thus simplifies to

$$\{\Psi\}_i^{\mathrm{T}} \frac{\partial \left([K] - \lambda_i[M]\right)}{\partial p} \{\Psi\}_i = \{0\} \tag{3.34}$$

or

$$\{\Psi\}_i^{\mathrm{T}} \left(\frac{\partial [K]}{\partial p} - \frac{\partial \lambda_i}{\partial p}[M] - \lambda_i \frac{\partial [M]}{\partial p} \right) \{\Psi\}_i = \{0\} \tag{3.35}$$

By assuming that the mode shapes are mass normalised as defined by (3.16), expression (3.35) can be rewritten as

$$\frac{\partial \lambda_i}{\partial p} = \{\Psi\}_i^{\mathrm{T}} \left(\frac{\partial [K]}{\partial p} - \lambda_i \frac{\partial [M]}{\partial p} \right) \{\Psi\}_i \tag{3.36}$$

The eigenvalues λ_i are related to the resonant frequencies f_i as

$$\lambda_i = \omega_i^2 = (2\pi f_i)^2 \tag{3.37}$$

The general expression for the resonant frequency sensitivities of an undamped structure is found by substitution of (3.37) into (3.36).

$$\frac{\partial f_i}{\partial p} = \frac{1}{8\pi^2 f_i} \{\Psi\}_i^{\mathrm{T}} \left(\frac{\partial [K]}{\partial p} - 4\pi^2 f_i^2 \frac{\partial [M]}{\partial p} \right) \{\Psi\}_i \tag{3.38}$$

For the identification of the material parameters, the sensitivities have to be calculated with respect to the elastic properties. Since a change of the elastic

properties does not affect the mass of the structure, the general sensitivity expression reduces to

$$\frac{\partial f_i}{\partial p} = \frac{1}{8\pi^2 f_i}\left(\{\Psi\}_i^{\mathrm{T}} \frac{\partial [K]}{\partial p}\{\Psi\}_i\right) \tag{3.39}$$

Semi-Analytical Sensitivities

The evaluation of equation (3.39) requires the derivative of the stiffness matrix with respect to the elastic material parameters. This derivative is often difficult to calculate analytically. For this reason, a semi-analytical approach, in which the derivatives of the stiffness matrix are approximated by finite differences, is commonly used [69]. The derivatives are usually calculated with a first-order forward approximation, or

$$\frac{\partial [K]}{\partial p} \approx \frac{\Delta [K]}{\Delta p} = \frac{[K(p+\Delta p)] - [K(p)]}{\Delta p} \tag{3.40}$$

This semi-analytical approach combines the advantages of both the finite difference and differential approach. Like the finite difference approach, it is applicable for every possible type of model parameter. However, the semi-analytical approach is much faster than the finite difference approach since it only requires the calculation of a perturbed stiffness matrix, it does not require to solve any additional FE-models. The gain in computation time obtained by using the semi-analytical approach can easily be illustrated by considering a standard FE-model used in material identification. Solving a finite element model can be split up in three steps: the computation of the stiffness matrix [K], the calculation of the mass matrix [M] and solving the eigenvalue problem (3.15). Table 3.4 presents the computation time that is required for these three steps. It illustrates very clearly that replacing the finite difference approximation of the partial derivatives of the FE-responses (3.18–3.20) by a finite difference approximation of the partial derivative of the stiffness matrix (3.39–3.40) will lead to a drastic reduction of the calculation time needed to perform the sensitivity analysis.

Table 3.4: *The computation time of the different steps of an FE-analysis for a typical material specimen.*

Calculation step	CPU Time [s]	Relative importance
Stiffness matrix $[K]$	1.99	6.4%
Mass matrix $[M]$	4.86	15.7%
Eigenvalue problem (3.15)	24.24	77.9%
Total FE-analysis	31.09	100.0%

Using Element Matrices

Table 3.4 does not provide an accurate estimation of the calculation time needed to perform a sensitivity analysis, since the computation of the partial derivative

of the stiffness matrix $[K]$ is not the only time-consuming step. A direct application of (3.39) implies a pre- and post-multiplication of the partial derivative of the stiffness matrix $[K]$ with the mode shape vector $\{\Psi\}_i$. Consider a three-dimensional FE-model, i.e. 3 displacement degrees of freedom per node, with n nodes. This model has a stiffness matrix $[K] \in \mathbb{R}^{3n\times 3n}$ and a mode shape vector $\{\Psi\}_i \in \mathbb{R}^{3n}$. In this case, the evaluation of (3.39) requires a multiplication of a $1\times 3n$ vector with a $3n\times 3n$ matrix, followed by the multiplication of a $1\times 3n$ vector with a $3n\times 1$ vector. Consequently, the vector-matrix and vector-vector product results in a total computational cost of $2(3n)^2 + 2(3n) = 18n^2 + 6n$ floating point operations (flops). This indicates that the computation time increases quadratically with the size of the FE-model. The stiffness matrix $[K]$ is a sparse matrix, so the majority of the floating point operations are superfluous since they are additions or multiplications with 0. Fortunately, these useless operations can be avoided. From the structure of the global stiffness matrix $[K]$ it can be seen that the expression (3.39) can be written in terms of element matrices as

$$\left(\frac{\partial f_i}{\partial p}\right)_e = \frac{1}{8\pi^2 f_i}\left(\{\Psi_e\}_i^{\mathrm{T}} \frac{\partial [K_e]}{\partial p}\{\Psi_e\}_i\right) \tag{3.41}$$

in which $[K_e]$ is the element stiffness matrix and $\{\Psi_e\}$ is the vector containing the nodal displacements of the nodes of the considered element. Expression (3.41) gives the influence of a stiffness change in a single element of the FE-model on the frequency f_i. To obtain the full sensitivity coefficient, expression (3.41) has to be summed over all the elements of the FE-model.

$$\frac{\partial f_i}{\partial p} = \frac{1}{8\pi^2 f_i}\sum_{e=1}^{n_e}\left(\{\Psi_e\}_i^{\mathrm{T}} \frac{\partial [K_e]}{\partial p}\{\Psi_e\}_i\right) \tag{3.42}$$

In the case of quadratic solid elements ($n = 20$), the element stiffness matrix $[K_e] \in \mathbb{R}^{60\times 60}$, and the mode shape vector $\{\Psi_e\}_i \in \mathbb{R}^{60}$. Expressed in floating point operations, the evaluation of the summation of expression (3.42) has a cost of $n_e\times(2\times 60^2+2\times 60) = 7320\times n_e$ flops. Using the formulation of (3.42), the computational cost of the sensitivity analysis only increases linearly with the size of the FE-model. From the flop cost, it can be estimated that for an FE-model with $25\times 25\times 2$ elements the evaluation of expression (3.42) will be about 160 times faster than the direct evaluation of expression (3.39). Note that the gain[8] in computation time for the full sensitivity analysis will be $160\times$(number of responses$\times$number of parameters).

Exploiting the Symmetry Properties

A characteristic that is often used to reduce the computation time of a finite element analysis is to exploit the (anti)symmetry of the structure. By introducing the appropriate boundary conditions, the model can then be limited to a half, a quarter, or even a smaller fraction of the structure. Unfortunately, this approach cannot be used in vibration-based material identification. Although

[8] This only considers the gain made with the evaluation of sensitivity expression, it does not consider the computation of the partial derivative of the stiffness matrix.

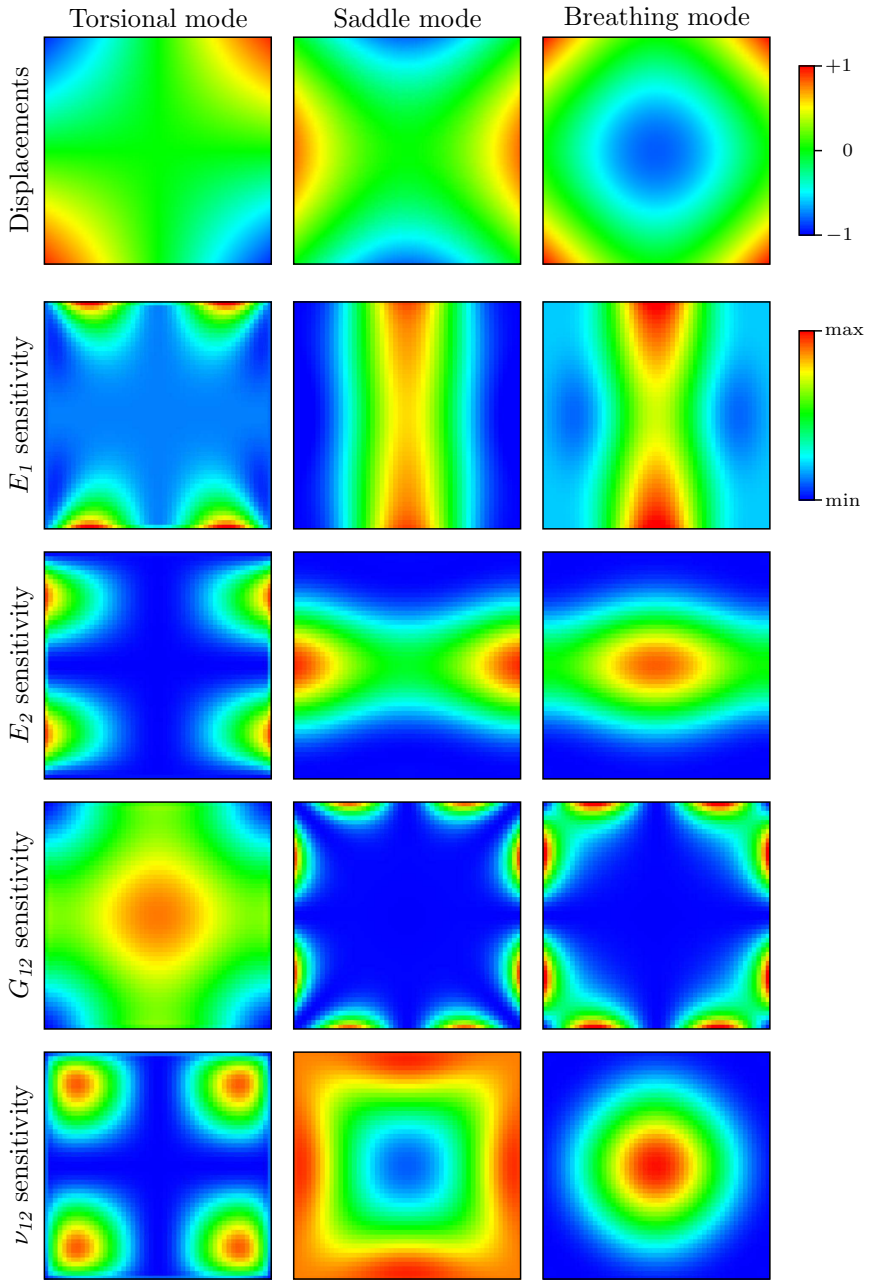

Figure 3.11: *The first row shows the relative amplitude of the nodal displacements of the first three vibration modes of a plate-shaped specimen. The other four rows show the element sensitivities of the same modes.*

the structures, i.e. beam- or plate-shaped specimens, have two orthogonal symmetry axes due to the fact that the material properties are considered to be homogeneous, the resulting modes do not have a unique symmetry pattern; for example, the torsional mode is anti-symmetric, while the breathing mode is symmetric as illustrated in the first row of figure 3.11. Therefore, it is impossible to find a set of boundary conditions for a half- or quarter-plate model that will result in the correct modes. Limiting the specimen to a half or a quarter would require solution of the FE-model with different sets of boundary conditions, and with thus not lead to a lower computation time.
However, since all the mode shapes are symmetric or anti-symmetric, the element sensitivities have a double symmetry pattern. Consider two symmetrically positioned elements of the FE-model of a homogeneous beam- or plate-shaped specimen. These two elements will have the same element stiffness matrices, so

$$\frac{\partial[K_1]}{\partial p} = \frac{\partial[K_2]}{\partial p} \tag{3.43}$$

For the i^{th} mode, the element mode shape vectors of the two elements will be related as

$$\{\Psi_1\}_i = \{\Psi_2\}_i \qquad \text{or} \qquad \{\Psi_1\}_i = -\{\Psi_2\}_i \tag{3.44}$$

for a symmetric or an anti-symmetric mode shape, respectively. So, expressions (3.43) and (3.44) show that the element sensitivities defined by (3.41) will be equal for these two symmetrically positioned elements, for both symmetrical and anti-symmetrical modes. Figure 3.11 presents the element sensitivities with respect to E_1, E_2, G_{12} and ν_{12} of the resonant frequencies of the first three vibration modes of a plate. It can be seen that for double symmetrical, e.g. saddle and breathing mode, as well as for double anti-symmetrical, e.g. torsional mode, the element sensitivities always have a double symmetrical pattern. This means that the overall sensitivity coefficients can be calculated from the element sensitivities of only one quarter of the finite element model, or

$$\frac{\partial f_i}{\partial p} = \frac{4}{8\pi^2 f_i} \sum_{e=1}^{\frac{n_e}{4}} \left(\{\Psi_e\}_i^{\mathrm{T}} \frac{\partial[K_e]}{\partial p} \{\Psi_e\}_i \right) \tag{3.45}$$

considering an appropriate numbering of the FE-model's elements. The use of this symmetry property will reduce the calculation time of the summation of (3.42) by a factor of 4. Note that in the case of laminates with a symmetric lay-up, it is even possible to consider only the upper or lower half of the quarter specimen to calculate the frequency sensitivities.

The Optimal Perturbation Step

Both the finite difference and the semi-analytical differential approach provide a numerical approximation of the sensitivity coefficients. The obtained sensitivity coefficients will therefore be corrupted with a numerical error.
To study this error [68], consider the forward finite difference approach. The

relation between the model responses for the parameter sets p and $p + \Delta p$ can be expressed with the following Taylor expansion.

$$r(p + \Delta p) = r(p) + \frac{\partial r(p)}{\partial p}\Delta p + \frac{1}{2}\frac{\partial^2 r(p)}{\partial p^2}\Delta p^2 + \vartheta(\Delta p^3) \tag{3.46}$$

The first derivative of the response r with respect to the parameter p can thus be written as

$$\frac{\partial r(p)}{\partial p} = \frac{r(p + \Delta p) - r(p)}{\Delta p} - \frac{1}{2}\frac{\partial^2 r(p)}{\partial p^2}\Delta p - \vartheta(\Delta p^2) \tag{3.47}$$

The calculated response of a numerical model $r_m(p)$ is only an approximation of the exact response $r(p)$ or

$$r(p) = r_m(p) + \epsilon_m(p) \tag{3.48}$$

where $\epsilon_m(p)$ represents the total round-off error introduced by the floating point operations of the numerical model. The substitution of expression (3.48) into equation (3.47) gives

$$\begin{aligned}\frac{\partial r(p)}{\partial p} = &\underbrace{\frac{r_m(p + \Delta p) - r_m(p)}{\Delta p}}_{\text{sensitivity coefficient}} + \underbrace{\frac{\epsilon_m(p + \Delta p) - \epsilon_m(p)}{\Delta p}}_{\text{round-off error}} \\ &\underbrace{- \frac{1}{2}\frac{\partial^2 r(p)}{\partial p^2}\Delta p - \vartheta(\Delta p^2)}_{\text{truncation error}}\end{aligned} \tag{3.49}$$

According to expression (3.49), the exact sensitivity coefficient can be divided into three parts [68]. The first part is the finite difference approximation of the sensitivity coefficient that results from the sensitivity analysis. The second term is the round-off error which is caused by the finite accuracy of the floating point numbers used in the numerical algorithm of the model. The influence of the round-off error is random and will decrease with an increase of the parameter perturbation Δp. The last term represents the truncation error which is introduced by ignoring the higher order terms of the Taylor expansion.

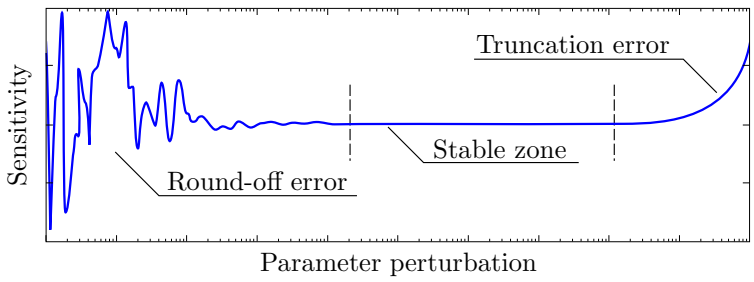

Figure 3.12: *The influence of the round-off and truncation error on the sensitivity coefficients.*

The truncation error is a systematic error and increases with an increase of the parameter perturbation. The optimal parameter perturbation should thus be a trade-off between minimising the round-off error and the truncation error. Figure 3.12 illustrates the influence on the round-off and truncation error on the sensitivity coefficients.

Expression (3.49) does not hold for the semi-analytical approach. However, in a similar way it can be shown that the exact sensitivity coefficient consists of the same three parts: the approximate sensitivity coefficient, the round-off error, and the truncation error.

Reference [71] presents a commonly used method to obtain the optimal parameter perturbation. The starting point of [71] is that the optimal parameter perturbation should be as small as possible, without causing an excessive round-off error. The presented theory relates the smallest acceptable parameter perturbation to the numerical precision of the floating point type of the computer platform η as

$$\Delta p^{\star} = \sqrt{\eta} p \tag{3.50}$$

According to (3.50), the influence of the round-off error is independent of the number of floating point operations that are needed for the sensitivity analysis. Expression (3.50) thus risks to underestimate the optimal parameter perturbation in the case of FE calculations. When considering a computer platform[9] with a floating point precision of $2.22 \cdot 10^{-16}$, expression (3.50) results in a value of $\frac{\Delta p^{\star}}{p} = 1.5 \cdot 10^{-8}$ for the optimal relative parameter perturbation.

To check the validity of this perturbation value, a sensitivity analysis with respect to the elastic properties was performed for relative parameter perturbations ranging from 1 to 10^{-10}. The considered structure is a brass[10] plate of 100×100×0.8 mm that was modelled with a 20×20×1 element grid. The sensitivity coefficients of the first five resonant frequencies with respect to the orthotropic material constants E_1, E_2, G_{12}, and ν_{12} were calculated using the semi-analytical differential approach. Figure 3.13 presents the results that were obtained for the third vibration mode. Similar results were found for the other vibration modes. The graphs clearly show the systematic influence of the truncation error and the random influence of the round-off error. The results also show that a relative parameter perturbation of 10^{-8} is usually located in the zone in which the sensitivity coefficients are heavily influenced by the round-off error. For material identification applications, a relative parameter perturbation of 10^{-4} appears to be a good compromise between the minimisation of the round-off and truncation error.

The uncertainty analysis procedures that are presented in chapter 7, also require the sensitivity of the resonant frequencies with respect to the sample length, width, thickness and mass. The solid lines of figure 3.14 represent the sensitivity coefficients that were obtained with the semi-analytical differential approach. The mass sensitivities display a behaviour that is similar to that of the stiffness sensitivities. However, there is a serious problem for the length,

[9] The FEMtools software running on Windows XP.

[10] For this analysis, the material properties of table 6.1 were used.

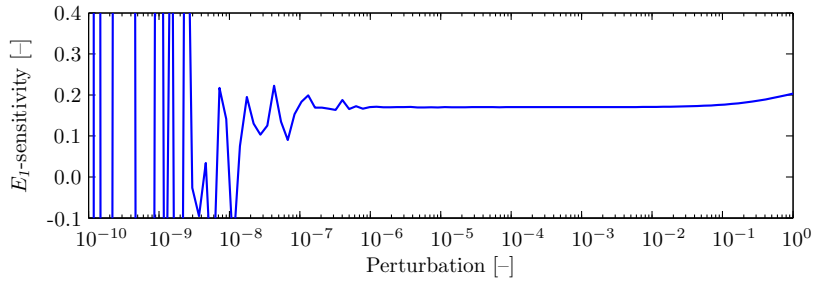

(a) E_1 sensitivity

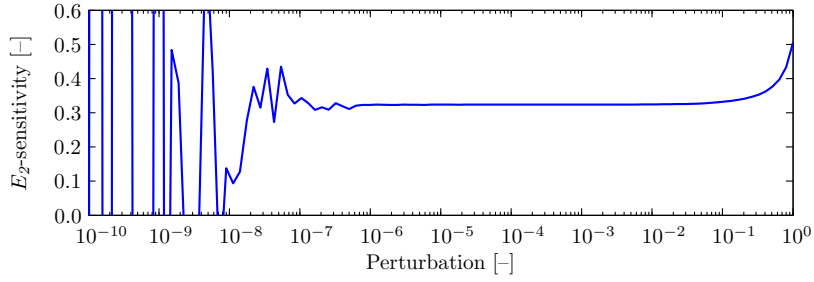

(b) E_2 sensitivity

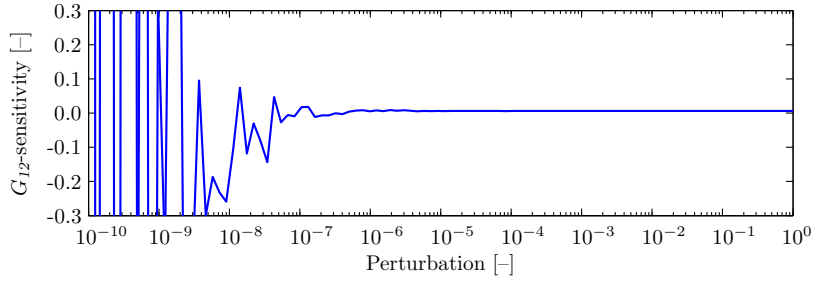

(c) G_{12} sensitivity

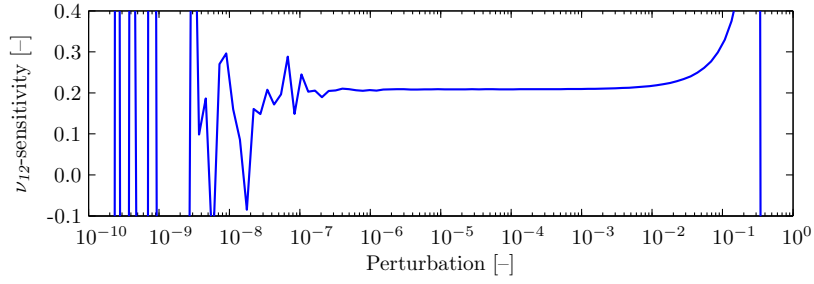

(d) ν_{12} sensitivity

Figure 3.13: *Stability of the sensitivity coefficients for the third vibration mode, i.e. breathing mode, of a brass plate using the semi-analytical differential approach.*

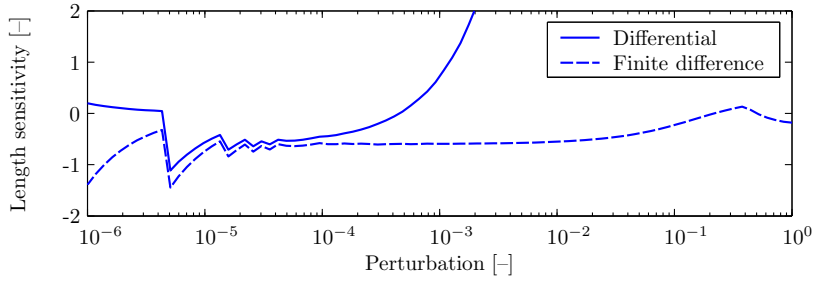

(a) Length sensitivity

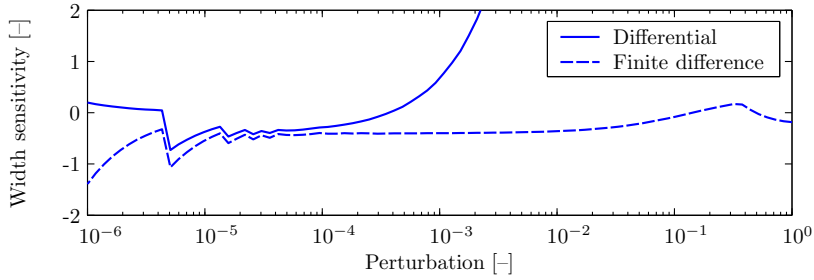

(b) Width sensitivity

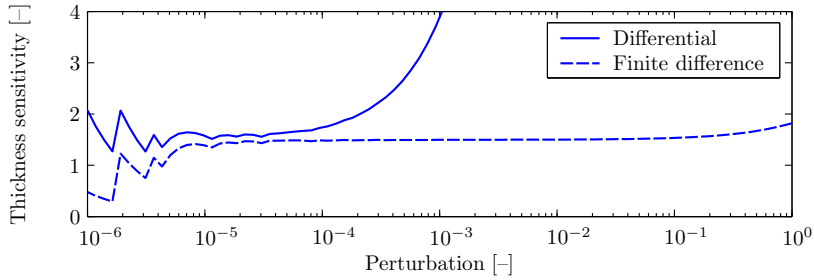

(c) Thickness sensitivity

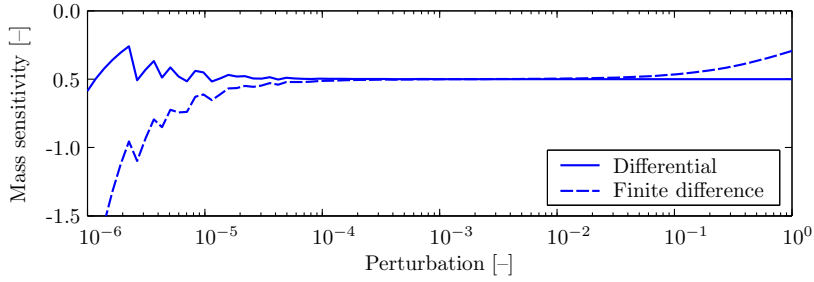

(d) Mass sensitivity

Figure 3.14: *Stability of the sensitivity coefficients for the third vibration mode, i.e. breathing mode, of a brass plate.*

width and thickness sensitivities. For these three parameters, there is no stable zone as the region that is corrupted by the round-off error is directly followed by the zone that is influenced by the truncation error. The sensitivity coefficients were also computed with the forward finite difference approach. The obtained results are represented by the dashed lines of figure 3.14. The finite difference sensitivities have a stable zone for relative parameter perturbations ranging between 10^{-4} and 10^{-2}.

The computation of the length, width and thickness sensitivities requires a perturbation of the nodes of the finite element mesh. The computation of the stiffness and mass sensitivities does not change the mesh, it only changes the internal element properties. This appears to have serious consequences for the sensitivity analysis. The stiffness and mass sensitivities can be computed with the computationally efficient semi-analytical differential approach, using a relative perturbation of 10^{-4}. The length, width and thickness sensitivities have to be computed using the much slower finite difference approach, with an advisable relative perturbation of 10^{-3}.

3.2.4. The Sensitivity Matrix

A single sensitivity coefficient expresses the influence of the change of one model parameter on a particular output quantity. Since the used sensitivity coefficients are first order linear approximations, the influence of a set of parameters on an output quantity can be expressed as the sum of the individual influences, or

$$\Delta r = \frac{\partial r}{\partial p_1}\Delta p_1 + \frac{\partial r}{\partial p_2}\Delta p_2 + \ldots + \frac{\partial r}{\partial p_{n_p}}\Delta p_{n_p} \tag{3.51}$$

in which

$$\begin{aligned} \Delta r &= r^{new} - r^{old} \\ \Delta p &= p^{new} - p^{old} \end{aligned}$$

In most cases, not a single but a whole set of output quantities is being used. In this case, the influence of the parameter set on the output set can be written as

$$\begin{aligned} \Delta r_1 &= \frac{\partial r_1}{\partial p_1}\Delta p_1 + \frac{\partial r_1}{\partial p_2}\Delta p_2 + \ldots + \frac{\partial r_1}{\partial p_{n_p}}\Delta p_{n_p} \\ &\vdots \\ \Delta r_{n_r} &= \frac{\partial r_{n_r}}{\partial p_1}\Delta p_1 + \frac{\partial r_{n_r}}{\partial p_2}\Delta p_2 + \ldots + \frac{\partial r_{n_r}}{\partial p_{n_p}}\Delta p_{n_p} \end{aligned} \tag{3.52}$$

In matrix form, (3.52) can be expressed as

$$\{\Delta r\} = [S]\{\Delta p\} \tag{3.53}$$

with

$$\{\Delta r\} = \begin{Bmatrix} \Delta r_1 \\ \vdots \\ \Delta r_{n_r} \end{Bmatrix}, \quad \{\Delta p\} = \begin{Bmatrix} \Delta p_1 \\ \vdots \\ \Delta p_{n_p} \end{Bmatrix}, \quad [S] = \begin{bmatrix} \dfrac{\partial r_1}{\partial p_1} & \cdots & \dfrac{\partial r_1}{\partial p_{n_p}} \\ \vdots & \ddots & \vdots \\ \dfrac{\partial r_{n_r}}{\partial p_1} & \cdots & \dfrac{\partial r_{n_r}}{\partial p_{n_p}} \end{bmatrix} \tag{3.54}$$

The vectors $\{\Delta r\}$ and $\{\Delta p\}$ are the response and parameter vector, respectively. The matrix $[S]$ is called the sensitivity matrix. A row of the sensitivity matrix contains the sensitivities of one particular response, a column contains the sensitivities with respect to one particular parameter. In MNETs, sensitivity analysis is used to estimate the parameter changes needed to achieve the required change of the model output, $\{\Delta r\}$. The required output changes are determined by the difference between the current model output $\{r^{num}\}$ and the experimentally measured output $\{r^{exp}\}$, so

$$\{\Delta r\} = \{r^{exp}\} - \{r^{num}\} \tag{3.55}$$

Since a unique solution is required, there have to be more outputs than parameters, so in general it will be impossible to exactly achieve the desired change. The difference between the desired change $\{\Delta r\}$ and the optimal achievable change $\{\Delta r^\star\}$ can be expressed by a residual vector $\{\epsilon\}$, or

$$\{\Delta r\} = \{\Delta r^\star\} + \{\epsilon\} \tag{3.56}$$

The optimal achievable response change is the change that minimises the residuals. In chapter 4 it will be shown that, if the residuals are minimised in a least-squares sense, the optimal parameter changes are given by the right hand side of expression (3.57).

$$\min \sum_{i=1}^{n_r} \epsilon_i^2 \;\Rightarrow\; \{\Delta p\} = \left([S]^{\mathrm{T}}[S]\right)^{-1} [S]^{\mathrm{T}} \{\Delta r^\star\} \tag{3.57}$$

Expression (3.57) is the most fundamental expression of sensitivity-based updating and justifies the existence of relative and normalised sensitivities. The sensitivity coefficients used in expression (3.52) are called absolute sensitivities. These absolute sensitivities have a number of disadvantages for MNETs. First of all, the residuals minimised in expression (3.57) are the differences between the absolute values of the desired and achieved model outputs. If improved model parameters are estimated by using absolute response differences, the least-squares minimisation will implicitly increase the importance of the output quantities which have a high absolute value. In the case where resonant frequencies are used as model output, this procedure results in a better match of the frequencies of the higher order modes. To obtain a more balanced weighting of the different output quantities, not the absolute response differences but the relative response differences should be minimised. The desired response changes should then be defined as

$$\Delta r_i = \frac{r_i^{exp} - r_i^{num}}{r_i^{num}} \tag{3.58}$$

To maintain the validity of expression (3.57) with this new definition of $\{\Delta r\}$, all the elements of the sensitivity matrix [S] have to be divided by the corresponding response. The sensitivity coefficients thus have to be redefined as

$$s_{ij} = \frac{\partial r_i}{\partial p_j} \frac{1}{r_i^{num}} \tag{3.59}$$

The sensitivity coefficients as defined by expression (3.59) are called relative sensitivities. As previously explained, the use of relative sensitivities ensures the correct weighting of response quantities with a large difference in absolute value. Note that relative sensitivities cannot be computed for quantities equal to zero. However, this does not cause any problems in the case of vibration-based MNETs since the responses are resonant frequencies.

Expression (3.57) also reveals another potential problem. The computation of the optimal parameter changes requires the inversion of the product $\left([S]^{\mathrm{T}}[S]\right)$. The product of a matrix with its transpose has the same rank as the initial matrix. This means that the sensitivity matrix may not be rank-deficient or ill-conditioned. The identification procedures discussed in this text aim at the estimation of the elastic properties of orthotropic materials, i.e. E_1, E_2, G_{12} and ν_{12}. In absolute values, the elastic and shear moduli are about 10 orders of magnitude larger than Poisson's ratios. Since the parameters are in the denominator of the sensitivity coefficients, the values of the sensitivity coefficients of the elastic and shear moduli will be a few orders of magnitude lower than the sensitivity coefficients of Poisson's ratio. When grouping these sensitivity coefficients into a sensitivity matrix, the resulting sensitivity matrix will be severely ill-conditioned making the inversion of $\left([S]^{\mathrm{T}}[S]\right)$ highly susceptible to numerical errors. To improve the conditioning of the sensitivity matrix, the different sensitivity coefficients should have about the same order of magnitude. This can be achieved by multiplying the sensitivity coefficients with the corresponding parameter value, so the sensitivity coefficients become

$$s_{ij} = \frac{\partial r_i}{\partial p_j} \frac{p_j}{1} \tag{3.60}$$

The new sensitivity coefficients are called normalised sensitivities. To maintain the validity of the updating expression (3.57) the elements of the parameter correction vector have to be redefined as

$$\Delta p_j = \frac{p_j^{new} - p_j^{old}}{p_j^{old}} \tag{3.61}$$

To combine a well conditioned sensitivity matrix with a correct weighting of the different model responses, normalised relative sensitivities should be used. Normalised relative sensitivities are defined as

$$s_{ij} = \frac{\partial r_i}{\partial p_j} \frac{p_j}{r_i} \tag{3.62}$$

They can be used in the sensitivity matrix of expression (3.57), if the response and parameter difference vectors are defined as in (3.58) and (3.61), respectively. From the discussion above, it is clear that the use of normalised relative sensitivities is preferred. All sensitivities used in the remainder of the text will be normalised relative sensitivities. For reasons of convenience, normalised relative sensitivity coefficients will simply be called sensitivity coefficients.

3.2.5. Conclusions

The optimal approach to determine the sensitivity coefficients of resonant frequencies of rectangular test specimens with respect to the material parameters, is to compute the element sensitivities of one quarter of the sample using the semi-analytical differential approach with a relative parameter perturbation of 10^{-4}. On the other hand, the determination of the sensitivity coefficients with respect to the sample's length, width, and thickness must be computed with the finite difference approach using a relative parameter perturbation of 10^{-3}. To improve the conditioning of the identification problem, the absolute sensitivity coefficients of the resonant frequencies with respect to the elastic material parameters should be transformed into normalised relative sensitivities.

3.3. Correlation Analysis

To update the finite element models of the test specimens, the numerical frequencies have to be compared with the experimentally measured resonant frequencies. To correctly update the model, every numerical frequency has to be compared with the experimental resonant frequency of the same physical mode. For example, the frequency of the numerical torsional mode has to be compared with the experimental torsional frequency. But the order of the numerical modes depends on the elastic properties of the numerical model, e.g. an over- or underestimation of the shear modulus of a beam-shaped sample can change the position of the fundamental torsional mode with respect to the other modes. The order of the modes of the finite element model is thus not necessarily the same as the order of the experimental modes, therefore the frequencies cannot be compared sequentially.

3.3.1. The Modal Assurance Criterion

The modal assurance criterion (MAC) defines a correlation coefficient between two mode shapes [72], and is commonly used to compare a set of numerical mode shapes with a set of experimental mode shapes. For real mode shapes, the modal assurance criterion is defined by

$$\mathrm{MAC}\big(\{\psi\}_{num}, \{\psi\}_{exp}\big) = \frac{\big(\{\psi\}_{num}^{\mathrm{T}}[W]\{\psi\}_{exp}\big)^2}{\big(\{\psi\}_{num}^{\mathrm{T}}[W]\{\psi\}_{num}\big)\big(\{\psi\}_{exp}^{\mathrm{T}}[W]\{\psi\}_{exp}\big)} \tag{3.63}$$

where $[W]$ is a weighting matrix which is usually taken equal to the unity or mass matrix[11]. If the two mode shapes are the same, upon a scaling factor, the MAC value equals 1. If there is absolutely no linear relation between the two considered mode shapes, the MAC value equals 0. If two mode shape sets are compared, the MAC value is computed for every mode combination and the obtained MAC values can be arranged into a MAC-matrix.

3.3.2. Automatic Mode Recognition

The specimens considered in this text have simple shapes such as rectangular beams or plates. Therefore, the mode shapes are a priori known and it is possible to specify a number of predefined mode shape types, e.g. the fundamental flexural mode. This implies that it is not necessary to actually measure the experimental mode shapes, it just has to be known with which predefined mode type each experimental resonant frequency is associated. The numerical frequencies will also have to be associated with one of these predefined mode types, which means that vibration-based material identification routines require an automatic mode shape recognition algorithm. Such a routine consists of three basic steps: building a database with reference mode shapes, defining the node-point pairs, and determining the mode shape pairs.

Reference Mode Shapes

For every predefined mode type, a reference mode shape should be generated.

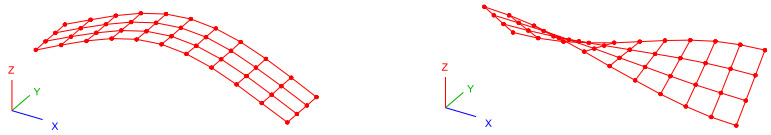

(a) The first flexural mode. (b) The first torsional mode.

Figure 3.15: *Two reference mode shapes for a beam-shaped specimen.*

The grid of these reference mode shapes can be quite coarse, but has to be fine enough to capture the general deformation pattern of the considered modes. Figure 3.15 presents two examples of reference mode shapes for a beam-shaped specimen. All the reference mode shapes are stored in a database according to a well-defined order.

Node-Point Pairs

The second step consists of finding the node-point pairs. Each pair combines a point of the reference grid with the closest finite element node. In theory, the application of the MAC requires the modal displacement of the two modes in the same location. However, the locations of the points and nodes do not always coincide. For automatic mode recognition purposes, an approximation

[11] In case of a structure with a homogeneous mass distribution, there is no significant difference between a MAC value computed with a weighting matrix equal to the unity or mass matrix.

by taking the closed node to each considered point suffices and an interpolation of the nodal displacements is not necessary.

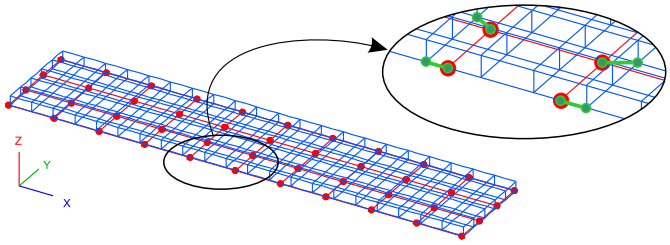

Figure 3.16: *The node-point pairs.*

Mode Shape Pairs

The last step consists of computing the MAC values between the numerical mode shapes and the mode shapes stored in the reference database. The combinations that result in the highest MAC-values are the mode shape pairs. Since the mode shape type of the reference modes are known, the mode type of the numerical modes is identified.

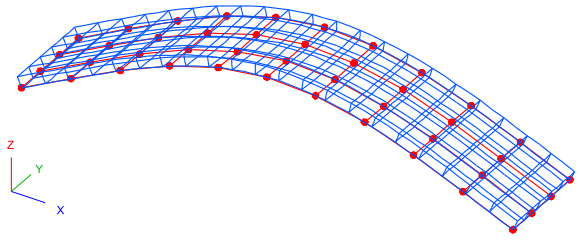

Figure 3.17: *A mode shape pair.*

3.3.3. Conclusions

It is possible to develop an automatic mode shape recognition algorithm. The type of a particular vibration mode can be identified by comparing the mode shape of the considered vibration mode with a set of reference mode shapes using the modal assurance criterion.

3.4. Summary

This chapter introduced the three mathematical tools needed in the numerical part of a vibration-based MNET procedure: finite element modelling, sensitivity analysis and correlation analysis. The theory of finite element modelling was briefly reviewed, while the use of finite element modelling in vibration-based material identification was evaluated and discussed more in detail. The part on sensitivity analysis introduced the theoretical foundation of sensitivity

analysis and derived the formulas of the semi-analytical differential approach to compute the sensitivity coefficients of the resonant frequencies of a vibrating structure. These formulas where then optimised for the computation of the sensitivity coefficients of beam- and plate-shaped test specimens. With the use of correlation analysis, a mode shaped recognition algorithm was developed in order to determine the mode type of the numerical modes in an automated way.

4

Optimisation Theory

Optimisation theory is a fundamental part of mixed numerical-experimental techniques. MNETs focus on estimating the values of physical parameters by comparing the data measured during an experiment with the responses of a numerical simulation of the experiment. The simulation results are controlled by a set of model parameters with unknown but 'tunable' values. It is assumed that the correct values of the physical properties under investigation correspond with the values of the model parameters resulting in the optimal match between the responses of actual and simulated experiment. The unknown parameter values can thus be identified by solving the optimisation problem that minimises the difference between the measured and simulated responses.

This chapter does not provide a general overview of optimisation theory, it only presents the theory needed to solve the MNET optimisation problem in an efficient way. It is assumed that the cost-function is the sum of the squared differences between the measured and calculated responses. The domain of the cost-function is considered to be the full n-dimensional real space; possible bounds on the search space are implemented with inequality constraints.

4.1. Introduction

The goal of optimisation theory is to provide procedures that can find the optimal solution to a particular mathematical problem. The optimal solution can only be defined, if there is an objective criterion to compare the optimality of two different solutions. Such a criterion is obtained by defining a cost-function that assigns a scalar value to every possible solution. Conventionally, cost-functions are chosen in such a way that the better solutions correspond with lower cost-function values. By using this convention, the quest of finding the optimal solution can mathematically be expressed as the problem of finding the minimum of the cost-function.

$$\begin{array}{lll} \underset{x}{\text{minimise}} & f_0(x) & \{x\} \in \mathbb{R}^n \\ \text{subject to} & f_i(x) \leqslant 0 & i = 1, \ldots, r \\ & h_i(x) = 0 & i = 1, \ldots, s \end{array} \tag{4.1}$$

The notation of equation (4.1) is called the standard form [73] and describes the problem of finding the location $\{x\}$ that minimises $f_0(x)$ among all feasible points. A point $\{x\}$ is called feasible, if it satisfies all the conditions $f_i(x) \leqslant 0$ and $h_i(x) = 0$. The function f_0: $\mathbb{R}^n \rightarrow \mathbb{R}$ is the cost-function and the vector $\{x\} \in \mathbb{R}^n$ is called the optimisation variable. The inequalities $f_i(x) \leqslant 0$ are called inequality constraints, and the corresponding functions $f_i(x)$: $\mathbb{R}^n \rightarrow \mathbb{R}$ are called inequality constraint functions. The equalities $h_i(x) = 0$ are called equality constraints and the corresponding functions $h_i(x)$: $\mathbb{R}^n \rightarrow \mathbb{R}$ are called equality constraint functions. If there are no constraints, the problem is said to be unconstrained.

4.1.1. Global and Local Minima

One of the major issues in optimisation theory is the presence of local minima. A global minimum is a point $x^\star$ for which the cost-function has the lowest value over its domain or $x^\star \leqslant x$, $\forall x \in \mathrm{dom} f_0$. A local minimum is a point for which there is a neighbourhood where the value of the cost-function is higher than at the local minimum, however the value of the cost-function at the local minimum is higher than the cost-function value at the global minimum. Figure 4.1 presents a one-dimensional example of a function with a local minimum.

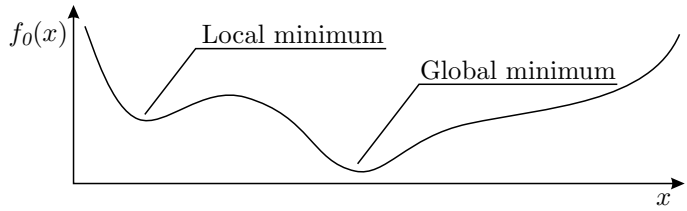

Figure 4.1: *A one-dimensional optimisation problem with a local minimum.*

Proving the absence of local minima is a highly complicated task. The problem is usually tackled in an indirect way by proving that the cost-function

is convex, since convexity implies the absence of local minima. Proving the convexity of the cost-function is an important step in solving an optimisation problem. In fact, "the great watershed in optimisation is not between linearity and non-linearity, but between convexity and non-convexity" [74]. However, the importance of convexity must not be overrated, since convexity is a very severe criterion. Convexity implies the absence of local minima, yet non-convexity does not imply the presence of local minima. Section 4.3 presents a more detailed discussion on convexity.

4.1.2. MNETs and Optimisation

The optimisation techniques used in mixed numerical-experimental techniques must meet a number of special requirements.

First of all, the cost-function of an MNET describes the difference between the measured and simulated responses. This means that every evaluation of the cost-function requires the solution of a finite element model, or a number of finite element models in case of an identification routine with multiple samples. The evaluation of the cost-function is thus a very time-consuming step. To identify the parameters in an efficient way, the number of cost-function evaluations has to be kept as low as possible.

With MNETs, the goal of the optimisation step is to identify the unknown values of a number of model parameters. Since these model parameters represent actual physical parameters, the optimisation problem must have a unique solution. According to the identifiability condition [75], a unique solution can only be obtained if the sensitivity matrix is non-singular. Furthermore, an MNET has to be robust with respect to measurement noise. A small change of the output responses should not result in a significant change of the identified parameters. Therefore, the minimum of the cost-function has to be well pronounced, i.e. it cannot lie in a valley characterized by long, narrow contour lines [75]. Mathematically, this requires a well-conditioned sensitivity matrix, i.e. a matrix with linearly independent columns. Figure 4.2 graphically represents the difference between a well and an ill-conditioned problem. Since an MNET must provide a unique solution, its optimisation algorithm does not have be able to handle singular or ill-conditioned problems. In these two cases, the MNET has to be redesigned instead of being solved, because it can never provide a reliable estimate of the unknown parameter values.

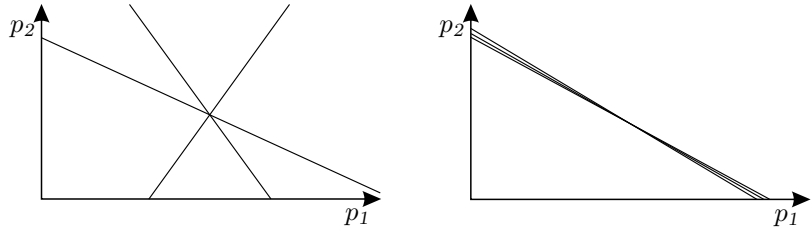

(a) Well-conditioned problem. (b) Ill-conditioned problem.

Figure 4.2: *A problem with three response quantities and two parameters.*

4.1.3. Overview of the Optimisation Techniques

Zero-Order Methods

Strictly spoken, zero-order or direct search methods are techniques that use a sequential examination of trial solutions involving comparison of each trial solution with the 'best' obtained up to that time, together with a strategy for determining, as a function of earlier results, what the next trial solution will be [76]. However, this text uses a more flexible definition. Here, direct search methods are defined as 'derivative-free' techniques that exclusively rely on values of the cost-function to solve the optimisation problem.

First-Order Methods

The gradient of a function at a particular point represents the direction perpendicular to the tangent hyperplane at the considered point. The gradient thus provides information about the behaviour of the function in the vicinity of the working point. Using gradient information, it is possible to determine the direction in which the function is descending the most. Since the gradient is based on a linear approximation, it only provides information about the direction in which the function is decreasing, it does not provide any information about the distance to the minimum.

Second-Order Methods

The combination of first and second-order derivatives provides a local parabolic approximation of the cost-function. Such a second-order approximation does not only provide a direction in which the cost-function decreases, it also gives an estimate of the distance to the minimum, as illustrated in figure 4.3(b). Derivative-based methods are usually iterative descent methods [73]. In these methods, each iteration step combines two actions: 1) finding a direction in which the cost-function decreases, 2) reducing the value of the cost-function by taking a step in the chosen direction. As such, the cost-function is gradually reduced until the minimum is found. The use of higher-order information usually leads to a substantial reduction in the number of iteration steps, and thus the number of cost-function evaluations. But the derivative-based methods also have a number of important disadvantages, e.g. they require the computation of the cost-function derivatives.

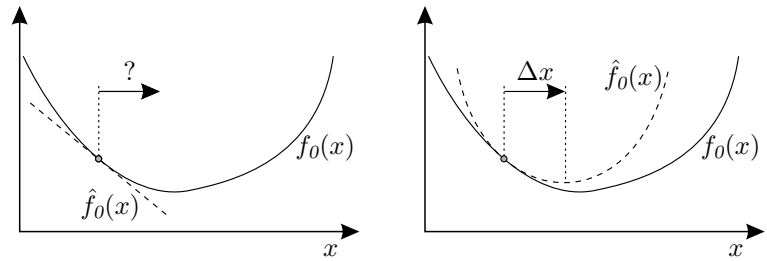

(a) First-order methods. (b) Second-order methods.

Figure 4.3: *Representation of the higher-order optimisation methods.*

4.2. Zero-Order Methods

This section discusses three zero-order techniques that are commonly used to solve inverse problems: simplex methods, genetic algorithms and neural networks. The principal goal of this discussion is to present the basics of these three methods and to assess whether these techniques are suitable to solve vibration-based material identification problems.

4.2.1. Simplex Methods

A simplex is a geometric figure that has a number of vertices, i.e. corners, equal to the number of dimensions of the considered space plus one [77]. So, in an n-dimensional space a simplex is defined by $n+1$ points. Figure 4.4 presents the shapes of a simplex in a one-, two- and three-dimensional space.

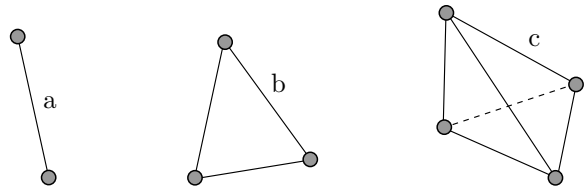

Figure 4.4: *Simplexes in a one-dimensional (a), two-dimensional (b) and three-dimensional (c) space.*

Simplex-based optimisation methods start by defining one simplex in the parameter space and the computation of the value of the cost-function in all the vertices of this simplex. In the next step, the simplex is shifted to an adjacent but optimal zone of the parameter space. With traditional simplex methods, this is achieved by performing a reflection operation on the initial simplex. A reflection operation moves the vertex that corresponds with the highest value of the cost-function by projecting it through the centre of gravity of the remaining vertices, i.e. the centroid. The result of the reflection operation is graphically illustrated in figure 4.5. In this figure, the old simplexes are plotted with dashed lines, the new simplexes with full lines, and the centroids are indicated by open circles. The value of the cost-function is evaluated in the new vertex and compared with the cost-function values of the old vertices. The worst vertex is identified and the new simplex is shifted with a new reflection move. This process is repeated until the solution has converged. The described procedure is called the 'fixed-size simplex' method and was introduced by Spendley, Hext and Himsworth [78].

To improve the performance of this procedure, Nelder and Mead [79] added two additional simplex operations: expansion and contraction. In expansion, the distance between the new vertex and the centroid is twice as large as with the reflection operation. In contraction, the distance between the new vertex and the centroid is half the distance of the reflection operation. There are two types of contractions, the first type keeps the new vertex on the same side as the reflection vertex, the second type flips the new vertex to the opposite side of the reflection vertex. All the possible operations of the Nelder-Mead procedure are represented in figure 4.5.

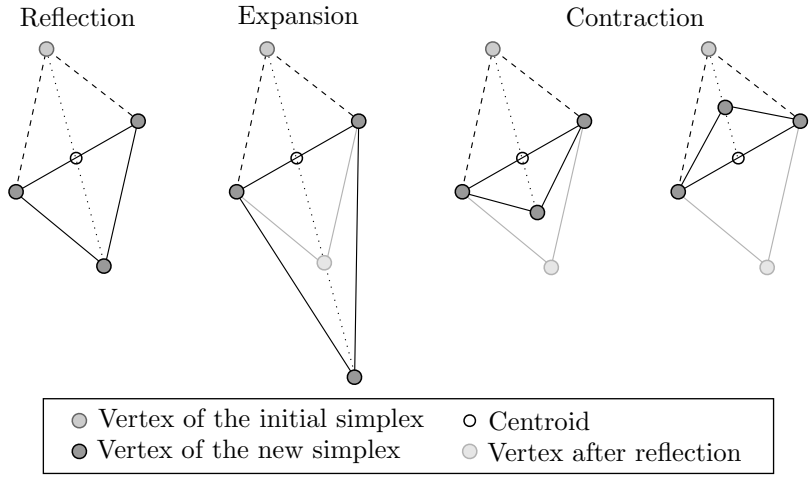

Figure 4.5: *The reflection, expansion and contraction operations of the Nelder-Mead algorithm.*

The Nelder-Mead algorithm is basically identical to the previously described fixed-size simplex algorithm, except from a small difference: at each step, a set of logical rules will decide which of the four possible simplex operations has to be used to create the new simplex. The Nelder-Mead simplex algorithm has become an extremely popular optimisation algorithm. Of all the direct search methods, the Nelder-Mead simplex algorithm is the most commonly used in numerical software packages [80]. Note that the expansion and contraction operations change the size of the simplex, therefore the Nelder-Mead algorithm is also called the 'variable-size simplex' method.

4.2.2. Genetic Algorithms

Genetic algorithms are optimisation techniques based upon the natural process of evolution [81]. The optimum is found with a stochastic but directed search, based on the principles of population genetics according to Darwin's principal of survival of the fittest.
In most genetic algorithms, the parameters are represented by finite-length binary-coded strings. For multi-parameter optimisation problems, the individual parameter codes are concatenated into a single string, which then represents a unique point in the parameter space of the problem. Figure 4.6 depicts the binary representation of a point in an n-dimensional parameter space where each parameter is encoded with an eight bit sequence.

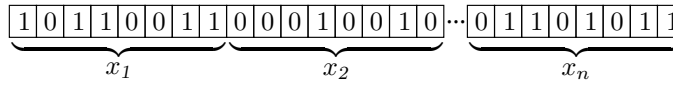

Figure 4.6: *Binary-coded representation of a point in n-dimensional space.*

The optimisation process starts by randomly selecting a number of points in the search space. The selected points are called individuals, and the collection of all these points is called the initial population. The first step evaluates the whole population by means of the fitness function. The fitness function, which is the inverse of the traditional cost-function, assigns a value to each individual of the population and allows to compare the quality of the different individuals. Because it is highly unlikely that the best individual of the initial population represents the optimal point in the search space, a new population has to be created and evaluated. By using the genetic information of the elite individuals of the current population, it should be possible to create a new population with improved fitness properties. The selected parents can produce offspring in three different ways: crossover, transfer and mutation.

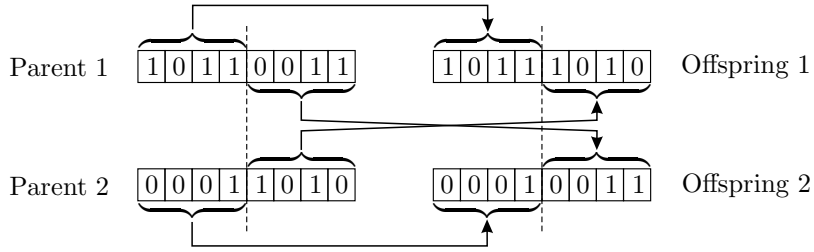

Figure 4.7: *Multipoint crossover.*

The crossover mechanism uses the genetic information of two parents to create the offspring. There are different ways to combine the parent's genetic information. One possible way is to exchange randomly selected substrings between the two parents. This mechanism is called multipoint crossover and is illustrated in figure 4.7. Another possible way is to create the offspring's binary code by copying the corresponding bit from one of the parents with equal probability. This mechanism is called uniform crossover and is illustrated in figure 4.8.

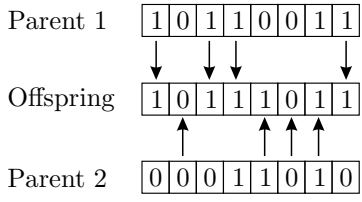

Figure 4.8: *Uniform crossover.*

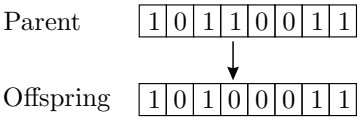

Figure 4.9: *Mutation.*

Transfer is the second reproductive mechanism. With this mechanism the genetic information of some of the elite individuals of the population is directly transferred to the new population, which means that the offspring are exact 'clones' of the parents.

Mutation is a sort of alternative reproductive mechanism. A mutant is obtained by randomly changing information in the genetic sequence of its parent. The

mutation mechanism is usually implemented by changing a randomly selected bit of the binary sequence as shown in the example of figure 4.9.
Once the new population is created, the individuals can be evaluated with the fitness function. This process is repeated until the solution has converged.

4.2.3. Neural Networks

Neural networks [82,83] are no genuine optimisation techniques like the simplex methods or genetic algorithms, however they can be applied to solve inverse problems by only using direct function evaluations. Neural networks are universal function approximators and can thus be used to approximate the output-input relation of the initial model. Once this output-input relation is defined, the inverse problem can be solved by inserting the desired model output into the neural network.

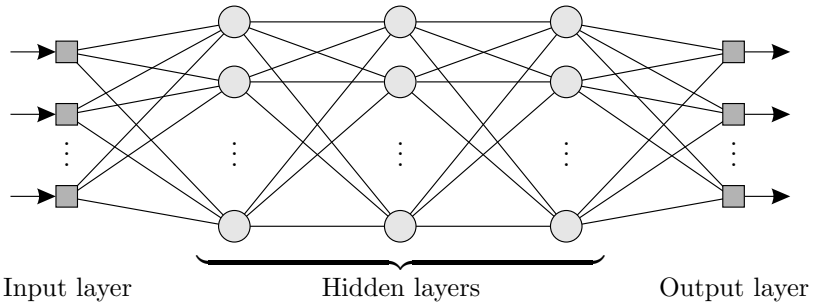

Figure 4.10: *A neural network with three hidden layers.*

A neural network is a computational model that consists of a set of hidden-layer neurons that connect the network's input parameters with the output parameters. Figure 4.10 presents the general structure of a neural network. At every neuron, the inputs are weighted and summed. The obtained sum is then inserted into the activation function f to produce the neuron output y_k. Figure 4.11 provides the general structure of a neuron.

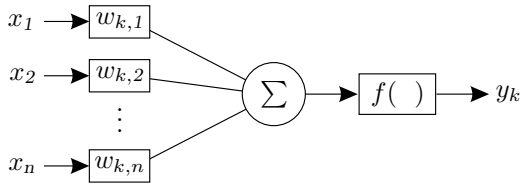

Figure 4.11: *The neuron model.*

The neural network architecture, figure 4.10, provides only the general form of the network's input-output relation. For every neuron, the user has to specify the weights w_i and the activation function f. The choice of the activation functions is usually based on the physics of the considered problem. The weights w_i are determined by training the network using a pool of training samples

that are generated with the direct model. This training pool groups a number of input parameters with their corresponding output values. The training pool represents the input-output relation of the initial model in an implicit and sampled form. During the iterative training process, the neuron weights w_i are tuned in such a way that the network reproduces the input parameter sets of the training pool from the output value sets in an optimal way[1].
The trained neural network provides an optimal fit of the response surfaces of the initial model, and the inverse problem can be solved by inserting the desired model output into the neural network.

4.2.4. Conclusions

The main advantage of the zero-order methods is that no derivative information like gradients or Hessians is required, which means that the implementation of the optimisation algorithm does not depend on the cost-function. Therefore, it is quite easy to implement these techniques in general purpose optimisation codes. As a result, the zero-order techniques have become very popular. But the theoretical discussion on zero-order methods raises the suspicion that the zero-order methods might require a large number of cost-function evaluations to find the optimum. This would be a serious disadvantage, since the evaluation of the MNET cost-function involves solving one or more FE-models.
There is a substantial number of publications that discusses the estimation of material parameters based on zero-order techniques. Applications of vibration-based elastic material parameter identification using the simplex method can be found in [84], applications using a genetic algorithm can be found in [33, 37, 85, 86] and applications that use neural networks can be found in [86–88]. Comparing the efficiency of the various zero-order methods from the results presented in these references is not straightforward, mainly because every publication considered a particular set-up. Furthermore, most references did not explicitly mention the number of cost-function evaluations required to find the minimum. However, references [33] and [86] considered the same test configuration. Both references used a laminated glass-epoxy plate of 200×200×5 mm. The considered laminate was made with 12 equal layers and had the following stacking sequence: $[0/+45/\text{-}45/90/\text{-}45/+45]_s$. Table 4.1 presents the in-plane elastic properties of the glass-epoxy layers.

Table 4.1: *The in-plane elastic properties of the glass-epoxy [33, 86].*

E_1 [GPa]	E_2 [GPa]	G_{12} [GPa]	ν_{12} [–]
38.48	9.38	3.41	0.292

Reference [33] presented results obtained with a genetic algorithm, while reference [86] presented results obtained with both a genetic algorithm and a neural network. To complete the comparison of the zero-order methods, the problem was also solved with the Nelder-Mead simplex algorithm and with the higher-order method that will be presented in section 4.6. Table 4.2 gives an overview

[1] The output of the initial model is the input of the neural network and vica versa.

of the obtained results. Apparently, the genetic algorithms required a very high number of direct function evaluations, while the residuals were about 1 %. The simplex algorithm found the correct material parameters but required a substantial number of FE-calculations. The neural network approach required only one third of the function evaluations of the simplex algorithm but resulted in residuals with an average magnitude of 0.13 %. Using derivative information, the correct solution could be identified with only 8 FE-model evaluations. This is about 14 times less than the number of FE-model evaluations of the optimal zero-order technique, i.e. the neural network approach.

Table 4.2: *Comparison of the zero-order methods.*

	Number of FE evaluations		E_1 (38.480)	E_2 (9.380)	G_{12} (3.410)	ν_{12} (0.292)
GA[2]	3001	value	38.340	9.240	3.480	0.293
		error	0.364 %	1.493 %	2.053 %	0.342 %
GA[3]	600	value	38.908	9.281	3.326	0.279
		error	1.112 %	1.055 %	2.463 %	4.452 %
NMS[4]	323	value	38.480	9.380	3.410	0.292
		error	0.001 %	0.001 %	0.003 %	0.006 %
NN[5]	110	value	38.486	9.389	3.409	0.291
		error	0.017 %	0.101 %	0.021 %	0.362 %
HO[6]	8	value	38.480	9.380	3.410	0.292
		error	0.000 %	0.000 %	0.001 %	0.001 %
			[GPa]	[GPa]	[GPa]	[–]

One may conclude that zero-order methods are powerful optimisation techniques. However, the example presented above demonstrates that the zero-order techniques require too many cost-function evaluations and are, therefore, not the proper class of techniques to solve the optimisation problem of the vibration-based MNET procedures.

4.3. Basic Concepts of Convex Optimisation

Proving that a cost-function does not have any local minima is a case-dependant matter. Since convex functions do not have local minima but only one global minimum, the absence of local minima is usually proven in an indirect way, by showing that the cost-function is convex. This section introduces the basic concepts of convex optimisation and is mainly based on the theoretical part of [73].

[2]Genetic algorithm, the results as published in [33].
[3]Genetic algorithm, the results as published in [86].
[4]Nelder-Mead simplex, using the implementation of MATLAB which is based on [89].
[5]Neural network, the results as published in [86].
[6]Higher-order method, using the routine described in section 4.6.

4.3.1. Convex Sets

A set C is convex, if the line segment between any two points of C lies in C. This implies that for any x_1 and $x_2 \in C$

$$\big(\theta x_1 + (1-\theta)x_2\big) \in C \tag{4.2}$$

and this for all $\theta \in [0,1]$. Roughly spoken, a set is convex if every point in the set can be seen by every other point along an unobstructed straight path between them, where 'unobstructed' means lying in the set [73]. Figure 4.12 presents an example of both a convex and a non-convex set.

(a) A convex set. (b) A non-convex set.

Figure 4.12: *An example a convex and a non-convex set.*

4.3.2. Convexity

A function $f\colon \mathbb{R}^n \rightarrow \mathbb{R}$ is convex if its domain is a convex set and if expression (4.3) holds for all $\{x\}, \{y\} \in \mathrm{dom} f$, and this for all $\theta \in [0,1]$.

$$f\big(\theta x + (1-\theta)y\big) \leqslant \theta f(x) + (1-\theta) f(y) \tag{4.3}$$

Geometrically, inequality (4.3) implies that the chord connecting $\big(x, f(x)\big)$ with $\big(y, f(y)\big)$ must lie above the graph of f. This principle is illustrated in figure 4.13.

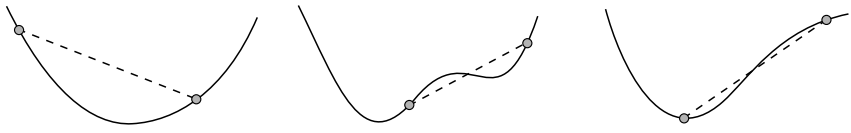

Figure 4.13: *Graphical representation of the definition of convexity.*

If function f is continuously differentiable on its domain, then f is convex if $\mathrm{dom} f$ is a convex set and if inequality (4.4) holds for all $\{x\}, \{y\} \in \mathrm{dom} f$.

$$f(y) \geqslant f(x) + \{\nabla f(x)\}^{\mathrm{T}} \left(\{y\} - \{x\}\right) \tag{4.4}$$

Expression (4.4) is called the first-order convexity condition and can be derived from (4.3) as shown in [73]. Figure 4.14 provides a graphical interpretation of this convexity condition.

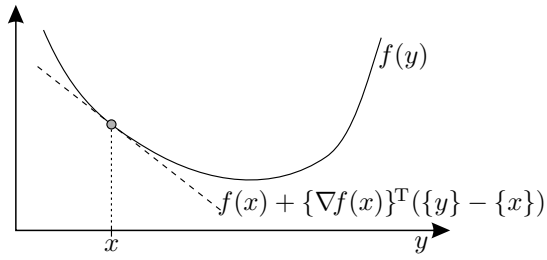

Figure 4.14: *Graphical interpretation of the first-order convexity condition.*

If f is twice continuously differentiable on its domain, then (4.3) can be transformed into the following second-order convexity condition [73]: the function f is convex, if dom$f$ is a convex set and if its Hessian is positive semi-definite.

4.3.3. Optimality Condition

Reference [73] proves that the vector $\{x^\star\}$ is the optimal solution of a convex optimisation problem, if and only if $\{x^\star\}$ is a feasible point for which

$$\{\nabla f_0(x^\star)\}^{\mathrm{T}}(\{y\} - \{x^\star\}) \geqslant 0 \tag{4.5}$$

and this for all feasible y. Note that (4.5) implies that a convex cost-function can have more than one minimum, as shown on figure 4.15. However, a convex cost-function cannot have any local minima, since this would conflict with the convexity condition (4.4).

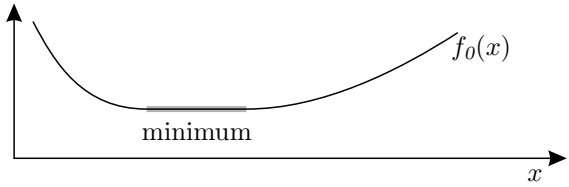

Figure 4.15: *A convex function with a non-unique minimum.*

4.4. Unconstrained Optimisation

Unconstrained optimisation focuses on solving the following problem

$$\underset{x}{\text{minimise}} \quad f_0(x) \qquad\qquad \{x\} \in \mathbb{R}^n \tag{4.6}$$

In this section, it will be assumed that the cost-function $f_0(x)$: $\mathbb{R}^n \rightarrow \mathbb{R}$ is convex and twice continuously differentiable.

4.4.1. Optimality Condition

According to section 4.3.3, convexity of the cost-function f_0 implies that

$$f_0(y) \geqslant f_0(x) + \{\nabla f_0(x)\}^{\mathrm{T}}(\{y\} - \{x\}) \tag{4.7}$$

for any $\{x\}, \{y\} \in \mathrm{dom} f_0$. If the cost-function f_0 attains its minimal value in $\{x^\star\}$ then $f_0(y) \geqslant f_0(x^\star)$ for all $\{y\} \in \mathrm{dom} f_0$. The combination of this inequality with the inequality of equation (4.7) yields

$$\{\nabla f_0(x^\star)\}^{\mathrm{T}}(\{y\} - \{x^\star\}) \leqslant 0 \tag{4.8}$$

Furthermore, according to the general optimality condition (4.5) the solution $\{x^\star\}$ is only optimal if

$$\{\nabla f_0(x^\star)\}^{\mathrm{T}}(\{y\} - \{x^\star\}) \geqslant 0 \tag{4.9}$$

The conditions (4.8) and (4.9) can only be met for all $\{y\} \in \mathrm{dom} f_0$ if the gradient $\nabla f_0(x)$ equals zero. So, if f_0 is differentiable, a necessary and sufficient condition for a point $\{x\}$ to be the optimal solution $\{x^\star\}$ is

$$\{\nabla f_0(x^\star)\} = \{0\} \tag{4.10}$$

Solving the unconstrained minimisation problem (4.6) is thus the same as finding the solution of (4.10), which is a set of n equations of the n variables $\{x_1\}, \ldots, \{x_n\}$. In a few special cases, the problem (4.10) can be solved in an analytical way, but for an arbitrary convex cost-function the problem has to be solved with an iterative algorithm that computes a sequence of points $\{x^{(0)}\}, \{x^{(1)}\}, \ldots \in \mathrm{dom} f_0$, where $f_0\big(x^{(k)}\big) \to f_0^\star$ as $k \to \infty$.

4.4.2. Analytical Solutions

A number of unconstrained optimisation problems can be solved analytically. These analytical solutions do not only provide a computationally efficient result, some of these solutions also form the foundation for the more advanced numerical optimisation methods.

The Linear Least-Squares Problem

Consider a set of m independent, linear equations of the n unknowns $\{x_1\}, \ldots, \{x_n\}$.

$$[A]\{x\} = \{b\} \tag{4.11}$$

When the number of equations m equals the number of unknowns n, a unique solution to the set of equations (4.11) exists. In the more general case, where the number of equations m exceeds the number of unknowns n, a vector $\{x\}$ that satisfies the set of equations no longer exists. This implies that there is no exact solution to (4.11), or that

$$[A]\{x\} - \{b\} = \{\epsilon\}, \quad \forall \{x\} \in \mathbb{R}^n \tag{4.12}$$

in which $\{\epsilon\} \in \mathbb{R}^m$ contains the residuals.
However, in this case, a quasi or optimal solution [90] can be defined as the vector $\{x^\star\}$ that satisfies the m equations as well as possible, according to a

particular criterion. The most popular criterion in engineering applications is the least-squares criterion, which states that the optimal solution is the solution that minimises the sum of the squared residuals, or mathematically

$$\underset{x}{\text{minimise}} \sum_{i=1}^{m} \epsilon_i^2 \qquad \text{or} \qquad \underset{x}{\text{minimise}} \left\| \{\epsilon\} \right\|^2 \tag{4.13}$$

where $\|\diamond\|$ denotes the Euclidean norm. By substituting (4.12) into (4.13) the least-squares solution to (4.11) can be expressed as

$$\underset{x}{\text{minimise}} \left\| [A]\{x\} - \{b\} \right\|^2 \tag{4.14}$$

Expression (4.14) is the standard form of the linear least-squares minimisation problem. The cost-function of (4.14) can be expressed in matrix form as

$$\begin{aligned} f_{ls} &= \left\| [A]\{x\} - \{b\} \right\|^2 \\ &= \{x\}^{\mathrm{T}}[A]^{\mathrm{T}}[A]\{x\} - 2\{b\}^{\mathrm{T}}[A]\{x\} + \{b\}^{\mathrm{T}}\{b\} \end{aligned} \tag{4.15}$$

Convexity — In order to be convex, the least-squares cost-function has to comply with the first-order convexity condition (4.4). This convexity condition can be rewritten as

$$f_{ls}(y) - f_{ls}(x) - \{\nabla f_{ls}(x)\}^{\mathrm{T}}(\{y\} - \{x\}) \geqslant 0 \tag{4.16}$$

The substitution of (4.15) into the left-hand side of (4.16) provides

$$\begin{gathered} \{y\}^{\mathrm{T}}[A]^{\mathrm{T}}[A]\{y\} - 2\{b\}^{\mathrm{T}}[A]\{y\} + \{b\}^{\mathrm{T}}\{b\} - \{x\}^{\mathrm{T}}[A]^{\mathrm{T}}[A]\{x\} + \\ 2\{b\}^{\mathrm{T}}[A]\{x\} - \{b\}^{\mathrm{T}}\{b\} - \big(2[A]^{\mathrm{T}}[A]\{x\} - 2[A]^{\mathrm{T}}\{b\}\big)^{\mathrm{T}}\big(\{y\} - \{x\}\big) \geqslant 0 \end{gathered} \tag{4.17}$$

By adding up the corresponding terms, expression (4.17) can be simplified to

$$\{x\}^{\mathrm{T}}[A]^{\mathrm{T}}[A]\{x\} - 2\{x\}^{\mathrm{T}}[A]^{\mathrm{T}}[A]\{y\} + \{y\}^{\mathrm{T}}[A]^{\mathrm{T}}[A]\{y\} \geqslant 0 \tag{4.18}$$

which can be contracted to

$$\Big([A]\{x\} - [A]\{y\}\Big)^2 \geqslant 0 \tag{4.19}$$

that proves the convexity of the least-squares cost-function.

Optimality — The least-squares cost-function f_{ls} is quadratic, and thus a continuously differentiable function. According to the optimality condition (4.10), the minimum will be attained in the point where the gradient equals zero. The optimal point $\{x^\star\}$ is thus found for

$$\nabla f_{ls}(x_{ls}^\star) = 2([A]^{\mathrm{T}}[A])\{x_{ls}^\star\} - 2[A]^{\mathrm{T}}\{b\} = \{0\} \tag{4.20}$$

so

$$\{x_{ls}^\star\} = \big([A]^{\mathrm{T}}[A]\big)^{-1}[A]^{\mathrm{T}}\{b\} \tag{4.21}$$

or

$$\{x^\star_{ls}\} = [A]^\dagger\{b\} \tag{4.22}$$

where $[\diamond]^\dagger$ denotes the Moore-Penrose pseudo inverse.

The Weighted Least-Squares Problem

In the previous section, all the residues ϵ_i had the same importance. However, the importance of the match of the i^{th} equation of (4.11), i.e. the importance of ϵ_i, can be increased or decreased by using weighting factors. The cost-function of this weighted least-squares problem can be written as

$$\underset{x}{\text{minimise}} \sum_{i=1}^{m} w_i\epsilon_i^2 \qquad \text{or} \qquad \underset{x}{\text{minimise}}\, \{\epsilon\}^{\mathrm{T}}[W]\{\epsilon\} \tag{4.23}$$

where the weighting matrix $[W] \in \mathbb{R}^{m\times m}$ is a diagonal matrix containing the weighting factors w_i. The introduction of (4.12) into (4.23) yields

$$\underset{x}{\text{minimise}} \big([A]\{x\} - \{b\}\big)^{\mathrm{T}}[W]\big([A]\{x\} - \{b\}\big) \tag{4.24}$$

As with the linear least-squares cost-function, the weighted least-squares cost-function f_{wls} is a twice continuously differentiable convex function. The optimal point is thus the point where the gradient equals zero, or

$$\nabla f_{wls}(x^\star_{wls}) = 2\big([A]^{\mathrm{T}}[W][A]\big)\{x^\star_{wls}\} - 2[A]^{\mathrm{T}}[W]\{b\} = \{0\} \tag{4.25}$$

or

$$\{x^\star_{wls}\} = \big([A]^{\mathrm{T}}[W][A]\big)^{-1}[A]^{\mathrm{T}}[W]\{b\} \tag{4.26}$$

The matrix $[\sqrt{W}]$ is the diagonal matrix that contains the square roots of the weighting factors w_i, therefore

$$[W] = [\sqrt{W}]^{\mathrm{T}}[\sqrt{W}] \tag{4.27}$$

By inserting (4.27) into (4.26), the latter can be rewritten as

$$\{x^\star_{wls}\} = \big([\sqrt{W}A]^{\mathrm{T}}[\sqrt{W}A]\big)^{-1}[\sqrt{W}A]^{\mathrm{T}}\{\sqrt{W}b\} \tag{4.28}$$

By adopting the notations $[A_w] = [\sqrt{W}A]$ and $\{b_w\} = \{\sqrt{W}b\}$, expression (4.28) becomes

$$\{x^\star_{wls}\} = ([A_w]^{\mathrm{T}}[A_w])^{-1}[A_w]^{\mathrm{T}}\{b_w\} \tag{4.29}$$

The solution of the weighted least-squares problem can thus be obtained with the same algorithm as the solution of the standard least-squares problem, if $[A]$ and $\{b\}$ are pre-multiplied with the square root of the weighting matrix $[W]$.

The Regularised Tychonov and Bayesian Formulation

The regularised Tychonov (4.30) and the Bayesian (4.31) cost-functions are two other least-squares formulations that are commonly used to solve inverse problems [90].

$$\underset{x}{\text{minimise}} \sum_{i=1}^{m} \epsilon_i^2 + \delta x_i^2 \quad \text{or} \quad \underset{x}{\text{minimise}} \left\|\{\epsilon\}\right\|^2 + \delta \left\|\{x\}\right\|^2 \tag{4.30}$$

$$\underset{x}{\text{minimise}} \sum_{i=1}^{m} w_{r_i}\epsilon_i^2 + w_{p_i} x_i^2 \quad \text{or} \quad \underset{x}{\text{minimise}} \{\epsilon\}^{\mathrm{T}}[W_r]\{\epsilon\} + \{x\}^{\mathrm{T}}[W_p]\{x\} \tag{4.31}$$

in which δ is a scalar weighting factor, $[W_r]$ and $[W_p]$ are the diagonal weighting matrices of the responses and parameters, respectively. Expressions (4.32) and (4.33) provide the optimal solution of these two cost-functions.

$$\{x^\star_{Tyc}\} = \left([A]^{\mathrm{T}}[A] + \delta[I]\right)^{-1}[A]^{\mathrm{T}}\{b\} \tag{4.32}$$

$$\{x^\star_{Bay}\} = \left([A]^{\mathrm{T}}[W_r][A] + [W_p]\right)^{-1}[A]^{\mathrm{T}}[W_r]\{b\} \tag{4.33}$$

The solution of the least-squares problem (4.22) depends on the inverse of the product $[A]^{\mathrm{T}}[A]$. The rank of this product equals the rank of matrix $[A]$, which means that the optimal solution is not defined if matrix $[A]$ is rank deficient. If $[A]$ is ill-conditioned but not singular, the inverse of $[A]^{\mathrm{T}}[A]$ can be calculated, but will be very sensitive to numerical noise. The main advantage of the regularised Tychonov and Bayesian formulation can be seen from the expressions of the optimal solution. In both cases, a diagonal matrix is added to the product $[A]^{\mathrm{T}}[A]$, which has a positive influence on the conditioning of the problem. The use of the regularised Tychonov and Bayesian formulation is thus only beneficial for ill-conditioned problems. Since ill-conditioned MNETs should be redesigned instead of solved, the regularised Tychonov and Bayesian formulation are not useful for parameter identification problems. They are, however, essential for solving conventional model updating problems.

4.4.3. Descent Methods

If is not possible to find an analytical solution for the minimum of an arbitrary cost-function. If there is no analytical solution, the optimisation problem has to be solved numerically. Descent methods [73, 91] are iterative algorithms that can provide an accurate approximation of the minimum of an arbitrary convex cost-function. They produce a minimising sequence of points $\{x^{(0)}\}, \{x^{(1)}\}, \ldots \in \mathrm{dom} f_0$, for which $f_0\big(x^{(k+1)}\big) < f_0\big(x^{(k)}\big)$. This implies that $f_0\big(x^{(k)}\big) \to f_0^\star$ as $k \to \infty$, or that $\{x^{(\infty)}\} = \{x^\star\}$. In the minimising sequence, each point is obtained from the previous point as

$$\{x^{(k+1)}\} = \{x^{(k)}\} + t^{(k)}\{v^{(k)}\} \tag{4.34}$$

where k denotes the iteration step. Geometrically, expression (4.34) has the following interpretation. At the point defined by $\{x^{(k)}\}$, a step with length $t^{(k)} > 0$ is taken in the direction defined by $\{v^{(k)}\}$. If the vector $\{v^{(k)}\}$ rep-

resents a descent direction, the cost-function is reduced. By considering the convexity condition (4.4), the descent requirement

$$f_0\big(x^{(k+1)}\big) < f_0\big(x^{(k)}\big) \tag{4.35}$$

can be reformulated as

$$\{\nabla f_0(x^{(k)})\}^{\mathrm{T}}\{v^{(k)}\} < 0 \tag{4.36}$$

If the search direction $\{v^{(k)}\}$ meets requirement (4.36), it is a descent direction and the working point $\{x^{(k)}\}$ is shifted in the direction of the optimal solution. To summarise, a descent method converges to the optimal point by alternating between two subroutines: the computation of a proper descent direction $\{v\}$, and the selection of an appropriate step size t. Figure 4.16 presents the general flowchart of a descent method.

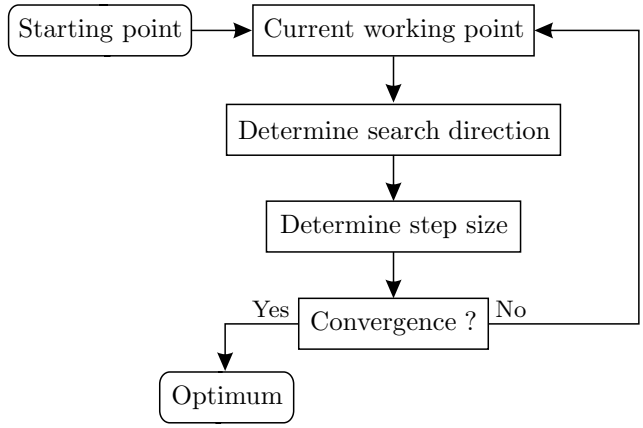

Figure 4.16: *The general flowchart of a descent method.*

First-Order or Gradient Descent Methods

First-order descent methods only use gradient information, i.e. first-order derivatives, to minimise the cost-function. The first step of these methods is the choice of the search direction. The most natural choice of the search direction is the direction defined by the negative gradient. Note that the negative gradient direction complies with (4.36), and is thus a valid descent direction. Apart from the most obvious choice, the negative gradient is also the optimal choice[7], at least in the situation where only first-order derivatives are available.
The second step of gradient descent methods is the selection of an appropriate step size. The optimal step is the step that shifts the working point to the minimum of the cost-function along the ray defined by the search direction, as illustrated by figure 4.17. The selection of the step size can be thus be defined as the one-dimensional optimisation problem

$$\underset{\alpha}{\text{minimise}} \quad \phi(\alpha) \tag{4.37}$$

[7]The proof of this statement is presented on page 78.

where ϕ is the cost-function reduced to the ray defined by the search direction, and α is the coordinate along this ray as shown in figure 4.17. This means that descent methods will solve a multi-dimensional optimisation problem by replacing it by a sequence of one-dimensional optimisation problems. Since they search the minimum of the cost-function along a line, the algorithms used to solve the problem (4.37) are called line search algorithms.

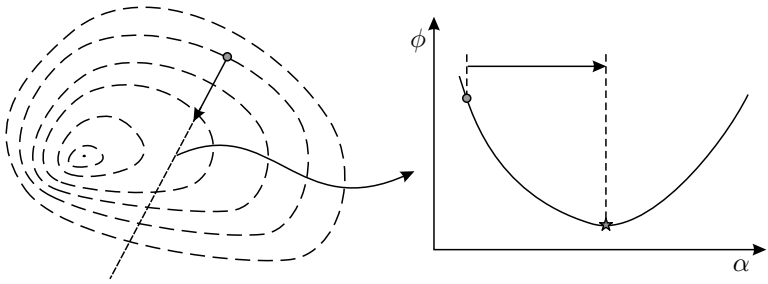

Figure 4.17: *Line search: the transformation of a multi-dimensional optimisation problem into an one-dimensional optimisation problem.*

Solving a one-dimensional optimisation problem is thus a key step in solving multi-dimensional optimisation problems. The availability of fast and stable procedures to solve one-dimensional optimisation problems is, therefore, essential for the practical use of descent methods. Line search algorithms can be divided into two classes: exact and inexact algorithms [73]. Exact line search algorithms calculate the absolute minimum of the cost-function. In most cases, the computation of the exact minimum is a time consuming operation, while it is possible to obtain a – rough – approximation of the minimum with a much smaller computational effort. Line search algorithms that only approximate the minimum are called inexact. Because of the much lower computational cost, most practical optimisation algorithms use inexact line search methods, such as the backtracking technique [73]. An overview of a number of exact and inexact line search algorithms can be found in [91]. Note that the behaviour of the line search algorithms heavily depends on the properties of the cost-function. The choice of the best line search algorithm is thus unique for each optimisation problem, and should be made after comparing the properties of the cost-function with the (dis)advantages of the different line search algorithms.

Second-Order Descent Methods

The main disadvantage of the gradient descent method is the computational inefficiency caused by the slow convergence rate. However, the convergence rate can be drastically increased by using second-order derivatives or curvature information. Newton's method is the basic second-order descent method. The Newton search direction $\{v_{nt}\}$ is derived from the second-order Taylor approximation $\hat{f}_0(v)$ of the cost-function at the working point $\{x\}$.

$$f_0(x+v) \approx \hat{f}_0(v) = f_0(x) + \{\nabla f_0(x)\}^{\mathrm{T}}\{v\} + \frac{1}{2}\{v\}^{\mathrm{T}}\left[\nabla^2 f_0(x)\right]\{v\} \qquad (4.38)$$

The descent direction used by Newton's method is the direction that minimises this second-order approximation. The choice of the descent direction is thus based on both gradient and curvature information. According to the unconstrained optimality condition (4.10), the minimiser $\{v^\star\}$ of the quadratic cost-function of (4.38) is found by

$$\{\nabla \hat{f}_0(v^\star)\} = \{\nabla f_0(x)\} + \left[\nabla^2 f_0(x)\right]\{v^\star\} = \{0\} \tag{4.39}$$

or

$$\{v_{nt}\} = -\left[\nabla^2 f_0(x)\right]^{-1}\{\nabla f_0(x)\} \tag{4.40}$$

The vector $\{v_{nt}\}$ is called the Newton step for cost-function at $\{x\}$. Note that the positive definiteness of the Hessian $\left[\nabla^2 f_0(x)\right]$ implies that

$$\{\nabla f_0(x)\}^{\mathrm{T}}\{v_{nt}\} = -\{\nabla f_0(x)\}^{\mathrm{T}}\left[\nabla^2 f_0(x)\right]^{-1}\{\nabla f_0(x)\} < 0 \tag{4.41}$$

unless $\{\nabla f_0(x)\} = \{0\}$, which shows that the Newton step $\{v_{nt}\}$ complies with (4.36) and proves that the Newton step provides a descent direction as long as $\{x\}$ is not the optimal point.

As shown in figure 4.18, the Newton step $\{v_{nt}\}$ can be interpreted as the difference between the minimiser of the approximated cost-function $\hat{f}_0(v)$ and the working point $\{x\}$. So, the Newton step does not only indicate an appropriate search direction, it also provides a suitable step length.

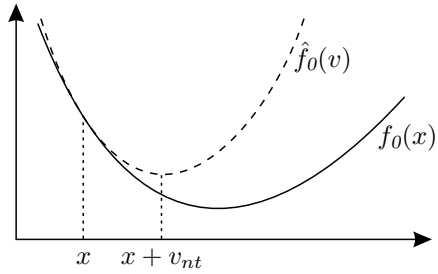

Figure 4.18: *The cost-function $f_0(x)$ and its second-order approximation $\hat{f}_0(v)$.*

To minimise a cost-function with Newton's method, one must use the Newton step $\{v_{nt}\}$ as descent direction in the flowchart of figure 4.16. A pure Newton method uses a step size of one and does not require a line search algorithm, a quasi Newton method uses a line search algorithm to improve the step size. Note that in case of a quadratic cost-function, e.g. a least-squares cost-function, the approximation $\hat{f}_0(v)$ equals the actual cost-function. As a consequence, Newton's method minimises the least-squares cost-function in a single iteration step.

Unified Formulation for First and Second-Order Methods

To conclude the section on unconstrained optimisation, consider the following unified formulation [91] for the search direction of the gradient descent method and Newton's method. The combination of equations (4.4), (4.35), and (4.36) shows that if the reduction of the cost-function value between $x^{(k)}$ and $x^{(k+1)}$ increases that then the value for the term $\{\nabla f_0(x)\}^{\mathrm{T}}\{v\}$ decreases. The optimal search direction is thus the direction that minimises the product $\{\nabla f_0(x)\}^{\mathrm{T}}\{v\}$. Unfortunately, this does not provide the desired search direction because the solution is not bounded. However, this problem can easily be overcome by adding the requirement that the search direction must have a unit length. The optimal search direction can thus be obtained as the solution of

$$\underset{v}{\text{minimise}} \quad \{\nabla f_0(x)\}^{\mathrm{T}}\{v\} \qquad \forall \{v\} \mid \|\{v\}\| = 1 \tag{4.42}$$

The solution of (4.42) depends on the definition of the norm used to measure the length of the search direction vector $\{v\}$. One of the possible norms is the general Euclidean norm which is defined as

$$\|\{v\}\|_N = \sqrt{(\{v\}^{\mathrm{T}}[N]\{v\})} \tag{4.43}$$

where $[N]$ is a symmetric positive-definite matrix. Note that for $[N] = [I]$, expression (4.43) becomes the definition of the standard Euclidean norm. Using a Lagragian function[8], the constrained optimisation problem (4.42) can be reformulated as the following unconstrained problem.

$$\underset{v}{\text{minimise}} \quad \{\nabla f_0(x)\}^{\mathrm{T}}\{v\} + \mu\big(\{v\}^{\mathrm{T}}[N]\{v\} - 1\big) \tag{4.44}$$

The optimal solution, defined by the point where the gradient of the cost-function of (4.44) becomes zero, equals

$$\{v^\star\} = -\frac{1}{2\mu}[N]^{-1}\{\nabla f_0(x)\} \tag{4.45}$$

The value of the scaling factor μ is determined by the value chosen for the norm in (4.42). Since the actual value of this norm is irrelevant, it can be assumed that the value of the norm in (4.42) was chosen is such a way that it corresponds with a scaling factor $\mu = \frac{1}{2}$. In this way, equation (4.45) reduces to

$$\{v^\star\} = -[N]^{-1}\{\nabla f_0(x)\} \tag{4.46}$$

When using the standard Euclidean norm $[N] = [I]$, the best downhill direction equals the negative gradient, which proves that the negative gradient is the optimal search direction, in case only gradient information is available. If the Hessian matrix is used as metric of the generalized Euclidean norm, the optimal search direction becomes $-\left[\nabla^2 f_0(x)\right]^{-1}\{\nabla f_0(x)\}$, which is the search direction of Newton's method.

[8] The use of the Lagrangian function to solve constrained optimisation problems is discussed in section 4.5.

4.5. Constrained Optimisation

In constrained optimisation problems, the values of the optimisation parameters are restricted by a number of equality or inequality constraints. Constrained optimisation thus focuses on solving the following problem.

$$\begin{array}{lll} \underset{x}{\text{minimise}} & f_0(x) & \{x\} \in \mathbb{R}^n \\ \text{subject to} & f_i(x) \leqslant 0 & i = 1, \ldots, r \\ & h_i(x) = 0 & i = 1, \ldots, s \end{array} \tag{4.47}$$

It will be assumed that the cost-function $f_0(x)\colon \mathbb{R}^n \to \mathbb{R}$, and the constraint functions $f_i(x)\colon \mathbb{R}^n \to \mathbb{R}$ and $h_i(x)\colon \mathbb{R}^n \to \mathbb{R}$ are convex and twice continuously differentiable. Both equality- and inequality-constrained optimisation problems are solved using the same strategy: reformulating the constrained problem as an unconstrained problem.

4.5.1. Optimality Conditions

Equality-Constrained Problems

If the cost-function is only subjected to equality constraints, the problem is called an equality-constrained optimisation problem. In this case, the general constrained optimisation problem (4.47) reduces to

$$\begin{array}{lll} \underset{x}{\text{minimise}} & f_0(x) & \{x\} \in \mathbb{R}^n \\ \text{subject to} & h_i(x) = 0 & i = 1, \ldots, s \end{array} \tag{4.48}$$

where $s < n$ to assure the existence of a solution to the posed problem. The equality-constrained optimisation problem (4.48) can be reformulated [91] as an unconstrained problem using a Lagrange function

$$\mathcal{L}(x, \eta) = f_0(x) + \sum_{i=1}^{s} \eta_i h_i(x) \tag{4.49}$$

in which η_i is the Lagrange multiplier of the i^{th} constraint. The summation terms $\eta_i h_i(x)$ can be seen as penalty functions, since they increase the value of the cost-function, if the considered constraint is violated. Because $\mathcal{L}(x, \eta)$ is an unconstrained function, the optimal solution must comply with (4.10), so

$$\nabla \mathcal{L}(x^\star, \eta^\star) = 0 \tag{4.50}$$

or

$$\begin{array}{lll} \dfrac{\partial \mathcal{L}}{\partial x_j} = \dfrac{\partial f_0(x^\star)}{\partial x_j} + \displaystyle\sum_{i=1}^{s} \eta_i^\star \frac{\partial h_i(x^\star)}{\partial x_j} = 0 & & j = 1, \ldots, n \\ \dfrac{\partial \mathcal{L}}{\partial \eta_i} = h_i(x^\star) = 0 & & i = 1, \ldots, s \end{array} \tag{4.51}$$

Solving this set of $n + s$ equations provides the optimal solution $\{x^\star\}$ together with the corresponding values of the Lagrange multipliers $\{\eta^\star\}$. Note that the

second equation of the optimality conditions (4.51) automatically ensures compatibility of the optimal solution with requirements of the imposed constraints. It also implies that the Lagrange function (4.49) equals the cost-function of (4.48) at the optimal point.

Inequality-Constrained Problems

If the cost-function is only subjected to inequality constraints, the problem is called an inequality-constrained optimisation problem. In the standard form, the inequality-constrained optimisation problem is formulated as

$$\begin{array}{lll} \underset{x}{\text{minimise}} & f_0(x) & \{x\} \in \mathbb{R}^n \\ \text{subject to} & f_i(x) \leqslant 0 & i = 1, \ldots, r \end{array} \tag{4.52}$$

The optimality conditions can be found by reformulating the inequality-constrained optimisation problem as an unconstrained problem using a Lagrange function [91].

$$\mathcal{L}(x, \lambda) = f_0(x) + \sum_{i=1}^{r} \lambda_i f_i(x) \tag{4.53}$$

The summation term of the Lagrange function can be considered as a penalty function. To ensure that a violation of the inequality constraints increases the Lagrange function, the Lagrange multipliers must be non-negative.

$$\lambda_i \geqslant 0 \tag{4.54}$$

The optimal solution results in a gradient of the Lagrange function that equals zero, or

$$\frac{\partial \mathcal{L}}{\partial x_j} = \frac{\partial f_0(x)(x^\star)}{\partial x_j} + \sum_{i=1}^{r} \lambda_i^\star \frac{\partial f_i(x^\star)}{\partial x_j} = 0 \qquad j = 1, \ldots, n \tag{4.55}$$

Equation (4.55) is not sufficient to provide the optimal solution, since it only provides n equations while there are $n + r$ unknown variables, i.e. the n components of $\{x^\star\}$ and the r components of $\{\lambda^\star\}$. The remaining r equations are found by demanding that the Lagrange function equals the initial cost-function at the optimal point, or

$$\lambda_i^\star f_i(x^\star) = 0 \qquad i = 1, \ldots, r \tag{4.56}$$

The optimality conditions for an inequality-constrained optimisation problem are commonly known as the Karush-Kuhn-Tucker (KKT) conditions and can be summarised as

$$\frac{\partial f_0(x^\star)}{\partial x_j} + \sum_{i=1}^{r} \lambda_i^\star \frac{\partial f_i(x^\star)}{\partial x_j} = 0 \qquad j = 1, \ldots, n \tag{4.57}$$

$$\lambda_i^\star f_i(x^\star) = 0 \qquad i = 1, \ldots, r \tag{4.58}$$

$$\lambda_i^\star \geqslant 0 \qquad i = 1, \ldots, r \tag{4.59}$$

$$f_i(x^\star) \leqslant 0 \qquad i = 1, \ldots, r \tag{4.60}$$

The first two equations provide the optimal solution. In case this set of equations provides more than one solution, the last two inequalities indicate the feasible optimal solution.

Interpretation of the KKT Conditions

The interpretation of the KKT conditions (4.58) and (4.60) is evident and does not require any additional explanation. Figure 4.19 provides a graphical interpretation [68] of the other two KKT conditions. This plot presents three different situations at three different points: (a) the negative cost-function gradient at point 1 can be written as a linear combination of the constraint gradients, i.e. KKT condition (4.57). However, one of the coefficients of the linear combination is negative, which is a violation of KKT condition (4.59). (b) It is impossible to express the negative gradient at point 2 as a linear combination of the constraint gradients. (c) The negative cost-function gradient at point 3 can be written as a linear combination of the constraint gradients, and for this point, all the coefficients of the linear combination are positive. Since point 3 also complies with KKT conditions (4.58) and (4.60), it has to be the optimal point. Note that the contour lines of the cost-function confirm that point 3 is indeed the optimal point.

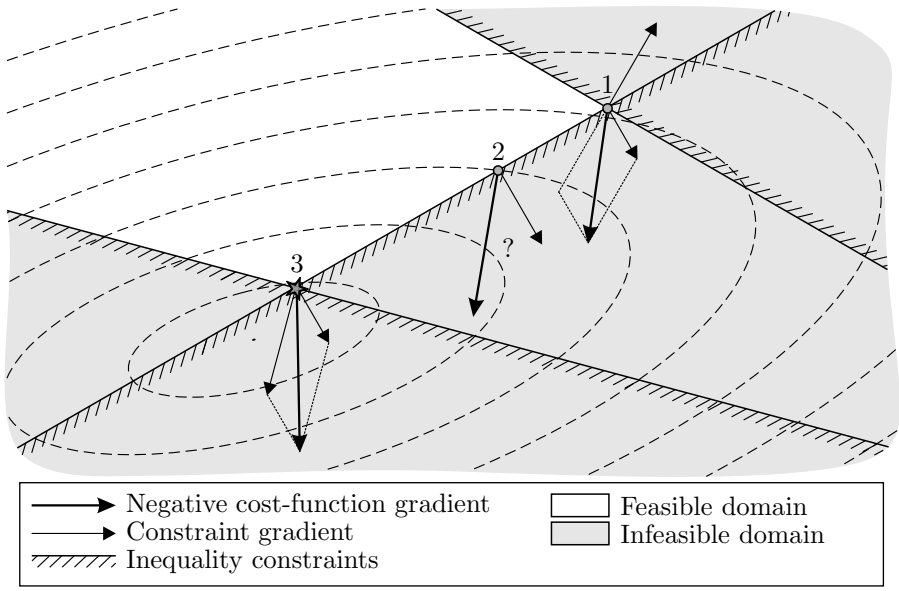

Figure 4.19: *Graphical interpretation of the KKT conditions.*

4.5.2. Solving the Equality-Constrained Problem

To simplify the problem, consider an equality-constrained optimisation problem with linear constraints. In this case, the optimisation problem can be formulated as

$$\begin{array}{lll} \underset{x}{\text{minimise}} & f_0(x) & \{x\} \in \mathbb{R}^n \\ \text{subject to} & \sum_{i=1}^{n} c_{ji}\, x_i + d_j = 0 & j = 1, \ldots, s \end{array} \tag{4.61}$$

The constraint equations can be written in matrix form as $[C]\{x\} + \{d\}$ where the matrix $[C] \in \mathbb{R}^{s \times n}$ groups the coefficients and the vector $\{d\} \in \mathbb{R}^s$ the constants of the equality constraints. This constrained optimisation problem can be solved with Newton's method as shown in [73]. The Newton search direction $\{v_{nt}\}$ is obtained from the second-order Taylor approximation of problem (4.61) at working point $\{x\}$.

$$\begin{array}{ll} \underset{v}{\text{minimise}} & \hat{f}_0(v) = f_0(x) + \{\nabla f_0(x)\}^{\mathrm{T}}\{v\} + \frac{1}{2}\{v\}^{\mathrm{T}}\left[\nabla^2 f_0(x)\right]\{v\} \\ \text{subject to} & [C](\{x\} + \{v\}) + \{d\} = \{0\} \end{array} \tag{4.62}$$

As explained in section 4.4.3, the Newton search direction is the direction that minimises this second-order approximation. According to the equality-constrained optimality conditions (4.51), the minimiser $\{v^\star\} = \{v_{nt}\}$ of problem (4.62) is found from

$$\begin{aligned} \{\nabla f_0(x)\} + \left[\nabla^2 f_0(x)\right]\{v^\star\} + [C]\{\eta^\star\}^{\mathrm{T}} &= \{0\} \\ [C](\{x\} + \{v^\star\}) + \{d\} &= \{0\} \end{aligned} \tag{4.63}$$

The current working point $\{x\}$ is a feasible point, so $[C]\{x\} + \{d\} = \{0\}$. The second equation of (4.63) can thus be simplified to $[C]\{v^\star\} = \{0\}$, and the constrained Newton search direction is found by solving

$$\begin{bmatrix} \left[\nabla^2 f_0(x)\right] & [C]^{\mathrm{T}} \\ [C] & [0] \end{bmatrix} \begin{bmatrix} \{v_{nt}\} \\ \{\eta^\star\} \end{bmatrix} = \begin{bmatrix} -\{\nabla f_0(x)\} \\ \{0\} \end{bmatrix} \tag{4.64}$$

The second equation of (4.63) shows that the point obtained by taking the step $\{v_{nt}\}$ automatically complies with the imposed constraints. Consequently, the equality-constrained optimisation problem (4.61) can be solved as an unconstrained problem by using the Newton step provided by (4.64). Note that the application of Newton's method to solve an equality-constrained optimisation problem requires a feasible starting point.

4.5.3. Solving the Inequality-Constrained Problem

The Penalty and Barrier Function Approach

Although a number of different approaches to handle inequality constraints exist, all the available techniques are based on the transformation of the constrained problem into an unconstrained problem. The two most important approaches are the penalty function [68] and barrier function [73] approach.
With the penalty function approach, an additional term is added to the cost-function, and this for every imposed constraint. The penalty function approach can be expressed as

$$\mathcal{F}_0(x) = f_0(x) + \gamma_k \sum_{i=1}^{s} F_i\big(f_i(x)\big) \tag{4.65}$$

where F_i is a function of the constraint $f_i(x)$ that results in a strictly positive value, if x violates the considered constraint and zero otherwise. The penalty factor γ is a positive weighting factor that determines the importance of the penalty term with respect to the cost-function. The constrained minimum is found by minimising the function $\mathcal{F}_0(x)$ for a sequence of increasing penalty factor values γ_k, in order to force the solution to converge to that of the initial problem (4.52).

The barrier function approach is another technique that is commonly used to reformulate an inequality-constrained problem into an unconstrained problem. This approach is similar to the penalty approach with the difference that the penalty functions are now smooth within, and infinite outside the feasible domain. The most important class of barrier functions are the logarithmic functions. The unconstrained cost-function of the logarithmic barrier approach is given by

$$\mathcal{F}_0(x) = f_0(x) - \gamma_k \sum_{i=1}^{s} \ln\big(-f_i(x)\big) \tag{4.66}$$

where ln denotes the natural logarithm. The barrier parameter γ_k regulates the importance of the barrier functions. The constrained minimum is obtained by searching the minimum of $\mathcal{F}_0$ for a sequence of γ_k values that gradually decrease to zero. A detailed discussion on the use of logarithmic barrier function can be found in [73].

The penalty and barrier function approaches are very powerful methods that can handle a wide variety of constraint functions. However, in case of linear constraint functions, both the penalty and barrier function approach are computationally inefficient in comparison to the projection approach.

The Projection Approach

Projection methods [91] are limited to linearly constrained optimisation problems, but they can solve them in a computationally efficient way. Consider the following reduced inequality-constrained optimisation problem

$$\begin{array}{lll} \underset{x}{\text{minimise}} & f_0(x) & \{x\} \in \mathbb{R}^n \\ \text{subject to} & \sum_{i=1}^{n} c_{ji}\, x_i + d_j \leqslant 0 & j = 1, \ldots, r \end{array} \tag{4.67}$$

In matrix form, the constraints of (4.67) are expressed as $[C]\{x\} + \{d\} \leqslant \{0\}$, with $[C] \in \mathbb{R}^{r \times n}$ and $\{d\} \in \mathbb{R}^r$. Each inequality constraint divides the optimisation space into two domains: a feasible and an infeasible domain. Since the constraints are linear, the boundary between the feasible and infeasible domain of each constraint is a hyperplane. The gradient vector $\{C_j\}$ of the j^{th} constraint is given by the transpose of the j^{th} row of the constraint coefficient matrix $[C]$. These gradient vectors represent the direction perpendicular to the hyperplane associated with the considered constraint.

Consider an optimisation procedure that has arrived at the k^{th} iteration step. Assume that, at this point, m linear constraints are active, the other $(r - m)$ constraints are inactive. Using the gradients of the active constraints, a matrix

$[N_a] \in \mathbb{R}^{n \times m}$ can be constructed as

$$[N_a] = [\{C_1\} \dots \{C_m\}] \tag{4.68}$$

To assure that the matrix $[N_a]$ is full rank, it is assumed that the number of active constraints is smaller than the number of optimisation variables, or that $m < n$. With descent algorithms, the cost-function is minimised in an iterative way by taking a step t in a particular direction $\{v_p\}$.

$$\{x^{(k+1)}\} = \{x^{(k)}\} + t^{(k)}\{v_p^{(k)}\} \tag{4.69}$$

In order to reduce the cost-function, the direction indicated by $\{v_p\}$ must be a descent direction. Assume that this vector lies at the intersection of all the active constraint hyperplanes, or

$$[N_a]^{\mathrm{T}}\{v_p\} = \{0\} \tag{4.70}$$

If expression (4.70) holds, the improved optimisation point $\{x^{(k+1)}\}$ will also lie at the intersection of the active constraint hyperplanes, which means that all the active constraints remain active and are respected. A suitable $\{v_p\}$ vector can be obtained by projecting a general descent direction $\{v\}$ onto the constraint intersection

$$\{v_p\} = [P_a]\{v\} \tag{4.71}$$

where $[P_a]$ is an orthogonal projection operator. An expression of the projection operator $[P_a]$ can be found as follows. The projected search direction is a solution of the optimisation problem (4.72).

$$\begin{array}{ll} \underset{v_p}{\text{minimise}} & \{\nabla f_0(x)\}^{\mathrm{T}}\{v_p\} \\ \text{subject to} & \|\{v_p\}\|_N = 1 \\ & [N_a]^{\mathrm{T}}\{v_p\} = \{0\} \end{array} \tag{4.72}$$

The minimisation of the product $\{\nabla f_0(x)\}^{\mathrm{T}}\{v_p\}$ provides the optimal downhill direction. The first constraint guarantees the boundedness of the solution, while the second constraint ensures that the obtained search direction lies in the subspace defined by the intersection of the active constraint hyperplanes. Using the Lagrange formulation, the problem (4.72) can be written as

$$\underset{v_p}{\text{minimise}} \quad \{\nabla f_0(x)\}^{\mathrm{T}}\{v_p\} + \mu\big(\{v_p\}^{\mathrm{T}}[N]\{v_p\} - 1\big) + \{\lambda\}[N_a]^{\mathrm{T}}\{v_p\} \tag{4.73}$$

in which $\mu \in \mathbb{R}$ and $\{\lambda\} \in \mathbb{R}^m$ are the Lagrange multipliers. The gradient of this Lagrangian equals zero for the directions $\{v_p\}$ that comply with

$$\{v_p\} = -\frac{1}{2\mu}[N]^{-1}\Big(\{\nabla f_0(x)\} + [N_a]\{\lambda\}\Big) \tag{4.74}$$

As explained in section 4.4.3, the value of the Lagrange multiplier μ is irrelevant for the search direction. However, a value of $\frac{1}{2}$ will result in a correct scaling of

the Newton step, when the Hessian is being used as metric for the Euclidean norm, so

$$\{v_p\} = -[N]^{-1}\Big(\{\nabla f_0(x)\} + [N_a]\{\lambda\}\Big) \tag{4.75}$$

The unknown Lagrange multipliers $\{\lambda\}$ can be found by inserting expression (4.75) into the second constraint of (4.72).

$$[N_a]^{\mathrm{T}}[N]^{-1}\Big(\{\nabla f_0(x)\} + [N_a]\{\lambda\}\Big) = \{0\} \tag{4.76}$$

Since $[N_a]$ is full rank, equation (4.76) can be solved for $\{\lambda\}$, which yields

$$\lambda = -\left([N_a]^{\mathrm{T}}[N]^{-1}[N_a]\right)^{-1}[N_a]^{\mathrm{T}}[N]^{-1}\{\nabla f_0(x)\} \tag{4.77}$$

By inserting expression (4.77) into (4.75), the projected search direction can be expressed as

$$\{v_p\} = -\Big([I] - [N]^{-1}[N_a]\left([N_a]^{\mathrm{T}}[N]^{-1}[N_a]\right)^{-1}[N_a]^{\mathrm{T}}\Big)[N]^{-1}\{\nabla f_0(x)\} \tag{4.78}$$

Since $\{v\} = -[N]^{-1}\{\nabla f_0(x)\}$ is the general search direction, expression (4.78) has the same form as (4.71) and, therefore, the project operator $[P_a]$ equals

$$[P_a] = [I] - [N]^{-1}[N_a]\left([N_a]^{\mathrm{T}}[N]^{-1}[N_a]\right)^{-1}[N_a]^{\mathrm{T}} \tag{4.79}$$

The Set of Active Constraints

An essential part of any projection algorithm is the determination of the set of active constraints. Since projection methods are iterative procedures, the set of active constraints has to be updated before each iteration step. The updating of the active set consists of two parts: (a) removing the constraints that have become inactive, and (b) checking whether there are no new constraints that should be added.

Adding a constraint — Initially, the optimisation algorithm computes the step size t without considering any constraints. The projection of the search direction assures that the constraints of the active set are respected. The other constraints can be respected by limiting the step size. The working point of the $(k+1)^{\mathrm{th}}$ iteration is found by taking a step t^k in the search direction

$$\{x^{(k+1)}\} = \{x^{(k)}\} + t^k\{v_p^{(k)}\} \tag{4.80}$$

Consider the i^{th} constraint, the maximal allowable step results at working point $\{x^{(k+1)}\}$ that lies on the constraint hyperplane; a larger step results in a violation of this constraint. If $\{x^{(k+1)}\}$ lies on the constraint hyperplane, then

$$\{C_i\}^{\mathrm{T}}\{x^{(k+1)}\} + \{d_i\} = \{0\} \tag{4.81}$$

Inserting (4.80) into (4.81) provides

$$\bar{t}_i = -\frac{\{C_i\}^{\mathrm{T}}\{x^{(k)}\} + \{d_i\}}{\{C_i\}^{\mathrm{T}}\{v_p^{(k)}\}} \tag{4.82}$$

where $\bar{t}_i$ is the upper limit of the step size, if only the i^{th} constraint is taken into account. To respect all the imposed constraints, the step size has to be smaller than all the steps $\bar{t}_i$. The largest step that can be taken is thus given by

$$\bar{t} = \min\{\bar{t}_i | \bar{t}_i > 0\} \quad \forall i \in 1, \ldots, r - m \tag{4.83}$$

The negative $\bar{t}_i$ values are ignored, because they relate to constraints that are violated if a step is taken in the direction opposite to the search direction. The step size $\bar{t}$ has to be compared with the unconstrained step size t. If $t \geqslant \bar{t}$, the step size has to be limited to $\bar{t}$; moreover, the i^{th} constraint, i.e. the constraint for which $\bar{t}_i = \bar{t}$, has to be added to the set of active constraints before a new iteration is started. However, if $t < \bar{t}$, the full search step can be taken without violating any of the constraints. In this case, a new iteration can be started with the same set of active constraints.

Removing a constraint — Determining whether a constraint remains active or becomes inactive can be done by checking the sign of the Lagrange multipliers λ_i. The optimal solution must comply with the KKT conditions (4.57–4.60), which implies that all the Lagrange multipliers must be non-negative. Constraints that are associated with negative Lagrange multipliers have to be removed from the active set, since they would prevent the compliance with the KKT conditions.

Alternatively, this requirement can be explained as follows. Inserting expression (4.46) into (4.75) provides $\{v\} = \{v_p\} - [N]^{-1}[N_a]\{\lambda\}$. The unconstrained search direction vector can thus be decomposed into a component that lies on the intersection of the active constraint hyperplanes, i.e. the projected search direction vector $\{v_p\}$, and a component that points away from this intersection, i.e. $-[N]^{-1}[N_a]\{\lambda\}$. The signs of the Lagrange multipliers λ_i thus determine whether the unconstrained search direction points to the infeasible or feasible domain, i.e. whether the corresponding constraint has to remain active or become inactive, respectively. Figure 4.20 provides an illustration.

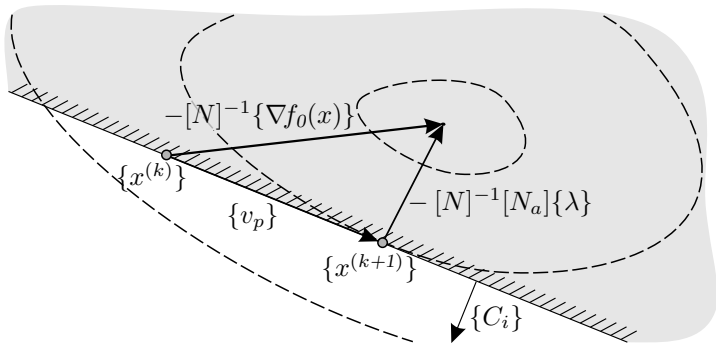

Figure 4.20: *The relation between the general and the projected search direction.*

Note that the solution provided by the projection algorithm also complies with the other requirement of the KKT conditions. Equation (4.76) shows that

$$\{\nabla f_0(x)\} + [N_a]\{\lambda\} = \{0\} \tag{4.84}$$

Since $[N_a]$ comprises the constraint gradients, (4.84) implies that the first KKT condition is met. For all the constraints of the active set $f_i(x) = 0$, the second KKT condition is thus also fulfilled. Since the projection approach prevents the violation of any constraint, compliance with the fourth KKT condition is automatically ensured, if the optimisation starts from a feasible point.

4.6. Solving the MNET Optimisation Problem

4.6.1. Introduction

Vibration-based identification techniques estimate elastic material properties by minimising the sum of the squared differences between a set of experimentally measured and numerically computed resonant frequencies. The choice of the optimisation algorithm should be based on the particular properties of this type of problem. The numerical resonant frequencies are calculated with finite element models. This has two important consequences. First, solving an FE-model is a computationally expensive step. Furthermore, chapter 3 showed that, once the finite element model is solved, the response gradients can be computed very efficiently. This implies that the preferred optimisation routine should limit the number of direct cost-function evaluations by exploiting the gradient information. In case of vibration-based material identification algorithms, direct search methods like simplex methods, genetic algorithms and neural networks are therefore inefficient in comparison to the derivative-based approach. This section presents some practical considerations of how to apply the techniques presented in the previous section in order to solve the MNET optimisation problem.

4.6.2. Sequential Quadratic Optimisation

In case of FE-based MNET procedures, the optimisation can be carried out in two different ways. The most obvious approach is illustrated by the left-hand side plot of figure 4.21. For this approach, the minimisation routine uses the following sequence of operations: solving the FE-model(s), performing a sensitivity analysis, building a quadratic approximation of the cost-function (4.85), computing the (projected) search direction, and taking a step in the descent direction. This approach thus requires an evaluation of the FE-model(s) for every step that is taken.

$$\big([S]\{x\} - \{\Delta f\}\big)^{\mathrm{T}}[W]\big([S]\{x\} - \{\Delta f\}\big) \tag{4.85}$$

The alternative approach is based on a more efficient use of the quadratic cost-function approximation. With the first approach, the cost-function approximation is only used to take a single step. However, this approximation is a simple analytical expression. The evaluation of the cost-function approximation is thus inexpensive. Instead of just taking a single step, it is more efficient

to minimise the approximation of the cost-function. This results in the process that is displayed by the right-hand plot of figure 4.21. The optimisation process is now split into two levels: main iterations and sub iterations. Although there is no reduction in the number of iteration steps, since the majority of the expensive main iterations has been replaced by cheap sub iterations, the alternative approach is much faster than the initial approach. Note that the alternative approach determines the minimum by minimising a sequence of quadratic cost-function approximations; therefore, this approach is called sequential quadratic optimisation[9] [68].

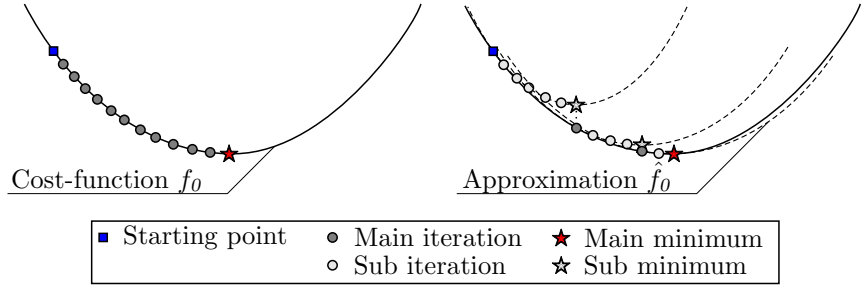

Figure 4.21: *The sequential quadratic optimisation approach.*

4.6.3. The MNET Cost-Function

Convexity

The cost-function of a vibration-based MNET is not convex[10]. However, this is not a such serious problem, since the MNET cost-function appears to be a function without local minima. During all the calculations that were performed in the framework of this thesis, not a single MNET cost-function with a local minimum was encountered. Although it is impossible to prove, the following theoretical reflection suggests that the MNET cost-function does not have any local minima.

Consider an MNET problem with a single material parameter and two experimental frequencies. Assume that the response surfaces are monotonic functions of the material parameters, e.g. the fundamental flexural frequency of an isotropic beam will always increase with an increase of the E-modulus, the fundamental torsional frequency will always decrease with an increase of Poisson's ratio. Under the assumption of monotonicity, the response curves have one of the four forms shown on figure 4.22. By squaring the difference between the response curve and the experimental response, one obtains the cost-functions presented on the second row of 4.22. The four types of response functions provide only two types of cost-functions. The cost-functions are clearly non-

[9] Note that sequential quadratic optimisation is not the same as sequential quadratic programming (SQP). The sequential quadratic programming method is an optimisation method, which focuses on the direct solution of the first-order optimality conditions and thus attempts to compute explicitly the Lagrange multipliers [92].

[10] This will be shown further on in this section.

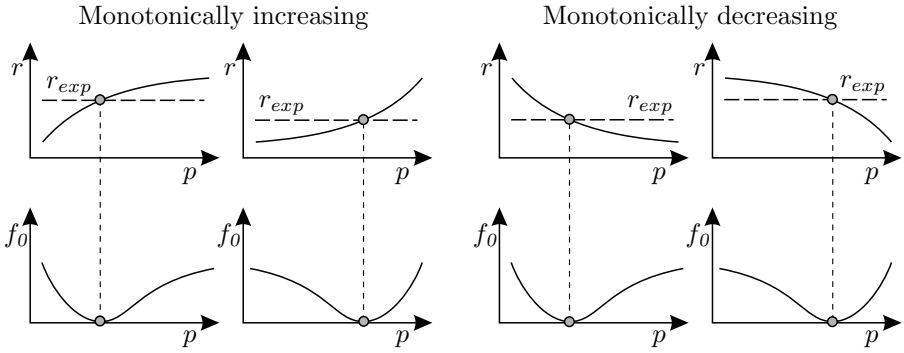

Figure 4.22: *The four types of response functions and the associated cost-functions.*

convex, however, they do not have any local minima. The total cost-function is the sum of the cost-functions of the individual responses. Figure 4.23 presents two different cases: the left-hand side plot presents the case with small residuals, the right-hand side plot presents the case with large residuals. The plots show that local minima appear only if the residuals are sufficiently large. The same result can be found by using a different combination of cost-function types, and by considering a higher number of parameters and responses.
To summarise, local minima only appear, if the residuals are large. This is not a severe problem, since large residuals are unacceptable anyway. Large residuals indicate that it is impossible to fit the experimental data with the considered theoretical model. This implies that there is either something wrong with the experimental data, or that the data is being fitted with a model that is unable to describe the observed phenomenon. In both cases, the results of the MNET cannot be trusted, irrespective of whether the cost-function has local minima. Note that the cost-function, and thus the presence of local minima, is independent of the starting values used to solve the identification problem.

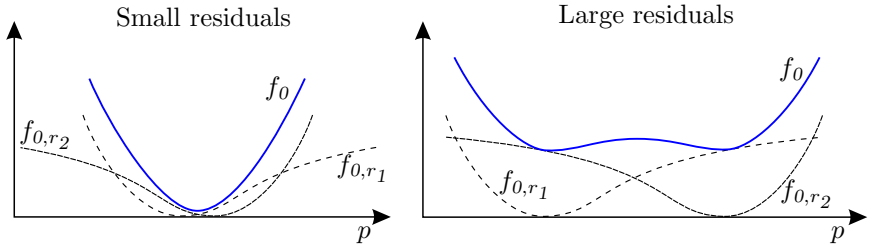

Figure 4.23: *The cost-function of the MNET's optimisation problem.*

Remember that this section does not provide a solid mathematical proof, it just presents a theoretical reflection on the MNET cost-function.

Quadratic Approximation

The combination of a well designed MNET with carefully executed experiments results in small residuals. In this situation, the cost-function does not have any local minima, implying that the minimum can be found with a convex

optimisation routine[11] despite the fact that the cost-function is non-convex. Newton's method is the most appropriate optimisation algorithm to solve the MNET's optimisation problem. A second-order descent method finds the minimum of a quadratic cost-function in a single step. However, this is only valid for non-constrained problems. Solving a constrained problem might require a higher number of iteration steps. Consider the optimisation problem of figure 4.24.

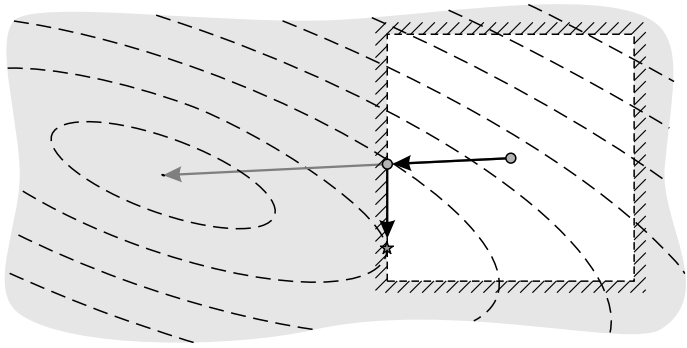

Figure 4.24: *An optimisation problem with a quadratic cost-function.*

The working point of the optimisation procedure moves in the optimal descent direction until it encounters one of the constraints. The search direction is then projected onto the constraint, and a new step is taken. Due to the fact that the step length is smaller than the distance to the nearest constraint and because the cost-function is quadratic, the optimal point is found. Since the cost-function is quadratic, the Newton direction is not an approximation of the optimal search direction; it points towards the absolute minimum. As a result, the working point always shifts towards the optimal point, and an active constraint can never become inactive. Therefore, the MNET optimisation routine does not require an algorithm to remove a constraint from the active set of constraints.

4.6.4. The Constraints

The MNET optimisation problem is a constrained optimisation problem. There are four types of constraints that can be taken into account: bounds on the material property corrections, bounds on the material properties, physical restrictions on the material properties, and relations between the material parameters.

Upper and Lower Bounds on the Material Property Corrections

With the MNET approach, the material properties are determined in an iterative way. The improved material parameters are based on a quadratic ap-

[11] This statement is valid because the MNET optimisation problem will not have any active constraints at the optimal point, see section 4.6.4.

proximation of the cost-function. Since this approximation is derived from the response surface gradients, it is only valid in the vicinity of the current working point. Estimating the necessary parameter corrections based on unreliable gradient information can result in a shift of the working point in the wrong direction. To avoid unstable behaviour of the identification routine, the parameter changes should be limited to a region in which the gradient provides an acceptable approximation of the cost-function, i.e. a trust region [93]. Since the gradient information is recomputed during each iteration step, the trust region moves together with the working point in the direction of the optimal solution. Consequently, the trust region bounds affect only the way the minimum is obtained, they do not affect the final solution. Figure 4.25 provides a graphical representation of the trust region approach. The overlay plot shows the trajectory of the working point from the initial parameter set to the optimal point.

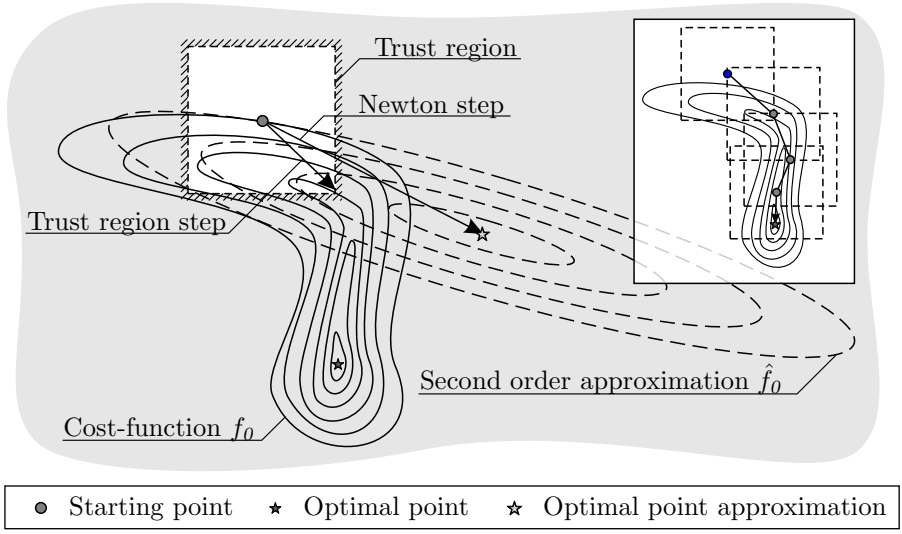

Figure 4.25: *Graphical representation of the trust region approach.*

If the parameter changes are limited by an upper and lower bound on the parameter changes, the trust region defines a hypercube in the parameter space. In this case, the trust region bounds can easily be implemented by means of the projection approach.

Upper and Lower Bounds on the Material Properties

Sometimes there is a priori information about the material parameters that have to be identified. This a priori information can be incorporated into the identification routine by using it to limit the extent of the search space. This can be very useful in the situation where the values of a few material parameters are approximately known. Take the example of a steel substrate covered with a coating of which the elastic properties are completely unknown. Assume

that the initial values of the coating properties are a severe overestimation of the real properties. At first, the identification routine will reduce the stiffness of both substrate and coating. Subsequently, the substrate properties will approximately return to their initial level, while the coating properties will further decrease to their correct physical values. During the first identification phase, the properties of the substrate can be reduced to a level that is physically impossible for steel. The number of necessary iteration steps can be reduced by putting a limit on the absolute values of the substrate properties and thus avoiding a severe undershoot during the initial phase of the identification. Since the bounds are simple box constraints, they can easily be implemented with the projection approach.
The bounds should be taken wide enough so that they are inactive at the point defined by the optimal solution, otherwise they will cause a distortion of the obtained results. Consequently, an optimal point with active bounds provides invalid material parameters. In this situation, the active bounds have to be widened and the MNET has to be solved again. Note that the material parameters obtained with the initial bounds provide a good set of starting values.

Ensuring the Physical Feasibility of the Material Properties

Chapter 2 introduced the physical limits elastic material parameters have to comply with. It is required to incorporate these limits into the optimisation routine, since a violation of these limits can result in a set of elastic parameters that causes the finite element solver to crash. Table 4.3 gives an overview of the physical limits of the parameters for both isotropic and orthotropic material behaviour.

Table 4.3: *The physical limits of the elastic material parameters.*

	Isotropic		Orthotropic	
E	$E > 0$	(4.86)	$E_1 > 0, E_2 > 0$	(4.88)
G	—		$G_{12} > 0$	(4.89)
ν	$-1 < \nu < \frac{1}{2}$	(4.87)	$\lvert\nu_{12}\rvert < \sqrt{\frac{E_1}{E_2}}$	(4.90)

Limits (4.86–4.89) are linear constraints, and can easily be implemented with the projection approach. The fifth limit, i.e. equation (4.90), is quite difficult to handle, since it is both a non-linear and a non-convex constraint. The non-linearity problem can be overcome by linearising the constraint around the starting point $\{x_0\} = \{0\}$. The McLauren series of this constraint provides

$$\hat{f}_{ph}(x) = -E_1\big(1 + x_{E_1}\big) + E_2\nu_{12}\big(1 + x_{E_2} + 2x_{\nu_{12}}\big) \tag{4.91}$$

where the x coefficients represent the parameter corrections during the considered iteration step. Note that by using the linearised constraint (4.91), the actual constraint (4.90) can be violated. After every iteration step, the so-

lution has be checked with respect to (4.90), and, if necessary, the working point has to be shifted back to the feasible domain. Figure 4.26 provides a one-dimensional illustration of this process.

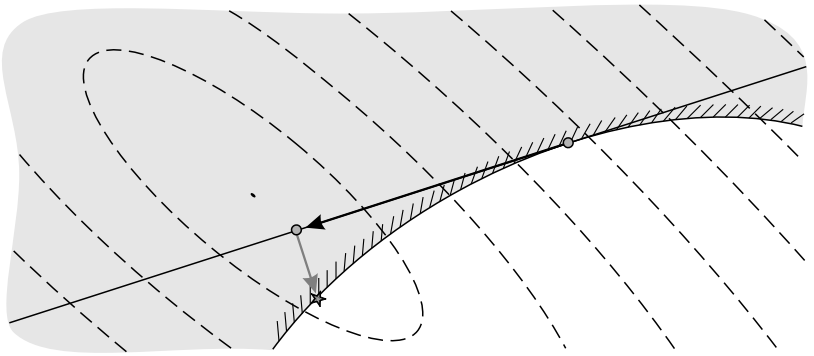

Figure 4.26: *Shifting the working point back to the feasible domain.*

The non-convexity of the fifth constraint is not a problem. This constraint represents a physical limit of the material properties, and should never be active at the point defined by the final solution. Therefore, it is impossible that the non-convexity distorts the results of the final solution.
Note that all the physical constraints have to be inactive at the point defined by the final solution. If one of these constraints was active, the identified material parameters would be thermodynamically infeasible in case the constraints (4.86–4.90) had not been incorporated into the optimisation routine. So, if one of these constraint was active at the final solution, then something went seriously wrong either during the experimental or during the identification phase.

Relations Between the Material Parameters

In some cases, a number of relations between the different material parameters may be taken into account. For example, consider a fibre-reinforced composite with different fibre volume fractions in two separate layers. The elastic properties of these two layers are related with the fibre volume fraction. If the fibre volume fractions of these two layers are known, the relation between them can be taken into account during the identification.
If the considered relation is linear, it can be enforced with the equality constraint technique of section 4.5.2. If the considered relation is non-linear, it can be linearised. Note that in case of linearised constraints, the working point has to be shifted back onto the original constraint after every iteration step.

Pre-Processing the Constraints

In case of vibration-based material identification routines, a well-conditioned sensitivity matrix can only be obtained by using relative normalised sensitivity coefficients as given by (3.62). This implies that the optimisation problem has to be solved in terms of relative parameters changes. Since the optimisation problem is solved in terms of relative parameter changes, all the constraints

have to be expressed in terms of relative parameter changes as well.
The optimisation parameters are related to the material parameters as

$$x = \frac{\Delta p}{p} \quad \text{or} \quad x^{(k)} = \frac{p^{(k+1)} - p^{(k)}}{p^{(k)}} \tag{4.92}$$

in which k specifies the iteration step. The previous sections introduced three sets of inequality constraints. The first set defines the maximum allowable parameter corrections during one iteration step. These constraints can easily be expressed in terms of parameter corrections as

$$x \geqslant \underline{x}_c \quad \text{and} \quad x \leqslant \overline{x}_c \tag{4.93}$$

The second set, i.e. the bounds on the absolute parameter values, cannot be handled as such by the optimisation routine; they first have to be converted into bounds on the parameter corrections as

$$x \geqslant \underline{x}_a \quad \text{and} \quad x \leqslant \overline{x}_a \tag{4.94}$$

In their initial form, these bounds are given by

$$p \geqslant \underline{p}_a \quad \text{and} \quad p \leqslant \overline{p}_a \tag{4.95}$$

The current parameter values are related to the improved parameters values as

$$p^{(k+1)} = p^{(k)}(1 + x) \tag{4.96}$$

By inserting (4.96) into (4.95), the latter can be rewritten as

$$x \geqslant \frac{\underline{p}_a}{p^{(k)}} - 1 \quad \text{and} \quad x \leqslant \frac{\overline{p}_a}{p^{(k)}} - 1 \tag{4.97}$$

In a similar way, the box constraints defined by the physical restrictions on the elastic material parameters can be expressed as

$$x \leqslant \overline{x}_{ph} \quad \text{and} \quad x \geqslant \underline{x}_{ph} \tag{4.98}$$

where

$$\underline{x}_{ph} = \frac{\underline{p}_{ph}}{p^{(k)}} - 1 \quad \text{and} \quad \overline{x}_{ph} = \frac{\overline{p}_{ph}}{p^{(k)}} - 1 \tag{4.99}$$

All these box constraints can be grouped into a single set of bounds

$$x \leqslant \overline{x} \quad \text{and} \quad x \geqslant \underline{x} \tag{4.100}$$

where

$$\overline{x} = \min(\overline{x}_c, \overline{x}_a, \overline{x}_{ph}) \tag{4.101}$$

$$\underline{x} = \max(\underline{x}_c, \underline{x}_a, \underline{x}_{ph}) \tag{4.102}$$

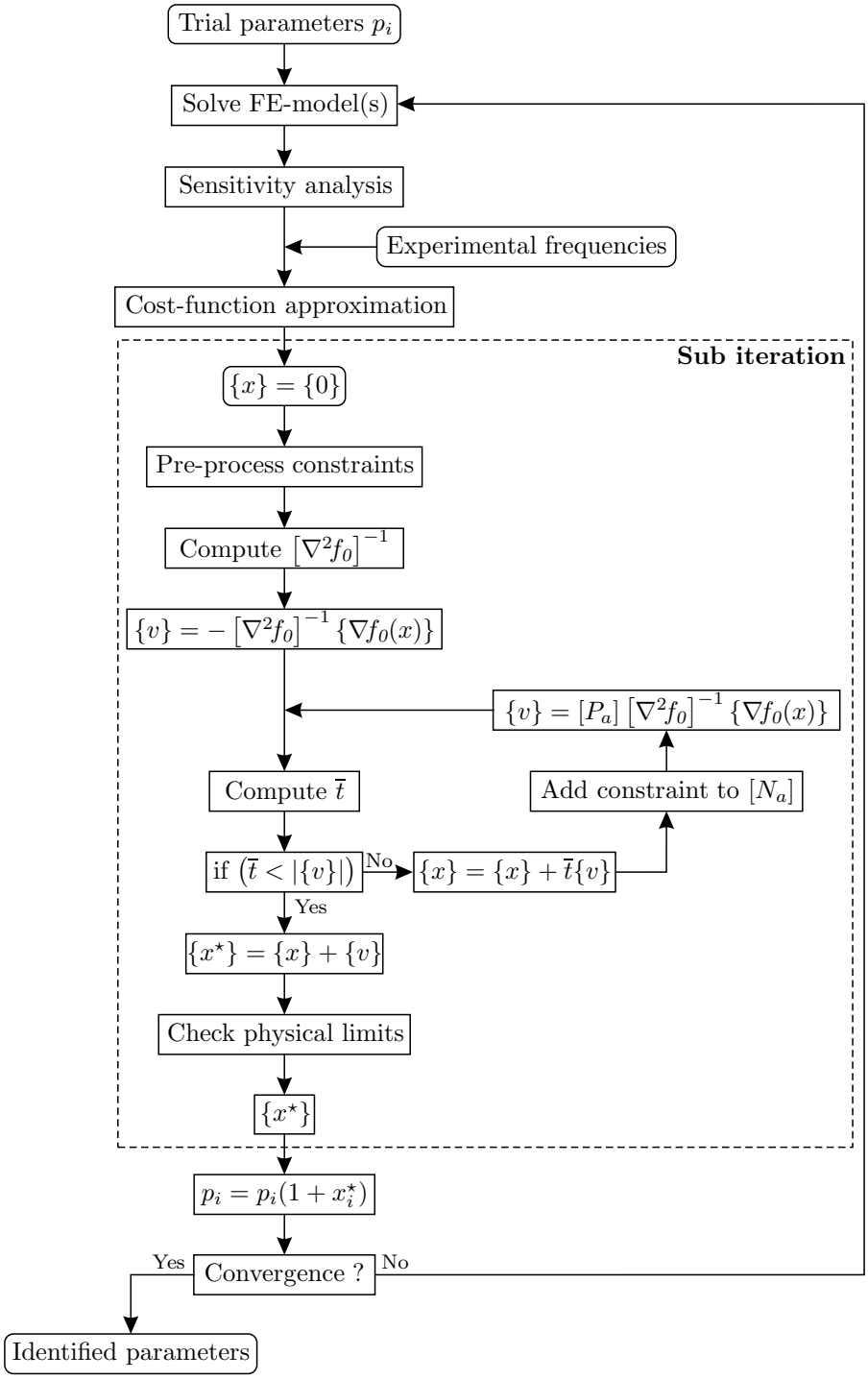

Figure 4.27: *Detailed flowchart of the MNET's optimisation routine.*

4.6.5. The MNET Optimisation Routine

The optimal approach to solve the MNET optimisation problem is a combination of the second-order projection method with the sequential quadratic approximation scheme. Figure 4.27 presents a detailed flowchart of the optimisation routine integrated in the framework of the MNET.
A set of trial values of the elastic parameters is used to compute the resonant frequencies of the test specimens. A cost-function approximation is build using the experimental frequencies and the frequency sensitivities with respect to the material parameters. This cost-function approximation (4.85) is minimised with the second-order projection method. Note that the iterations in the dashed box of figure 4.27 correspond with the sub iterations of figure 4.21. The sub iterations provide the minimum of the cost-function approximation. This minimum is used to compute a set of improved material parameters. The improved material parameters are inserted in the FE-models and provide a new cost-function approximation. The main iteration loop stops once the parameter corrections are smaller than a pre-defined threshold.

4.7. Summary

This chapter provided the theoretical foundation of optimisation theory. It presented a short review of the most popular zero-order techniques, and explained why these techniques are not optimal for the implementation of vibration-based MNETs. It also provided a condensed overview of higher-order descent methods to solve unconstrained and constrained convex optimisation problems. In the last section, these technique were used to develop a general framework to solve the optimisation problem of a vibration-based MNET.

5

Vibratory Behaviour of Layered Materials

Chapter five starts with the introduction of the classical lamination theory. This theory describes the mechanical behaviour of layered plates and can be used to study the fundamentals of the vibratory behaviour of layered materials. The goal of this chapter is to provide a theoretical background on the possibilities of vibration-based layered material identification, i.e. which material parameters can be identified and what experimental data does this require.

5.1. Classical Lamination Theory

5.1.1. Introduction

The classical lamination theory (CLT) or classical laminated plate theory is an extension of the standard Kirchhoff thin plate theory towards layered materials. It originates from the domain of composite materials and is presented in detail in [52, 53, 94]. The main goal of the classical lamination theory is to predict the mechanical properties of a layered material from the properties of its constituent layers, the stacking sequence and the layer orientation.
The classical lamination theory is based on a series of assumptions and hypotheses. First of all, it requires that the deformations are sufficiently small so that linear elastic material behaviour can be assumed. It also presumes that a line, originally straight and perpendicular to the middle surface of the plate, remains straight and perpendicular to the middle surface when the plate is stretched or bent. Requiring a normal to the middle surface to stay straight and normal under deformation is equivalent to ignoring the shear strains in the planes perpendicular to the middle surface. Using the notations of figure 5.1, this means that γ_{xz} and γ_{yz} are assumed to be zero. In addition, the thickness of the plate is also assumed to remain constant during loading, i.e. $\varepsilon_z = 0$. Together, these hypotheses are called the Kirchhoff assumptions and can be combined into the requirement that the plate is sufficiently thin.
Finally, the classical lamination theory presumes that the laminate consists of perfectly bonded laminae with infinitesimally thin bonds that are not shear-deformable. This means that none of the layers can slip relative to another so that the through-thickness displacement field is continuous over the layer interfaces.

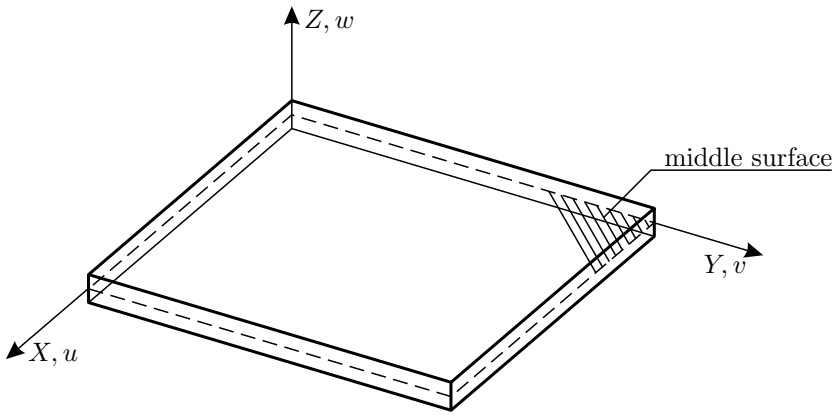

Figure 5.1: *Definition of the conventional CLT axis system.*

This section does not present a full overview of the classical lamination theory, it only presents the part that is needed to understand the vibratory behaviour of layered materials. The summary presented in this thesis is entirely based on the text of [52].

5.1.2. The Strain Field under the Kirchhoff Assumptions

The implications of the Kirchhoff assumptions for the displacement components u, v, and w, can be derived by considering the cross-section in the xz-plane shown in figure 5.2. According to the Kirchhoff assumptions, the line ABD must remain straight under deformation of the laminate. The displacement in the x-direction of an arbitrary point C, situated on the same normal as B, can thus be written as

$$u_C = u^0 + u'_C \tag{5.1}$$

where u^0 and u'_C are defined as indicated on figure 5.2. The assumption of small deformations implies that

$$\sin\beta \approx \beta \approx \tan\beta = \frac{\partial w^0}{\partial x} \tag{5.2}$$

Since u'_C, z_C, and $\mathrm{d}x > 0$ and $\mathrm{d}w_0 < 0$, one can state that

$$u'_C = -\frac{\partial w^0}{\partial x} z_C \tag{5.3}$$

The displacement in the x-direction of an arbitrary point of the plate can thus be expressed as

$$u = u^0 - \frac{\partial w^0}{\partial x} z \tag{5.4}$$

where u^0 is the displacement in the x-direction of the middle surface at the position of the considered point.

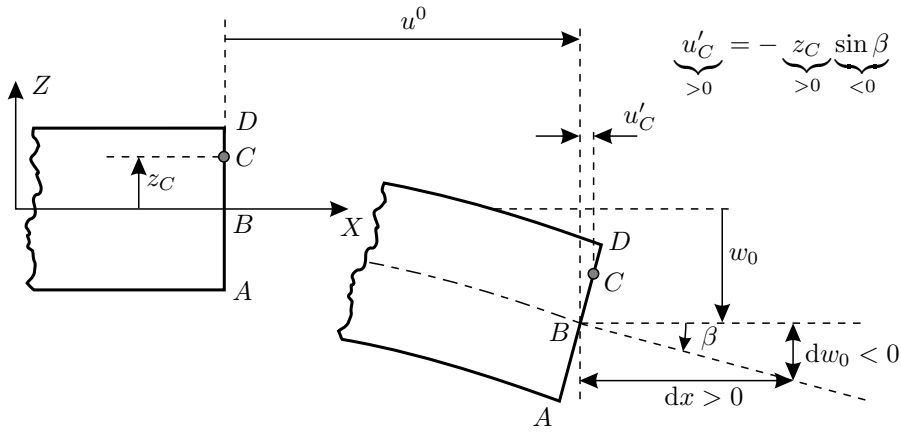

Figure 5.2: *Representation of the deformations in the xz-plane.*

An expression for the displacement in the y-direction can be found in a similar way.

$$v = v^0 - \frac{\partial w^0}{\partial y} z \tag{5.5}$$

where v^0 is the displacement in the y-direction of the middle surface at the

position of the considered point.
By accepting the Kirchhoff assumptions, the following three strain components are zero: $\gamma_{xz} = \gamma_{yz} = \varepsilon_z = 0$. Under the assumption of small deformations, the remaining three strain components can be expressed in function of the displacements as

$$\varepsilon_x = \frac{\partial u}{\partial x}, \qquad \varepsilon_y = \frac{\partial v}{\partial y}, \qquad \gamma_{xy} = \frac{\partial u}{\partial y} + \frac{\partial v}{\partial x} \tag{5.6}$$

By substituting equations (5.4) and (5.5) into (5.6) the following expressions for the strain components are obtained.

$$\begin{aligned} \varepsilon_x &= \varepsilon_x^0 + \kappa_x^0 z \\ \varepsilon_y &= \varepsilon_y^0 + \kappa_y^0 z \\ \gamma_{xy} &= \gamma_{xy}^0 + \kappa_{xy}^0 z \end{aligned} \tag{5.7}$$

in which ε_x^0, ε_y^0 and γ_{xy}^0 are the middle surface strains which are defined as

$$\varepsilon_x^0 = \frac{\partial u^0}{\partial x}, \qquad \varepsilon_y^0 = \frac{\partial v^0}{\partial y}, \qquad \gamma_{xy}^0 = \frac{\partial u^0}{\partial y} + \frac{\partial v^0}{\partial x} \tag{5.8}$$

and κ_x^0, κ_y^0 and κ_{xy}^0 are the middle surface curvatures which are defined as

$$\kappa_x^0 = -\frac{\partial^2 w^0}{\partial x^2}, \qquad \kappa_y^0 = -\frac{\partial^2 w^0}{\partial y^2}, \qquad \kappa_{xy}^0 = -2\frac{\partial^2 w^0}{\partial x \partial y} \tag{5.9}$$

The three expressions of (5.7) can be contracted into a vector formulation as

$$\{\varepsilon\} = \left\{\varepsilon^0\right\} + \left\{\kappa^0\right\} z \tag{5.10}$$

where $\{\varepsilon\}$ is the strain vector on a particular z-level, $\{\varepsilon^0\}$ is the strain vector at the middle surface and $\{\kappa^0\}$ is the curvature vector. The relation of (5.10) expresses the deformation in an arbitrary plane parallel to the middle surface as a function of the distance to the middle plane, the displacement of the middle plane and the curvature at the location of the considered point. Note that the assumptions of the classical lamination theory result in a continuous in-plane displacement field that varies linearly through the thickness of the plate.

5.1.3. The Stress-strain Relation in a Layered Material

Consider a layered plate that consists of n_l homogeneous and elastically orthotropic layers. If the Kirchhoff assumptions are respected, the stress-strain relation in the k^{th} layer of the considered plate is given by

$$\begin{Bmatrix} \sigma_x \\ \sigma_y \\ \tau_{xy} \end{Bmatrix}_k = \begin{bmatrix} \overline{Q}_{11} & \overline{Q}_{12} & \overline{Q}_{16} \\ \overline{Q}_{12} & \overline{Q}_{22} & \overline{Q}_{26} \\ \overline{Q}_{16} & \overline{Q}_{26} & \overline{Q}_{66} \end{bmatrix}_k \begin{Bmatrix} \varepsilon_x \\ \varepsilon_y \\ \gamma_{xy} \end{Bmatrix}_k \tag{5.11}$$

in which the $\overline{Q}_{ij}$ coefficients are the reduced stiffnesses expressed in the local axis system. Under the assumptions posed by the classical lamination theory,

the strain field shows a linear variation in the through-thickness direction as expressed by (5.10). The combination of (5.10) and (5.11) results in equation (5.12), which relates the stress field in each layer to the deformation of the central plane.

$$\begin{Bmatrix} \sigma_x \\ \sigma_y \\ \tau_{xy} \end{Bmatrix}_k = \begin{bmatrix} \overline{Q}_{11} \overline{Q}_{12} \overline{Q}_{16} \\ \overline{Q}_{12} \overline{Q}_{22} \overline{Q}_{26} \\ \overline{Q}_{16} \overline{Q}_{26} \overline{Q}_{66} \end{bmatrix}_k \left\{ \begin{Bmatrix} \varepsilon_x^0 \\ \varepsilon_y^0 \\ \gamma_{xy}^0 \end{Bmatrix} + \begin{Bmatrix} \kappa_x^0 \\ \kappa_y^0 \\ \kappa_{xy}^0 \end{Bmatrix} z \right\} \tag{5.12}$$

Because two successive layers can have different elastic properties, equation (5.12) implies that the linear strain field can be transformed into a discontinuous stress field, where the discontinuities are situated at the layer interfaces. Since the individual layers are considered to be homogeneous, the stress field in a single layer of the layered plate has to be continuous and linear.

5.1.4. Extensional, Coupling and Bending Stiffnesses

Consider a layered material with the structure of the plate of figure 5.3.

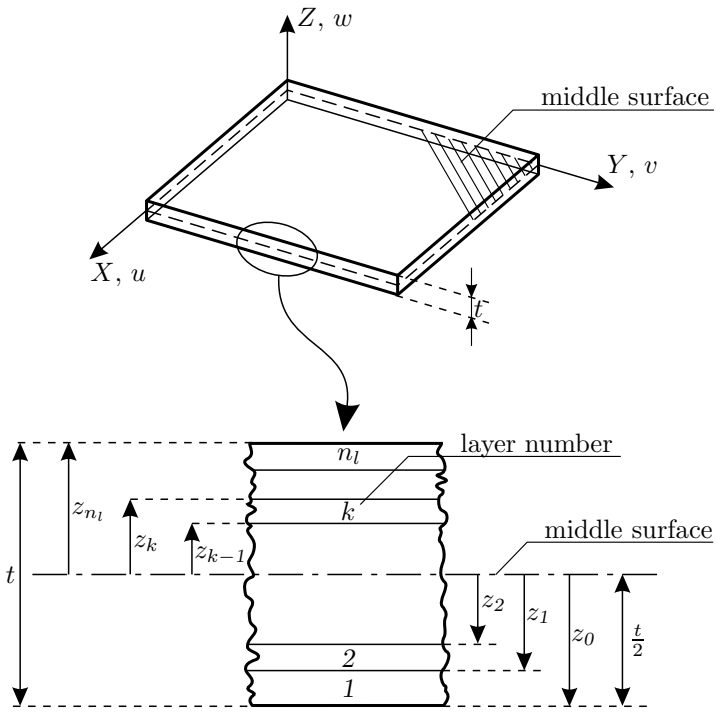

Figure 5.3: *The geometry of the considered layered material.*

The resultant forces and moments acting on a cross-section of this material are obtained by integrating the stresses in each layer through the thickness of the plate. Figure 5.4 presents this principle for the calculation of the normal force N_x and the bending moment M_x.

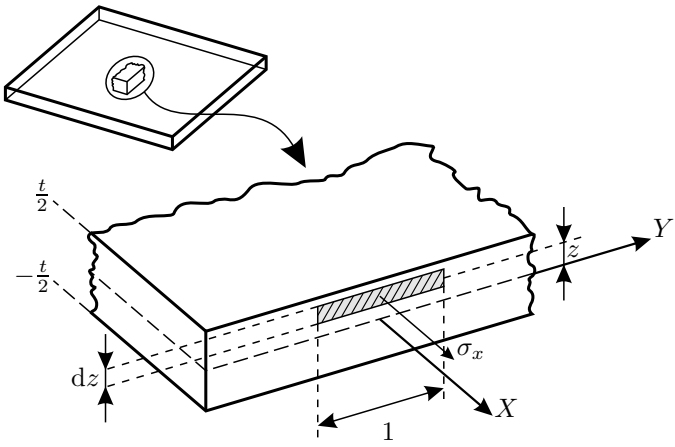

Figure 5.4: *Determination of the resultant normal force N_x and the bending moment M_x.*

Eventually, the following section forces and moments are obtained.

$$N_x = \int_{-t/2}^{t/2} \sigma_x \,\mathrm{d}z, \qquad M_x = \int_{-t/2}^{t/2} \sigma_x z \,\mathrm{d}z \tag{5.13}$$

$$N_y = \int_{-t/2}^{t/2} \sigma_y \,\mathrm{d}z, \qquad M_y = \int_{-t/2}^{t/2} \sigma_y z \,\mathrm{d}z \tag{5.14}$$

$$N_{xy} = \int_{-t/2}^{t/2} \tau_{xy} \,\mathrm{d}z \qquad M_{xy} = \int_{-t/2}^{t/2} \tau_{xy} z \,\mathrm{d}z \tag{5.15}$$

N_x and N_y are the in-plane normal forces, M_x and M_y are the bending moments, and N_{xy} and M_{xy} are the in-plane shear force and twisting moment, respectively. Note that all the section forces and moments are expressed per unit of length. By splitting the integrals over the total thickness into a sum of integrals over the layer thicknesses, the resulting forces and moments can be expressed as

$$\begin{Bmatrix} N_x \\ N_y \\ N_{xy} \end{Bmatrix} = \int_{-t/2}^{t/2} \begin{Bmatrix} \sigma_x \\ \sigma_y \\ \tau_{xy} \end{Bmatrix} \mathrm{d}z = \sum_{k=1}^{n_l} \int_{z_{k-1}}^{z_k} \begin{Bmatrix} \sigma_x \\ \sigma_y \\ \tau_{xy} \end{Bmatrix}_k \mathrm{d}z \tag{5.16}$$

$$\begin{Bmatrix} M_x \\ M_y \\ M_{xy} \end{Bmatrix} = \int_{-t/2}^{t/2} \begin{Bmatrix} \sigma_x \\ \sigma_y \\ \tau_{xy} \end{Bmatrix} z \,\mathrm{d}z = \sum_{k=1}^{n_l} \int_{z_{k-1}}^{z_k} \begin{Bmatrix} \sigma_x \\ \sigma_y \\ \tau_{xy} \end{Bmatrix}_k z \,\mathrm{d}z \tag{5.17}$$

Inserting the stress-strain relations of (5.12) into the equations of (5.16) and (5.17) provides

$$\begin{Bmatrix} N_x \\ N_y \\ N_{xy} \end{Bmatrix} = \sum_{k=1}^{n_l} \begin{bmatrix} \overline{Q}_{11} \overline{Q}_{12} \overline{Q}_{16} \\ \overline{Q}_{12} \overline{Q}_{22} \overline{Q}_{26} \\ \overline{Q}_{16} \overline{Q}_{26} \overline{Q}_{66} \end{bmatrix}_k \left\{ \int_{z_{k-1}}^{z_k} \begin{Bmatrix} \varepsilon_x^0 \\ \varepsilon_y^0 \\ \gamma_{xy}^0 \end{Bmatrix} \mathrm{d}z + \int_{z_{k-1}}^{z_k} \begin{Bmatrix} \kappa_x^0 \\ \kappa_y^0 \\ \kappa_{xy}^0 \end{Bmatrix} z \mathrm{d}z \right\} \tag{5.18}$$

$$\begin{Bmatrix} M_x \\ M_y \\ M_{xy} \end{Bmatrix} = \sum_{k=1}^{n_l} \begin{bmatrix} \overline{Q}_{11} \overline{Q}_{12} \overline{Q}_{16} \\ \overline{Q}_{12} \overline{Q}_{22} \overline{Q}_{26} \\ \overline{Q}_{16} \overline{Q}_{26} \overline{Q}_{66} \end{bmatrix}_k \left\{ \int_{z_{k-1}}^{z_k} \begin{Bmatrix} \varepsilon_x^0 \\ \varepsilon_y^0 \\ \gamma_{xy}^0 \end{Bmatrix} z \mathrm{d}z + \int_{z_{k-1}}^{z_k} \begin{Bmatrix} \kappa_x^0 \\ \kappa_y^0 \\ \kappa_{xy}^0 \end{Bmatrix} z^2 \mathrm{d}z \right\} \tag{5.19}$$

The middle plane strains and curvatures do not depend on z, and can, therefore, be removed from under the summation signs. In this way, equations (5.18) and (5.19) can be reformulated as

$$\begin{Bmatrix} N_x \\ N_y \\ N_{xy} \end{Bmatrix} = \begin{bmatrix} A_{11} A_{12} A_{16} \\ A_{12} A_{22} A_{26} \\ A_{16} A_{26} A_{66} \end{bmatrix} \begin{Bmatrix} \varepsilon_x^0 \\ \varepsilon_y^0 \\ \gamma_{xy}^0 \end{Bmatrix} + \begin{bmatrix} B_{11} B_{12} B_{16} \\ B_{12} B_{22} B_{26} \\ B_{16} B_{26} B_{66} \end{bmatrix} \begin{Bmatrix} \kappa_x^0 \\ \kappa_y^0 \\ \kappa_{xy}^0 \end{Bmatrix} \tag{5.20}$$

$$\begin{Bmatrix} M_x \\ M_y \\ M_{xy} \end{Bmatrix} = \begin{bmatrix} B_{11} B_{12} B_{16} \\ B_{12} B_{22} B_{26} \\ B_{16} B_{26} B_{66} \end{bmatrix} \begin{Bmatrix} \varepsilon_x^0 \\ \varepsilon_y^0 \\ \gamma_{xy}^0 \end{Bmatrix} + \begin{bmatrix} D_{11} D_{12} D_{16} \\ D_{12} D_{22} D_{26} \\ D_{16} D_{26} D_{66} \end{bmatrix} \begin{Bmatrix} \kappa_x^0 \\ \kappa_y^0 \\ \kappa_{xy}^0 \end{Bmatrix} \tag{5.21}$$

where

$$A_{ij} = \sum_{k=1}^{n_l} \left(\overline{Q}_{ij}\right)_k (z_k - z_{k-1}) \tag{5.22}$$

$$B_{ij} = \frac{1}{2} \sum_{k=1}^{n_l} \left(\overline{Q}_{ij}\right)_k (z_k^2 - z_{k-1}^2) \tag{5.23}$$

$$D_{ij} = \frac{1}{3} \sum_{k=1}^{n_l} \left(\overline{Q}_{ij}\right)_k (z_k^3 - z_{k-1}^3) \tag{5.24}$$

$$\tag{5.25}$$

The A_{ij}, B_{ij} and D_{ij} coefficients are the integrated stiffness coefficients and represent the stiffness of the layered material. The A_{ij} coefficients, which are called the extensional stiffnesses, relate the strain of the central plane to the in-plane forces. The D_{ij} coefficients relate the curvature of the central plane to the resulting moments; these coefficients are called the bending stiffnesses. The B_{ij} coefficients describe a coupling between bending and extension of a layered material; consequently, these coefficients are called the coupling stiffnesses. If the layer structure of the material is not symmetrical, the coupling stiffnesses will be non-zero. In this case, the extension of the central plane will result in a bending and/or torsion moment, while its curving or twisting will induce in-plane forces.

5.2. Vibratory Behaviour of a Layered Material

5.2.1. Equations of Motion

Consider a differential rectangular element $\mathrm{d}x\,\mathrm{d}y$ of a thin layered plate as in figure 5.5. The equations of motion of a vibrating laminated plate can be obtained from the translational and rotational equilibria of the forces and moments acting on this differential element [94].

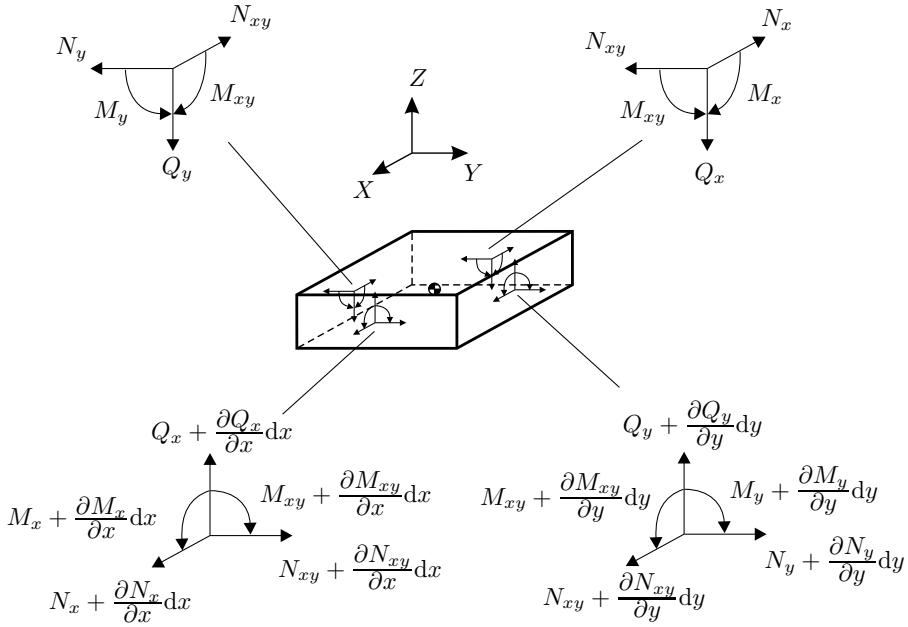

Figure 5.5: *The section forces and moments acting on a differential element.*

In figure 5.5, Q_x and Q_y are the transverse shear forces. The translational equilibrium in the x-direction yields

$$\begin{aligned}\rho\,\mathrm{d}x\,\mathrm{d}y\,h\frac{\partial^2 u_0}{\partial t^2} =& -N_x\mathrm{d}y + \left(N_x + \frac{\partial N_x}{\partial x}\mathrm{d}x\right)\mathrm{d}y - N_{xy}\mathrm{d}x \\ &+ \left(N_{xy} + \frac{\partial N_{xy}}{\partial y}\mathrm{d}y\right)\mathrm{d}x\end{aligned} \tag{5.26}$$

and can be simplified to

$$\rho h\frac{\partial^2 u_0}{\partial t^2} = \frac{\partial N_x}{\partial x} + \frac{\partial N_{xy}}{\partial y} \tag{5.27}$$

Note that in equations (5.26) and (5.27) the symbol t represents the time variable. To avoid confusion, the plate thickness will temporarily be denoted as h. The equilibrium equations in the y-direction (5.28) and z-direction (5.29) can be obtained in a similar way.

$$\rho h \frac{\partial^2 v_0}{\partial t^2} = \frac{\partial N_y}{\partial y} + \frac{\partial N_{xy}}{\partial x} \tag{5.28}$$

$$\rho h \frac{\partial^2 w_0}{\partial t^2} = \frac{\partial Q_x}{\partial x} + \frac{\partial Q_y}{\partial y} \tag{5.29}$$

The rotational equilibrium about the x- and y-axis provides two additional equilibrium equations.

$$\frac{\partial M_y}{\partial y} + \frac{\partial M_{xy}}{\partial x} - Q_y = 0 \tag{5.30}$$

$$\frac{\partial M_x}{\partial x} + \frac{\partial M_{xy}}{\partial y} - Q_x = 0 \tag{5.31}$$

By inserting the rotational equilibrium equations into the translational equilibrium equation in the z-direction, expressions (5.30), (5.31) and (5.29) can be combined into (5.32).

$$\rho h \frac{\partial^2 w_0}{\partial t^2} = \frac{\partial^2 M_x}{\partial x^2} + 2\frac{\partial^2 M_{xy}}{\partial x \partial y} + \frac{\partial^2 M_y}{\partial y^2} \tag{5.32}$$

Inserting the relations of (5.20) and (5.21) into equations (5.28), (5.29) and (5.32) yields a set of three partial differential equations (5.33–5.35) that describe the vibratory behaviour of a layered plate.

$$\begin{aligned}\rho h \frac{\partial^2 u_0}{\partial t^2} = {} & A_{11}\frac{\partial^2 u_0}{\partial x^2} + 2A_{16}\frac{\partial^2 u_0}{\partial x \partial y} + A_{66}\frac{\partial^2 u_0}{\partial y^2} + A_{26}\frac{\partial^2 v_0}{\partial y^2} \\ & + (A_{12} + A_{66})\frac{\partial^2 v_0}{\partial x \partial y} - B_{11}\frac{\partial^3 w_0}{\partial x^3} - 3B_{16}\frac{\partial^3 w_0}{\partial x^2 \partial y} \\ & - (B_{12} + 2B_{66})\frac{\partial^3 w_0}{\partial x \partial y^2} - B_{26}\frac{\partial^3 w_0}{\partial y^3}\end{aligned} \tag{5.33}$$

$$\begin{aligned}\rho h \frac{\partial^2 v_0}{\partial t^2} = {} & A_{16}\frac{\partial^2 u_0}{\partial x^2} + (A_{12} + A_{66})\frac{\partial^2 u_0}{\partial x \partial y} + A_{26}\frac{\partial^2 u_0}{\partial y^2} + A_{66}\frac{\partial^2 v_0}{\partial x^2} \\ & + 2A_{26}\frac{\partial^2 v_0}{\partial x \partial y} + A_{22}\frac{\partial^2 v_0}{\partial y^2} - B_{16}\frac{\partial^3 w_0}{\partial x^3} \\ & - (B_{12} + 2B_{66})\frac{\partial^3 w_0}{\partial x^2 \partial y} - 3B_{26}\frac{\partial^3 w_0}{\partial x \partial y^2} - B_{22}\frac{\partial^3 w_0}{\partial y^3}\end{aligned} \tag{5.34}$$

$$\begin{aligned}\rho h \frac{\partial^2 w_0}{\partial t^2} = {} & D_{11}\frac{\partial^4 w_0}{\partial x^4} + 4D_{16}\frac{\partial^4 w_0}{\partial x^3 \partial y} + 2(D_{12} + 2D_{66})\frac{\partial^4 w_0}{\partial x^2 \partial y^2} \\ & + 4D_{26}\frac{\partial^4 w_0}{\partial x \partial y^3} + D_{22}\frac{\partial^4 w_0}{\partial y^4} - B_{11}\frac{\partial^3 u_0}{\partial x^3} - 3B_{16}\frac{\partial^3 u_0}{\partial x^2 \partial y} \\ & - (B_{12} + 2B_{66})\frac{\partial^3 u_0}{\partial x \partial y^2} - B_{26}\frac{\partial^3 u_0}{\partial y^3} - B_{16}\frac{\partial^3 v_0}{\partial x^3} \\ & - (B_{12} + 2B_{66})\frac{\partial^3 v_0}{\partial x^2 \partial y} - 3B_{26}\frac{\partial^3 v_0}{\partial x \partial y^2} - B_{22}\frac{\partial^3 v_0}{\partial y^3}\end{aligned} \tag{5.35}$$

Note that the effects of rotatory inertia and material damping were ignored during the derivation of the equations of motion.

5.2.2. Discussion

Solving the set of partial differential equations of (5.33–5.35) in combination with the appropriate boundary condition equations, yields the resonant frequencies and mode shapes of the considered layered plate. The boundary condition equations are functions of N_x, N_y, N_{xy}, M_x, M_y and M_{xy} and can, therefore, only depend on the plate's material properties through the A_{ij}, B_{ij} and D_{ij} stiffness coefficients. This shows that the modal parameters of a layered plate are not a function of the material properties of the individual layers, but that the dynamic behaviour is entirely controlled by the overall stiffnesses defined by the A_{ij}, B_{ij} and D_{ij} stiffness coefficients. Two plates with the same dimensions and weight but with a completely different layer configuration, will respond dynamically in an identical manner, if they have the same A_{ij}, B_{ij} and D_{ij} coefficients.

From an identification point of view, this observation implies that only the values of the A_{ij}, B_{ij} and D_{ij} coefficients can be obtained from the measured vibration data of a layered plate. Since the $[A]$, $[B]$ and $[D]$ matrices are symmetric, there are 18 identifiable coefficients. In case of elastically orthotropic layers, the six reduced stiffness coefficients $\overline{Q}_{ij}$ depend on the values of the principal stiffness parameters Q_{11}, Q_{12}, Q_{22} and Q_{66}. This implies that only four of the six A_{ij} coefficients are independent. The same reasoning can be made for the B_{ij} and D_{ij} coefficients. The modal data is thus entirely controlled by 12 independent coefficients, therefore there are only 12 independent equations linking the material properties of the layers to the (measured) modal quantities. Because the layers of the plate are considered to have orthotropic material properties, these 12 equations can only yield the material properties of three layers.

However, this maximum of three layers is a theoretical limit. In the case of real experiments, the number of identifiable layers will be lower, since normally only resonant frequencies of transverse modes are measured. These transverse modes are virtually insensitive to changes of the extensional stiffnesses A_{ij} and the coupling stiffness coefficients B_{ij}. So, in most practical cases, only the values of the bending stiffnesses D_{ij} can be identified with sufficient accuracy, reducing the number of identifiable parameters to 4. Apparently, the properties of only a single orthotropic layer can be identified.

5.2.3. Numerical Example

The goal of this example is to illustrate the main conclusion of the CLT, i.e. the insensitivity of the plate's resonant frequencies to the elastic properties of the individual layers.

Consider a coated steel plate, 150×150 mm, with the layer configuration of figure 5.6. Table 5.1 presents the material properties of the three constituent layers. According to the lamination theory, the frequencies should be entirely controlled by the overall plate stiffness. This can be verified by randomly chang-

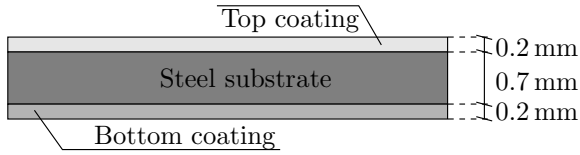

Figure 5.6: *The layer configuration of the coated steel plate.*

Table 5.1: *The material properties of the three layers.*

	E_1 [GPa]	E_2 [GPa]	G_{12} [GPa]	ν_{12} [–]	ρ [kg/m^3]
Top coating	73.00	70.00	25.00	0.340	2700
Steel substrate	201.00	200.00	78.00	0.290	7900
Bottom coating	68.00	71.00	24.00	0.320	2700

ing the properties of the third layer while optimising the properties of the first two layers in such a way that the overall plate stiffness remains constant. However, in this particular case, there are 12 equations, i.e. the 12 plate stiffnesses, and only 8 unknowns, i.e. the elastic properties of the first two layers. Therefore, it is not possible to find a new set of layer properties that result in exactly the same plate stiffness. Since the transverse vibrations are mainly controlled by the values of the bending stiffnesses, the optimisation focuses on matching the D_{ij} coefficients. The solution presented in table 5.2 is obtained by solving a weighted least-squares problem, in which the residuals of the bending stiffness coefficients D_{ij} are weighted with a factor 1000 while the A_{ij} and B_{ij} stiffness coefficients are weighted with a factor 1. Figure 5.7 presents the differences between the elastic properties of the initial and the equivalent plate.

Table 5.2: *The layer properties of the equivalent plate.*

	E_1 [GPa]	E_2 [GPa]	G_{12} [GPa]	ν_{12} [–]	Status
Top coating	85.04	58.93	33.00	0.320	Optimised
Steel substrate	166.55	227.70	54.96	0.310	Optimised
Bottom coating	80.00	60.00	32.00	0.300	Fixed

Table 5.3 compares the resonant frequencies of the first fifteen vibration modes of the initial and equivalent plate. The observed frequency differences are insignificant for identification problems, since they are smaller than the uncertainty on the experimental frequencies. The observed differences are caused by the influence of aspects that were ignored in the classical lamination theory – the most important source – and by the residual differences between the stiffness coefficients of the initial and equivalent plate, which are presented in figure 5.8. Note that the good frequency match of table 5.3 was obtained with substantial differences between the extensional stiffness coefficients, i.e. $\pm$ 15 %.

Table 5.3: *The frequencies of the initial (f_{in}) and equivalent (f_{eq}) plate.*

f_{in} [Hz]	f_{eq} [Hz]	Diff. [%]
129.306	129.285	−0.02
191.908	191.902	0.00
239.766	239.753	−0.01
337.398	337.334	−0.02
337.549	337.485	−0.02
605.269	605.200	−0.01
605.975	605.897	−0.01
617.166	616.980	−0.03
677.494	677.345	−0.02
760.831	760.662	−0.02
1028.171	1027.770	−0.04
1028.500	1028.095	−0.04
1171.034	1170.832	−0.02
1228.201	1227.997	−0.02
1308.205	1307.907	−0.02

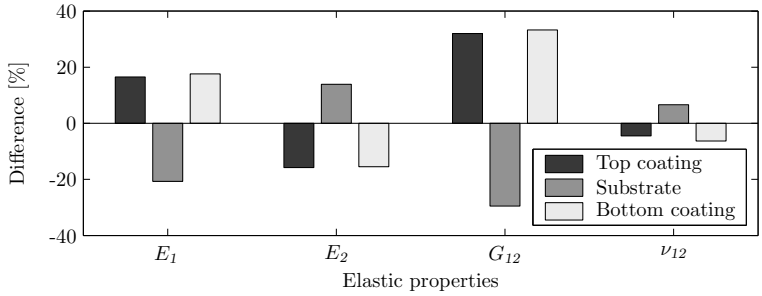

Figure 5.7: *The differences between the elastic properties of the initial and equivalent plate.*

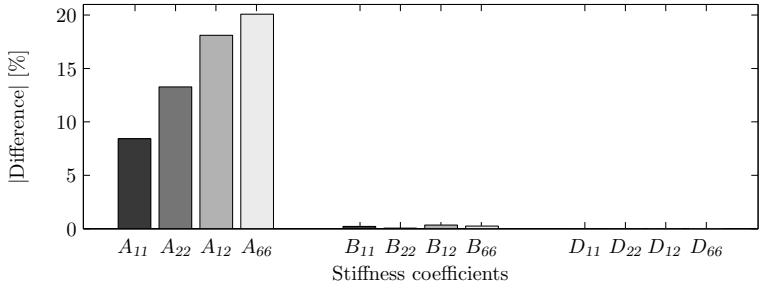

Figure 5.8: *The differences between the stiffness coefficients of the initial and equivalent plate.*

This confirms the assumption that the extensional stiffness coefficients do not have a significant influence on the out-of-plane vibratory behaviour.

The influence of the through-thickness mass distribution is investigated by comparing the frequencies of a plate with the mass densities of table 5.1 with those of a plate with an homogeneous mass density distribution, i.e. all three layers have the same average mass density of $6009.06\,\mathrm{kg/m^3}$. The frequency differences of the first fifteen modes are about $0.007\,\%$, which confirms that the vibratory behaviour is controlled by the overall mass properties and not by the mass densities of the individual layers. This is a quite convenient property for the identification procedures, since it implies that the mass densities of the layer materials do not have to be known; it suffices to know the overall mass density of the layered material.

This numerical example confirms the conclusion of the classical lamination theory that the vibratory behaviour of layered materials is not controlled by the properties of the individual layers but by the overall properties of the material. The example also shows that it is possible to find multiple sets of layer properties resulting in the same resonant frequencies. This implies that the inverse problem, i.e. estimating the layer properties from the resonant frequencies, cannot have a unique solution. In fact, the identification problem will have an infinite number of solutions, of which one represents the correct layer properties.

5.3. Identifying the Layer Properties

The lack of sensitivity of the resonant frequencies with respect to the layer properties does not mean that the layer properties cannot be identified. It just implies that the layer properties cannot be identified from the resonant frequencies of a single test specimen. A well-chosen set of test specimens can provide enough information to identify the correct elastic properties of the constituent layers.

The resonant frequencies of the out-of-plane vibration modes of a single test specimen provide the necessary information for the identification of the bending stiffness coefficients D_{ij}. The key point is to find a way to decompose the integrated stiffness coefficients into the layer properties. This can be done with a number of different sets of stiffness coefficients, which all depend on the layer properties in a different way, since in this situation there is only one set of layer properties that can reproduce all the stiffness coefficients.

The bending stiffness coefficients depend on the layer properties through the term $\left(z_k^3 - z_{k-1}^3\right)$, as described in equation (5.24). The relation between the stiffness coefficients and the layer properties can thus only be altered by changing the layer stacking sequence or by changing the thickness of one or more layers. Changing the size or shape of the test specimen will not have any effect on the bending stiffnesses, and will thus not solve the uniqueness problem. This implies that layered material identification requires a number of purpose-built samples with a different layer configuration.

The only question that remains is the number of sample configurations required to guarantee the uniqueness of the obtained solution. Consider a layered plate

with elastically orthotropic layers. In this case, the elastic behaviour of every layer is characterised by four material parameters. The total number of parameters that must be identified equals $4\times n_m$, considering the notations of table 5.4. The resonant frequencies of every sample configuration provide four plate stiffness coefficients[1]. Consequently, the total number of equations thus equals $4\times n_c$. A set of equations results in a unique solution if the number of equations is greater than or equal to the number of unknowns. Consequently, a unique solution is obtained, if $n_c \geqslant n_m$.
Despite the fact that isotropic material behaviour only requires two material parameters, the number of necessary sample configurations does not change, if the material has isotropic layers. In this case, the total number of unknown material parameters equals $2\times n_m$. For isotropic materials, the bending stiffness coefficients D_{ij} are determined only by two independent reduced stiffnesses, i.e. Q_{11} and Q_{12}. Consequently, the resonant frequencies of every sample configuration provide only two independent bending stiffness coefficients, so that the total number of equations equals $2\times n_c$. This set of equations has a unique solution, if $n_c \geqslant n_m$. This requirement is also valid for a material that has a mix of orthotropic and isotropic layers. In comparison with a full orthotropic laminate, every isotropic layer will reduce the number of unknowns by 2. The number of independent stiffness coefficients, i.e. the number of equations, is also reduced by 2. Once again, a unique solution requires $n_c \geqslant n_m$.

Table 5.4: *Definitions.*

n_m	the total number of different homogeneous materials constituting the layers of a particular laminate
n_c	the number of sample configurations

5.4. Summary

This chapter used the classical lamination theory to show that the vibratory behaviour of layered material samples is controlled by the overall stiffness of the material and not by the stiffness of the individual material layers. As a result, the vibratory behaviour of one test specimen does not provide enough information to identify the layer properties. The elastic properties of the individual layers can only be identified from a set of test samples which all have a different layer configuration. It is shown that the minimum number of layer configurations that is required to identify the layer properties equals the number of layer materials that have to be characterised.

[1] In case only out-of-plane vibration modes are taken into account.

6
Identification Routines

In this chapter, all the methods and techniques that have been discussed in the previous chapters are combined into a number of identification routines for elastic material properties. The presented identification routines use two different types of test specimens: beam-shaped and plate-shaped. This chapter starts with a detailed discussion about the possibilities of beam- or plate-shaped specimens. Next, the identification routines are first introduced for non-layered materials. Finally, these routines are extended to layered materials.

6.1. The Specimen Shape

Finding samples that have one or more resonant frequencies sensitive to changes of the identification parameters is an important issue in vibration-based material identification. In this section, the influence of the sample shape and orientation on the sensitivity of the resonant frequencies with respect to the elastic material properties is investigated numerically. Two types of samples are being considered: beam-shaped and plate-shaped. The sensitivity analysis is performed with a number of finite element models which represent homogeneous brass or carbon-epoxy samples. Table 6.1 provides the properties of the considered materials. The evaluation is restricted to the lower order vibration modes, since they can be measured and modelled more accurately than the higher order ones.

Table 6.1: *The properties of the considered materials.*

	Brass	Carbon-Epoxy		Units
		UD[1]	BD[2]	
E_1	105	100	100	[GPa]
E_2	100	10	50	[GPa]
G_{12}	38	8	15	[GPa]
ν_{12}	0.36	0.25	0.20	[–]
ρ	8200	1400	1400	[kg/m^3]

[1] Uni-directionally reinforced
[2] Bi-directionally reinforced

6.1.1. Beam-Shaped Specimens

For beam-shaped specimens, the sensitivity analysis is performed using a finite element model of a brass beam. This beam has a length of 100 mm, a width of 20 mm and a thickness of 2 mm. The long-axis of the sample makes an angle of 55° with the principal material direction, i.e. the rolling direction of the brass. The global axis system, i.e. the material orientation, and the local axis system, i.e. the sample orientation, are defined as indicated in figure 6.1.

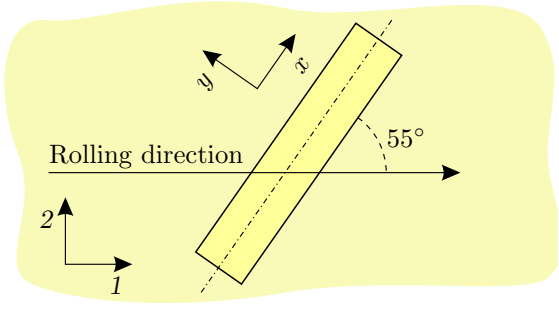

Figure 6.1: *The global and local axis system for the brass specimen.*

The first five vibration modes of the considered sample are all out-of-plane modes. Table 6.2 presents the mode shapes and resonant frequencies. The out-of-plane vibration modes of a beam-shaped sample can be divided into two classes, i.e. flexural modes and torsional modes.

Table 6.2: *The first five vibration modes of the brass beam.*

Mode 1	Mode 2	Mode 3	Mode 4	Mode 5
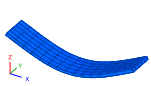	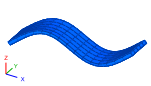	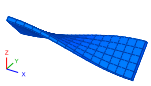	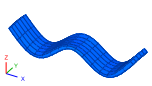	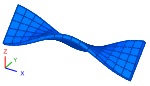
725.9 Hz	2014.2 Hz	2108.6 Hz	3978.5 Hz	4327.5 Hz
OOP-1	OOP-2	Tors-1	OOP-3	Tors-2

The sensitivity analysis is performed in two coordinate systems. First it is performed using the local axis system, the second time using the global axis system. Each time, the sensitivity coefficients are calculated for the first five vibration modes.

Using the local axis system, the frequency sensitivities are calculated with respect to the material parameters E_x, E_y, G_{xy}, and ν_{xy}. The obtained frequency sensitivities are graphically presented in figure 6.2. The sensitivity analysis shows that the flexural modes are only sensitive to changes of the E_x modulus, i.e. the elastic modulus in the direction of the beam's long-axis. Moreover, the torsional modes are only influenced by a variation of the apparent shear modulus G_{xy}. Both flexural and torsional modes are insensitive to changes of the E_y modulus and Poisson's ratio. This implies that only information about the elastic modulus E_x and the shear modulus G_{xy} can be extracted from the resonant frequencies of the out-of-plane vibration modes of a beam-shaped sample of an orthotropic material.

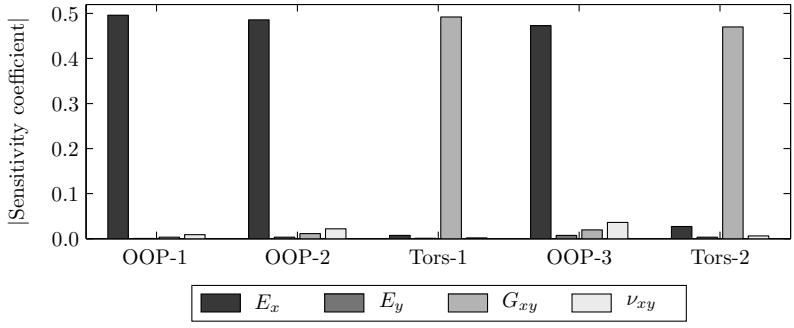

Figure 6.2: *The sensitivity coefficients of the first five modes of a beam-shaped specimen, using the local axis system.*

The sensitivity coefficients are also computed using the global axis system. With this coordinate system, the frequency sensitivity coefficients are calculated with respect to the principal material parameters E_1, E_2, G_{12}, and ν_{12}. Figure 6.3 presents the results of this sensitivity analysis. Now, there is a good sensitivity with respect to all material parameters. This means that the resonant frequencies of this beam provide information about the four material parameters. However, this does not imply that all four parameters can be simultaneously identified from these five frequencies. Figure 6.3 indicates that the three flexural modes, i.e. modes one, two and four, contain almost identical information about the elastic properties. The same can be said about the torsional modes, i.e. modes three and five. This implies that there are only two independent information sets and that only two material parameters can be identified, which corresponds with the results of the sensitivity analysis performed in the local axis system. Note that the sensitivity coefficients change, when the orientation of the beam with respect to the rolling direction changes. For example, if the long-axis of the beam is parallel with the rolling direction, a sensitivity pattern like that presented in figure 6.2 is obtained. A beam with a different orientation consequently provides additional information on the elastic properties.

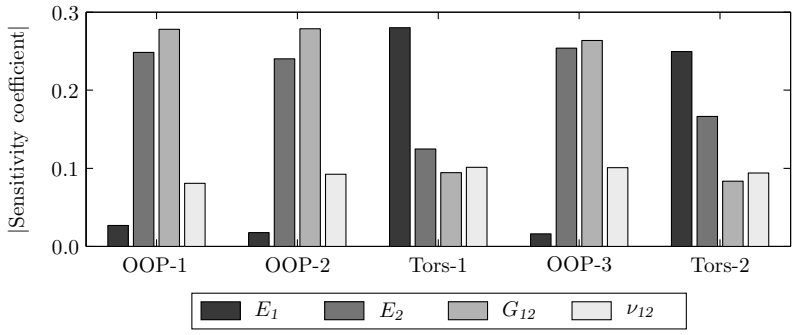

Figure 6.3: *The sensitivity coefficients of the first five modes of a beam-shaped sample, using the global axis system.*

6.1.2. Plate-Shaped Specimens

The evaluation of the frequency contents of a plate-shaped specimen presented in this section is an alternative interpretation of the work of [5, 19]. Consider a square bi-directionally reinforced carbon-epoxy plate with a thickness of 2 mm and sides with a length of 300 mm. The sensitivity coefficients with respect to the four orthotropic material parameters E_1, E_1, G_{12}, and ν_{12} are evaluated for the resonant frequencies of the first ten vibration modes. Table 6.3 presents the mode shapes and the associated resonant frequencies; figure 6.4 is a plot of the sensitivity coefficients.

The results show that there is a good sensitivity with respect to the elastic moduli E_1 and E_2 and the shear modulus G_{12}; however the Poisson's ratio sensitivities are very low. The third mode has the highest ν_{12}-sensitivity, but

Table 6.3: *The first ten vibration modes of the square carbon-epoxy plate.*

Mode 1	Mode 2	Mode 3	Mode 4	Mode 5
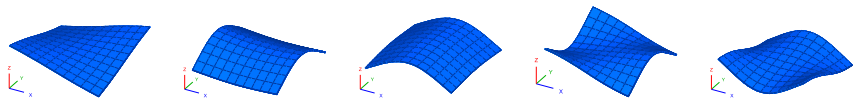				
77.1 Hz Torsional	136.8 Hz Flex-1-Y	196.2 Hz Flex-1-X	208.3 Hz TorFlex-Y	248.7 Hz TorFlex-X
Mode 6	**Mode 7**	**Mode 8**	**Mode 9**	**Mode 10**
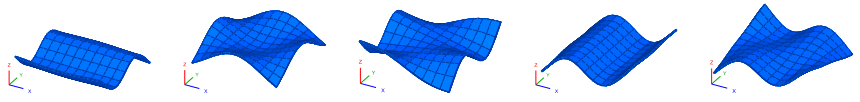				
387.0 Hz Flex-2-Y	389.3 Hz —	449.2 Hz —	545.3 Hz Flex-2-X	594.1 Hz —

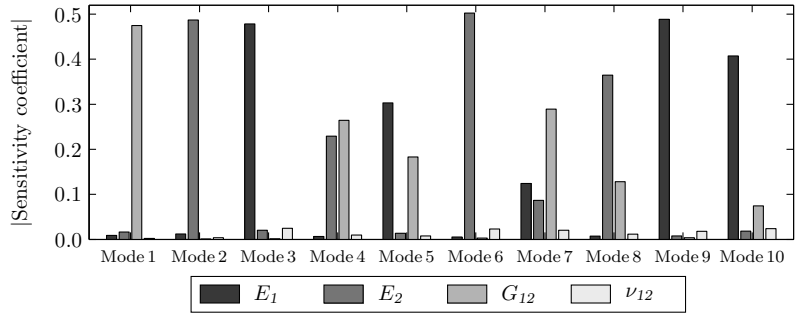

Figure 6.4: *The sensitivity coefficients of the first ten modes of a plate-shaped specimen.*

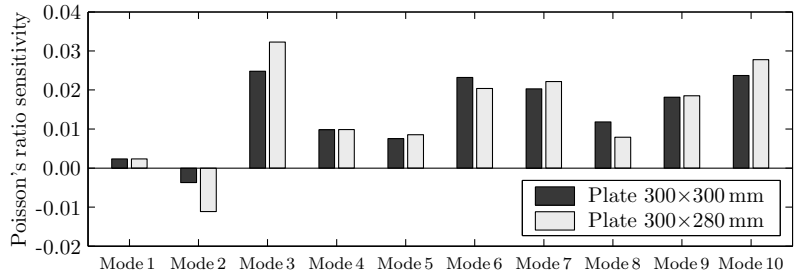

Figure 6.5: *Comparison of the ν_{12}-sensitivities of the first ten vibration modes of the 300×300 mm and the 300×280 mm plates.*

the sensitivity is about twenty times smaller than the sensitivity of the most sensitive parameter of this mode, i.e. E_1. The same sensitivity coefficients are also calculated for a 300×280 mm carbon-epoxy plate. Figure 6.5 compares the new Poisson's ratio sensitivity coefficients with the previous ones. The third mode remains the most sensitive mode, and its ν_{12}-sensitivity increased by about 30 %. The sensitivity of the second mode has benefited the most from the dimensional change of the plate, since the ν_{12}-sensitivity has tripled for this mode. Apparently, the aspect ratio[3] of a plate has a considerable influence on the Poisson's ratio sensitivities. To examine the influence of the aspect ratio in detail, the ν_{12}-sensitivities are calculated for a set of plates with aspect ratios varying between 0.6 and 2.4. The results, which are plotted in figure 6.6, confirm the strong influence of the aspect ratio on the Poisson's ratio sensitivities. They also reveal the presence of a number of optimal aspect ratios. The highest Poisson's ratio sensitivities are obtained for the plate with a aspect ratio of 1.19, but the plates with a aspect ratio of 0.76 and 1.86 also show an increased ν_{12}-sensitivity.

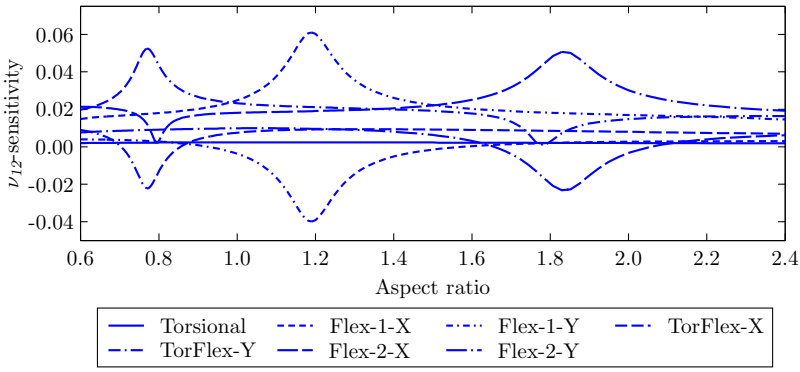

Figure 6.6: *The Poisson's ratio sensitivity in function of the aspect ratio of the plate.*

The presence of the peaks in the Poisson's ratio sensitivity curves can be explained by analysing the mode shape plots. Table 6.3 shows that a plate-shaped specimen has two first-order flexural modes, one in the x-direction (Flex-1-X) and one in the y-direction (Flex-1-Y). For the square carbon-epoxy plate, these two flexural modes are uncoupled; this means that the flexural mode in the x-direction has almost no deformation component in the y-direction, and vice versa. Since the Poisson's ratio describes the link between the deformation in two mutually orthogonal directions, a good Poisson's ratio sensitivity can only be obtained with a mode that has a deformation component in both the x- and y-direction. Such a deformation pattern should be obtained when the first-order flexural modes are coupled. This is exactly what happens with the two first-order flexural modes of the plate with the aspect ratio of 1.19. The second mode of this plate, the anti-clastic mode, is the combination of Flex-1-X and Flex-1-Y mode with a phase difference of 180°. The third mode, which

[3]This is the ratio of the length over the width.

is called the sin-clastic mode, is the in-phase combination of the Flex-1-X and Flex-1-Y mode. Table 6.4 presents the mode shapes of these two modes. Because of their physical appearance, the anti-clastic and sin-clastic modes are usually referred to as the saddle and the breathing mode, respectively.

Table 6.4: *The mode shapes of the two most sensitive modes for ν_{12}.*

anti-clastic	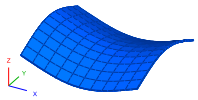	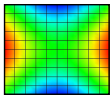
sin-clastic	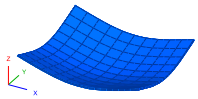	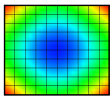

The other peaks in the sensitivity curves of figure 6.6 are also the result of a coupling between a flexural mode in the x-direction and one in the y-direction. For the plate with a aspect ratio of 0.76, the Flex-1-X and the TorFlex-Y modes are coupled. For the plate with the aspect ratio of 1.86 a coupling between the Flex-1-Y and the TorFlex-X modes can be observed. Table 6.5 presents the modes shapes of these coupled modes. In fact, every aspect ratio that results in a coupling between a mode with a flexural deformation in the x-direction and a mode with a flexural deformation in the y-direction results in an increased ν_{12}-sensitivity. However, the highest sensitivities are obtained for the coupling between the two first-order flexural modes. Subsequently, a plate with a aspect ratio that results in two coupled first-order flexural modes is called a Poisson-plate [19].

Table 6.5: *The higher order sin-clasic and anti-clastic modes.*

	aspect ratio = 0.76	aspect ratio = 1.86
anti-clastic	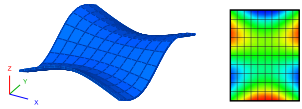	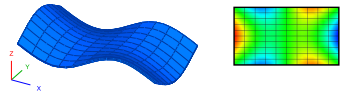
sin-clastic	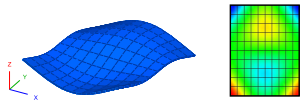	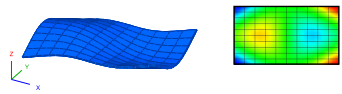

To exploit the advantages of the Poisson-plate, there has to be a simple tool to predict the optimal aspect ratio. As shown in [5], such a tool can be derived from the fact that a Poisson-plate requires two coupled first-order flexural modes. Two modes can be coupled by making their resonant frequencies to coincide. The frequency of the fundamental flexural mode in the length direction of a plate can be approximated [95] by

$$f = \frac{\varsigma}{2\pi l^2}\sqrt{\frac{E_1 t^2}{12\rho\left(1-\nu_{12}^2\right)}} \tag{6.1}$$

The resonant frequency of the first flexural mode in the y-direction can be estimated in the same way.

$$f = \frac{\varsigma}{2\pi w^2}\sqrt{\frac{E_2 t^2}{12\rho\,(1-\nu_{21}^2)}} \tag{6.2}$$

In expressions (6.1) and (6.2), l represents the plate length, w denotes the plate width and ς is a coefficient that depends only on the considered vibration mode. By demanding that the two first-order flexural modes have the same resonant frequencies, (6.1) and (6.2) can be combined into

$$\frac{l^2}{w^2} = \sqrt{\frac{E_1\,(1-\nu_{21}^2)}{E_2\,(1-\nu_{12}^2)}} \tag{6.3}$$

Since, for most materials

$$\sqrt{\frac{(1-\nu_{21}^2)}{(1-\nu_{12}^2)}} \approx 1 \tag{6.4}$$

equation (6.3) can be simplified to

$$\frac{l}{w} = \sqrt[4]{\frac{E_1}{E_2}} \tag{6.5}$$

Expression (6.5) provides an efficient tool to calculate the optimal aspect ratio of a test plate. A plate with this aspect ratio has two coupled first-order flexural modes, and, consequently, a maximal Poisson's ratio sensitivity. Applying formula (6.5) to the considered carbon-epoxy plate results in an optimal aspect ratio of 1.19, which is exactly the position of the highest peak of the Poisson's ratio sensitivities of figure 6.6. Figure 6.7 presents the sensitivity coefficients of the resonant frequencies of the first ten vibration modes of the optimised test plate. The third mode remains the most sensitive mode for ν_{12}. For this mode, the Poisson's ratio sensitivity has increased to one sixth of the value of the maximal sensitivity coefficient of this mode.

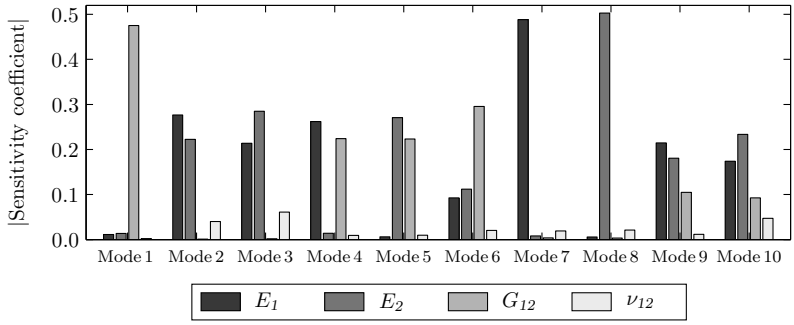

Figure 6.7: *The sensitivity coefficients of the first ten vibration modes of the optimal test plate.*

6.2. Identification Routines for Non-Layered Materials

This section introduces the MNET-based identification routines for the characterisation of non-layered materials. The non-layered material routines form the foundation for the development of the layered material routines. In this section, all the materials are considered to be uniform, homogeneous and elastically orthotropic.

6.2.1. Using Beam-Shaped Specimens

The Single-Orientation Routine

The sensitivity analysis of section 6.1.1 revealed that the resonant frequencies of the out-of-plane vibration modes of beam-shaped specimens provide only two independent information sets. Orthotropic material behaviour requires a material model with four independent parameters, therefore it is impossible to characterise orthotropic materials with the resonant frequencies of a single beam. However, isotropic material behaviour requires only two independent parameters, and can thus be fully characterised using the resonant frequencies of a single beam-shaped specimen. Of the two information sets provided by the resonant frequencies of a beam, one set is provided by the flexural frequencies, the other one by the torsional frequencies. Measuring more than

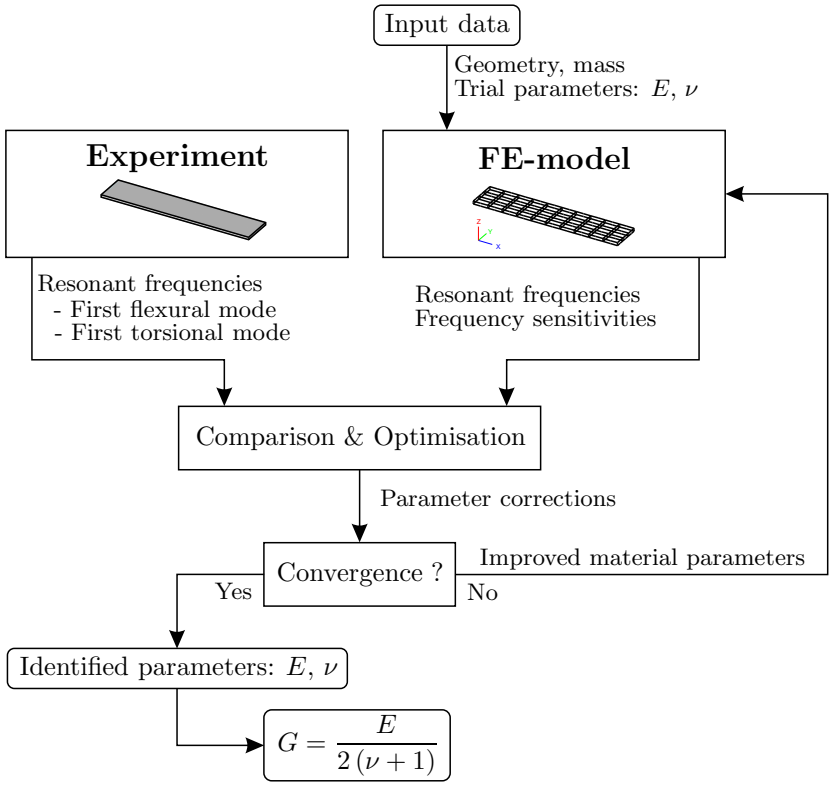

Figure 6.8: *The flowchart of the single-orientation MNET procedure.*

one flexural/torsional frequency is not useful, because all the flexural/torsional frequencies provide the same information. Furthermore, finite element models converge faster for lower order vibration modes, therefore it is advisable to use only the resonant frequencies of the fundamental vibration modes as input data for the identification routine.

Figure 6.8 presents the flowchart of the single-orientation MNET routine. The FE-model of the test sample uses an isotropic material model. The two elastic parameters, E and ν, are fine-tuned in order to match the experimental and numerical resonant frequencies of the fundamental flexural and torsional vibration mode. From a physical point of view, it would make more sense to use the elastic and shear modulus as optimisation parameters, but in finite element modelling isotropic material behaviour is often described with E and ν.

The single-orientation routine starts by calculating the resonant frequencies of the test specimen using a set of trial values for E and ν. The numerical frequencies are compared with the experimentally measured resonant frequencies and a set of parameter corrections is estimated in order to reduce the observed frequency differences. The material parameters are corrected and a new iteration step is performed. Once the material parameter corrections are lower than a pre-defined threshold, the iteration cycle is aborted and the values of E and ν are retrieved from the database of the FE-model. In a post-processing step, the material's shear modulus is derived from the values of E and ν using equation (2.31).

Although the single-orientation routine assumes isotropic material behaviour, it can be used for the characterisation of orthotropic materials. Consider the sensitivity analysis performed on the brass beams in section 6.1.1. Figure 6.2 presents the results of the sensitivity analysis performed in the local axis system. These results reveal that the fundamental flexural and torsional frequencies are virtually insensitive to a change of E_y and ν_{xy}. While being orthotropic, for these two vibration modes, the material behaves like an isotropic material, i.e. it is controlled by only two material parameters. So, by applying the single-orientation routine on an orthotropic material, the apparent E- and G-modulus in the direction parallel to the beam's long-axis, can be identified.

The identification test was simulated to assess the error made by applying a method that assumes isotropic behaviour on orthotropic materials. Consider a

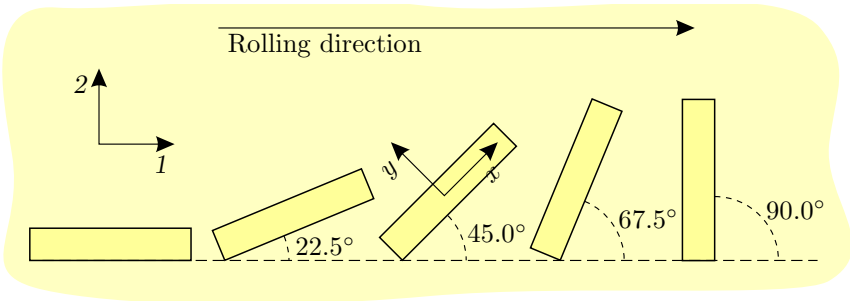

Figure 6.9: *A set of five beams with a different material orientation.*

set of beams, 100×15×2 mm, that are cut out of a brass plate. The sample set comprises five beams which make an angle of 0°, 22.5°, 45°, 67.5°, and 90° with the rolling direction. Figure 6.9 presents the considered sample set.
These five beams are modelled using the orthotropic brass properties of table 6.1. The FE-models provide the fundamental flexural and torsional frequency of the test beams. For each beam, these two resonant frequencies are entered into the identification routine of figure 6.8 and the elastic properties are estimated. The obtained results are presented in the plots of figure 6.10. In these graphs, the dashed lines represent the correct orthotropic brass properties, while the diamonds represent the results of the single-orientation identification routine. It can be seen that values of the elastic and shear modulus are correctly identified. The single-orientation routine even allows the identification of the variation of these two elastic parameters in function of the material orientation. However, as illustrated by the considered example, the correctness of the identified Poisson's ratios cannot be guaranteed. For this example, the trend of the variation in function of the orientation does even not correspond with the correct trend. Table 6.6 gives an overview of the error between the identified and correct values.

Table 6.6: *Accuracy of the single-orientation identification routine.*

Orientation	Error E_x	Error G_{xy}	Error ν_{xy}
0.0°	−0.08	−0.01	19.41
22.5°	−0.05	−0.03	4.84
45.0°	0.07	−0.11	−11.14
67.5°	0.03	−0.06	−4.53
90.0°	−0.03	0.00	5.31
	[%]	[%]	[%]

At first sight, it might seem quite suspicious that the shear moduli, which are derived from incorrect Poisson's ratio values, are correct. There is, however, a logical explanation. In the single-orientation routine, the E-modulus is mainly controlled by the value of the flexural frequency while Poisson's ratio is primarily determined by the torsional frequency of the beam. Since torsion is a physical phenomenon that results in a shearing deformation, the value of Poisson's ratio is optimised for shearing and thus results in a correct value of the shear modulus. If the Poisson's ratio would have been derived from a physical phenomenon that was controlled by the coupling of two orthogonal strain components, the value of ν would be correct and the post-processing step would result in an incorrect value of the shear modulus.
In case of mildly orthotropic materials like sheet metals, the single-orientation routine identifies the correct values of the apparent elastic and shear modulus. However, the correctness of E_x and G_{xy} cannot be guaranteed for genuinely orthotropic materials, such as fibre reinforced plastics. Consider the uni-directionally reinforced carbon-epoxy material of table 6.1. Figure 6.11 presents the differences between the correct properties and the values identified with the single-orientation routine, using 100×20×2 mm beam-shaped

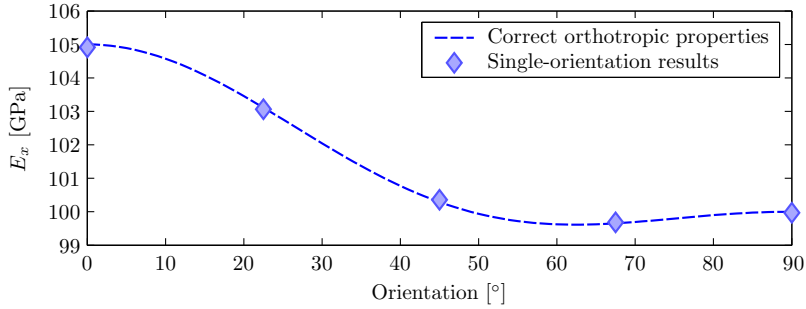

(a) The elastic modulus E_x

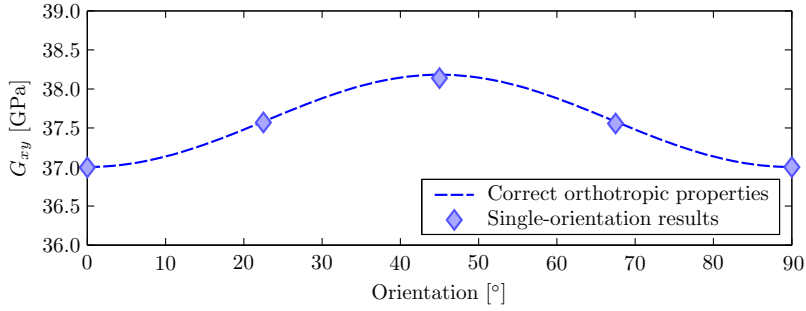

(b) The shear modulus G_{xy}

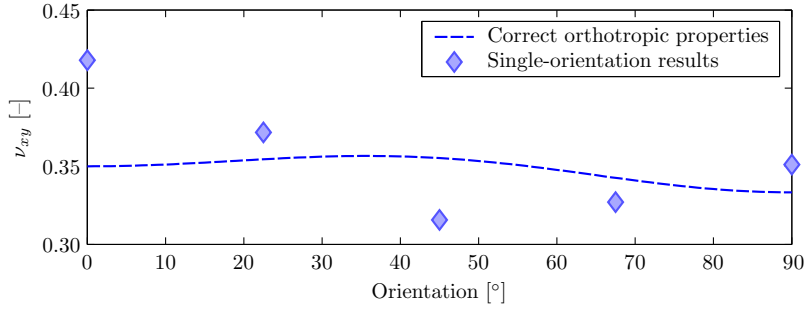

(c) Poisson's ratio ν_{xy}

Figure 6.10: *The results obtained from the orthotropic brass beams.*

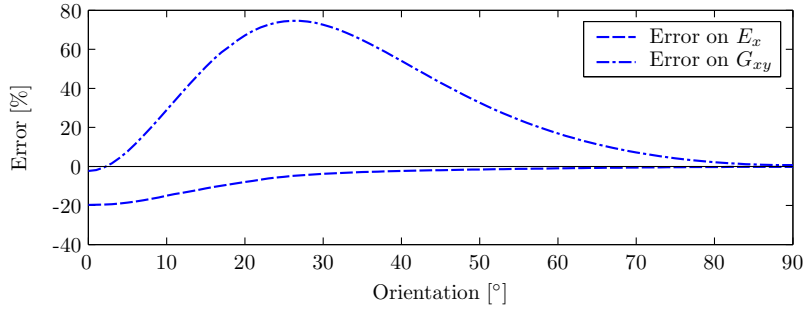

Figure 6.11: *The difference between the identified and correct properties for the uni-directionally reinforced carbon-epoxy.*

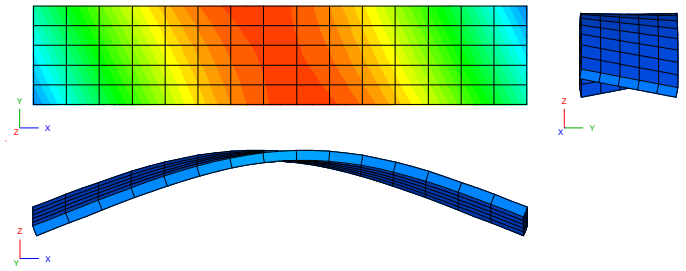

(a) The real mode shape of the carbon-epoxy beam.

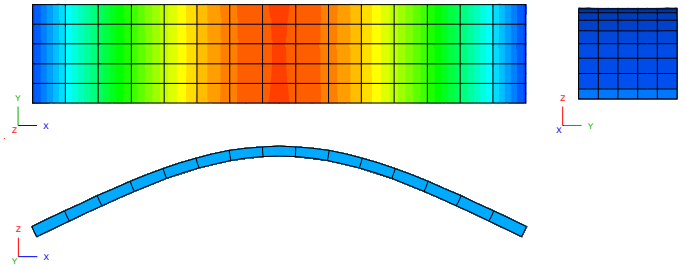

(b) The mode shape of the identification model.

Figure 6.12: *Mode shape of the fundamental flexural frequency of the carbon-epoxy beam.*

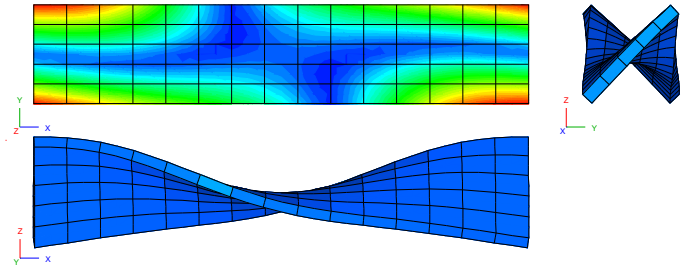

(a) The real mode shape of the carbon-epoxy beam.

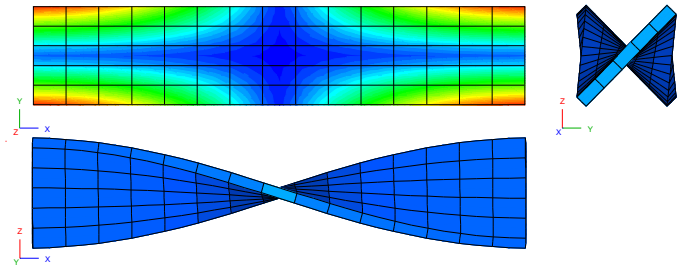

(b) The mode shape of the identification model.

Figure 6.13: *Mode shape of the fundamental torsional frequency of the carbon-epoxy beam.*

samples. The huge discrepancies between the correct and identified properties are caused by two different mechanisms: an overestimated transverse shear stiffness, and incorrect modal displacement fields. As already explained, the single-orientation routine derives the value of Poisson's ratio from the torsional frequency. If the material is not isotropic, this results in an error in Poisson's ratio, which is proportional to the degree of anisotropy. With an isotropic material model, an overestimation of the Poisson's ratio results in an increased transverse shear stiffness of the beam. This implies that the measured resonant frequency of the flexural mode can be reproduced with a lower flexural stiffness, since the underestimation of the flexural stiffness is compensated by the transverse shear stiffness. In case of the uni-directionally reinforced carbon-epoxy material, the single-orientation routine results in an unrealistic Poisson's ratio of 4.1 for the 0° direction. The Poisson's ratio gradually decreases in function of the orientation and reaches an acceptable level, according to (2.61), at ±33°. The identification should thus result in an underestimation of the E-modulus, which is most pronounced in the range between 0° and 33°. This is exactly what is observed in figure 6.11.

The increased transverse shear stiffness can, however, not explain the overestimation of the shear modulus. Figures 6.12 and 6.13 present the modal displacement fields of the actual test specimen at a 40° orientation. The displacement fields of the actual test specimen are not aligned with the specimen's long-axis. The displacement field is rotated or twisted around the z-axis due to the presence of the reinforcing fibres. The identification routine uses a finite element model with isotropic material behaviour. Such a model has the same properties in every direction, so the modal displacement fields have to be aligned with the sample edges, as shown in figures 6.12 and 6.13. Unlike the real test specimens, the identification model is not stiffened by an additional twisting deformation being, therefore, too flexible. Identifying material parameters with a model that is too flexible, results in an overestimation of the material properties. Note that the displacement fields of samples oriented along the principal material directions are not affected. Figure 6.11 presents a behaviour that qualitatively corresponds with the effects of this twisting phenomenon.

To conclude, it should be mentioned that the single-orientation routine is the MNET equivalent of the resonant beam techniques presented in the ASTM standard [4]. All the considerations and remarks about the single-orientation routine are, therefore, also applicable for the ASTM test procedures.

The Multi-Orientation Routine

Section 6.1.1 showed that the resonant frequencies of a single beam-shaped specimen do not provide enough information to fully characterise the constitutive behaviour of orthotropic materials. The amount of useful information can be increased by using a number of beams with a different material orientation. Figure 6.14 shows the sensitivity coefficients of the fundamental flexural and torsional frequency of the five test beams of figure 6.9. The results indicate that each beam provides a different set of information about the four orthotropic material parameters.

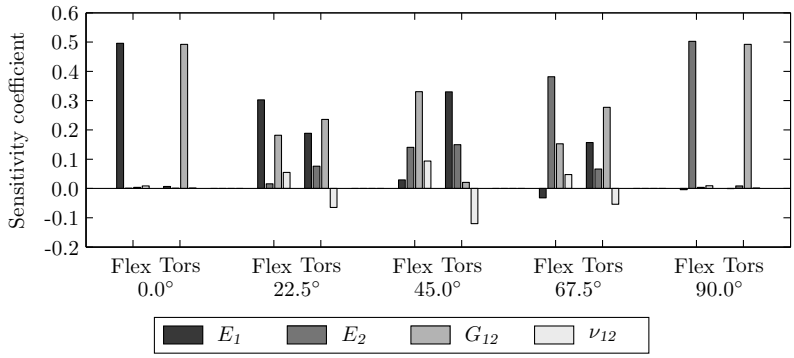

Figure 6.14: *The sensitivity coefficients of the set of brass beams of figure 6.9 for the first flexural and torsional resonant frequency.*

The multi-orientation routine extracts the elastic material parameters from the frequencies of a set of test samples, each of which representing a different material orientation. Figure 6.15 gives the flowchart of the multi-orientation routine. The routine requires an FE-model of each sample of the test sample set and one orthotropic material model. All these FE-models share this material model.

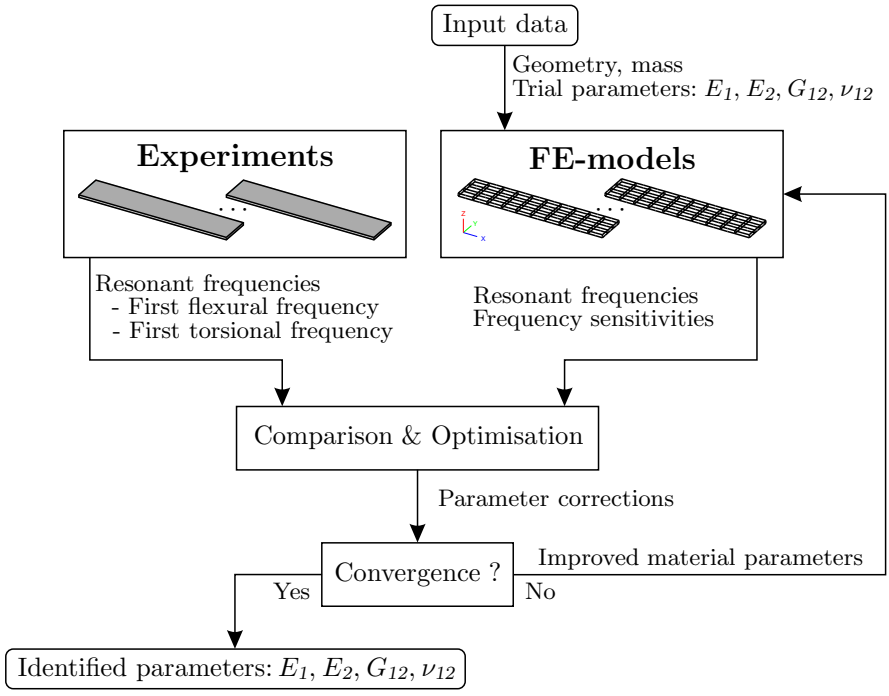

Figure 6.15: *The flowchart of the multi-orientation MNET procedure.*

The routine starts with the calculation of the resonant frequencies of all the test specimens using a set of trial values for E_1, E_2, G_{12}, and ν_{12}. The numerical frequencies of the considered test samples are compared with the experimentally measured resonant frequencies, and a set of parameter corrections is estimated in order to reduce the observed frequency differences. The parameters of the material model are corrected and inserted into all the FE-models so that a new iteration step can be performed. Once the material parameter corrections are lower than a predefined threshold, the iteration cycle is aborted and the material parameters are retrieved from the database of the material model.

Figure 6.14 presents the sensitivity coefficients of the fundamental flexural and torsional frequency of the five test beams. At first sight, the sensitivity coefficients look linearly independent but they are not. The condition number[4] of the global sensitivity matrix that groups the sensitivity coefficients of these ten frequencies equals 5.4, which confirms that this data set provides enough information to identify the unknown orthotropic material parameters. Grouping only the sensitivity coefficients of the flexural frequencies results in a sensitivity matrix with a condition number of $3{\cdot}10^5$. The sensitivity matrix that just contains the torsional frequency sensitivities is also ill-conditioned; it has a condition number of $3{\cdot}10^4$. A full orthotropic identification thus requires a mix of both flexural and torsional frequencies.

A full orthotropic identification does not require the frequencies of five different beams. Two well-chosen beams can provide the necessary information. The flexural and torsional frequencies of the 0° and 45° beams provide enough information, since they result in a sensitivity matrix with a condition number of 5.0. The combination of the flexural and torsional frequencies of the 0° and 90° beams results in a sensitivity matrix condition number of $5{\cdot}10^4$, which implies that the identification requires at least one beam in an off-axis direction. The opposite is not true: the beams in the on-axis directions are not strictly necessary, however it is advisable to use them[5].

In some situations, it might even be desirable to use only one frequency per sample. For example, suppose the elastic properties have to be measured in a particular temperature range. For such a test, the resonant frequencies have to be measured, while the sample is being heated in a furnace. Because a flexural and torsional frequency demand a different set-up, it is difficult to measure both frequencies at the same time. This implies that the frequencies have to be measured in two different runs. Unfortunately, the first temperature cycle may alter the properties of the sample, as every heat treatment. To avoid such problems, the properties have to be identified with only one frequency per sample. For the considered set of brass beams, all test configurations that use a single frequency per beam were investigated and compared. The optimal configuration is the combination of the flexural frequencies of the 0°, 45°, and 90° beams with the torsional frequencies of the 22.5° and 67.5° beams. This

[4]The condition number of a matrix is the ratio of the largest singular value over the smallest singular value, and varies between 1 and ∞. According to [96], updating problems with condition numbers larger than 10^3 are ill-conditioned, and problems with conditions numbers larger than 10^7 are singular.

[5]The influence of the sample set on the quality of the obtained results is discussed in detail in chapter 7.

test configuration has a sensitivity matrix condition number of 5.3, which shows that using only one frequency per sample is possible, even without a reduction of the amount of provided information.

6.2.2. Using Plate-Shaped Specimens

The routine presented is this section is a modified version of the routine introduced in [5]. This routine identifies the material parameter from the resonant frequencies of the first three vibration modes of a plate-shaped specimen and the fundamental flexural frequencies of two beam-shaped specimens oriented in the two principal material directions. It is, however, possible to identify the material properties from the resonant frequencies of only the plate-shaped specimen. The sensitivity analysis of section 6.1.2 showed that the resonant frequencies of a plate-shaped specimen provide information about all four elastic material parameters, if the geometry of the plate complies with (6.5). This particular geometry is needed to ensure the sensitivity with respect to the Poisson's ratio. However, this geometry has another advantage. The order of the first three vibration modes of a Poisson-plate is fixed [5]. The first mode is the torsional mode, the second mode is the saddle mode, and the third mode is always the breathing mode. The fourth and fifth mode are the torsional-flexural modes in the x- and y-direction. The relative order of these last two modes is not fixed and varies from plate to plate. Note that the first five modes of a

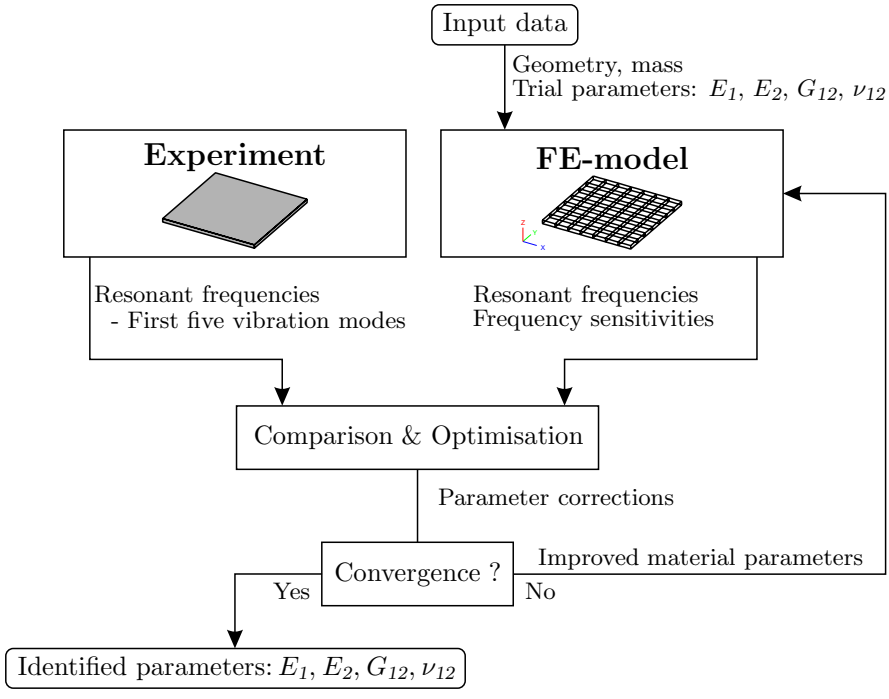

Figure 6.16: *Flowchart of the MNET procedure for plate-shaped specimens.*

Poisson-plate provide enough information to fully identify an orthotropic material; to be precise, the sensitivity matrix grouping the sensitivity coefficients of the first five modes of figure 6.7 has a condition number of 9.4.
Figure 6.16 shows the flowchart of a routine that extracts the elastic parameters from the first five resonant frequencies of a plate-shaped specimen. This identification routine requires a finite element model of the test plate with an orthotropic material behaviour. A set of trial values of the elastic parameters E_1, E_2, G_{12}, and ν_{12} is used to compute the first five resonant frequencies of the test plate. The resulting numerical frequencies are compared with the resonant frequencies of the equivalent experimental modes. The observed frequency discrepancies are minimised by optimising the material parameters of the finite element model. Once the solution has converged, the iterative procedure is aborted and the elastic properties are retrieved from the material database of the finite element model.
Let us conclude with the following experimental consideration. Theoretically, a Poisson-plate results in a fourth and fifth vibration mode with exactly the same resonant frequency. Although a real test plate is never a perfect Poisson-plate, the frequencies of the fourth and fifth mode will remain very close to each other. This phenomenon complicates the experimental modal analysis phase[6]. Potential problems can easily be avoided by choosing a plate that is almost a Poisson-plate, e.g. a plate with a width that is 98 % of the optimal width. Figure 6.6 shows that the peaks of the Poisson's ratio sensitivities are not very sharp; this means that a nearly optimal plate still has a very good Poisson's ratio sensitivity. But, such a plate has the additional advantage that the frequencies of the fourth and fifth modes are well separated.

6.3. Layered Materials

In this section, the identification routines for non-layered materials are extended to layered materials. All samples are considered to have perfectly bonded layers with a uniform thickness. The layer materials are assumed to be homogeneous and elastically orthotropic.

6.3.1. The Required Test Specimens

Chapter 5 showed that layered material identification requires a number of purpose-built samples. To guarantee the uniqueness of the solution, the elastic properties of n_m layer materials have to be identified from the vibratory behaviour of a set of test samples that comprises samples with n_c different layer configurations, where $n_c \geqslant n_m$. Remember that an additional layer configuration can only be created by changing the relative thickness of one or more layers or by altering the layer sequence.
In some situations, the required layer configurations can be obtained quite easily, e.g. coated materials. With coated materials, the required layer configurations can be produced by varying the thickness of the substrate or coating. However, with some materials it is difficult or even impossible to change the layer thickness or sequence. In that situation, the most obvious solution is to –

[6]The experimental test set-up is presented in appendix B.

partially – remove one or more layers. The main difficulty of this approach is to remove a part of the material without damaging the rest of the sample. An alternative way to make an additional layer configuration is to add a layer to the sample. If the properties of the added layer are known, i.e. are measured before adding the layer to the sample, a new layer configuration is obtained without introducing any new unknowns. Glass has proven to be an excellent material for use as additional layer. Glass sheets are homogeneous, flat, have a uniform thickness, are available with a variety of thicknesses and can easily be cut to the correct size. Glass is also transparent, which means that the glue layer between the glass layer and the initial sample can be inspected visually, e.g. for the presence of air bubbles.

The creation of additional beam-shaped layer configurations is quite straightforward. Creating additional plate-shaped layer configurations is more challenging. Consider a layered plate for which the integrated stiffness in the x-direction is considerably higher than the integrated stiffness in the y-direction. Assume that the additional layer configuration is made by adding a glass layer to the sample. Glass is an isotropic material and thus has the same stiffness in the x- and y-direction. A combination of the initial plate with an additional glass layer results in a material that is less anisotropic than the initial plate. The optimal aspect ratio of this configuration is thus lower than the optimal aspect ratio of the initial plate. So, in case of plate-shaped specimens, an optimal aspect ratio has to be determined for every layer configuration[7].

6.3.2. The Identification Routines

The three identification routines for non-layered materials can quite easily be extended to layered materials by using the concept of multiple layer configurations. During the experimental phase, the resonant frequencies of each sample have to be measured for each considered layer configuration. The finite element model library of the identification routine has to be extended with the models of each measured layer configuration and the material database has to be expanded so that it contains the elastic properties of each layer material. Otherwise, the identification schemes for layered materials are similar to those used for non-layered materials, i.e. the flowcharts of figures 6.8, 6.15 and 6.16.

Using Beam-Shaped Specimens

The Single-Orientation Routine — The layered version of the single-orientation routine requires n_c sample configurations of a sample with a particular material orientation. The fundamental flexural and torsional frequencies of the test samples have to be measured for each layer configurations. The routine provides both E and ν of the layer materials as a direct output. The shear modulus of the layers is obtained in a post-processing step as shown in figure 6.8. Note that the discussion about the limitations of the non-layered single-orientation routine applies also to the layered version, which translates into correct results for isotropic materials, incorrect Poisson's ratio values for

[7] Chapter 8 illustrates this problem with an experimental example.

mildly orthotropic[8] materials, and incorrect material properties for genuine orthotropic materials.

The Multi-Orientation Routine — The multi-orientation approach requires a set of beam-shaped samples, each of which represents a different material orientation. The layered version of this technique requires n_c layer configurations of the complete sample set. The material orientations of the samples and the used frequencies, i.e. fundamental flexural and/or torsional frequency, are chosen in a similar way as for a non-layered material. The routine provides the four orthotropic constants, E_1, E_2, G_{12}, and ν_{12} for all the layer materials.

Using Plate-Shaped Specimens

The layered version of this identification routine requires the resonant frequencies of the first five vibration modes of n_c different layer configurations of the test plate. Note that every layer configuration requires a particular aspect ratio in order to ensure the sensitivity with respect to the Poisson's ratios. The routine provides the four orthotropic parameters of every material layer.

6.4. The General Vibration-Based MNET Framework

All identification routines presented in the two previous sections are applications of the same MNET approach. This section presents the mathematical framework of the general identification problem. The implementation of a particular identification routine can be found by simplifying this general framework, in accordance to the properties of the considered test procedure.

6.4.1. The Identification Routine

Figure 6.17 presents a detailed flowchart of the generalised identification procedure. Before the elastic properties can be identified, the resonant frequencies of the considered modes of all the samples with their respective layer configurations have to be measured. The numerical part of the MNET procedure requires a finite element model of every sample and layer configuration and a database containing the elastic properties of the layer materials.

The identification of the elastic properties starts by computing the resonant frequencies and mode shapes of the first five[9] vibration modes of all test specimens by using a set of trial values[10] for the elastic properties of the different layer materials. In the next step, the automatic mode shape recognition algorithm[11] determines the mode shape type of the numerical modes. The frequency sensitivities are computed from the numerical mode shapes and resonant frequencies with (3.39). Since the mode shape types of both experimental and numerical modes are known, the mode pairs can be identified and the frequency differences can be computed. The sensitivity matrices and frequency difference

[8] Quasi isotropic materials, like sheet metals.

[9] The fundamental flexural and torsional modes of a beam-shaped specimen are normally situated within the first five vibration modes.

[10] The trail values represent the order of magnitude of the elastic properties and are based on the a priori knowledge about the material, .e.g. the class of material it belongs to.

[11] The automatic mode shape recognition algorithm is described in detail in chapter 3.

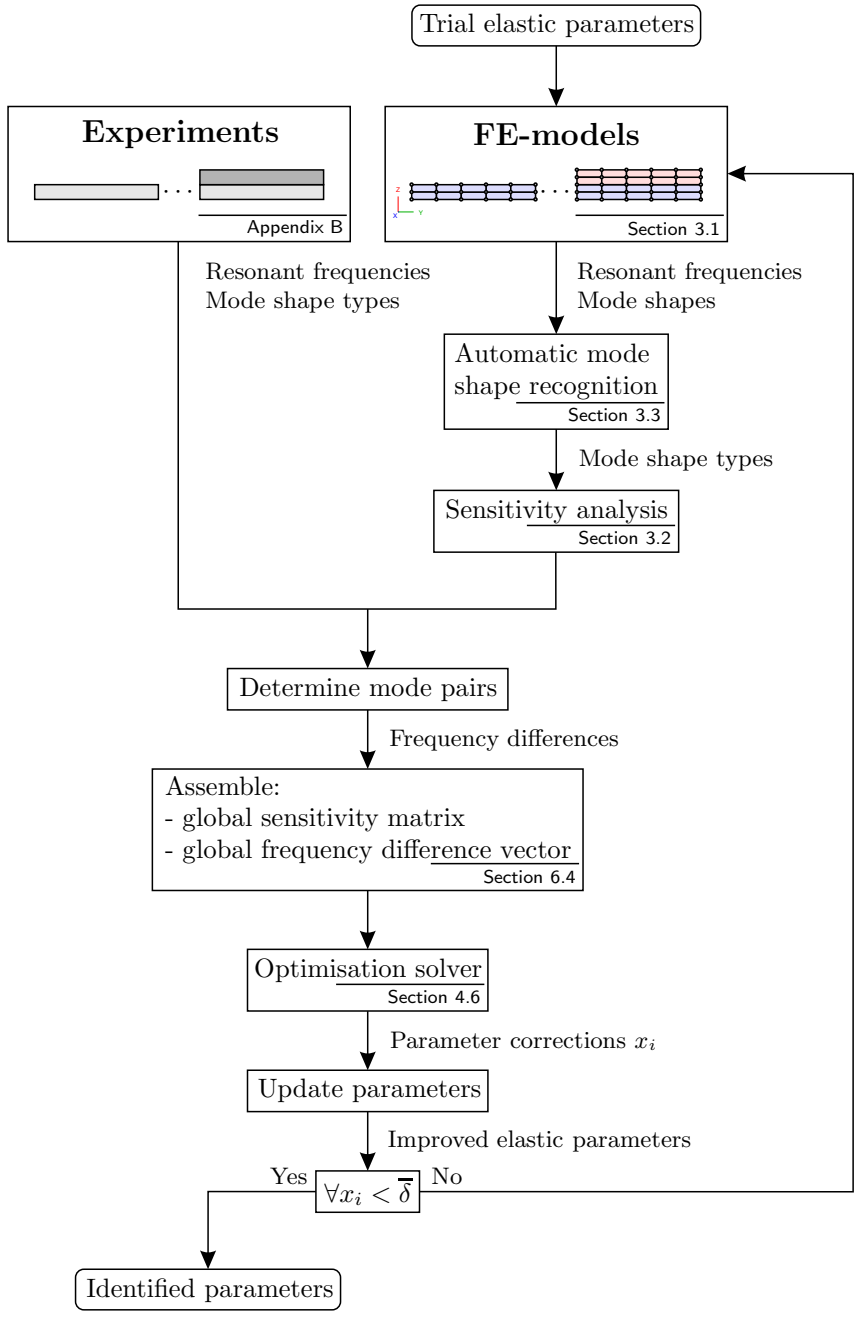

Figure 6.17: *The flowchart of the generalised MNET material identification procedure.*

vectors of all the test samples are assembled into one global sensitivity matrix and frequency difference vector. The global sensitivity matrix and frequency difference vector are inserted into the optimisation solver, which provides the optimal parameter corrections. Finally, the elastic parameters in the material database are updated, and the parameter corrections are compared to a predefined convergence threshold. If one of the parameter corrections is larger than the convergence threshold, a new iteration cycle is started, otherwise the procedure is aborted and the identified elastic properties are retrieved from the material database.

6.4.2. The Global Sensitivity Matrix

In case of a multi-specimen identification routine, the sensitivity matrices and frequency difference vectors of the considered test samples have to be combined into one global sensitivity matrix and frequency difference vector.
Consider an identification problem where the properties of n_m layer materials are identified from the resonant frequencies of n_s test samples comprising n_c different layer configurations. Note that for identifiability reasons $n_c \geqslant n_m$. Assume that the constitutive behaviour of these n_m materials can be modelled with n_p independent material parameters. For each sample, the resonant frequencies of n_{f_k} vibration modes are measured, where k denotes the sample index. The relative frequency differences and normalised relative frequency sensitivities are calculated for every test specimen. This yields the following n_s sets of equations.

$$\{\Delta r\}_k = [S]_k \{\Delta p\}, \quad \forall k = 1, \ldots, n_s \tag{6.6}$$

where $\{\Delta r\}_k \in \mathbb{R}^{n_{f_k}}$ contains the relative frequency differences of the considered modes of the k^{th} specimen, $[S]_k \in \mathbb{R}^{n_{f_k} \times n_p}$ is the sensitivity matrix of the k^{th} specimen, and $\{\Delta p\} \in \mathbb{R}^{n_p}$ groups the relative parameter variations of different material properties. Equations (6.7) and (6.8) give the mathematical expressions of these three components.

$$\{\Delta r\}_k = \begin{Bmatrix} \dfrac{f_{exp,1} - f_{num,1}^{(i)}}{f_{exp,1}} \\ \vdots \\ \dfrac{f_{exp,n_f} - f_{num,n_f}^{(i)}}{f_{exp,n_f}} \end{Bmatrix}_k \qquad \{\Delta p\} = \left\{ \begin{array}{l} \left.\begin{array}{c} \dfrac{p_{1,1}^{(i+1)} - p_{1,1}^{(i)}}{p_{1,1}^{(i)}} \\ \vdots \\ \dfrac{p_{n_p,1}^{(i+1)} - p_{n_p,1}^{(i)}}{p_{n_p,1}^{(i)}} \end{array}\right\} \text{Material 1} \\ \vdots \\ \left.\begin{array}{c} \dfrac{p_{1,n_m}^{(i+1)} - p_{1,n_m}^{(i)}}{p_{1,n_m}^{(i)}} \\ \vdots \\ \dfrac{p_{n_p,n_m}^{(i+1)} - p_{n_p,n_m}^{(i)}}{p_{n_p,n_m}^{(i)}} \end{array}\right\} \text{Material } n_m \end{array} \right\} \tag{6.7}$$

$$[S]_k = \left[\begin{array}{cccc} \overbrace{\begin{array}{ccc} \frac{\partial f_1}{\partial p_{1,1}}\frac{p_{1,1}}{f_1} & \cdots & \frac{\partial f_1}{\partial p_{n_p,1}}\frac{p_{n_p,1}}{f_1} \\ \vdots & \ddots & \vdots \\ \frac{\partial f_{n_f}}{\partial p_{1,1}}\frac{p_{1,1}}{f_{n_f}} & \cdots & \frac{\partial f_{n_f}}{\partial p_{n_p,1}}\frac{p_{n_p,1}}{f_{n_f}} \end{array}}^{\text{Material 1}} & \cdots & \overbrace{\begin{array}{ccc} \frac{\partial f_1}{\partial p_{1,n_m}}\frac{p_{1,n_m}}{f_1} & \cdots & \frac{\partial f_1}{\partial p_{n_p,n_m}}\frac{p_{n_p,n_m}}{f_1} \\ \vdots & \ddots & \vdots \\ \frac{\partial f_{n_f}}{\partial p_{1,n_m}}\frac{p_{1,n_m}}{f_{n_f}} & \cdots & \frac{\partial f_{n_f}}{\partial p_{n_p,n_m}}\frac{p_{n_p,n_m}}{f_{n_f}} \end{array}}^{\text{Material } n_m} \end{array} \right]_k^{(i)} \tag{6.8}$$

In these expressions, f denotes resonant frequency, p represents a material parameter, and the superscript between brackets specifies the iteration cycle. The first subscript of the material parameters indicates the parameter number, while the second subscript specifies the material index, e.g. $p_{1,j}^{(i)}$ denotes the first parameter of the j^{th} material during the i^{th} iteration cycle. For each specimen, a set of equations like (6.6) can be written. These n_s sets can be combined into one global set of equations as

$$\underbrace{\left\{ \begin{array}{c} \{\Delta r_1\} \\ \{\Delta r_2\} \\ \vdots \\ \{\Delta r_{n_s}\} \end{array} \right\}}_{\{\Delta r\}} = \underbrace{\left[\begin{array}{c} [S_1] \\ [S_2] \\ \vdots \\ [S_{n_s}] \end{array} \right]}_{[S]} \{\Delta p\} \tag{6.9}$$

where $\{\Delta r\}$ is the global relative frequency difference vector and $[S]$ is the global sensitivity matrix. The parameter corrections $\{\Delta p\}$ are found by solving the system of equations (6.9) in a least-squares sense. The improved material parameters are obtained as

$$p^{(i+1)} = p^{(i)} \left(1 + \Delta p^{(i)}\right) \tag{6.10}$$

6.4.3. Constrained and Weighted Least-Squares

The sensitivity coefficients, from which the parameter corrections are derived, are based on a linearisation of the response surfaces of the considered finite element model, and are, therefore, only valid in the vicinity of the working point; in other words, they are only valid for small parameter corrections. Large parameter variations will not change the resonant frequencies as predicted and will, most likely, result in an unstable behaviour of the iterative procedure. Consequently, it is advisable to avoid large parameter corrections by using a constrained least-squares cost-function. Constraints that bound the parameter corrections during one iteration step to 25 % have proven to be sufficient to stabilise the iterative procedure. Note that these bounds do not really have a negative impact on the convergence rate, since they allow the parameters to double or to halve in three iteration steps.

In some cases, it is also advisable to use a weighted least-squares cost-function. Take the situation where the properties of a coating are identified from the

resonant frequencies of three samples. The first sample (sample 1) is a pure substrate, the other two samples (samples 2 and 3) are coated substrates.

One possible way to measure the properties is to identify them from the frequencies of sample 1 and 2, or from the frequencies of sample 1 and 3. Due to experimental errors and noise, these two sample sets result in slightly different properties. The average of the properties obtained from the two sample sets is usually taken as the final solution.

Alternatively, the elastic properties can be identified from the resonant frequencies of all three samples with a single identification procedure. The main advantage of this approach is the reduction of the computation time, i.e. there are only three FE-models in the iteration procedure instead of four ($= 2\times2$). However, the alternative approach has an undesired side effect. The two layer configurations, i.e. uncoated and coated, do not have the same importance. Since two out of three sample are coated, the coated layer configuration has a weight of $\frac{2}{3}$ instead of $\frac{1}{2}$. Furthermore, it is actually quite common to have more coated than uncoated samples, since the spread of the identified properties of the coating is usually much higher than the spread of the substrate properties. So, in most cases there is an imbalance between uncoated and coated layer configurations. Fortunately, this imbalance can easily be restored by using a weighted least-squares cost-function. If, in case of the considered example, the weighting factors are fixed at 2, 1 and 1, the two layer configurations are balanced and the alternative approach provides exactly the same result as the initial procedure but in a computationally more efficient way.

In fact, the alternative approach is a much more natural way of using the MNET procedures. Assume that there were three uncoated and six coated specimens. With the initial approach it would become very unclear which sample combinations should be used. Considering all eighteen possible combinations is very time consuming, since it requires the equivalent of thirty six FE-models. For the same test configuration, the alternative approach using weighted least-squares only requires nine FE-models, and is thus four times faster.

To summarise, the most efficient approach to identify the elastic properties is to define the cost-function using a weighted least-squares formulation, where the weighting coefficients are chosen in such a way that the different layer configurations are equally important, and solve it by imposing 25 % bounds on the parameter corrections.

6.5. Numerical Validation

The parameter identification algorithm of the considered MNET can be numerically validated with the following procedure: make the finite element models of the specimens of a particular sample set, compute the resonant frequencies of the samples using these finite element models, and identify the elastic material properties with the MNET routine using the computed frequencies as experimental frequencies. If the MNET routine is well conceived, the identified properties will equal the material properties of the FE-models used to generate the 'experimental' resonant frequencies.

Table 6.7: *The properties of the considered materials.*

	E_1	E_2	G_{12}	ν_{12}	ρ
Substrate	202	200	76	0.29	7800
Coating	60	60	25	0.20	3000
	[GPa]	[GPa]	[GPa]	[–]	kg/m^3

Consider a single-sided coated steel sheet, which is available in two layer configurations: 200 µm and 400 µm of coating. Both layer configurations use a substrate with a thickness of 1 mm. For every layer configuration, there is a sample at a 0°, 45°, and 90° orientation. Figure 6.18 provides an overview of the test sample set. Table 6.7 presents the material properties of both substrate and coating materials.

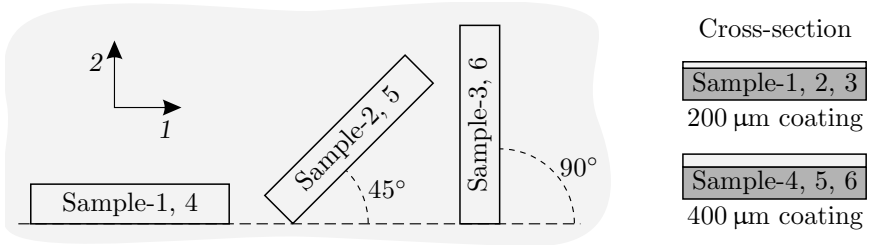

(a) The sample orientations (b) The configurations

Figure 6.18: *The considered sample set.*

The six specimens of the considered sample set are modelled, and the resonant frequencies of the fundamental flexural and torsional vibration mode are computed. Subsequently, the elastic parameters of both substrate and coating are identified from these resonant frequencies with the multi-orientation routine. The starting values of the elastic parameters are randomly chosen in such a way that no parameter differs more than 50 % of the correct value. Figure 6.19

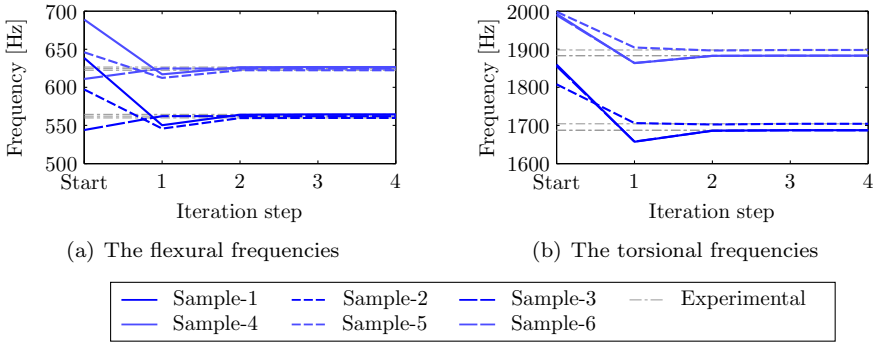

(a) The flexural frequencies (b) The torsional frequencies

Figure 6.19: *The convergence plots for the resonant frequencies.*

presents the numerical resonant frequencies for the different iterations steps. It can be seen that the resonant frequencies converge to the correct values in about three iterations steps.

Figure 6.20 presents the error in the elastic material parameters as a function of the iteration step. All eight material parameters converge in a quick and stable way to the correct values. The considered identification problem was also solved with different sets of starting values. For all these sets, the material parameters converged to the correct values in less than four iterations steps. The single-orientation routine and the plate-shaped specimen-based MNET routines were evaluated in a similar way. Both routines provided the correct material parameters.

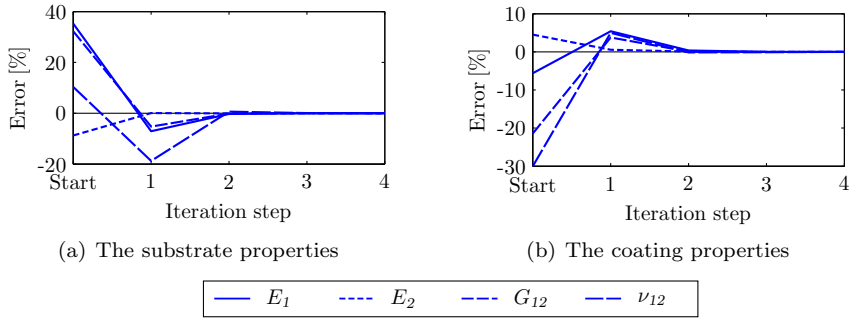

(a) The substrate properties (b) The coating properties

Figure 6.20: *The convergence plots for the elastic material properties.*

The numerical validation tests of the MNET routines for layered materials show that the routines provide the correct elastic parameters of the constituent layers, if a sufficient number of layers configurations is being used. All three MNET routines converge after a limited number of iteration steps.

6.6. Discussion, Conclusions and Overview

Table 6.8 gives an overview of the potential of the three identification routines introduced in the previous sections: the single-orientation routine using beam-shaped samples (SO), the multi-orientation routine that using beam-shaped samples (MO), and the routine based on plate-shaped samples (PS).

Table 6.8: *The potential of the three different MNET identification routines.*

Routine	Isotropic		Mildly orthotropic				Genuinely orthotropic			
	E	G	E_1	E_2	G_{12}	ν_{12}	E_1	E_2	G_{12}	ν_{12}
SO	✓	✓	✓	✗	✓	✗	✗	✗	✗	✗
MO	✓	✓	✓	✓	✓	✓	✓	✓	✓	✓
PS	✓	✓	✓	✓	✓	✓	✓	✓	✓	✓

✓ Can be identified.
✗ Cannot be identified.

Table 6.9: *Comparison of the three MNET identification routines.*

	SO	MO	PS
Isotropic materials	+	+	+
Orthotropic materials	−	+	+
Sample preparation	+	∘	+
Layer configurations	+	+	−
Robustness to curvature	+	+	−
Robustness to edge damage	∘	∘	+
Frequency measurements	+	∘	∘
High damping materials	+	+	∘
High temperature set-up	+	+	−
Computation time	+	∘	+

Table 6.9 compares the three considered MNET identification routines. The ratings provided by table 6.9 are based on the following observations and considerations:

- The SO routine has the major disadvantage that it cannot identify the properties of orthotropic materials.
- Both SO and PS routines identify the properties from a single sample, while the MO routine requires at least two samples with a different material orientation. This implies that the multi-orientation has a more elaborate sample preparation phase.
- It is relatively easy to produce the required layer configurations for beam-shaped samples. With plate-shaped specimens, this is much more complicated. First of all, plates with different layer configurations usually have a different optimal aspect ratio. Furthermore, it is also more complicated to add an additional glass layer to a plate-shaped specimen than to a beam-shaped specimen. Difficulties related to the sample preparation of plate-shaped specimens include the elimination of air bubbles in the glue layer or the formation of a glue layer with a uniform thickness.
- Appendix C shows that the resonant frequencies of plate-shaped samples are very sensitive to an out-of-plane deformation of the sample, while the resonant frequencies of beam-shaped samples are very robust to sample deformations. Since it is impossible to avoid an out-of-plane deformation of the substrate during a thermal coating process, the beam-shaped based routines are preferred for the identification of coating properties.
- Machining test specimens out of a material sample may damage the sample along its edges, especially in case of uni-directionally reinforced plastics or brittle materials. Plate-shaped samples have a higher surface to edge ratio than beam-shaped samples, hence the influence of the edge damage is smaller.
- Measuring the resonant frequency of the fundamental flexural and torsional mode of beam-shaped samples is fairly easy. Measuring the resonant frequency of the first five modes of a plate requires a more complicated

test set-up and a more experienced technician.

- In case of high damping materials, the degree of difficulty of measuring a resonant frequency increases with the order and complexity of the vibration mode. Therefore, it is more convenient to measure the fundamental flexural and torsional frequency of a number of beam-shaped specimens than the resonant frequencies of the first five vibration modes of a plate-shaped specimen.
- Measuring the resonant frequencies of a beam-shaped sample in a furnace at high temperature is feasible with commercially available equipment. Measuring the resonant frequencies of a plate-shaped sample at high temperature requires a highly complicated test set-up.
- Computing the resonant frequencies of a finite element model of a beam-shaped or plate-shaped sample with a converged mesh takes about the same amount of time. From a computational point of view, the multi-orientation routine is thus the slowest routine.

It is difficult to determine which routine is the best of the three, since the optimal technique varies from material to material. However, experience shows that the multi-orientation routine provides high quality results without an excessive amount of work or inconvenient experimental problems. The information of table 6.9 can be compiled into the following flowchart for selecting the optimal MNET routine in function of the testing conditions.

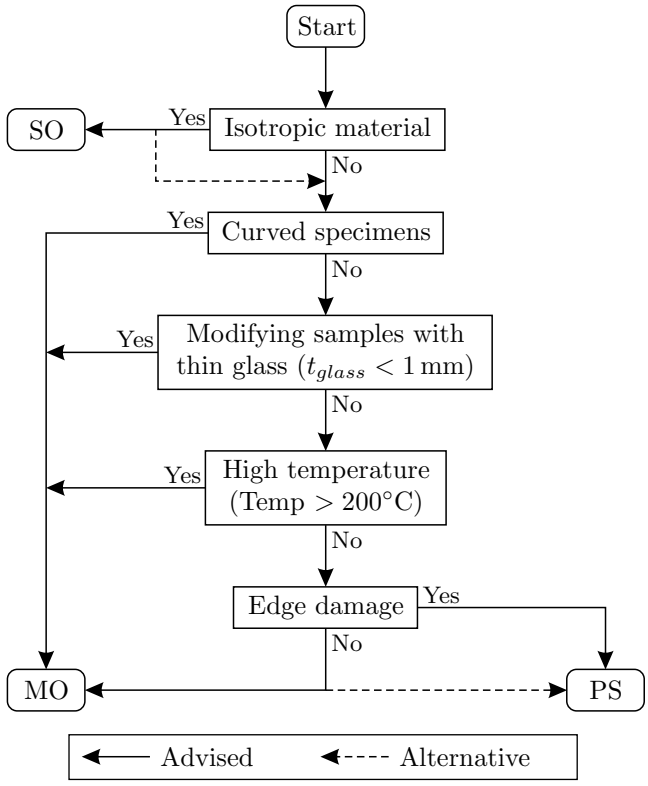

Figure 6.21: *Selection of the optimal MNET routine.*

6.7. Summary

This chapter provides an evaluation of the information contents of the resonant frequencies of the out-of-plane vibration modes of beam- and plate-shaped specimens. It is shown that a beam-shaped specimen only provides information about the apparent elastic and shear modulus in the direction of the sample's long-axis. However, a set of beam-shaped specimens, all having a different material orientation, or a plate-shaped specimen with a particular aspect ratio provide enough information to estimate the four principal in-plane material parameters of an orthotropic material. Using this knowledge, three vibration-based MNETs are presented: a routine that can identify the elastic properties of isotropic materials using beam-shaped specimens with the same material orientation, a routine that can identify the elastic properties of orthotropic materials using a set of beam-shaped specimens with a different material orientation, and a routine that identifies the elastic properties of orthotropic materials using plate-shaped specimens. All three routines can be implemented using the framework of a generalised vibration-based MNET procedure.

7
Uncertainty Analysis

A measured value of a physical parameter is not really meaningful, if it is not accompanied by a statement of its reliability or quality. Such a reliability statement should be based on technical and scientific knowledge, i.e. on objective facts. However, since a judgement is involved, a reliability statement will always remain subjective. General acceptance of such a quality judgement can only be achieved, if it is clearly stated in which way this judgement has been obtained. The aim of this chapter is to provide a transparent uncertainty analysis framework for the MNET-based material identification techniques presented in the previous chapter.

7.1. Essentials of Expressing Measurement Uncertainty

The Guide to the expression of Uncertainty in Measurement (GUM), published by ISO[1] [97], is a key document for evaluating the uncertainty of the output of a measurement system. The ISO guide is not a standard in the conventional sense. However, it has been accepted internationally as reference for the determination of the measurement uncertainty, and is also used as the foundation of standards dealing with metrological subjects.

7.1.1. Basic Definitions

ISO defines the uncertainty of a measurement as "a parameter associated with the result of a measurement that characterises the dispersion of the values that could reasonably be attributed to the measurand" [97]. This parameter can be a standard deviation, the width of a confidence interval[2], etc.

Figure 7.1 presents the definition of the standard uncertainty, i.e. the interval defined by one standard deviation. The GUM uses the standard uncertainty as the basic measure of uncertainty. The ISO guide provides a framework for computing the standard uncertainty of the measurand from the standard uncertainty of measured input quantities using the law of uncertainty propagation. This framework comprises the following four steps: specifying the measurands, identifying the uncertainty sources, quantifying the uncertainty components, and calculating the combined uncertainty.

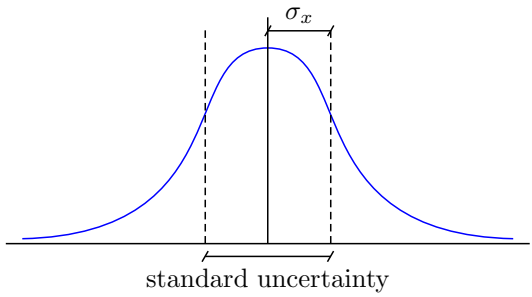

Figure 7.1: *Definition of the standard uncertainty.*

7.1.2. Step 1: Specifying the Measurands

In case of an indirect measurement, the measurands p_i are not measured directly but are derived from n_{in} other quantities q_1, q_2, ... , $q_{n_{in}}$ through a functional relation f_{p_i}, often called the measurement equation.

$$p_i = f_{p_i}(q_1, q_2, \ldots, q_{n_{in}}) \qquad \forall i = 1, \ldots, n_{out} \tag{7.1}$$

The GUM suggests to write down a clear statement of what is being measured,

[1] International Organisation for Standardisation (Geneva, Switzerland).

[2] A confidence interval is an interval in which a measurement corresponding to a given probability falls [97]. The considered probability is usually referred to as confidence level.

including the relationship between the measurand and the input quantities, i.e. the measurement equations.

7.1.3. Step 2: Identifying the Uncertainty Sources

The measurement equations of (7.1) express the physical law between the measurand and the input parameters. However, the equations used in the uncertainty analysis should represent the measurement process rather than a fundamental physical law [98]. The equations should contain all quantities that contribute a significant uncertainty to the measurement results. For example, in case of MNET procedures, the analysis should also consider the uncertainty introduced by the modelling errors associated with the FE-models of the test samples.
The GUM advises to identify all the contributing uncertainty sources and extend the measurement equations, if necessary.

7.1.4. Step 3: Quantifying the Uncertainty Components

The GUM distinguishes two different types of input parameters based on the way their uncertainty is evaluated: type-A and type-B. A type-A evaluation of standard uncertainty may be based on any valid statistical method for treating data, e.g. calculating the standard deviation of the mean of a series of independent observations. A type-B evaluation of standard uncertainty is usually based on scientific judgement using all of the relevant information available. This may include: previous measurement data, experience with the employed instruments, manufacturer's specifications, calibration data, and uncertainties assigned to reference data taken from handbooks.
The GUM requires a measure or estimate of the standard uncertainty associated with each potential uncertainty source.

7.1.5. Step 4: Calculating the Combined Uncertainty

The combined standard uncertainty of the measurand, $u_c(p_i)$, is calculated from the standard uncertainty of the uncertainty sources, $u(q_j)$, as

$$u_c(p_i) = \sqrt{\sum_j \left(s_{ij}\, u(q_j)\right)^2} \tag{7.2}$$

where s_{ij} is the sensitivity coefficient[3] of the measurand p_i with respect to the uncertainty source q_j. The GUM assumes the knowledge of distribution of the measurand p_i, since otherwise it is impossible to assign a confidence level to the standard uncertainty. If the measurand has a normal distribution, the standard uncertainty is associated with a confidence level of 68.3 %.

7.1.6. Expanded Uncertainty

The GUM also introduces the expanded uncertainty (u_e), and defines it as "the interval about the result of a measurement that may be expected to encompass

[3]The sensitivity coefficients in (7.2) are absolute sensitivities.

a large fraction of the distribution of values that could reasonably be attributed to the measurand". The expanded uncertainty is obtained by multiplying the combined uncertainty by a coverage factor (k), which is determined by the required level of confidence. For a normal distribution, the coverage factor and confidence level are related as [99]

$$P_{k\sigma} = \mathrm{erf}\left(\frac{k}{\sqrt{2}}\right) \quad \text{or} \quad k = \sqrt{2}\,\mathrm{erf}^{-1}(P_{k\sigma}) \tag{7.3}$$

in which $\mathrm{erf}(z)$ is the error function[4], and $P_{k\sigma} = P(\mu - k\sigma < x < \mu + k\sigma)$ is the probability that a measurement falls within k standard deviations σ of the mean μ. The first equation of (7.3) provides the confidence level of a given coverage factor, while the second equation provides the coverage factor corresponding to a particular confidence level. Note that for k = 1, $P_{k\sigma}$ represents the confidence associated with the standard uncertainty. Other commonly used coverage factors are 2 and 3, which correspond to confidence levels of 95.5 % and 99.7 %, respectively, in the case of a normal distribution.

7.2. The Uncertainty Sources

It is important to make a clear distinction between error and uncertainty. Error is defined as the difference between an individual result and the true value[5] of the measurand. As such, an error is a single value. In principle, the value of a known error can be applied as a correction to the result. Uncertainty, on the other hand, takes the form of a range that characterises the dispersion of the considered quantity. The value of the uncertainty cannot be used to correct a measurement result. Error and uncertainty are of course related, i.e. uncertainty is the result of errors with an unknown amplitude.

7.2.1. Measurement Errors

Roughly spoken, it is possible to classify each measurement error as one of the following three types: an illegitimate error, a systematic error, or a random error.

Illegitimate errors are mistakes and blunders caused by carelessness or poor judgement, e.g. misreading the display of the measurement device. Since illegitimate errors can be avoided, they are disregarded in the remainder of this text.

A systematic error can be defined as a reproducible error that biases the measured value in a given direction [98], i.e. a systematic overestimation or underestimation of the true value. A systematic error is by definition reproducible, it can, therefore, not be reduced by averaging the values of a large number of measurements. However, the reproducible character of the systematic error makes it possible to estimate the bias on the measured value by means of a calibration procedure. The systematic error can then be compensated with the estimated value of the bias. Note that systematic errors can only be reduced

[4] $\mathrm{erf}(z) = \frac{2}{\sqrt{\pi}} \int_0^z e^{-t^2}\, dt$

[5] The value that is consistent with the definition of a particular quantity [100].

by calibrating the measurement equipment, they cannot be avoided.

A random error causes fluctuations in the results of a measurement when the measurement is repeated a number of times [98]. Random errors are errors, which fluctuate from one measurement to the other. They yield results that are distributed about a mean value. Random errors occur for a variety of reasons, and are usually attributed to noise or other external disturbances that cannot be taken into account. Unlike systematic errors, random errors displace the measured value in an arbitrary direction. This stochastic behaviour allows the reduction of random errors by averaging the results of a large number of measurements.

7.2.2. Modelling Errors

The MNET procedures require a numerical model of the used test specimens. The assumptions made to build these models result in an error on the numerical frequencies, and eventually in an error on the identified material parameters.

The beam- and plate-shaped test specimens are assumed to have a uniform length, width, thickness, and mass density. But even for carefully machined samples, both length and width vary slightly along the edges, the thickness varies over the surface of the sample, and the mass density varies from point to point in the material. Furthermore, the elastic properties that have to be identified vary, to a certain extend, from point to point in the test sample. The assumption of a material with uniform elastic properties will thus also introduce a modelling error.

The importance of the error introduced by these assumptions was evaluated in detail in [101]. The evaluation indicated that a systematic error on the properties of the sample has a much larger impact on the resonant frequencies than a randomly distributed point-wise variation. The observed influence of the systematic error was a few orders of magnitude larger than the error resulting from the homogenisation of the sample proprieties. This implies that the modelling errors can be ignored, as long as the variation of the homogenised parameters is random.

The discretisation error of the finite element models also introduces an error on the numerical frequencies. Although the discretisation error is small, due to the use of converged finite element models, it should not be ignored.

7.2.3. Conclusions

The MNET procedures require the experimental values of the following quantities: length, width, thickness, mass and resonant frequencies of the samples. All these quantities can be accurately measured using a calliper, micrometer, balance, and digital frequency analyser. When the test specimens are carefully machined out of a uniform material sample, the spread of the measured quantities is much lower than the uncertainty of the offset of the measurement device. In this situation, it is advisable to use the accuracy of the measurement device as uncertainty of the measured quantities. In GUM terminology, this implies that all the input uncertainties are uncertainties of type-B.

7.3. First-Order Approximation of the MNET Equations

The application of the GUM method to evaluate the measurand uncertainty according to (7.2) requires the sensitivity coefficients of the measurands with respect to the measured input quantities. Since MNET procedures are numerical routines, it is impossible to obtain the sensitivity coefficients through analytical derivation. A direct numerical evaluation of the sensitivity coefficients, e.g. using a finite difference approach, would be very time consuming, since an MNET procedure contains one or more finite element models in its iteration loop. A more practical approach is to linearise the MNET using the solution of the last iteration step as working point. In that case, the derivation of the sensitivity coefficients is straightforward since the sensitivities are the coefficients of the linearised MNET equations.

7.3.1. Single-Model Routines

Linearising the response surfaces of the finite element model by computing the first-order Taylor approximation at the point defined by the model parameters provides relation (7.4). This equation describes the influence of a variation of the model parameters on the resonant frequencies of the test specimen. For convenience, the model parameters are divided into two groups: the elastic material parameters p, and the sample parameters s

$$\{\Delta f\} = [S_p]\{\Delta p\} + [S_s]\{\Delta s\} \tag{7.4}$$

in which vector $\{\Delta p\}$ contains the applied elastic parameter changes, vector $\{\Delta s\}$ contains the applied changes of the sample's length, width, thickness and mass, matrix $[S_p]$ groups the sensitivity coefficients of the resonant frequencies with respect to the elastic material parameters, matrix $[S_s]$ groups the sensitivity coefficients of the resonant frequencies with respect to geometry and mass, and vector $\{\Delta f\}$ provides the resulting frequency changes.

In general, the set of equations (7.4) is overdetermined and can, therefore, not be inverted in a direct way. In the MNET procedure, $\{\Delta p\}$ is obtained by considering a weighted least-square problem. The inverse of (7.4) can thus be expressed as

$$\{\Delta p\} = \Big([S_p]^{\mathrm{T}}[W][S_p]\Big)^{-1}[S_p]^{\mathrm{T}}[W]\Big(\{\Delta f\} - [S_s]\{\Delta s\}\Big) \tag{7.5}$$

$$= [S_p]^{\dagger_w}\Big(\{\Delta f\} - [S_s]\{\Delta s\}\Big) \tag{7.6}$$

$$= \underbrace{[S_p]^{\dagger_w}\{\Delta f\}}_{\substack{\text{frequency}\\ \text{contribution}}} \underbrace{-[S_p]^{\dagger_w}[S_s]\{\Delta s\}}_{\substack{\text{geometry \& mass}\\ \text{contribution}}} \tag{7.7}$$

Expression (7.7) allows the conversion of a variation of the resonant frequencies, sample geometry and mass into a variation of the obtained material parameters.

By grouping the terms of (7.7) as

$$[\chi] = \left[[S_p]^{\dagger_w} \quad -[S_p]^{\dagger_w} [S_s] \right] \tag{7.8}$$

$$\{\Delta q\} = \begin{Bmatrix} \{\Delta f\} \\ \{\Delta s\} \end{Bmatrix} \tag{7.9}$$

The influence of a change of the resonant frequencies and sample parameters on a particular elastic material parameter can be written as

$$\Delta p_i = \sum_j \chi_{ij} \, \Delta q_j \tag{7.10}$$

The χ matrix thus groups the sensitivity coefficients of the measurands p_i with respect to the input parameters q_j.

7.3.2. Multi-Model Routines

The first-order MNET approximation can easily be extended to multi-model identification routines. Consider a multi-model identification routine that uses resonant frequencies of n_s different test samples. The following set of equations can be written for each of the n_s models

$$\left\{\Delta f^{(k)}\right\} = \left[S_p^{(k)}\right] \{\Delta p\} + \left[S_s^{(k)}\right] \left\{\Delta s^{(k)}\right\} \qquad \forall k \in 1, \ldots, n_s \tag{7.11}$$

in which the superscript $\diamond^{(k)}$ indicates that a particular quantity of the k^{th} specimen is being considered. The equations of all the test samples can be combined into one global system of equations as

$$\left\{\Delta f^{glob}\right\} = \left[S_p^{glob}\right] \{\Delta p\} + \left[S_s^{glob}\right] \{\Delta s\} \tag{7.12}$$

where $\{\Delta f^{glob}\}$ and $\{\Delta s^{glob}\}$ are the global frequency and sample parameter difference vector, while the matrices $[S_p^{glob}]$ and $[S_s^{glob}]$ are the global sensitivity matrices for the material properties and sample parameters, respectively. $\{\Delta f^{glob}\}$ and $\{\Delta s^{glob}\}$ are both block vectors, where the k^{th} block line contains the data of the k^{th} specimen, or

$$\left\{\Delta f^{glob}\right\} = \begin{Bmatrix} \left\{\Delta f^{(1)}\right\} \\ \vdots \\ \left\{\Delta f^{(n_s)}\right\} \end{Bmatrix} \qquad \{\Delta s^{glob}\} = \begin{Bmatrix} \left\{s^{(1)}\right\} \\ \vdots \\ \left\{s^{(n_s)}\right\} \end{Bmatrix} \tag{7.13}$$

The matrices $[S_p^{glob}]$ and $[S_s^{glob}]$ are both block matrices and are defined as

$$\left[S_p^{glob}\right] = \begin{bmatrix} \left[S_p^{(1)}\right] \\ \vdots \\ \left[S_p^{(n_s)}\right] \end{bmatrix} \qquad [S_s^{glob}] = \begin{bmatrix} \left[S_s^{(1)}\right] \cdots & [0] \\ \vdots & \ddots & \vdots \\ [0] & \cdots \left[S_s^{(n_s)}\right] \end{bmatrix} \tag{7.14}$$

Expression (7.12) can be inverted in a similar way as equation (7.4). The inversion provides the changes in the elastic parameters as a function of the

resonant frequency and sample parameter changes as

$$\Delta p_i = \sum_j \chi_{ij}\, \Delta q_j \tag{7.15}$$

where $[\chi]$ and $\{\Delta q\}$ have the same structure as specified by (7.8) and (7.9), but are calculated using the global vectors and matrices as defined by (7.13) and (7.14).

7.3.3. Extending the Measurement Equations

The linearisation of the MNET equations provides

$$\{\Delta p\} = [S_p]^{\dagger_w} \Big(\{\Delta f\} - [S_s]\{\Delta s\} \Big) \tag{7.16}$$

This equation represents the physical relation between the input parameters and the measurands. As advised by the GUM, the measurement equations should be expanded in such a way that they include all the uncertainty sources. Equation (7.16) takes all the uncertainty related to the experimental errors into account, i.e. the uncertainty of the experimental frequencies, the sample dimensions, and the sample mass. However, there is also an uncertainty of the numerical frequencies due to the discretisation error. To take this additional uncertainty source into account, the measurement equations have to be extended as

$$\{\Delta p\} = [S_p]^{\dagger_w} \Big(\{\Delta f_{exp}\} + \{\Delta f_{num}\} - [S_s]\{\Delta s\} \Big) \tag{7.17}$$

7.4. The Probabilistic Approach

Traditionally, the uncertainty of measured quantities is characterised by means of probability distributions and confidence intervals. The probabilistic approach aims at estimating the confidence intervals of the identified material parameters from the probability distributions of the measured quantities.

7.4.1. Verification of the Analytical Approach

The GUM suggests to evaluate the measurand uncertainties with expression (7.2). The UNCERT code of practice 13 [102] presents a GUM compliant framework to handle uncertainties in the material identification procedures described in the ASTM[6] and CEN[7] standards. Remember that the application of the GUM requires the type of the distribution of the measurand values. The UNCERT code of practice assumes that all the input and output parameters are normally distributed. However, it does not present any justification for the assumption of normally distributed measurand values, therefore, this assumption has to be verified.

Monte Carlo simulations provide an alternative approach to evaluate uncer-

[6] The routines of the ASTM standard are presented in appendix [4].

[7] Comité Européen de Normalisation: prEN 14146, Determination of dynamic elastic modulus by measuring the fundamental resonant frequency, European norm under approval.

tainty, and are useful for validating the results produced by the application of the GUM [103]. By propagating the distributions rather than just the uncertainty of the inputs q_j through the measurement model, Monte Carlo simulations provide much richer information. The simulations produce the distribution of the outputs p_i, which can then be used to determine the confidence intervals, or other statistical information. If no agreement with GUM results is observed, "it is appropriate to regard the Monte Carlo results as being scientifically more sound" [103].
To verify the procedure proposed in the UNCERT Code of practice [102], the obtained results are validated with a Monte Carlo simulation, and this for one particular test case. Consider the identification of the elastic and shear moduli of the steel beam described in table 7.1 with the ASTM procedure. The two elastic moduli are identified from the beam's fundamental flexural and torsional frequency using formulas (A.1) and (A.3). The plots of figure 7.2 show the histograms of the output distributions of the Monte Carlo simulation. The assumption of a normal probability distribution of E and G is obviously incorrect.

Table 7.1: *The properties of the considered steel beam.*

l [mm]	w [mm]	t [mm]	m [g]	f_f [Hz]	f_t [Hz]
100.00	20.00	1.500	23.400	797.47	2367.66
±0.02	±0.01	±0.003	±0.001	±0.80	±2.37

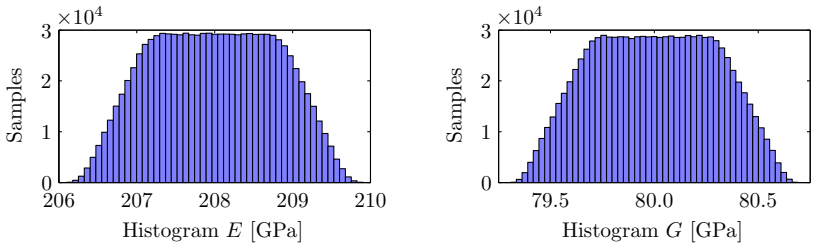

Figure 7.2: *Histograms of the Monte Carlo output distributions for E and G.*

Figure 7.3 compares the confidence intervals obtained using the method proposed by the UNCERT code of practice with the intervals obtained using Monte Carlo simulations. The code of practice approach appears to underestimate the interval bounds for confidence levels lower than 90 %. For confidence levels higher than 90 %, the code of practice procedure overestimates the interval bounds. These problems are caused by the erroneous assumption that the measurand values are normally distributed. Because of this, there is no justification behind the assumption that the standard uncertainty obtained with (7.2) is associated with a confidence level of 68.3 %.
Table 7.2 presents the numerical results for the standard and expanded uncer-

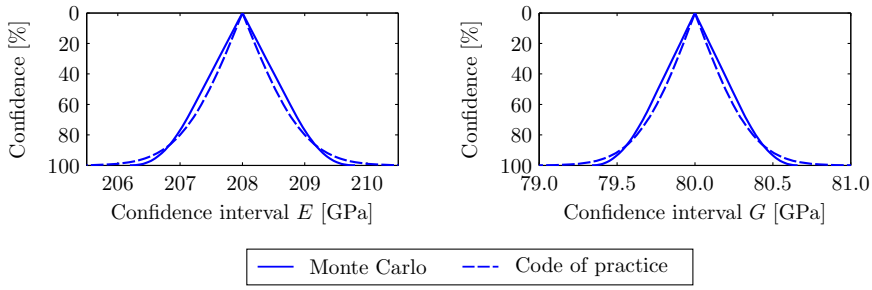

Figure 7.3: *Comparison between the confidence intervals obtained with the analytical and the Monte Carlo approach.*

tainty. For these two confidence levels, the difference between the two methods is about 10 % for both E- and G-modulus. Note that Monte Carlo simulations of other test cases reveal measurand probability distributions that differ from the distributions of figure 7.2. It is thus impossible to make an a priori statement about the probability distribution of the identified parameters.

Table 7.2: *Comparison of the confidence intervals of the measurands estimated with the code of practice (CoP) and Monte Carlo (MC).*

	Width confidence interval of E		
	MC [GPa]	CoP [GPa]	Diff. [%]
u_s(68.3 %)	1.74	1.54	13.0
u_e(95.5 %)	2.80	3.06	−8.5

	Width confidence interval of G		
	MC [GPa]	CoP [GPa]	Diff. [%]
u_s(68.3 %)	0.64	0.58	10.3
u_e(95.5 %)	1.04	1.18	−11.9

7.4.2. Estimation of the Confidence Intervals

The procedure proposed in the code of practice [102] requires the knowledge of the probability distribution of obtained material parameters. Simulations have shown that this distribution varies from case to case. Simply assuming that the measurand values are normally distributed results in significant errors on the bounds of the confidence intervals. Furthermore, in the case of layered materials, the input uncertainties are no longer uncorrelated, implying that (7.2) is no longer valid. Extending (7.2) to correlated uncertainties is possible, but complicated. However, correlated input uncertainties do not pose any serious problems with the Monte Carlo approach. Because there is a computationally efficient linear approximation of the MNET procedure available, it makes more sense to estimate the confidence intervals with Monte Carlo simulations than with an extended version of expression (7.2).

Non-Layered Materials

A Monte Carlo simulation requires a sequence of input values for every input parameter. Because the uncertainty of the input parameters is mainly determined by the accuracy of the measurement device[8], the input parameters are assumed to have a uniform probability distribution between their upper and lower bound. The first step consists of creating a sequence of Δq_j values for every input parameter, using a random number generator configured to produce a uniformly distributed set of test values that respects the upper and lower bounds imposed on the considered parameter. The input distortion sequences are then fed into the extended MNET equations (7.17), which provide the output parameter distortion sequences $V_{\Delta p_i}$. The easiest way to find the confidence intervals is to sort the elements of $V_{\Delta p_i}$ in ascending order. For the example discussed in the previous section, this results in the plot of figure 7.4.

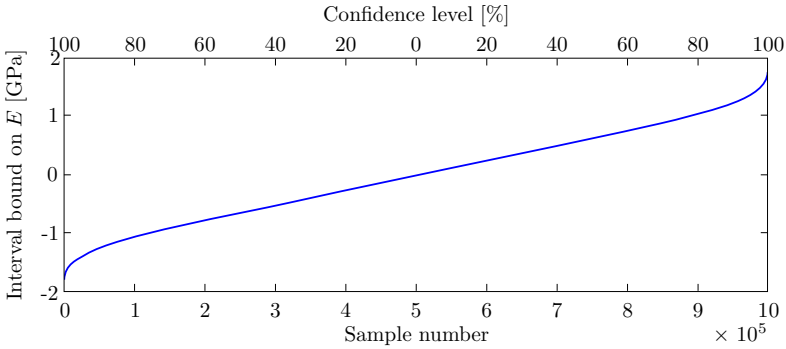

Figure 7.4: *The sorted E-modulus distortions $V_{\Delta E}$.*

The confidence interval for a confidence level α can now easily be found by taking the first $\frac{\alpha}{2}$ % samples on the left and right side of the mean value. For example, in case of figure 7.4, there are one million Monte Carlo samples. The sample with a value closest to the mean value is sample 499976. This implies that the confidence interval of 80 % is bounded by the values of samples 99976 ($= 499976 - 400000$) and 899976 ($= 499976 + 400000$).

Layered Materials

In case of layered materials, not all the input uncertainties are uncorrelated. The uncertainties of the layer thicknesses are not independent, since the sum of all the layer thicknesses must equal the total sample thickness.
The uncertainties of the length, width, mass and resonant frequencies are still uncorrelated, and the Monte Carlo sample sequences can be generated as described in the previous section. The sequence of the layer thickness values is generated in a slightly different way. For each layer, a thickness distortion value is generated using a random number generator configured to produce uniformly distributed numbers. All the layer thickness distortions are added

[8] As explained in section 7.2.

to get the distortion on total sample thickness. If the total sample thickness distortion complies with the imposed bounds, the thickness value set is added to the Monte Carlo sequence, otherwise the thickness value set is rejected. This process is to be repeated until a sequence with the required length is obtained. Like in the case of non-layered materials, the Monte Carlo sequences are processed by feeding them into the extended MNET equations (7.17). The confidence intervals are derived from the output sequences as described in the previous section.

7.5. The Non-Probabilistic Approach

The uncertainty of the input parameters of the MNET routine is mainly determined by the accuracy of the measurement device used to measure the considered input quantity. The accuracy of the measurement device defines an upper and lower bound of the value of the input parameter, it does not provide the probability distribution of the input parameters.
The probabilistic approach that was presented in the previous section requires the probability distribution of the input parameters of the MNET routine. As explained, this information is not available. In the probabilistic approach, this problem is overcome in a pragmatic way by assuming a uniform distribution of the input parameters. An alternative solution is to consider a non-probabilistic approach. Non-probabilistic methods aim at estimating the uncertainty of the output parameters without using the probability distributions of the input parameters.

7.5.1. Uncertainty Intervals

An uncertainty interval defines an upper and lower bound between which the value of the considered parameter can vary. It does not provide any information about the probability distribution of the values between the upper and lower bound. The following notation is used to represent an uncertainty interval

$$q_j \in [\underline{q}_j, \overline{q}_j] \qquad \forall j = 1, \ldots, n_{in} \tag{7.18}$$

where q_j is one of the n_{in} uncertain input parameters of the model, and can take any value larger than or equal to $\underline{q}_j$ and smaller than or equal to $\overline{q}_j$. By considering the relations between the input and output parameters f_{p_i}

$$p_i = f_{p_i}(q_1, q_2, \ldots, q_{n_{in}}) \qquad \forall i = 1, \ldots, n_{out} \tag{7.19}$$

the input intervals can be used to derive the uncertainty intervals of the output parameters p_i.

$$p_i \in [\underline{p}_i, \overline{p}_i] \qquad \forall i = 1, \ldots, n_{out} \tag{7.20}$$

The lower bound $\underline{p}_i$ of this interval is the lowest possible value that can be obtained for the output parameter p_i, when all the input parameters q_j can take any value between $\underline{q}_j$ and $\overline{q}_j$. The upper bound $\overline{p}_i$ represents the highest possible value that can be obtained for the output parameter p_i. The bounds

of the output intervals can be interpreted as worst-case values.

7.5.2. Interval Calculations

The most straightforward way to perform calculations with intervals is to redefine the standard mathematical operators like additions, subtractions, multiplications, and divisions in such a way that they can handle intervals instead of the traditional integers or floats. This approach is generally referred to as the interval arithmetic approach, and is mainly based on the work of Moore [104]. The interval arithmetic approach has two major drawbacks. The first drawback deals with the practical problem of implementation. The use of the interval arithmetic concept to estimate the uncertainties of the material parameters implies that the whole identification procedure, i.e. finite element routines, sensitivity analysis and cost-function minimisation, has to be reimplemented using interval operations. The second drawback is a phenomenon that is called conservatism, and can be illustrated with the following example: consider a variable x that varies between 0 and 1, and calculate the interval of the variable y if $y = x^2 - x$. The application of the interval arithmetic approach results in the following solution: $y \in [-1, 1]$. However, the correct solution to this problem is $y \in [-0.25, 0]$ and can only be obtained, if the correlation between x and x^2 is taken into account. This simple example clearly indicates that ignoring existing variable correlations yields erroneous results. More details about the presented example, together with an extensive discussion on the conservatism induced by interval arithmetics can be found in [105]. So far, it has not been investigated whether it is possible to keep track of the existing correlations between the variables of complex numerical procedures. With the current state of affairs, it is not possible to avoid conservatism in complex routines like finite element solvers. Therefore, the use of interval arithmetics should not be considered to handle uncertainties in MNET-based identification routines.

An alternative way to solve the interval arithmetical problem, is to reformulate it as a constrained optimisation problem where the input variables q_j are the optimisation parameters, and the input-output relation is the cost-function. The upper bound of the uncertainty interval of a particular output parameter p_i can be found by maximising the cost-function, i.e. the value of the output parameter p_i, while considering the bounds of the uncertainty intervals of the input parameters as constraints on the optimisation parameters.

$$\begin{aligned} \overline{p}_i \rightarrow \text{maximise} \quad & f_{p_i}(q_1, \ldots, q_{n_{in}}) \\ \text{subject to} \quad & q_j \geqslant \underline{q}_j \qquad \forall j = 1, \ldots, n_{in} \\ & q_j \leqslant \overline{q}_j \qquad \forall j = 1, \ldots, n_{in} \end{aligned} \tag{7.21}$$

The lower bound of the uncertainty interval can be found by minimising the cost-function, using the same constraints on the optimisation parameters. Now, consider an n_{in} dimensional space, of which each point defines a unique set of values for the various input parameters. In this input parameter space, the constraints of (7.21) define an n_{in}-dimensional hypervolume. Only the points inside this hypervolume are valid points, i.e. points associated with parameter

values that comply to the considered parameter intervals. One of the commonly used approaches in solving the optimisation problem (7.21) is to sample the hypervolume defined by the input parameter intervals, and to calculate the values of the output parameters for every sample. The highest and lowest value obtained for a particular output parameter defines the upper and lower bound of the uncertainty interval of this parameter. Figure 7.5 presents a two dimensional example. A general implementation of this approach was proposed by Hanss [106, 107] and is called 'the standard transformation method'. The procedure is applicable to a wide variety of problems, but has a number of important shortcomings. The total number of sampling points that has to be evaluated equals $m^{n_{in}}$, where m represents the number of sampling points used to sample one uncertainty interval, e.g. m equals 8 in case of figure 7.5. With the standard method, the total number of sampling points, and thus the necessary computation time, increases exponentially with the number of input parameters. A second drawback is that the obtained results are only approximations of the true intervals, unless both minimum and maximum of the cost-function happen to coincide with a sampling point. In the example of figure 7.5, the true maximum of the cost-function is found, but the obtained minimum is an approximation. The accuracy of the solution can only be improved by decreasing the sampling distance, which leads to an exponential increase in sampling points. A small improvement of the accuracy is, therefore, associated with a dramatic increase of the required computation time.

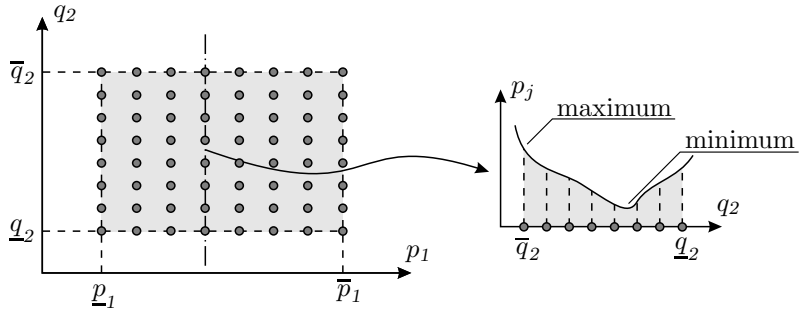

Figure 7.5: *A two-dimensional example of the standard transformation method.*

These two drawbacks are absent when the relations between the input and output parameters f_{p_j} are monotonic functions, as shown in figure 7.6. In case of monotonic input-output relations, the extreme values of the output parameters have to lay in points where the different input parameters are maximal or minimal. This means that only the sampling points located on the vertices of the hypervolume have to be considered; all the other sampling points may be ignored, since they cannot lead to an extreme value of any of the output parameters. Monotonicity of the input-output relations thus reduces the number of sampling points that must be evaluated down to $2^{n_{in}}$. Monotonicity also guarantees the exactness of the obtained interval bounds, since the extreme values of the cost-function are achieved in the locations of the sampling points. The

procedure that only considers the vertex points is called 'the reduced transformation method'.

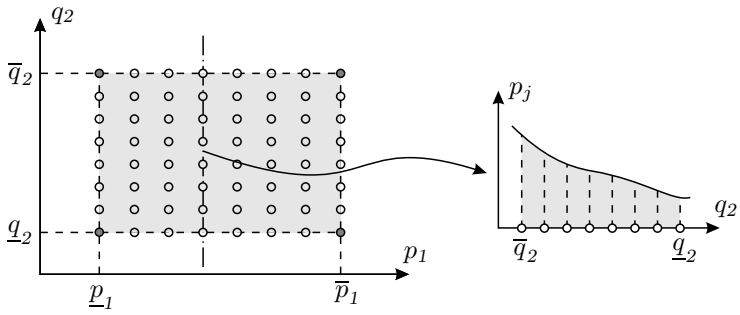

Figure 7.6: *A two-dimensional example of the reduced transformation method.*

7.5.3. Computing the Uncertainty Intervals

In case of MNET identification procedures, even the application of the reduced transformation method requires an extensive computational effort. Consider a multi-orientation procedure using three beam-shaped specimens. Such a routine has eighteen input parameters. The application of the reduced transformation method requires $2^{18} = 262144$ runs of the identification procedure. Even with a computer platform that could run the whole identification procedure in one second, the uncertainty analysis would take about 3 days. However, the use of the linear approximation of the MNET procedure provides a dramatic reduction of the computation cost. Also note that the use of the linearised MNET automatically ensures the monotonicity of the input-output relations.

Non-Layered Materials

By linearising the MNET equations, the variation of the measurand p_i caused by the variation of the input parameters q_j can be expressed as

$$\Delta p_i = \sum_j \chi_{ij}\, \Delta q_j \tag{7.22}$$

To obtain the bounds of the uncertainty interval of the material property p_i, the maximum and minimum of Δp_i have to be calculated. To maximise Δp_i, the contributions of the different summation terms $\chi_{ij}\Delta q_j \left(= \Delta p_{i_j}\right)$ have to be maximised. To express the maximum value of Δp_{i_j} in function of the input uncertainties, two different cases have to be considered. In the case where χ_{ij} is non-negative, the maximum of the contribution of the input parameter q_j is given by

$$\max\ \Delta p_{i_j} = \chi_{ij}\, \Delta \overline{q}_j \tag{7.23}$$

where $\Delta \overline{q}_j$ is the upper bound of the uncertainty interval of q_j. When χ_{ij} is negative, the maximum of the contribution to p_i is given by

$$\max\ \Delta p_{i_j} = \chi_{ij}\ \Delta \underline{q}_j = |\chi_{ij}|\ \Delta \overline{q}_j \tag{7.24}$$

where $\Delta \underline{q}_j$ is the lower bound of the uncertainty interval of q_j. The second equality of equation (7.24) is valid, since the uncertainty intervals of the input parameters are assumed to be symmetrical, i.e. $\Delta \overline{q}_j = -\Delta \underline{q}_j$. The combination of (7.23) and (7.24) provides the following expression of the maximum of Δp_i.

$$\max\ \Delta p_i = \sum_{j=1}^{n_{in}} |\chi_{ij}|\ \Delta \overline{q}_j \tag{7.25}$$

The expression for the minimum of Δp_i can be derived in a similar way. Elaboration of the problem shows that

$$\min\ \Delta p_i = \sum_{j=1}^{n_{in}} |\chi_{ij}|\ \Delta \underline{q}_j = -\max\ \Delta p_i \tag{7.26}$$

which implies that the uncertainty intervals of the identified material properties are also symmetric. Also note that the relative importance of the uncertainty of a particular input parameter q_j in the total uncertainty of the material property p_i can be expressed as

$$\frac{|\chi_{ij}|\ \Delta \overline{q}_j}{\sum\limits_{k=1}^{n_{in}} |\chi_{ik}|\ \Delta \overline{q}_k} \tag{7.27}$$

Equation (7.27) allows the identification of the principal sources of uncertainty of a particular material parameter.

Layered Materials

As explained in section 7.4.2, the uncertainties of the layer thicknesses are correlated. As in the probabilistic approach, this correlation requires an adaptation of the uncertainty analysis routine.

The routine that was introduced for non-layered materials uses only sampling points on the vertices, i.e. the upper and lower bounds of the input parameters, and is, therefore, a clear application of the reduced transformation method. The correlation of the layer thickness uncertainties has two important consequences for the computation of the uncertainty bounds: first, every considered combination of input parameters has to be checked with respect to whether it violates any of the input parameter relations. Moreover, there is no longer any guarantee that the worst-case parameter combination is situated on one of the vertices of the parameter space. This implies that the uncertainty intervals should be computed with the standard transformation method.

The optimal approach is to divide the uncertainty analysis into two steps. During the first step, only the length, width, mass, and resonant frequencies are considered. Since the uncertainties of these parameters are still uncorrelated, the overall uncertainty they introduce can be evaluated with the method presented in the previous section. The second phase computes the uncertainty

introduced by the layer thicknesses. This can be done by sampling the uncertainty intervals of the layer thicknesses. All the obtained layer thickness combinations have to be checked to see whether they are feasible or not, i.e. whether their sum lays within the uncertainty bounds of the total thickness, and the infeasible sets have to be rejected. The feasible sets of layer thicknesses are processed with the linearised MNET equations to find the associated material parameters. The uncertainty contribution of the layer thicknesses is found as the minimum and maximum of the obtained material parameters.
Eventually, the total uncertainty is obtained by adding up these two uncertainty contributions. Note that the obtained uncertainty intervals are only an approximation of the true uncertainty. The accuracy of the obtained intervals depends on the sampling density of the layer thicknesses.

7.6. Examples

7.6.1. Comparison of the Probabilistic and Non-Probabilistic Approach

The goal of this first example is to compare the results of the probabilistic approach with the results of the non-probabilistic approach. Consider a brass[9] plate with the following dimensions: $100\times100\times1$ mm. The material properties are determined from the first five resonant frequencies of the test plate, using the routine of section 6.2.2. Table 7.3 provides the uncertainty of the input parameters.

Table 7.3: *The values and uncertainties of the input parameters.*

	Value	Units	Uncertainty interval			Bounds	Units
Length	100.00	[mm]	99.98	—	100.02	± 0.02	[mm]
Width	100.00	[mm]	99.98	—	100.02	± 0.02	[mm]
Thickness	1.000	[mm]	0.998	—	1.002	± 0.002	[mm]
Mass	82.000	[g]	81.999	—	82.001	± 0.001	[g]
Freq-1	225.71	[Hz]	225.26	—	226.16	± 0.2	[%]
Freq-2	330.49	[Hz]	329.83	—	331.15	± 0.2	[%]
Freq-3	427.37	[Hz]	426.52	—	428.23	± 0.2	[%]
Freq-4	587.01	[Hz]	585.83	—	588.18	± 0.2	[%]
Freq-5	592.32	[Hz]	591.13	—	593.50	± 0.2	[%]

The plots of figure 7.7 present the uncertainty and confidence intervals of the material parameters. The confidence intervals are calculated using 10^6 Monte Carlo samples. To avoid overloading the plots, figure 7.7 presents only the first 1000 Monte Carlo samples. The results clearly show that all the Monte Carlo samples are situated within the uncertainty intervals, which is strictly necessary since the uncertainty interval bounds represent the worst-case values. The probability to obtain one of the worst-case values is extremely low, but not zero.
Table 7.4 shows the relative contributions of the input parameters to the uncertainty of the output parameters as obtained with expression (7.27). The

[9]The brass properties are given in table 6.1.

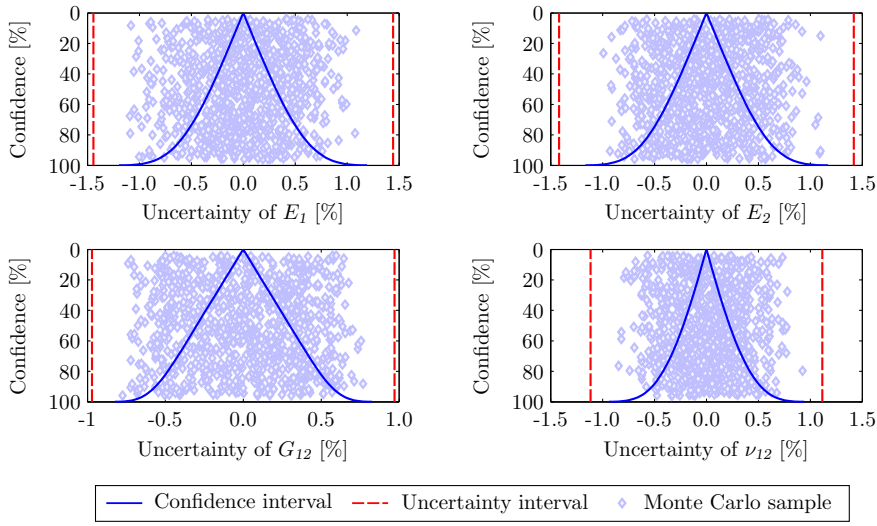

Figure 7.7: *The uncertainty and confidence intervals of the material parameters.*

uncertainty of the two Young's moduli and the shear modulus is dominated by the thickness uncertainty, which implies that an accurate determination of the thickness is necessary to obtain reliable material properties. The uncertainty of Poisson's ratio is mainly controlled by the uncertainty of the resonant frequencies. The uncertainty of both specimen thickness and mass does practically not influence the uncertainty of Poisson's ratio. This observation can be explained as follows: the change of the thickness or the mass has the same effect on all the resonant frequencies of the test plate, which means that there is no effect on the relative difference between the resonant frequencies. Since Poisson's ratio is not controlled by the absolute values of the resonant frequencies but by the relative difference between the various frequencies [5], the uncertainty of the mass or thickness does not affect the uncertainty of Poisson's ratio. Note that this conclusion is only valid for plate-shaped specimens, in the case of beam-shaped specimens the uncertainty on the thickness will influence the uncertainty of identified Poisson's ratio.

Table 7.4: *The relative contributions of the various input parameters to the uncertainties of material properties.*

Prop.	Input parameters									Units
	f_1	f_2	f_3	f_4	f_5	l	w	t	m	
E_1	2.1	9.4	2.8	**17.5**	**21.2**	4.1	1.3	**41.5**	0.1	[%]
E_2	1.8	10.3	3.1	**19.7**	**17.2**	1.5	4.3	**42.1**	0.1	[%]
G_{12}	13.7	3.1	3.6	6.9	6.8	2.0	2.1	**61.7**	0.1	[%]
ν_{12}	0.4	**30.7**	**31.2**	**15.8**	14.9	3.5	3.5	0.1	0.0	[%]
Mean	4.5	13.4	10.2	**15.0**	**15.0**	2.8	2.8	**36.3**	0.1	[%]

The material properties can also be derived from the resonant frequencies of more than one test plate. Figure 7.8 shows the uncertainties obtained for E_1 using one, two, three, and four test plates. The two uncertainty approaches react in a completely different way. Increasing the number of test samples leads to narrower confidence intervals, while the uncertainty intervals remain constant. By using a higher number of test samples, the number of input parameters changes and the chance that a worst-case value is obtained decreases. However, the worst-case values themselves do not depend on the used number of samples.

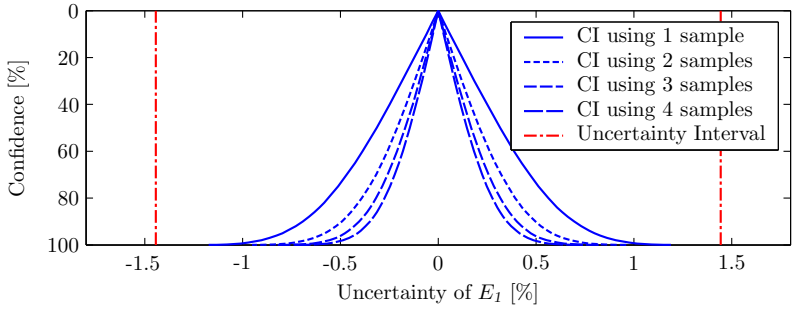

Figure 7.8: *The influence of the size of the test sample set.*

The comparison between the two uncertainty approaches leads to the conclusion that each approach has its own field of application. The probabilistic approach is the optimal approach to estimate the uncertainties of the material properties of an actual experiment, because the reliability of the obtained parameters increases with an increase of the number of used samples. Furthermore, probability and confidence intervals are concepts that are widely accepted in the world of experimental testing. On the other hand, it is advisable to use the non-probabilistic approach for determining the optimal configuration of the experiment. The uncertainty intervals that are provided by the non-probabilistic approach are independent of the number of used samples. This is an essential quality of a method that is used to compare different test configurations. Consider two multi-orientation routines, the first one uses test beams of three material directions, the second one uses test beams of six material directions. Assume that the probabilistic approach would be used to compare these two test configurations. The confidence intervals of the second test configuration would be narrower than those of the first configuration, simply because the second test averages the results of six samples instead of three. The correct way to compare the two methods with the probabilistic approach is to use two samples in each direction for the first test. In this way, both tests use the same number of samples. The non-probabilistic approach, of which the results are independent of the number of samples, is clearly better suited to compare the quality of different test configurations. Also remember that the non-probabilistic approach can provide the contributions of the input parameters to the output uncertainties in a computationally efficient way, which means the principal uncertainty sources can be easily identified. This information can then serve as a

starting point to improve the quality of the considered test configuration.
To summarise, the probabilistic approach should be used to estimate the reliability of the measured material parameters, while the non-probabilistic approach is the optimal approach to evaluate the quality of a particular test configuration.

7.6.2. Validation of the Linear MNET Approximation

Consider the same test procedure as in the previous example. The signs of the χ coefficients (7.8) indicate which parameter combination provides the worst-case values. For example, the minimal value of E_1 is obtained for maximum thickness, second, third, and fifth resonant frequency, in combination with a minimum length, width, mass, the first and fourth resonant frequency. The lower bounds on the material parameters were computed with both the full MNET routine and the linear approximation. Table 7.5 presents the results.

Table 7.5: *Comparison of the lower worst-case values.*

	Approx.	MNET	Error
E_x	103.48	103.49	$-0.010\,\%$
E_y	98.58	98.59	$-0.012\,\%$
G_{xy}	37.63	37.63	$-0.005\,\%$
ν_{xy}	0.3560	0.3558	$0.042\,\%$

It is clear that the linearised MNET equations provide a very accurate estimate of the material parameters. Note that the comparison is performed for a worst-case value. The approximation is even more accurate for the Monte Carlo samples, which are located inside the uncertainty intervals.
A final remark; figure 7.7 might give the impression that the bounds provided by the non-probabilistic approach are an overestimation of the actual worst-case values. The fact that there are no Monte Carlo samples in the vicinity of the interval bounds is only due to the low probability of ending up in this region. Table 7.5 proves that it is possible to reach the bounds of the uncertainty intervals.

7.6.3. Optimal Sample Orientations for the MO Routine

The multi-orientation identification routine requires a number of beam-shaped samples with a different material orientation. The number of sample orientations and the frequencies[10] used for each test sample are design parameters of the test configuration with an important influence on the quality of the obtained results. For optimal results, the test configuration has to be optimised with a pre-test analysis.
Traditionally, the quality of an inverse problem is checked by calculating the condition number of the sensitivity matrix. Table 7.6 presents the sensitivity

[10]The fundamental flexural and/or fundamental torsional resonant frequency.

matrix condition number of thirteen different sample/frequency combinations, for a sample set that comprises the five brass beams of figure 6.9. The condition number of the set that uses the fundamental flexural and torsional frequency of all the beams equals 5.4, which clearly indicates that this data set provides enough information to identify the material parameters. However, table 7.6 indicates that there are smaller sample sets that also provide the necessary information.

Table 7.6: *Sensitivity matrix condition numbers for a number of sample/frequency sets.*

Set	0.0°		22.5°		45.0°		67.5°		90.0°		Cond. Num.
	f_f	f_t	f_f	f_t	f_f	f_t	f_f	f_t	f_f	f_t	
1	⋆	⋆	⋆	⋆	⋆	⋆	⋆	⋆	⋆	⋆	5.4
2	⋆	–	⋆	–	⋆	–	⋆	–	⋆	–	$3.0{\cdot}10^5$
3	–	⋆	–	⋆	–	⋆	–	⋆	–	⋆	$2.9{\cdot}10^4$
4	⋆	⋆	–	–	⋆	⋆	–	–	⋆	⋆	5.7
5	⋆	⋆	–	–	⋆	⋆	–	–	–	–	5.0
6	–	–	–	–	⋆	⋆	–	–	⋆	⋆	8.3
7	⋆	⋆	⋆	⋆	–	–	–	–	–	–	18.9
8	–	–	⋆	⋆	⋆	⋆	–	–	–	–	7.5
9	–	–	–	–	⋆	⋆	⋆	⋆	–	–	11.7
10	–	–	–	–	–	–	⋆	⋆	⋆	⋆	32.5
11	⋆	⋆	–	–	–	–	–	–	⋆	⋆	$5.0{\cdot}10^4$
12	–	–	⋆	⋆	⋆	⋆	⋆	⋆	–	–	5.4
13	⋆	–	–	⋆	⋆	–	–	⋆	⋆	–	5.3

The sensitivity matrix condition number evaluates the relations between the input and output parameters without taking the uncertainty of the input parameters into account. The condition number, therefore, quantifies only the quality of the inverse problem, it does not evaluate the quality of the test procedure. A genuine uncertainty analysis does not only consider the input uncertainties, it also allows to compare two test configurations in a more physical way, i.e. comparing the uncertainties of the identified parameters.
The following input uncertainties are used to derive the output uncertainties: length and width ±0.02 mm, thickness ±1 µm, mass ±0.001 g and resonant frequencies ±0.05 %. The obtained results are shown in the plots of figure 7.9. Note that all the sets that have a sensitivity matrix condition number larger than 10 were rejected, so only sets 1, 4, 5, 6, 8, 12 and 13 were retained for further investigation. Figure 7.9 indicates that the smallest overall uncertainties are obtained for sets 1 and 4. Set 1 uses the flexural and torsional frequencies of all five beams, set 4 just uses the frequencies of the 0°, 45° and 90° beams. Apparently, omitting the frequencies of the 22.5° and 67.5° beams does not really affect the uncertainty of the material parameters. Although set 5 has a lower sensitivity matrix condition number than sets 1 and 4, it does not yield better results, especially the uncertainty of E_2 is too high. However, in general,

high condition numbers lead to larger uncertainty intervals, e.g. sets 6 and 8. The identification set-up that uses only one frequency per sample, i.e. set 13, yields excellent results for E_1 and E_2, but the uncertainty intervals of G_{12} and ν_{12} are about two times as wide as the uncertainty intervals obtained with sets 1 and 4. Consequently, in a one-frequency-per-beam situation, it is preferable to measure the shear modulus or Poisson's ratio by measuring the fundamental flexural and torsional frequencies of two separate beams in the 0°, 45° and 90° direction, i.e. measuring the frequency information of set 4, than using the test scheme of set 13.

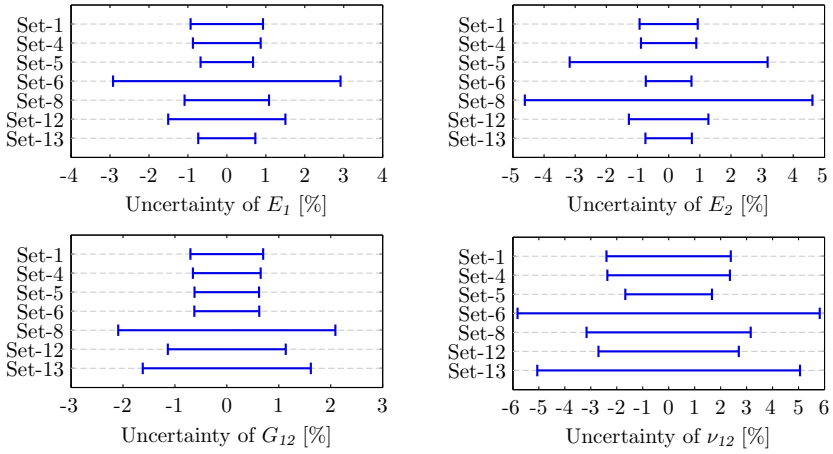

Figure 7.9: *The output uncertainties of the sample sets of table 7.6 with a sensitivity matrix condition number smaller than 10.*

That a lower condition number does not automatically lead to a lower uncertainty can be explained by the fact that the condition number is only a measure of the quality of the information provided by the resonant frequencies. The condition number does not relate to the way the unknown material parameters are extracted from this information. Therefore, a low condition number does not necessarily result in small uncertainty intervals. However, a very high condition number will result in large uncertainties, because no matter which identification routine is used, it is impossible to extract information which is not present in the test data. The sensitivity matrix condition number should thus only be used as an indicator to make a first selection. The final selection of the optimal test configuration should be based on the results of a genuine uncertainty analysis.

7.7. Summary

This chapter dealt with uncertainty analysis in vibration-based MNETs and introduced both a probabilistic and a non-probabilistic procedure to determine the uncertainties of the identified elastic properties from the uncertainties of the input parameters. It was shown that the probabilistic approach is optimal for the evaluation of the uncertainties during real experiments; the

non-probabilistic approach is preferred for determining the optimal test configuration in the pre-test phase.

8
Validation Tests

This chapter presents the validation tests performed on two different reference materials in order to validate the MNET-based procedures of chapter 6 in an experimental way.

8.1. Introduction

This chapter presents two experimental test-cases of layered material identification. The two considered test-cases are intended to validate the MNET-based identification routines in an experimental way. The materials used in this chapter do not have an industrial application, they were especially designed and produced to serve as reference materials for the experimental validation of the MNET routines.
Note that all the experiments were performed with the same equipment and test set-up. The test samples were supported by, or suspended with thin wires in order to reproduce the free-free boundary conditions of the FE-models as well as possible. The test samples were excited with a loudspeaker and the vibration response was captured with a doppler laser vibrometer. The test procedures and set-up are discussed in detail in appendix B. Also note that this chapter does not present all the experimental data and results. In general, only the data that is needed to understand the discussions and conclusions is provided. Appendix E presents a detailed description of all the test samples[1], sample models[2], together with the obtained elastic properties.

8.2. Brass-Steel Bi-Metal

8.2.1. Introduction

Goal and Description of the Validation Test

The identification routines were successfully validated in a numerical way[3]. However, a genuine validation of a test method should be performed in an experimental way. Since there are no standardised methods for layered material identification, the main problem with an experimental validation is the choice of the reference properties with which the identified properties have to be compared. In such a validation test, this problem is overcome by using a layered material of which the layer materials are also available in a homogeneous, i.e. non-layered, form. In this way, the reference properties can be obtained with non-layered identification routines from the resonant frequencies of the homogeneous test samples. The used reference material is a purpose-built brass-steel bi-metal produced by gluing a stainless steel layer to a brass sample.

The Test Material

Seventy beam-shaped samples, 100×20 mm, and 14 plate-shaped samples, 105×100 mm, were cut from a 0.8 mm thick brass sheet with a high pressure water cutting device. The samples were cut in five different material directions. An identical sample set was cut out of a 0.5 mm thick stainless steel sheet. Table 8.1 provides an overview of the produced samples. Note that the 0° direction is the direction orthogonal to the rolling direction.

[1] The length, width, (layer)thickness, mass and resonant frequencies.
[2] The mesh size of the converged FE-model.
[3] A numerical validation is performed by generating the resonant frequencies of a set of layered samples with FE-models, identifying the layer properties from these 'experimental' frequencies with the MNET routines, and comparing the identified properties with the reference properties, i.e. the properties used to generate the resonant frequencies.

Table 8.1: *The sample set that was cut out of the metal sheets.*

Type	Dir. [°]	Quantity	
		Brass	Steel
Beam	0.0	14	14
Beam	22.5	14	14
Beam	45.0	14	14
Beam	67.0	14	14
Beam	90.0	14	14
Plate	0.0	14	14

The layered specimens were produced by gluing a brass sample to a stainless steel sample with the two-component epoxy glue Permabond E32. This glue is especially designed for metals, and usually ensures a strong bonding between the glued layers. The main disadvantage of the Permabond E32 glue is its high viscosity, which requires the glueing of the test specimens in a press. Optimal results were obtained by applying a uni-axial pressure of 4000 kPa. In this way, glue layers with a thickness of about 10 µm were obtained. To ensure that the samples did not stick to the press, the plates of the press were protected with a teflon foil. The samples were removed from the press after twelve hours. At least twenty four hours later, the sample edges were sanded to remove the solidified excess glue, and to correct the inevitable miss-alignment of the two

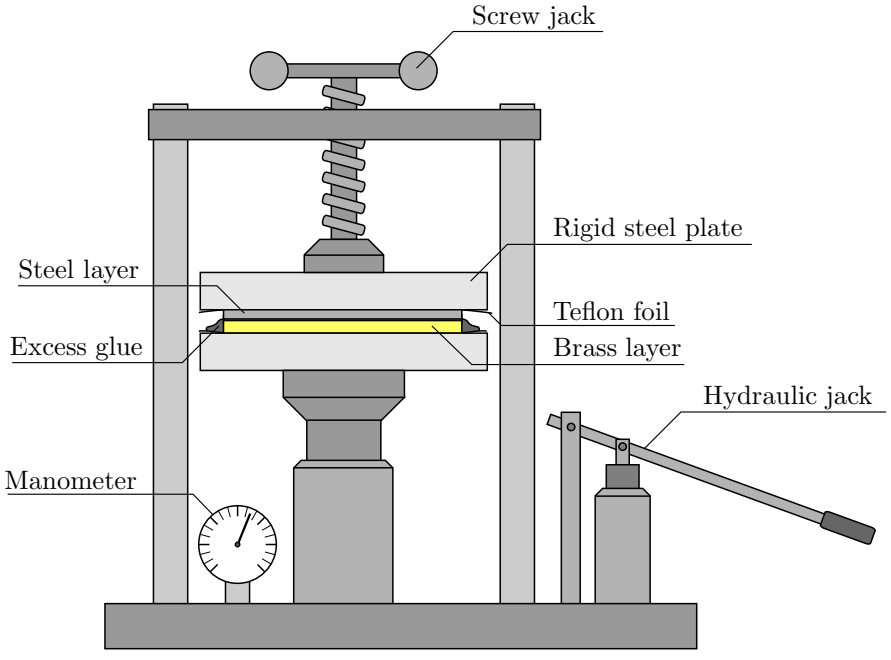

Figure 8.1: *The set-up to glue the sample layers.*

sample layers, as shown in figure 8.2. The homogeneous samples were produced in the same way, but by combining two brass or steel layers. Figure 8.1 presents the set-up that was used to produce the layered samples.

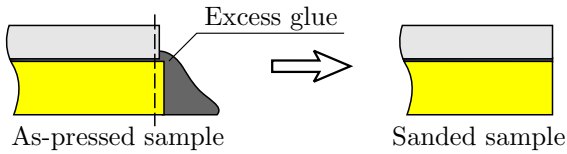

Figure 8.2: *The effect of the sanding process.*

8.2.2. Homogeneous Brass Samples

In total, twenty four homogeneous brass samples were produced: 4 beams in the 0°, 22.5°, 45°, 67.5°, and 90° direction, and 4 plates in the 0° direction. The dimensions, mass, and resonant frequencies of all the test samples were measured with the procedures described in appendix B. The elastic properties of the used brass were identified from the resonant frequencies of the beam-shaped specimens with both the single- and multi-orientation routine, and from the resonant frequencies of the plate-shaped specimens. The identified properties are presented in tables 8.2 and 8.3 and displayed in the plots of figure 8.3.

Table 8.2: *The averages of the single-orientation results.*

Dir. [°]	E [GPa]	G [GPa]	ν [–]
0.0	106.88	37.07	0.442
22.5	105.37	37.95	0.388
45.0	102.26	38.77	0.319
67.5	101.44	38.27	0.326
90.0	101.61	37.51	0.350

Table 8.3: *The results of the multi-orientation and plate-shaped routine.*

	E_1 [GPa]	E_2 [GPa]	G_{12} [GPa]	ν_{12} [–]
Multi-orientation	107.38	101.75	37.41	0.358
Average plate-shaped	106.88	101.71	37.21	0.351

The brass appeared to be elastically anisotropic. The elastic modulus decreased from the 0° to the 90° direction, and the difference between the stiffest and most flexible direction was about 5 %. The shear modulus varied within a range of 3 %, and was maximal in the 45° direction. The Poisson's ratio varied about 7 % as a function of the material orientation. The correlation between the average properties obtained with the different MNETs was comparable

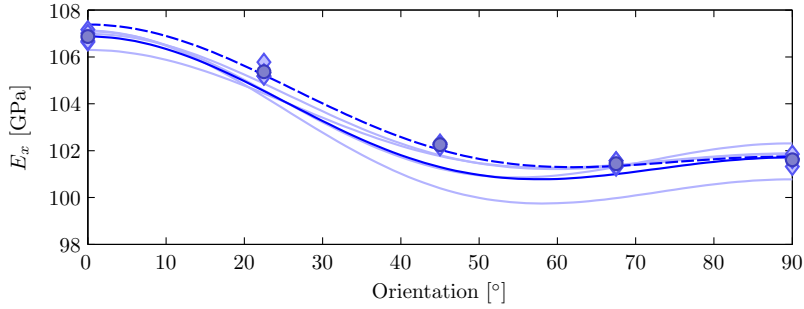

(a) The elastic modulus

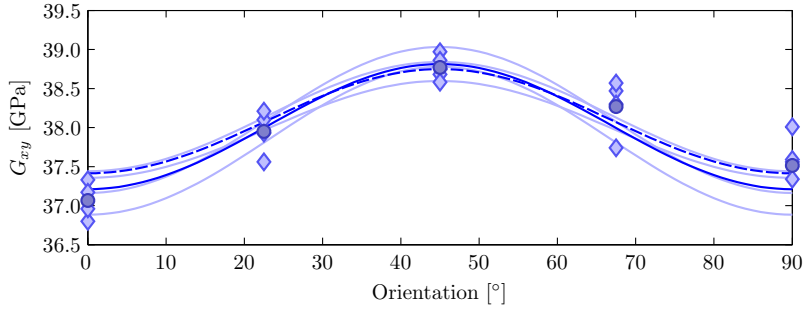

(b) The shear modulus

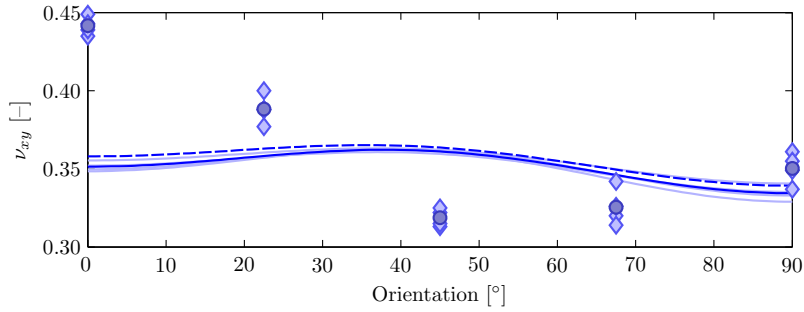

(c) The Poisson's ratio

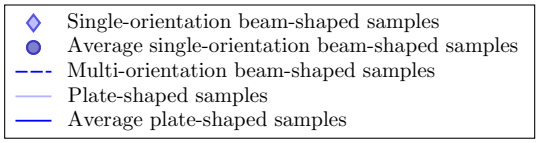

Figure 8.3: *The elastic properties of the homogeneous brass samples.*

with the spread of the results obtained on the different samples, except for the ν_{12} values obtained with the single-orientation routine. The latter confirms that the single-orientation routine does not provide a correct estimation of the Poisson's ratio, if the material is not isotropic[4].

8.2.3. Homogeneous Stainless Steel Samples

Like in the case of brass, twenty four homogeneous stainless samples were produced: 4 beams in the 0°, 22.5°, 45°, 67.5°, and 90° direction, and 4 plates in the 0° direction. The dimensions, mass, and resonant frequencies of all the test samples were measured with the procedures described in appendix B. Moreover, the elastic properties were identified from the resonant frequencies of the beam-shaped specimens with both the single- and multi-orientation routine, and from the resonant frequencies of the plate-shaped specimens. The properties identified for the homogeneous steel specimens are presented in tables 8.4 and 8.5 and displayed in the plots of figure 8.4.

Table 8.4: *The averages of the single-orientation results.*

Dir. [°]	E [GPa]	G [GPa]	ν [–]
0.0	201.44	72.78	0.384
22.5	196.99	75.20	0.310
45.0	192.33	79.35	0.212
67.5	196.68	76.16	0.291
90.0	200.92	72.78	0.381

Table 8.5: *The results of the multi-orientation and plate-shaped routine.*

	E_1 [GPa]	E_2 [GPa]	G_{12} [GPa]	ν_{12} [–]
Multi-orientation	202.28	201.82	72.83	0.279
Average plate-shaped	201.06	200.76	72.16	0.280

The considered stainless steel was anisotropic. The elastic modulus was maximal in the 0° and 90° direction and minimal in the 45° direction. The overall variation of the elastic modulus was about 5 %. Both the shear modulus and Poisson's ratio were maximal in the 45° direction, and varied about 9 % and 13 % respectively in function of the orientation. Like in the case of brass, the correlation between the average properties obtained with the three MNET identification approaches was smaller or equal to the spread of the properties obtained on the different test samples, while the single-orientation routine did not provide a correct estimation of the Poisson's ratio.

[4]This problem was extensively discussed with the introduction of the single-orientation routine in chapter 6.

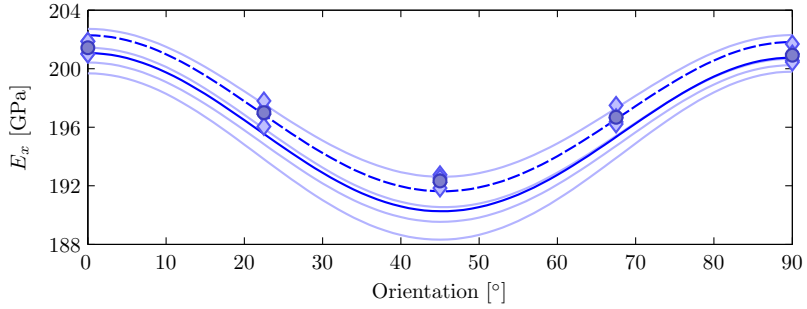

(a) The elastic modulus

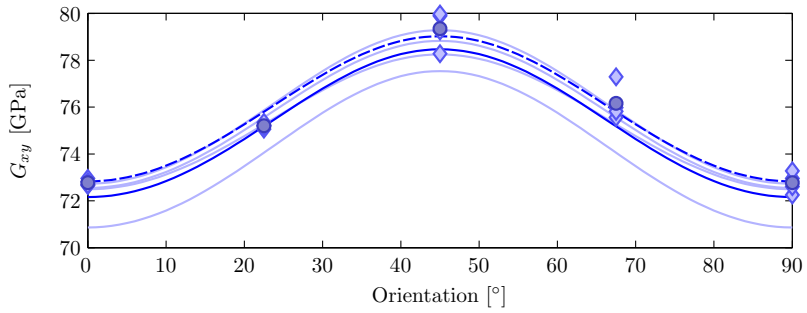

(b) The shear modulus

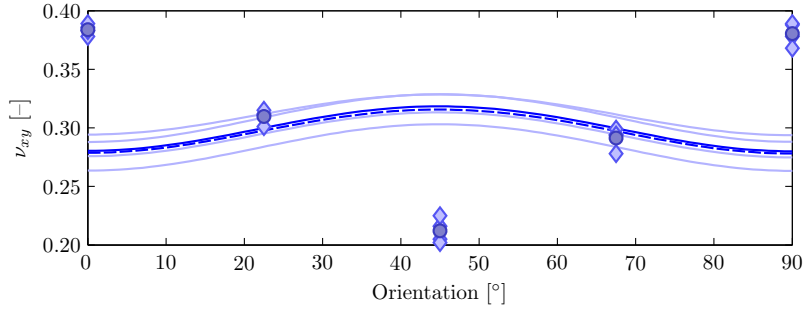

(c) The Poisson's ratio

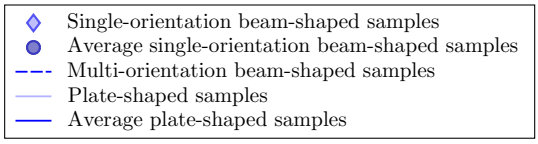

Figure 8.4: *The elastic properties of the homogeneous stainless steel samples.*

8.2.4. Brass-Steel Bi-Metal Samples

The layered sample set comprised thirty six test specimens: 6 beams in the 0°, 22.5°, 45°, 67.5° and 90° direction, and 6 plates in the 0° direction. The layer properties were identified from the resonant frequencies of these samples, using two different identification approaches.

The First Identification Approach

With the first approach, the properties of one of the layers were considered to be known. In this case, there was only one material with unknown properties; the identification, therefore, required only a single layer configuration. The brass properties were identified from the resonant frequencies of the layered samples, while the steel properties were fixed to the reference values obtained from the homogeneous samples. The steel properties were identified in a similar way by fixing the properties of the brass layers to their reference values. Tables 8.6 and 8.7 present the results together with the relative difference with the reference properties. Figures 8.5 and 8.6 provide a graphical representation of these results.

Table 8.6: *The averages of the single-orientation results.*

Dir. [°]	Brass				Steel			
	E [GPa]		G [GPa]		E [GPa]		G [GPa]	
0.0	107.32	0.4 %	37.62	1.5 %	202.43	0.5 %	74.34	2.1 %
22.5	105.98	0.6 %	38.09	0.4 %	198.56	0.8 %	75.62	0.5 %
45.0	101.50	−0.7 %	38.65	−0.3 %	190.91	−0.7 %	79.01	−0.4 %
67.5	101.05	−0.4 %	38.20	−0.2 %	195.62	−0.5 %	75.98	−0.2 %
90.0	101.66	0.0 %	37.50	0.0 %	202.25	0.7 %	72.43	−0.5 %

Table 8.7: *The results of the multi-orientation routine (MO) and the averages of the plate-shaped (PS) routine.*

	E_1 [GPa]		E_2 [GPa]		G_{12} [GPa]		ν_{12} [–]	
MO Brass	107.68	0.3 %	101.59	−0.2 %	37.53	0.3 %	0.359	0.3 %
MO Steel	203.04	0.4 %	201.36	−0.2 %	73.14	0.4 %	0.280	0.4 %
PS Brass	106.95	0.1 %	101.61	−0.1 %	37.33	0.3 %	0.352	0.2 %
PS Steel	201.27	0.1 %	200.50	−0.1 %	72.48	0.4 %	0.282	0.4 %

All three routines proved to be capable of identifying the layer properties. The spread of the results[5] of the single-orientation routine is about three times higher than the spread of the results obtained from the homogeneous samples. For the plate-shaped routine, there is no clear increase in the spread of the identified properties.

[5]Here quantified by the standard deviation.

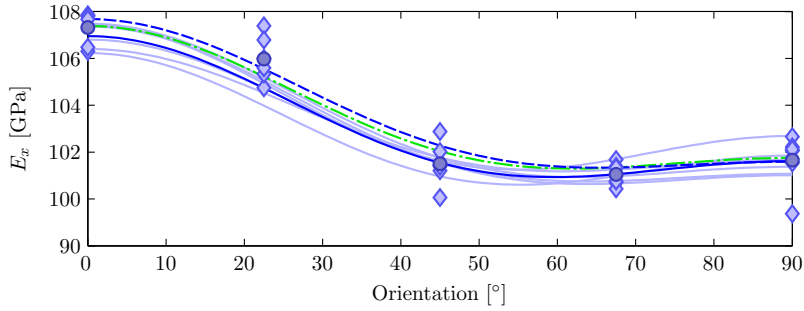

(a) The elastic modulus

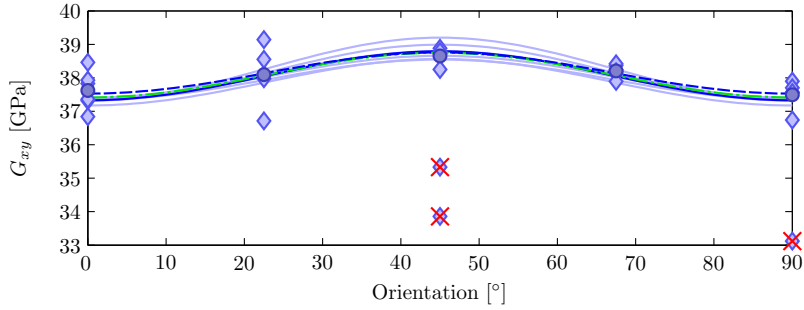

(b) The shear modulus

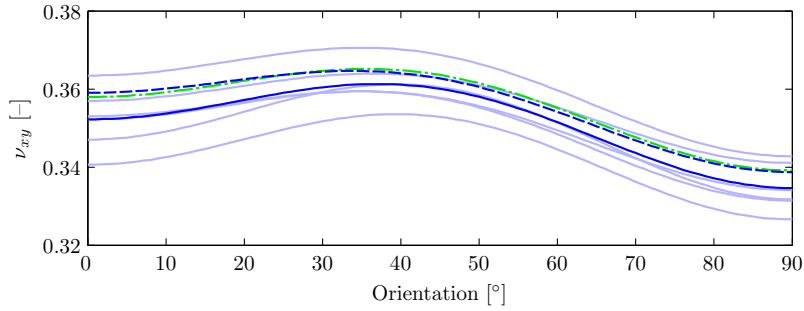

(c) The Poisson's ratio

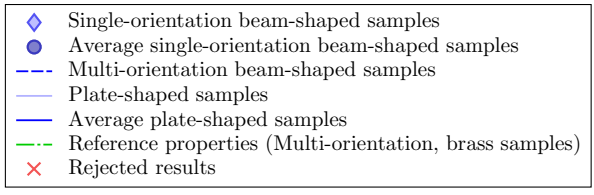

Figure 8.5: *The elastic properties of the brass layer, approach 1.*

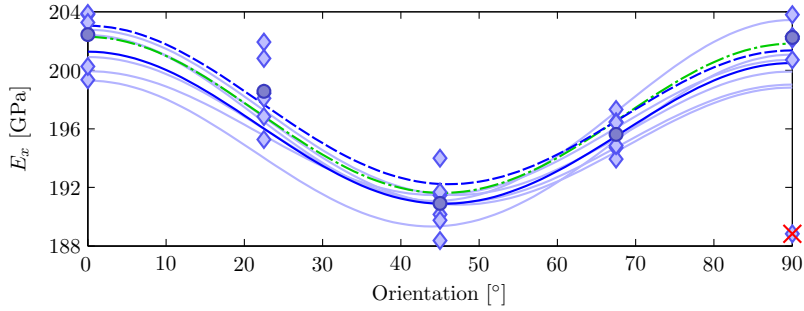

(a) The elastic modulus

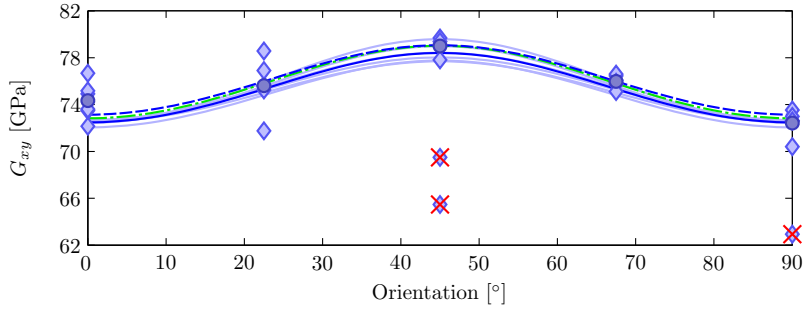

(b) The shear modulus

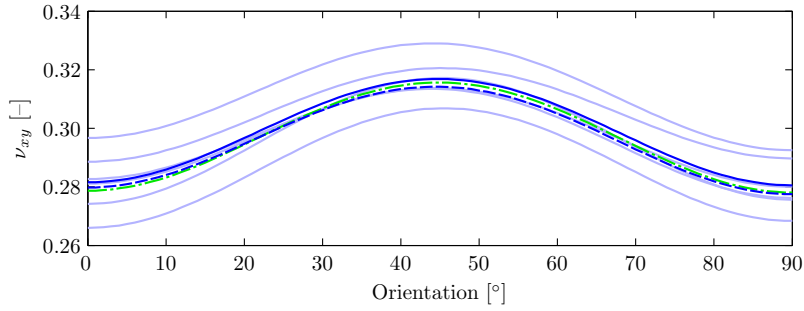

(c) The Poisson's ratio

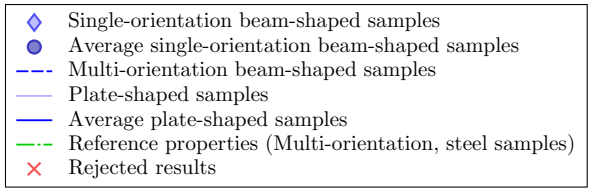

Figure 8.6: *The elastic properties of the stainless steel layer, approach 1.*

The shear moduli obtained from samples BSB-17, BSB-18, and BSB-29 were rejected. Most likely, the glue layer of these samples was damaged during the sanding process, leading to a reduction of the overall torsional stiffness and an underestimation of the shear modulus. Note that the torsional modes of these three samples had a much higher damping then the torsional modes of the other samples. In case of sample BSB-29, the identification routine had to keep the value of Poisson's ratio equal to 0.5 in order to ensure the feasibility of the elastic properties. Note that the underestimation of the elastic modulus of sample BSB-29, figure 8.6(a), was related to the overestimation of the Poisson's ratio and not to the influence of the damaged glue layer on the resonant frequency of the fundamental flexural mode. This was confirmed by the results of the multi-orientation routine. During the last iteration step, the frequency residual of the flexural frequency was 0.03 % while the residual of the torsional frequency was −4.2 %; this clearly proved that there was no problem with the resonant frequency of the flexural mode.

The Second Identification Approach

The second approach aimed at the identification of the layer properties without using any homogeneous test samples. This approach required two different layer configurations. The first configuration was the initial brass-steel bi-metal sample, the second configuration was obtained by adding a glass layer to the samples. Glass sheets with two different thicknesses were used for this purpose: sheets with a thickness of 0.6 mm and 0.7 mm. Six specimens of every sample type[6] were produced. Of those six specimens, two specimens had a 0.7 mm glass layer on the brass side, two specimens had a 0.7 mm glass layer on the steel side, one specimen had a 0.6 mm glass layer on the brass side, and one specimen had a 0.6 mm glass layer on the steel side. Figure 8.7 presents all these layer configurations.

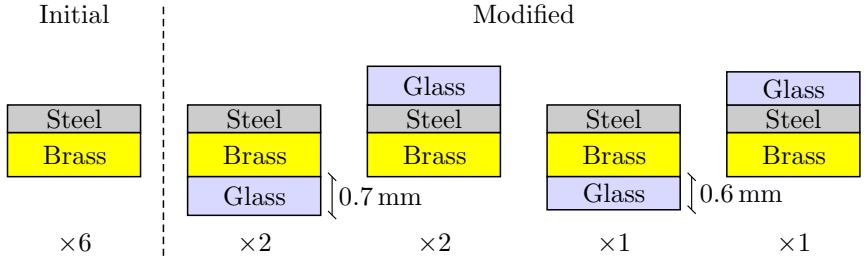

Figure 8.7: *The layer configurations of the initial and modified specimens.*

Although the E32 glue was suited to glue glass to metal, it could not be used to make the additional layer configurations, since the glass layers could not withstand the pressure required to obtain a thin glue layer. Therefore, the glass layers were glued with the Böhle U-682 UV-curing glue. This glue is designed to fix glass on metal and has two major advantages for the considered application. First of all, it has a low viscosity, which means that only a very

[6] A beam-shaped specimen in a particular orientation or a plate-shaped specimen.

low pressure was required to push the excess glue away. The second advantage is related to the UV-curing property of the glue. Because of this property, there was enough time to carefully position the glass layer on the initial sample and to press[7] it so as to remove the excess glue. Once the glass layer was correctly positioned, the glue could be fully cured in about 30 seconds by radiating it with a UV-lamp. The UV-curing glue has proven to be a very convenient solution to glue the glass layers. Note that the elastic properties of the glass layers were identified before they were glued to the bi-metal samples. The dimensions, mass, resonant frequencies, and elastic properties of the glass samples are given in appendix E.

The layer properties were identified using the three MNET identification procedures. With the single-orientation routine, the layer properties were estimated from the resonant frequencies of the initial and modified layer configuration of each sample. During the identification, the properties of the glass layers were fixed to the properties presented in tables E.44 and E.45. Table 8.8 presents the averages of the obtained properties together with the relative deviation from the reference properties. Figure 8.8 and 8.9 present the individual results of the single-orientation routine. A number of shear modulus values were rejected because they differed too much from the rest of the values. Note that there were also two rejected elastic moduli, i.e. E_{brass} of sample BSB-06 and E_{steel} of sample BSB-29. The properties of these two layers were rejected because the identification had to block the Poisson's ratio value to 0.5 to ensure the feasibility of the properties of the considered layer. To conclude, it is interesting to point out that the average difference between the identified and reference properties is estimated at 0.5 % for the brass properties, and at 0.65 % for the steel properties.

Table 8.8: *The averages of the single-orientation results.*

Dir. [°]	Brass				Steel			
	E [GPa]		G [GPa]		E [GPa]		G [GPa]	
0.0	107.48	0.6 %	37.05	−0.1 %	202.67	0.6 %	72.29	−0.7 %
22.5	105.60	0.2 %	38.16	0.5 %	197.68	0.3 %	76.69	2.0 %
45.0	102.16	−0.1 %	38.27	−1.3 %	190.70	−0.8 %	80.11	1.0 %
67.5	100.79	−0.6 %	38.24	−0.1 %	197.43	0.4 %	76.12	−0.1 %
90.0	102.33	0.7 %	37.11	−1.1 %	201.69	0.4 %	73.00	0.3 %

The layer properties were also identified with the multi-orientation routine. In a first phase, the elastic properties were identified from the fundamental flexural and torsional frequencies of the two layer configurations of all the samples. All the frequencies had a weighting coefficient of 1, and the properties of the glass layers were fixed to the values of tables E.44 and E.45. The sixty test

[7] To keep the glass layers intact, the samples were not placed in a press. Pressing the samples with a press requires a complicated set-up in order to keep the glass layer in place so that it is no crushed at the edges. Instead of using a press, the excess glue was removed by putting a piece of cloth over the samples and pressing them by hand as hard as possible.

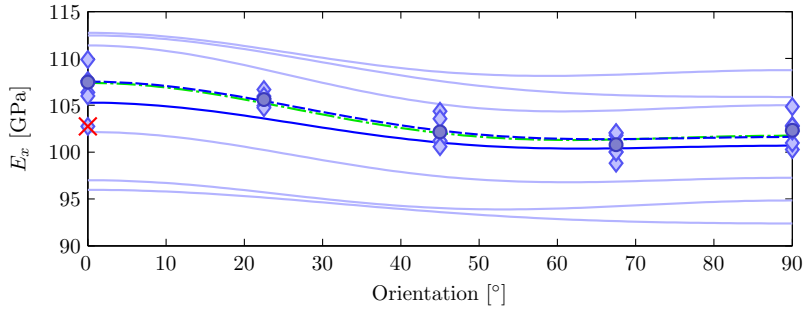

(a) The elastic modulus

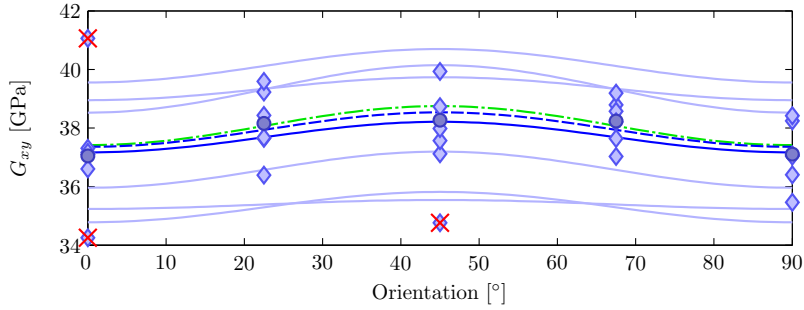

(b) The shear modulus

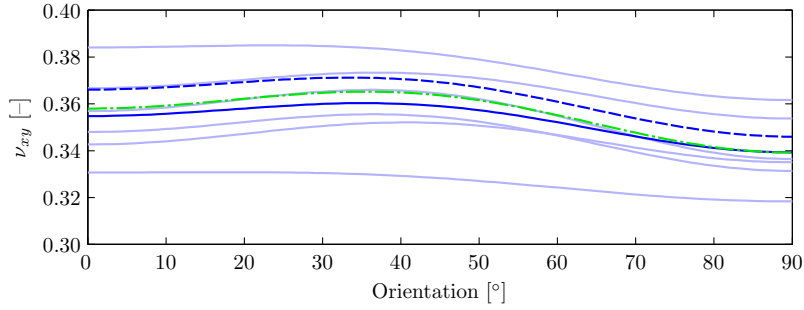

(c) The Poisson's ratio

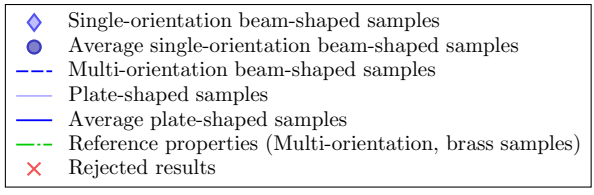

Figure 8.8: *The elastic properties of the brass layer, approach 2.*

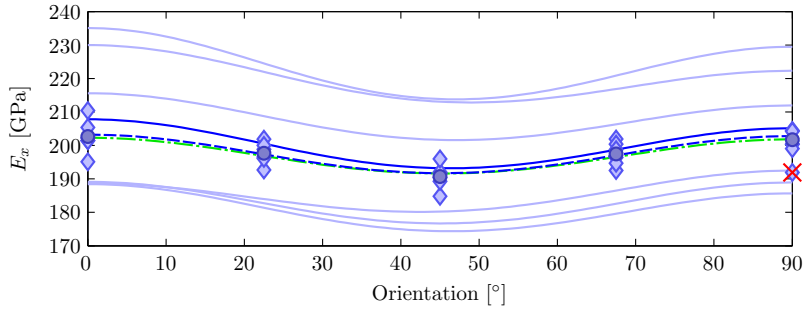

(a) The elastic modulus

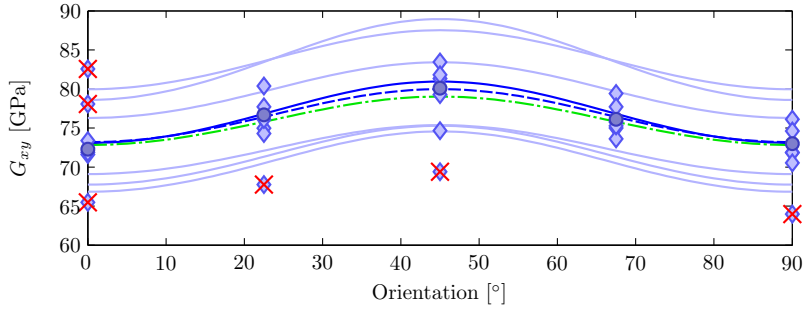

(b) The shear modulus

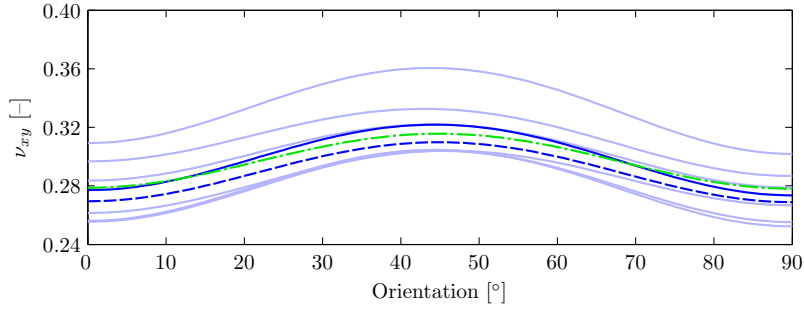

(c) The Poisson's ratio

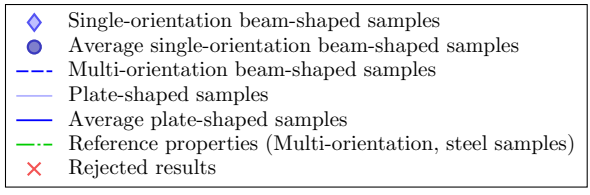

Figure 8.9: *The elastic properties of the stainless steel layer, approach 2.*

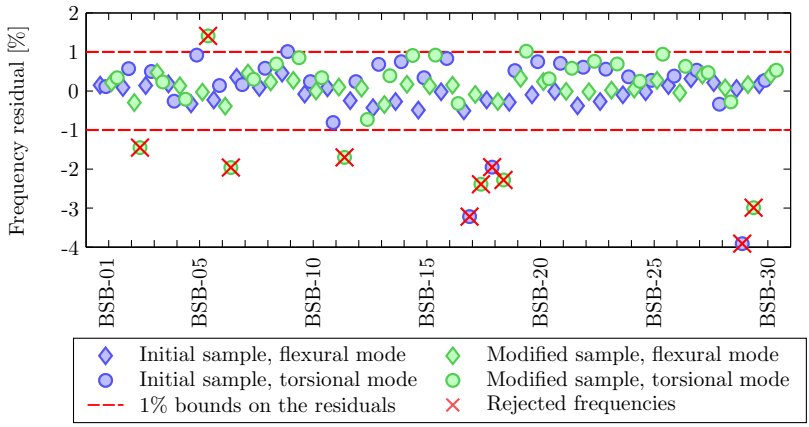

Figure 8.10: *The frequency residuals of the multi-orientation routine.*

sample models were simultaneously updated in a single identification routine. The solution converged after four iteration steps, and figure 8.10 presents the frequency residuals of the last iteration step. Apparently, there were ten torsional frequencies that could not be reproduced within an error range of 1 %, which is about twice the average residual error. The majority of the associated samples showed an increase of the damping ratio of the torsional mode in comparison to the samples that gave residuals smaller than 1 %. Therefore, these ten frequencies were rejected, based on the assumption that the large residuals were related to defects of the test samples, e.g. an imperfection in one of the glue layers. Note that these ten frequencies are only associated with seven samples. For samples BSB-17, BSB-18 and BSB-29, there was a problem with the torsional frequencies of the initial bi-metal, it is thus logical that the torsional frequencies of the modified samples have to be rejected as well. The frequency weights were adapted is such a way that each mode of each sample configuration had the same importance; the corresponding weighting coefficients are presented in table E.38. This modified identification problem provided the properties of table 8.9. Figures 8.9 and 8.8 reveal that the correlation between the identified and reference properties is much smaller than the spread on the properties identified on different samples. Table 8.9 also indicates that the difference between the identified and reference values was smaller than 0.5 % for E and G, and smaller than 3.5 % for ν. Note that the deviation between the identified and reference properties was higher for the steel than for the brass material. This was related to the relative thickness of the two layers; the thinner steel layer was more sensitive to disturbances than the thicker brass layer.

Finally, the layer properties were derived from the resonant frequencies of two different layer configurations of the plate-shaped specimens. During the identification, the glass properties were kept fixed to the values of table E.46. The averages of the obtained results are presented in table 8.10. In addition, figures 8.9 and 8.8 present the results of the individual samples.

Although the average results deviated less then 3.5 % from the reference val-

Table 8.9: *The results of the multi-orientation routine.*

	E_1 [GPa]		E_2 [GPa]		G_{12} [GPa]		ν_{12} [–]	
Brass	107.52	0.13 %	101.62	−0.13 %	37.36	−0.15 %	0.366	2.27 %
Steel	203.22	0.47 %	202.78	0.47 %	73.18	0.49 %	0.270	−3.31 %

Table 8.10: *The average results of the plate-shaped routine.*

	E_1 [GPa]		E_2 [GPa]		G_{12} [GPa]		ν_{12} [–]	
Brass	105.28	−1.5 %	100.69	−1.0 %	37.17	−0.1 %	0.355	1.0 %
Steel	207.81	3.4 %	205.13	2.2 %	73.09	1.3 %	0.277	−1.2 %

ues, the spread of the results of the plate-shaped specimens was suspiciously high. In terms of standard deviation, the spread was on average eight times higher than the spread of the results of the single-orientation routine. Also note that on the plots of figures 8.8(a), 8.8(b), 8.9(a), and 8.9(b), three curves that were clearly above the average and three curves were clearly below the average. The properties of the layer glued to the glass were systematically underestimated, while the properties of the other layer were always overestimated. This indicated that there was a serious problem with the modified plates.
The problems were most likely related to the fact that the glue layer had a non-uniform thickness. To avoid the inclusion of air bubbles in the glue layer, the glue was poured in the centre of the sample. The glass layer was put on top of the glue, and was pressed to push the glue to the edges of the plate. Figure 8.11 schematically represents this process.

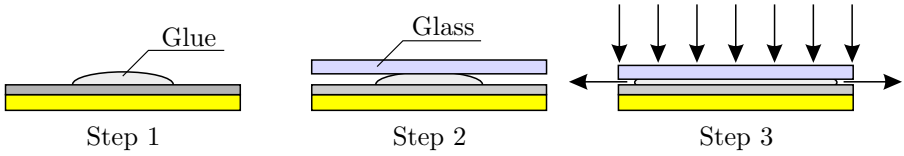

Figure 8.11: *Gluing the glass layer to the plate-shaped samples.*

Because there was no appropriate set-up available, the glass sheet could not be pressed very out of fear of cracking it. Because of that, the glue layer was thicker in the centre than along the edges, as shown in figure 8.12. With a standard micrometer screw, the thickness could only be measured along the edges. As a consequence, the thickness of the plate was underestimated. In the identification routine, the underestimation of the sample thickness was compensated by an overestimation of the elastic properties. This can be explained as follows. Initially, an underestimation of the thickness resulted in an underestimation of the stiffness of the sample. The easiest way to increase the stiffness of the sample was to increase the stiffness of the outer layers. For the sample in figure 8.12, this resulted in an overestimation of the brass properties, since the

properties of the glass layer were kept constant. The identification routine also included a pure bi-metal sample. In order to match the experimental frequencies of this sample, the elastic properties of the other layer, i.e. the steel layer for the sample in figure 8.12, had to be underestimated, which was exactly the effect observed in the results of the plate-shaped routine.

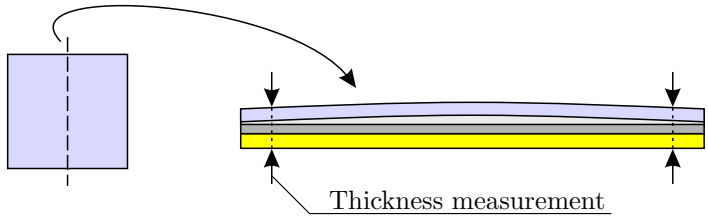

Figure 8.12: *The non-uniform glue layer of the modified plates.*

Conclusions

This validation test provided an irrefutable proof of the experimental feasibility of the vibration-based MNET routines for the identification of the elastic properties of the constituent layers of layered materials. The following conclusions can be drawn from this validation test:

- It is possible to identify the layer properties with a sample set that comprises one homogeneous and one layered test sample. For the considered validation test, the three identification approaches succeeded in finding the layer properties with an average deviation, with respect to the reference properties of 0.6 % in case of the SO routine, 0.3 % in case of the MO routine, and 0.2 % in case of the PS routine.
- It is possible to identify the layer properties from a sample set that comprises one initial and one modified test sample. For the considered validation test, the three identification approaches succeeded in finding the layer properties with an average deviation, with respect to the reference properties of 0.7 % in case of the SO routine, 0.9 % in case of the MO routine, and 1.4% in case of the PS routine. However, in the case of the MO routine, the average deviation of the elastic and shear moduli was 0.3 %, while the average deviation of the Poisson's ratios was 2.8 %. The average deviation of the elastic and shear moduli identified by the PS routine was 1.6 %, while the average deviation of the Poisson's ratios was 1.1 %. Furthermore, since the SO routine does not provide an estimation of the Poisson's ratios, it makes sense to compare the quality of the results of the three MNET routines by comparing the average deviation of the elastic and shear moduli, i.e. 0.7 % for the SO routine, 0.3 % for the MO routine, and 1.6 % for the PS routine.
- Modifying the samples by adding a glass layer appears to be a successful concept, in case of beam-shaped specimens. In the case of plate-shaped samples, the gluing process requires special care in order to ensure the uniformity of the glue layer. A press, with a clamping system to keep the glass layer in position, is a necessity. Note that the use of UV-curing glue results in an acceptable sample preparation time.

- A number of samples seemed to have a glue layer of inferior quality. Apparently, it is impossible to avoid this, since the additional layers were glued very carefully and still the problem persisted. Therefore, it is advisable to make a few samples more than those strictly needed. Note that a poor bonding of the sample to the glass layer mainly decreases the torsional frequency.
- With the single-orientation routine, a problem with the torsional frequency can lead to an incorrect Young's modulus. Note that this problem is always related to an unrealistically high value of the identified Poisson's ratio.
- The multi-orientation routine uses a largely overdetermined system. Incorrect frequencies, e.g. due to a mistake or a poor quality glue layer, can be detected by inspecting the frequency residuals. If a particular sample has an incorrect value for one of the experimental resonant frequencies, only that frequency needs to be removed from the data set. The correctly measured frequencies of this sample can still be used since they provide additional information to the routine.
- Layered material identification results in a higher spread of the values identified on different samples than homogeneous material identification. Therefore, it is advisable to use a larger set of test specimens for layered than for homogeneous materials.
- For this test case, the multi-orientation routine appeared to be the most flexible and reliable identification procedure.

8.3. Carbon-Epoxy Composite

8.3.1. Introduction

This test case presents a second, less elaborate, validation test. This time, the test material was a carbon-epoxy composite with a $[0_3\ 90_3]_s$ stacking sequence. The carbon-epoxy material was produced by manually stacking the twelve unidirectionally reinforced prepreg layers[8]. During the lay-up process, special care was taken to ensure the correct ply orientation. After the lay-up process, the material was cured in an autoclave using the prescribed temperature and pressure cycle. To allow the evacuation of superfluous resin during the curing process, the material surface was covered with a peel ply. As a result, the bottom and top surfaces of the composite were not smooth but had the imprint of the peel ply texture. Figure 8.13 schematically represents the lay-up and the surface condition of the composite material. Figure 8.14 shows a light microscope picture of the imprint of the peel ply on the material surface.

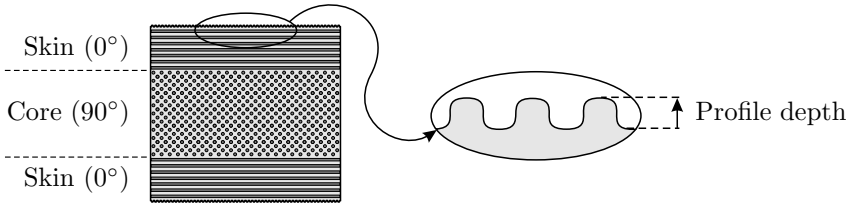

Figure 8.13: *The stacking sequence and surface condition.*

[8]The used prepreg material was Hexcel Fibredux 920 CX-TS-6K-5-42 %.

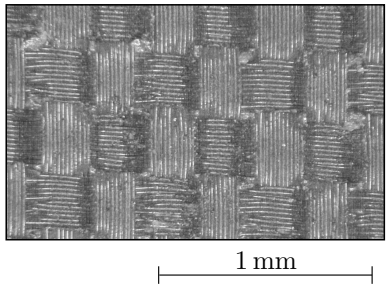

Figure 8.14: *The light microscope image of the peel ply imprint on the material surface.*

The skin and core were made with the same prepreg material; the layers were just rotated over an angle of 90°. The constitutive behaviour of this composite material could thus be described with four elastic material parameters, which implied that the properties of the prepreg layers could be identified from the resonant frequencies of a single plate-shaped specimen. Since this test was equivalent to a non-layered identification, the obtained properties were used as reference values.
It would also be possible to disregard the relation between the properties of the three layers, and to consider the composite as a sandwich material, where the skin and core materials have independent properties. In this situation, the identification of the skin and core properties would require the resonant frequencies of two plate-shaped specimens with a different layer configuration. A successful validation should result in skin properties that equal the reference properties, while the core properties should have a phase lag of 90° with respect to the reference properties.

8.3.2. Equivalent Thickness of the Material

The MNET routine needs an accurate finite element model of the test specimens. Because of this, the peel ply imprint on the top and bottom surfaces of the composite required special attention. Incorporating the imprint profile in the finite element model required such a fine mesh that it led to an unmanageable number of elements. For an acceptable computation time, the elements of the FE-model had to be an order of magnitude larger than the wavelength of the surface profile. Because of this, the influence of the peel ply imprint could only be modelled in an indirect way. The most convenient way to do this was to replace the real, i.e. rough, plate by an equivalent smooth plate with a uniform thickness. The only problem with this approach was the estimation of the thickness of the equivalent plate.
The first step in the estimation of the equivalent thickness (t_{eq}) was the determination of the depth of the surface profile; the profile depth was defined as indicated in figure 8.13. The profile depth was measured with a surface analyser[9], and the resulting cumulative distribution function is presented in figure 8.15.

[9] A Taylor-Hobson form Talysurf 120L.

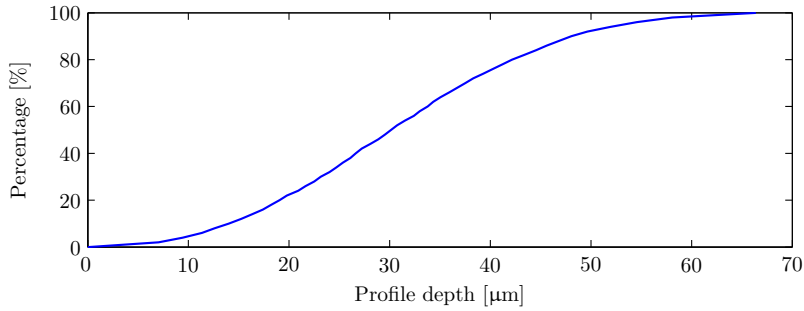

Figure 8.15: *The cumulative distribution function of the profile depth.*

The total thickness of the material (t_{mi}) was measured with a micrometer screw. This thickness value represented the distance between the outermost points of the top and bottom surface profiles as illustrated in figure 8.16.

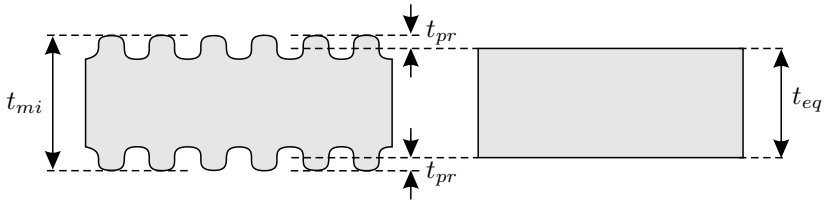

Figure 8.16: *The definition of the thicknesses t_{mi}, t_{eq}, and t_{pr}.*

The equivalent thickness was determined by comparing the frequencies of two finite element models. Both models had 50×50 plate elements with linear shape functions (Quad4). The first finite element model represented a plate with a peel ply imprint and is, therefore, referred to as the 'profile model'. In the profile model, the element thicknesses varied from element to element, and were obtained as follows. First, a set of 2500 random numbers was generated. This set had the same cumulative distribution function as the measured profile depth distribution of figure 8.15. Next, the random numbers were doubled and subtracted from the thickness t_{mi}. The resulting values were used as element thicknesses of the profile model. Once completed, the profile model was used to compute the resonant frequencies of the first five vibration modes of a plate with a peel ply imprint. In the second finite element model, which is called the 'equivalent model', all the elements had the same thickness. The equivalent thickness was estimated by updating the thickness of the equivalent model with the goal of reproducing the first five resonant frequencies of the profile model as good as possible. Eventually, the average surface profile depth (t_{pr}) was estimated as $\frac{1}{2}(t_{mi} - t_{eq})$ and equalled 37.1 µm. Note that this corresponds with the profile depth that has cumulative distribution of 64 %. Figure 8.17 shows the profile model, while table 8.11 presents the frequency match of the profile model and the updated equivalent model.

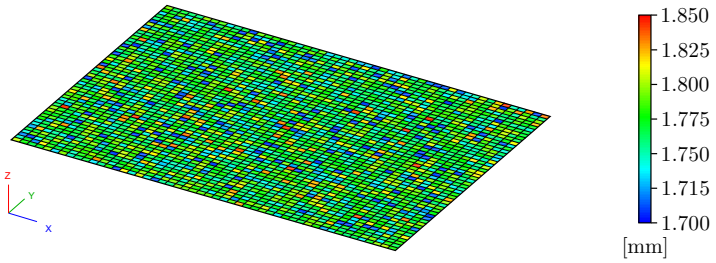

Figure 8.17: *The element thicknesses of the profile model.*

Table 8.11: *The frequency match between the profile and updated equivalent model.*

	Profile Model Freq. [Hz]	Equivalent Model Freq. [Hz]	Diff. [%]
Mode 1	201.74	201.71	−0.02
Mode 2	595.48	595.59	0.02
Mode 3	623.59	623.61	0.00
Mode 4	727.29	727.45	0.02
Mode 5	737.80	737.59	−0.03

8.3.3. The Test Specimens

The identification of the skin and core properties required two different layer configurations. The first layer configuration was the pure composite material, the second configuration was obtained by adding a 2 mm thick glass layer to the composite. Figure 8.18 presents these two layer configurations.

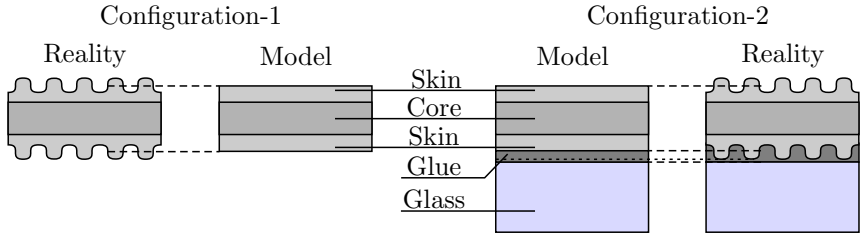

Figure 8.18: *The two layer configurations.*

For an optimal Poisson's ratio sensitivity, the dimensions of a plate-shaped specimen had to comply with equation (6.5).

$$\frac{l}{w} = \sqrt[4]{\frac{E_1}{E_2}}$$

For the carbon-epoxy material, E_1 and E_2 represent the average flexural stiffness of the material, i.e. the stiffness of an equivalent homogeneous material. Since the values of E_1 and E_2 were unknown, they had to be estimated before

the test plates could be made. Normally, E_1 and E_2 are measured on two beam-shaped samples oriented along the two principal material directions. However, in order to save material and time, E_1 and E_2 were estimated from the stacking sequence of the two layer configurations in combination with an initial estimate of the elastic moduli of the prepreg layers and glass. The average thickness of the composite material (t_{mi}) was estimated at 1.85 mm, which resulted in an equivalent thickness (t_{eq}) of 1.776 mm. Since the skin was made with three prepreg layers and the core with six, the skin and the core were assumed to have a thickness of $0.25\,t_{eq}$ and $0.50\,t_{eq}$, respectively. The glue layer was assumed to have a thickness of about 10 µm. However, the thickness of the glue layer in the model was the sum of the thickness of the actual glue layer and the surface profile, as shown in figure 8.18. The equivalent thickness of the glue layer was thus estimated at 50 µm. The prepreg material was assumed to have a stiffness in the fibre direction (E_l) of 100 GPa and a transverse stiffness (E_t) of 5 GPa. Table 8.12 presents the estimated layer thicknesses and stiffnesses.

Table 8.12: *A tentative estimation of the layer thicknesses and stiffnesses.*

	t_{eq} [mm]	E_1 [GPa]	E_2[GPa]
Skin	0.444	100.0	5.0
Core	0.888	5.0	100.0
Glass	2.000	70.0	70.0
Glue	0.050	3.0	3.0

The First Layer Configuration

The first layer configuration was the pure composite material. The equivalent overall stiffness in flexure (E_{eq}) could be estimated from the plate stiffness stiffness as

$$D_{eq} = D_{core} + D_{skin} \tag{8.1}$$

By using the estimated thicknesses and stiffnesses of table 8.12, this provides

$$E_1 = \frac{E_t h_1^3 + E_l(h_2^3 - h_1^3)}{h_2^3} = 88.1\,\text{GPa} \tag{8.2}$$

$$E_2 = \frac{E_t(h_2^3 - h_1^3) + E_l h_1^3}{h_2^3} = 16.9\,\text{GPa} \tag{8.3}$$

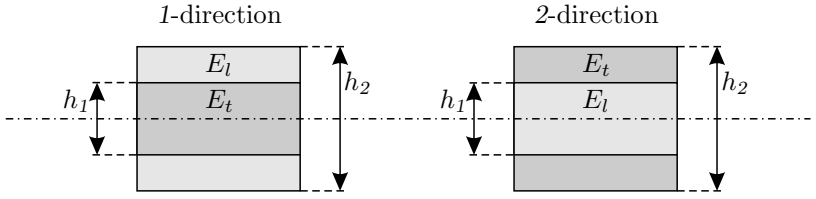

Figure 8.19: *A cross-section of the composite material.*

The estimated overall stiffnesses of the carbon-epoxy provided an optimal aspect ratio of 1.51. Based on that, a test plate[10] of 158×104 mm was cut out of the composite material. The resonant frequencies of the first five vibration modes were measured and the homogenised properties were identified, as shown in table 8.13.

Table 8.13: *The homogenised elastic properties of sample PCE-01.*

E_1 [GPa]	E_2 [GPa]	G_{12} [GPa]	ν_{12} [–]
82.85	18.31	3.53	0.129

The measured properties indicated that the considered material required an optimal aspect ratio of 1.46, therefore the length of the test plate was reduced from 158 mm to 151 mm.

The Second Layer Configuration

The second layer configuration was a combination of the initial composite material with a 2 mm thick glass layer. The overall stiffnesses of the second layer configuration was obtained from

$$D_{eq} = D_{core} + D_{skin} + D_{glue} + D_{glass} \tag{8.4}$$

The estimated properties of table 8.12 resulted in an E_1 of 64.8 GPa and an E_2 of 57.7 GPa, which provided an optimal aspect ratio of 1.03. A test plate[11] with this aspect ratio was produced by gluing a glass layer to a carbon-epoxy plate with the Permabond E32 epoxy glue. During the curing of the glue, the material was placed in a press that applied a uni-axial pressure of 1500 kPa. Once the glue was cured, the sample was removed from the press and the sample edges were sanded. Table 8.14 presents the homogenised elastic properties measured for this test sample. The experimental values confirmed that 1.03 was indeed the optimal aspect ratio.

Table 8.14: *The homogenised elastic properties of sample PCE-03a.*

E_1 [GPa]	E_2 [GPa]	G_{12} [GPa]	ν_{12} [–]
67.22	60.25	9.82	0.136

8.3.4. Identification of the Layer Properties

The Reference Properties

Both skin and core were made with the same type of prepreg layers, but the core layers were rotated over an angle of 90° with respect to the skin layers.

[10] Sample PCE-01; the experimental data for this sample are presented in appendix E.
[11] Sample PCE-03a; the experimental data for this sample are presented in appendix E.

When this relation between the skin and core properties was taken into account, the constitutive behaviour of the composite material could be described with four elastic parameters, i.e. the four elastic properties of the prepreg layers. This implies that the properties can be identified from the first five resonant frequencies of a single plate-shaped specimen. The material properties obtained in this way were used as reference values.

Table 8.15: *The prepreg properties identified on sample PCE-02.*

E_1 [GPa]	E_2 [GPa]	G_{12} [GPa]	ν_{12} [–]
103.76	9.30	3.99	0.260

Table 8.16: *Match between experimental and numerical frequencies.*

Mode	f_{exp} [Hz]	f_{num} [Hz]	Diff. [%]
1	196.63	196.73	−0.052
2	614.06	614.43	−0.060
3	638.36	638.83	−0.073
4	738.72	738.05	0.090
5	743.81	743.11	0.094

The prepreg properties were identified from the resonant frequencies of sample PCE-02. The four elastic constants of the prepreg material were identified using the identification scheme of figure 6.16 in combination with a finite element model, where the core properties equalled the skin properties rotated over an angle of 90°. Table 8.15 presents the identified properties, while table 8.16 provides the associated frequency residuals.

The Layer Properties

The properties of the skin and core material could also be identified in case the relation between the layer properties was ignored. In that case, the properties of two independent layer materials had to be measured, which required two different layer configurations. The first layer configuration was represented by the pure carbon-epoxy specimen PCE-02, the second layered configuration was represented by specimen PCE-03a, which was the combination of the carbon-epoxy specimen PCE-03 and the glass specimen Gla-2.0-01[12]. The layer properties were identified from the first five resonant frequencies of these two samples using the identification routine of section 6.3.2. Table 8.17 presents the obtained properties, and table 8.18 provides the associated frequency residuals.

Table 8.17: *The measured skin and core properties.*

	E_1 [GPa]	E_2 [GPa]	G_{12} [GPa]	ν_{12} [–]
Skin	103.68	9.36	3.99	0.259
Core	9.92	103.38	3.97	0.024

[12] Appendix E provides a detailed description of these test specimens.

Table 8.18: *Match between experimental and numerical frequencies.*

	Carbon-Epoxy (PCE-002)			Carbon-Epoxy + Glass (PCE-03a)		
Mode	f_{exp} [Hz]	f_{num} [Hz]	Diff. [%]	f_{exp} [Hz]	f_{num} [Hz]	Diff. [%]
1	196.63	196.73	−0.052	388.83	388.91	−0.020
2	614.06	614.45	−0.063	917.89	917.03	−0.015
3	638.36	638.95	−0.092	1010.04	1008.23	−0.019
4	738.72	738.09	0.085	1224.54	1226.28	0.021
5	743.81	743.19	0.084	1251.06	1253.79	0.022

Discussion of the Obtained Properties

Table 8.19 compares the properties of the skin and the core with the reference properties. Note that the core properties in table 8.19 were rotated over an angle of 90°. The error between the layer and reference properties was smaller than 0.7 %, except for E_2 and ν_{12} of the core for which the error was smaller than 7 %. The overall error on the skin properties was lower than the error on the core properties, which may be explained by the higher sensitivity of the skin layers. The plots of figure 8.20 compare the match of the skin and core properties with the reference properties for the orientations ranging between 0° and 90°. These plots might give the impression that the correlation of the E-moduli is better that the correlation of the shear moduli and Poisson's ratios. However, this not the case. The correlation of the E-moduli only looks better because of the scale that is necessary to present the large variation of the E-modulus in function of the orientation.

Table 8.19: *Comparison of the skin, core, and reference properties.*

		E_1 [GPa]	E_2 [GPa]	G_{12} [GPa]	ν_{12} [–]
Reference		103.76	9.30	3.99	0.260
Skin	Value	103.68	9.36	3.99	0.259
	Error	−0.1 %	0.7 %	0.0 %	−0.6 %
Core (↻ 90°)	Value	103.38	9.92	3.97	0.245
	Error	−0.4 %	6.7 %	−0.3 %	−5.7 %

8.3.5. Conclusions

The tests performed on the layered carbon-epoxy material provided a second successful experimental validation of the layered identification routine. The most important conclusion that could be drawn from this test case is that the use of plate shaped-specimens to identify the layer properties of strongly anisotropic materials is not straightforward, since every layer configuration requires a specimen with a different aspect ratio. For this a test, the problem

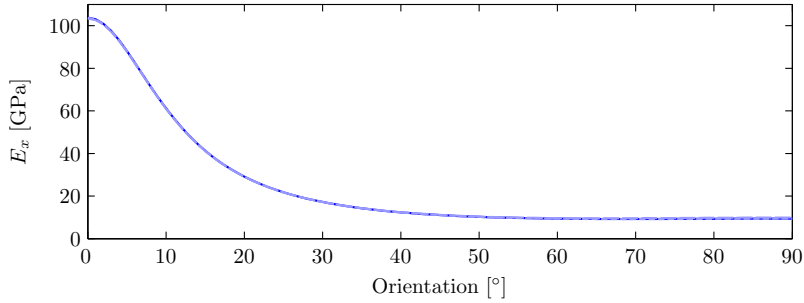

(a) The elastic modulus

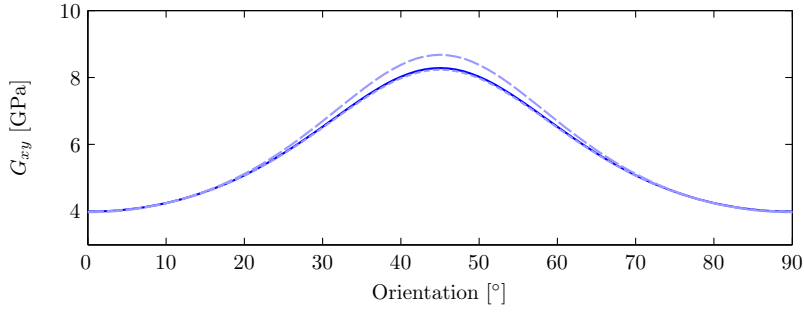

(b) The shear modulus

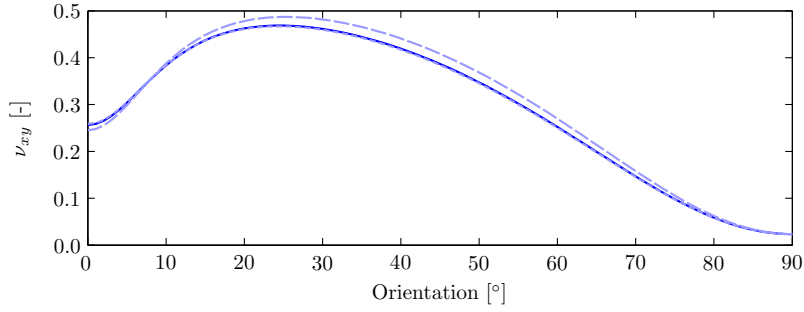

(c) The Poisson's ratio

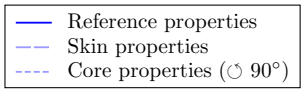

Figure 8.20: *The comparison of the skin and core properties with the reference properties.*

could be solved quite elegantly by deriving the optimal aspect ratios from an initial estimate of the elastic moduli of the layers. However, in case this information is not available a priori, the optimal aspect ratio has to be determined in an experimental way, i.e. by machining a beam-shaped specimen in both the *1*- and the *2*-direction, identifying the homogenised flexural stiffnesses from the resonant frequencies of these samples, and deriving the optimal aspect ratio from the identified stiffnesses. This process has to be repeated for every layer configuration.

8.4. Summary

This chapter presented the results of two experimental validation tests of the vibration-based MNETs for the identification of the elastic properties of the individual layers of layered materials. The first validation test was performed on a brass-steel bi-metal, the second test was performed on a purpose-built carbon-epoxy composite plate. The validation test showed that three MNET routines proposed in chapter 6 are able to identify the layer properties.

9
Applications

This chapter presents a number of applications of layered material identification, using the MNET-based procedures introduced in chapter 6, to identify the elastic properties of different types of ceramic coatings.

9.1. Introduction

This chapter presents two applications of layered material identification to determine the elastic properties of thermal barrier coatings. The air plasma sprayed coatings were provided by the University of Sheffield, the electron beam physical deposited coatings were produced by das Deutsches Zentrum für Luft- und Raumfahrt. Both coatings were produced in the framework of the European SICMAC project.

Note that all the experiments were performed with the same equipment and test set-up as in chapter 8. Remember that this test set-up is discussed in detail in appendix B. Also note that this chapter does not present all the experimental data and results. In general, only the data that is needed to understand the discussions and conclusions is provided. Appendix E presents a detailed description of all the test samples[1], sample models[2], together with the obtained elastic properties.

9.2. Air Plasma Sprayed Coatings

9.2.1. Introduction

In the automotive and aerospace industries, ceramic coatings are commonly used to shield metallic components from high temperatures and corrosive environments. Widely known as thermal barrier coatings (TBCs), they usually consist of two separate layers: a bond coat (BC) and a top coat (TC). The ceramic top coats are designed to shield the substrate from high temperatures, while the metallic bond coat protects the substrate from oxidation. Moreover, the bond coat bridges the thermal expansion coefficient mismatch that exists between the substrate and the TC, minimising the risk of delamination of the TC during cooling from the processing temperature.

There is a number of different ways to apply the coating on the substrate. Air plasma spraying (APS) is a thermal spraying process that consists of injecting ceramic powder particles into a direct current plasma jet. The high temperature jet melts the particles, without decomposing or vaporising them, and projects them towards the substrate. The liquid droplets strike the substrate's surface at high velocity, flatten to a disc and solidify. The coating process consists of various passes of the spraying torch over the substrate's surface, forming a coating layer with the required thickness.

The microstructure of an APS coating consists of a complex network of pores and cracks. The typical shape of the solidified droplets is that of a thin lamellae with a 'pancake' like form, known as splats. Certain cracks run along the splat interfaces, i.e. intersplat cracks, other cracks run across the splats, i.e. intrasplat cracks. This microstructure has a severe impact on the mechanical properties of the coating; the elastic modulus of an APS coating can be up to 20 times lower than the elastic modulus of the corresponding bulk material [108].

This test case considers a NiCoCrAlY bond coat and an yttria-stabilised zirconia (8YSZ) top coat. Figures 9.1 and 9.2 display the main microstructural

[1]The length, width, (layer)thickness, mass and resonant frequencies.

[2]The mesh size of the converged FE-model.

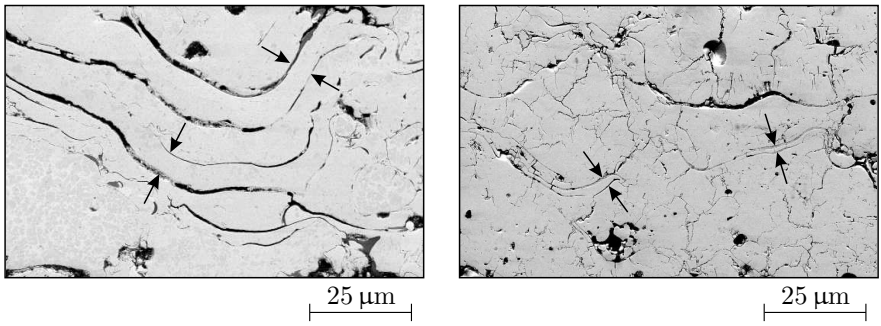

(a) Bond coat (b) Top coat

Figure 9.1: *Backscattered electron (BSE) images of the microstructure of APS-deposited (a) NiCoCrAlY bond coat, and (b) 8YSZ top coat. In both images, some of the splats are indicated by arrows. (SEM pictures used with kind permission of K. Lambrinou.)*

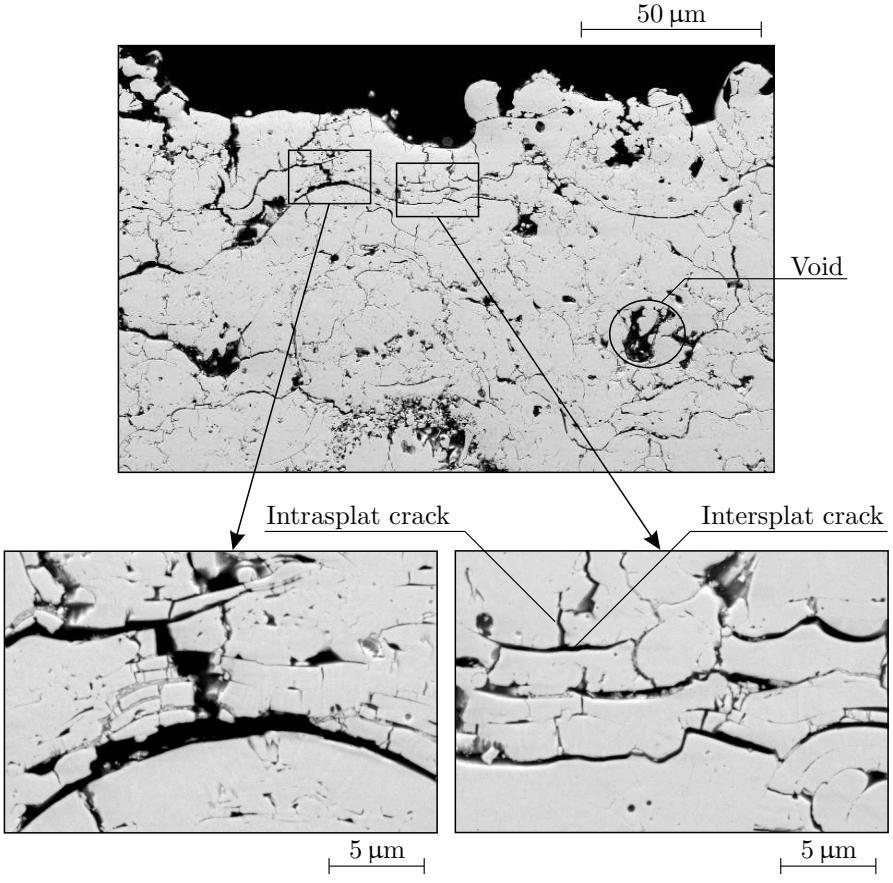

Figure 9.2: *BSE images of the microstructure of an APS 8YSZ top coat. (SEM pictures used with kind permission of K. Lambrinou.)*

features[3] of APS TBCs, i.e. pancake-like splats, inter- and intrasplat cracks, and voids. These figures clearly indicate that the APS ceramic top coat has a higher crack density than the APS metallic bond coat.

9.2.2. The Initial Samples

The test samples were plate-shaped specimens with a nominal dimension of 150×145 mm. The first specimen, ACS-01, was a pure steel substrate with a nominal thickness of 2 mm. Specimens ACB-01 and ACB-11 were steel plates coated with a layer of 250 µm and 500 µm of BC, respectively. The last two specimens, ACT-01 and ACT-11, were steel plates coated with a layer of 250 µm and 500 µm of TC, respectively. Tables E.56 and E.57 of appendix E provide a detailed description of these test samples.
The five test plates were far from optimal. First of all, the steel substrates were cut with a guillotine. As a result, the pure steel specimen has a dent along one of its sides. The coated specimens were also not flat. The difference between the thermal expansion coefficients of the substrate and coating materials resulted in a curvature of the specimens. These two sample deformations are schematically represented in figure 9.3.

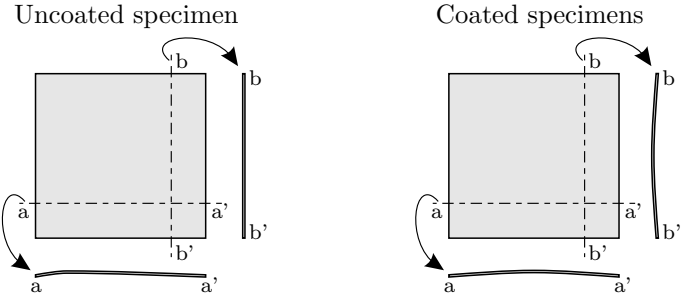

Figure 9.3: *The deformation of the plate-shaped samples.*

The Substrate Properties

The properties of the steel substrate were identified from the first five resonant frequencies of the pure steel sample ACS-01. Table 9.1 presents the obtained elastic parameters.

Table 9.1: *The elastic properties of the substrate.*

	E_1 [GPa]	E_2 [GPa]	G_{12} [GPa]	ν_{12} [–]
ACS-01	203.75	208.66	77.86	0.229

[3]The microstructural characterisation of the APS coatings presented in this thesis was performed by Dr. K. Lambrinou of the department of metallurgy and material engineering of the Katholieke Universiteit Leuven.

The Bond Coat Properties

The bond coat properties were identified in two different ways. First, the properties were identified from the first five resonant frequencies of a sample set consisting of one pure substrate sample and one coated sample: ACS-01/ACB-01 and ACS-01/ACB-11. Next, the properties were identified from the resonant frequencies of two coated samples: ACB-01/ACB-11. The obtained elastic properties of both substrate and BC are presented in tables 9.2 and 9.3.

Table 9.2: *The elastic properties of the steel substrate.*

	E_1 [GPa]	E_2 [GPa]	G_{12} [GPa]	ν_{12} [–]
ACS-01/ACB-01	203.79	208.68	77.85	0.229
ACS-01/ACB-11	203.75	208.66	77.85	0.229
ACB-01/ACB-11	193.31	204.00	71.55	0.353

Table 9.3: *The elastic properties of the NiCoCrAlY BC.*

	E_1 [GPa]	E_2 [GPa]	G_{12} [GPa]	ν_{12} [–]
ACS-01/ACB-01	Err.	Err.	Err.	Err.
ACS-01/ACB-11	30.92	25.27	11.81	0.121
ACB-01/ACB-11	28.38	17.26	16.29	0.043

For the sample combination ACS-01/ACB-01, there is no convergence of the bond coat properties. For the results of table 9.3, it can derived that the offset between the individual and the mean BC properties ranged between 4 % and 58 %, with an average of 24 %.

The Top Coat Properties

Like the bond coat properties, the TC properties were identified in two different ways: using uncoated/coated and coated/coated sample combinations. Tables 9.4 and 9.5 present the identified parameters. All three sample combinations provided an estimate of the TC properties. The difference between the individual and mean TC properties varied between 5 % and 67 %, with an average of 19 %.

Table 9.4: *The elastic properties of the steel substrate.*

	E_1 [GPa]	E_2 [GPa]	G_{12} [GPa]	ν_{12} [–]
ACS-01/ACT-01	203.75	208.66	77.85	0.229
ACS-01/ACT-11	203.75	208.66	77.85	0.229
ACB-01/ACT-11	206.19	209.95	76.56	0.271

Table 9.5: *The elastic properties of the 8YSZ TC.*

	E_1 [GPa]	E_2 [GPa]	G_{12} [GPa]	ν_{12} [–]
ACS-01/ACT-01	20.77	19.05	8.30	0.757
ACS-01/ACT-11	26.05	24.69	10.49	0.391
ACB-01/ACT-11	25.07	24.17	11.27	0.187

Discussion

The results were not very satisfactory. First of all, it appeared to be impossible to identify the coating properties of sample ACB-01. There was also a large variation in the properties obtained with different sample combinations, and this for both BC and TC. In addition, the agreement between the substrate properties identified from the pure substrate, and those identified from the coated/coated sample combinations was far from perfect.

There are clearly a number of severe problems with the identification of the coating properties, problems that are most likely related to the curvature of the test specimens. Appendix C shows that a double curvature, i.e. curvature in two orthogonal directions, of a plate-shaped sample has a severe influence on the resonant frequency of the third vibration mode. Since the frequency of the third mode is important for the estimation of Poisson's ratio, the identification of ν_{12} of curved samples is expected to be problematic. This expectation was confirmed by the identification of the Poisson's ratio of the 8YSZ TC, shown in Table 9.5.

9.2.3. The Beam-Shaped Specimens

The identification of the coating properties from the initial samples did not provide satisfactory results. The encountered problems were most likely caused by the curvature of the test plates. As illustrated in appendix C, the resonant frequencies of beam-shaped samples were much less sensitive to the sample deformation. Therefore, it was decided to cut a number of beam-shaped samples from the initial test plates and check whether these samples provided more consistent coating properties. A pre-test analysis showed that the curvature did not have a significant influence on the resonant frequencies of beam-shaped samples that measure 40×12 mm. Subsequently, these sample dimensions were used in a non-probabilistic uncertainty analysis. The results of this analysis indicate that a sample set comprising beams in the 0°, 45°, and 90° directions provided an accurate estimate of the coating properties and that an extension of this sample set with beams in the 22.5° and 67.5° directions did not improve the reliability of the identified coating properties.

Therefore, it was decided to cut nine 40×12 mm beam-shaped samples from every test plate, i.e. 3 sets of 3 samples in the 0°, 45°, and 90° direction. A preliminary cutting test was performed to find the optimal technique to cut the coated plates. Figure 9.4 presents the results of the preliminary cutting test of a TC-coated specimen, i.e. ACT-11. The test revealed that the TC spalls

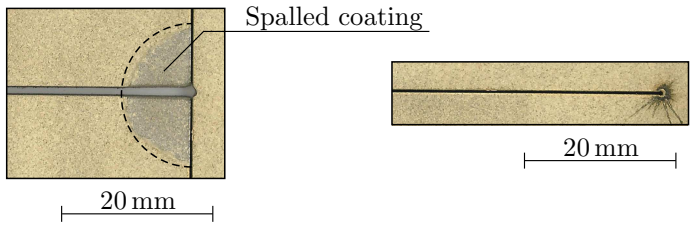

(a) High pressure water jet (b) Laser

Figure 9.4: *The results of a preliminary cutting test on a specimen coated with TC.*

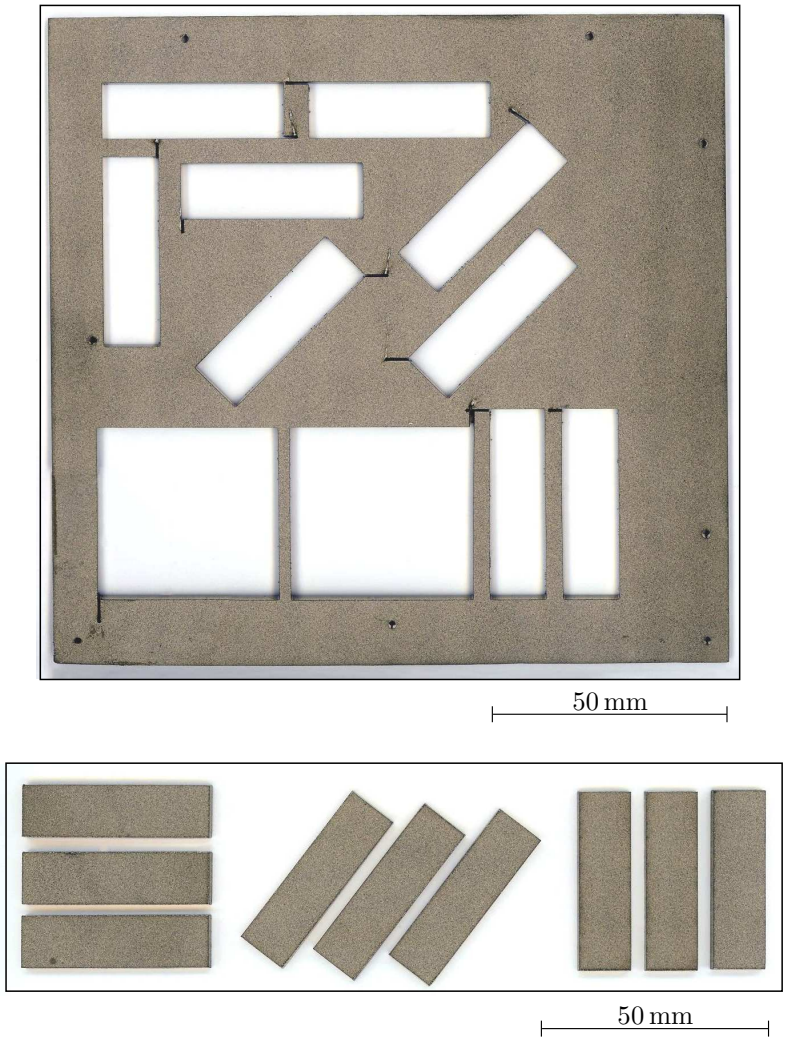

Figure 9.5: *The sample set cut out of the initial test plate ACB-01.*

off with high pressure water jet cutting. However, it is possible to cut the specimens without damaging the coating, using a laser. Figure 9.5 shows the sample set that was cut out of specimen ACB-01 with a laser cutting device. A similar sample set was cut out of the other four test plates.

The Substrate Properties

The substrate properties were identified from the fundamental flexural and torsional frequencies of the test beams with both the single- and multi-orientation routine. The plots of figure 9.6 present the identified elastic parameters, while tables 9.6 and 9.7 give the results in a numerical form. Note that appendix E provides a detailed description of all the specimens and the obtained results. The substrate appeared to be elastically anisotropic. The elastic modulus varied about 4.5 % in function of the material orientation, and was maximal for the direction perpendicular to the rolling direction. The difference between the minimal and maximal shear modulus was about 5 %. The single-orientation Poisson's ratios are not presented here, since they are incorrect in case of an anisotropic material; however, appendix E provides the numerical values of all the identified elastic parameters.

Table 9.6: *The results of the single-orientation routine.*

Dir. [°]	E [GPa]	G [GPa]
0.0	200.66	77.09
45.0	195.99	80.97
90.0	204.80	76.73

Table 9.7: *The results of the multi-orientation routine.*

E_1 [GPa]	E_2 [GPa]	G_{12} [GPa]	ν_{12} [–]
200.85	205.26	76.91	0.246

The Bond Coat Properties

The elastic properties of the bond coat were identified in two different ways.

Approach 1 — The coating properties were identified keeping the properties of the substrate fixed at the values identified from the pure substrate specimens. With the single-orientation routine, the coating properties were identified from the fundamental flexural and torsional frequencies of a single beam-shaped specimen. The substrate properties were fixed to the values of table 9.6 for the appropriate material orientation. With the multi-orientation routine, the coating properties were identified using all the beam-shaped samples with the same nominal coating thickness, i.e. 250 µm or 500 µm. During the identification, the substrate properties were fixed to the values of table 9.7.

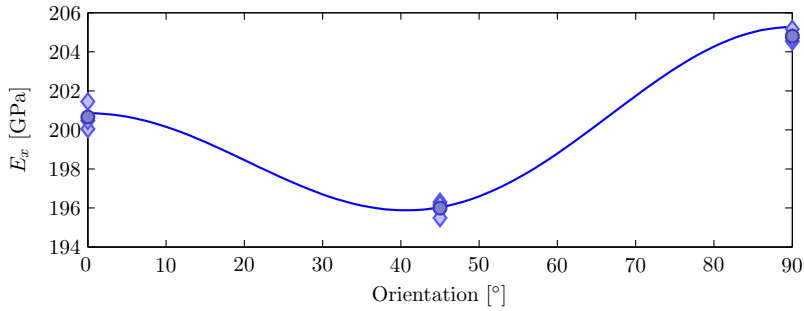

(a) The elastic modulus

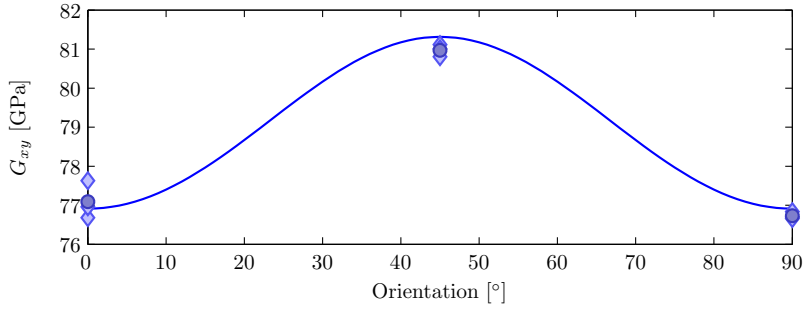

(b) The shear modulus

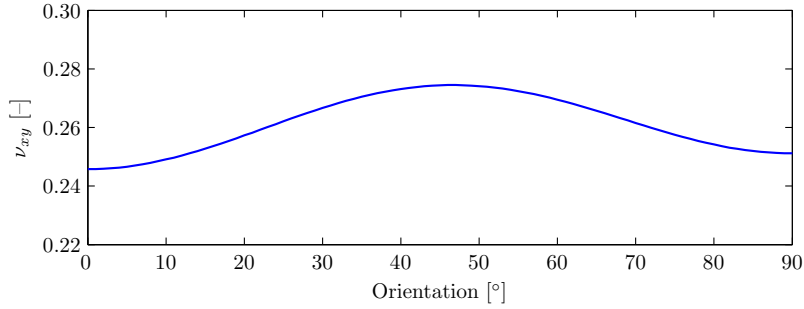

(c) The Poisson's ratio

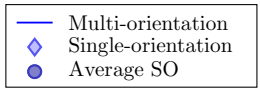

Figure 9.6: *The elastic properties of the steel substrate.*

Approach 2 — Since there were two different layer configurations available, i.e. a coating thickness of 250 µm and 500 µm, it was possible to identify the properties of both substrate and coating from the coated samples. Using the single-orientation routine, the properties were identified from the resonant frequencies of a sample set that comprised all the test beams cut in the same material direction. With the multi-orientation routine, the elastic properties were identified from the resonant frequencies of the sample set that comprised all the coated beam-shaped specimens.

Table 9.8: *The averages of the single-orientation results, approach 1.*

	250 µm coating			500 µm coating		
Dir. [°]	E [GPa]	G [GPa]	ν [–]	E [GPa]	G [GPa]	ν [–]
0.0	22.64	8.81	0.284	27.63	11.27	0.226
45.0	23.43	8.98	0.306	28.89	11.24	0.285
90.0	23.32	9.17	0.272	27.99	11.63	0.203

Table 9.9: *The multi-orientation results, approach 1.*

	E_1 [GPa]	E_2 [GPa]	G_{12} [GPa]	ν_{12} [–]
250 µm coating	22.83	23.59	9.04	0.287
500 µm coating	27.94	28.47	11.50	0.256

Table 9.8 and 9.9 present the single- and multi-orientation results of the first identification approach; figure 9.7 provides a graphical representation. The average difference between the properties obtained with the single- and multi-orientation routine is about 1.1 % for the elastic and shear modulus. The differences between the single- and multi-orientation Poisson's ratios was 5.2 % or 16.6 % for the 250 µm or 500 µm thick coating layer, respectively. The obtained results do not show a significant variation of the properties in function of the material orientation, which indicated that the bond coat was elastically isotropic. But the coating properties appeared to be varying in function of the coating thickness[4]. The 500 µm thick coating had an elastic and shear modulus that were about 20 % higher than the respective moduli of the 250 µm thick coating.

A microstructural characterisation of the bond coat revealed that the 250 µm thick layer had a slightly higher concentration of microcracks and other imperfections than the 500 µm layer. The SEM results thus supported the statement that the elastic and shear modulus increased with an increasing coating thickness. With an uncertainty analysis, it is possible to determine whether the difference between the properties of the 250 µm and 500 µm coating can be due

[4]The elastic properties of the coating vary as a function of the coating thickness. This is not the same as claiming that the elastic coating properties vary in the thickness direction. In the identification procedure, the coatings were considered to be homogeneous. This implies that these tests did not provide any information on the variation of the layer properties in the thickness direction.

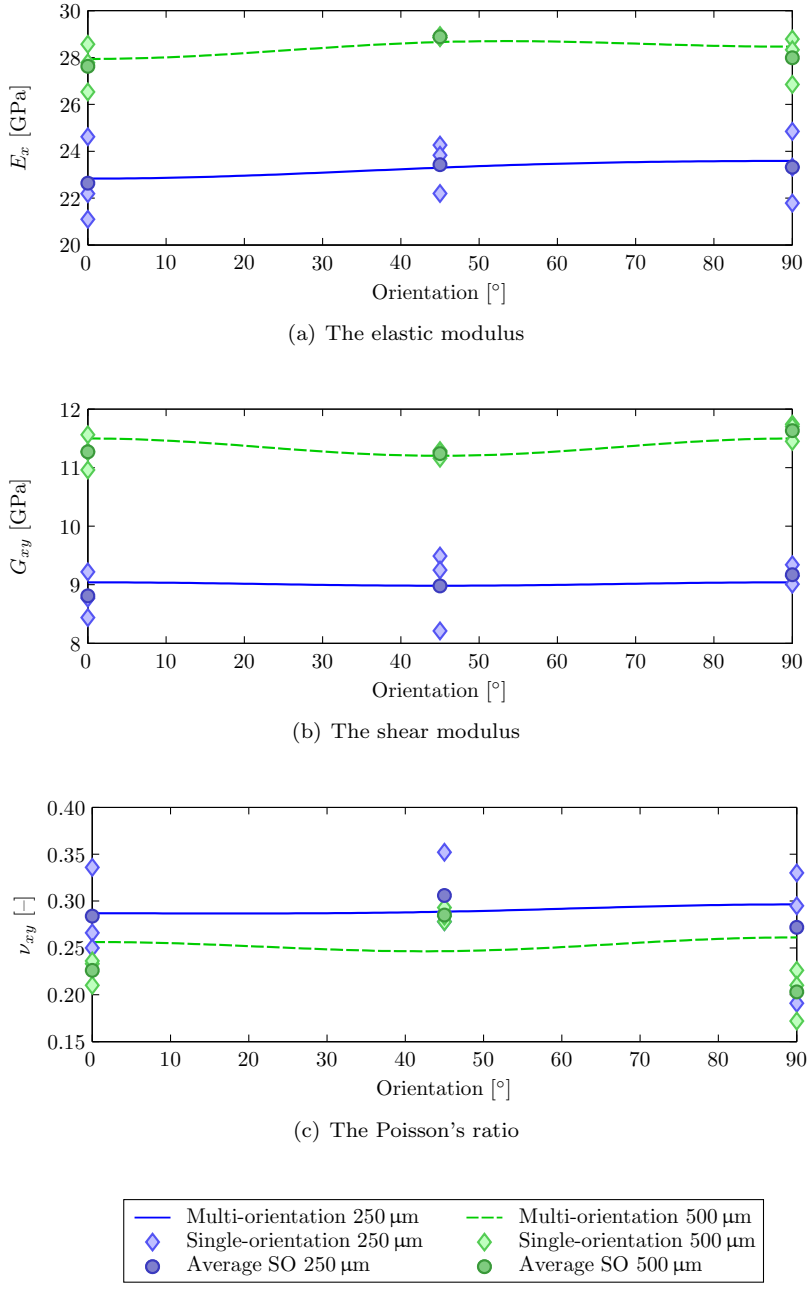

Figure 9.7: *The properties of the NiCoCrAlY BC, approach 1.*

to the spread of the identified parameters, or if the two layers actually have significantly different elastic properties. Consider the following uncertainties of the input parameters.

Table 9.10: *The uncertainties of the input parameters.*

	Uncertainty	Units
Length	± 0.02	[mm]
Width	± 0.02	[mm]
Mass	± 0.001	[g]
Substrate thickness	± 0.002	[mm]
Coating thickness	± 0.040	[mm]
Resonant frequencies	± 0.1	[%]

The most uncertain parameter is the coating thickness. As a precaution, the uncertainty of the average coating thickness was taken relatively high. This was done so as to make sure that the uncertainty of the identified parameters was not underestimated. The output uncertainties were estimated with the probabilistic uncertainty analysis routine introduced in chapter 7. Figure 9.8 presents the obtained confidence intervals. The plots reveal that the difference between the properties of the 250 µm and 500 µm coating layers was not the result of the input parameter uncertainties. The confidence intervals of the elastic moduli only overlaped for confidence levels higher than 97 %, while the confidence intervals of the shear modulus did not even overlap for a confidence level as high as 99.7 %. Based on this, it is clear that the two coating layers have different elastic and shear moduli. However, the difference in Poisson's ratio can easily be the result of the uncertainty of the input parameters.

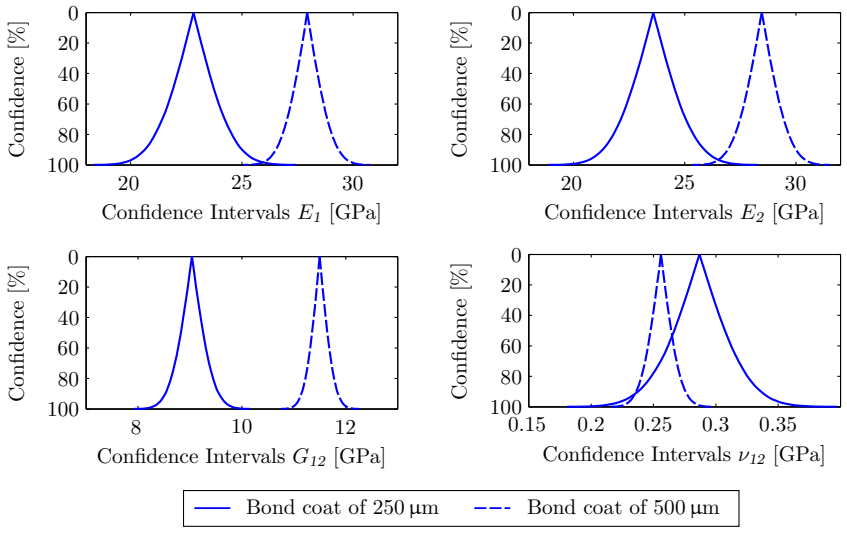

Figure 9.8: *The confidence intervals of the BC properties.*

The second identification approach provided the properties of both substrate and coating. However, in the case of the considered bond coat this approach could not be used. The 250 µm and 500 µm thick coatings did not have the same elastic properties, while the second identification approach made the assumption that the properties of the coating did not vary with the coating thickness. It is thus very unclear how the identified parameters should be interpreted. For reasons of completeness, appendix E provides an overview of the properties obtained with the second identification approach.

The Top Coat Properties

The technician who cut the test beams from the initial plates made a mistake while cutting the specimens with the 250 µm thick TC. Instead of cutting three samples in every material direction, he cut four samples in the 0° direction and only two specimens in the 90°direction. The initial test plates also had a number of suspension holes which can be seen in figure 9.5. Unfortunately, the technician did not notice these holes and cut a sample from an area that covered one of the suspension holes. Furthermore, after measuring the specimens and comparing the obtained data, it appeared that specimen ACT-14 had a much higher damping than all the other samples. This is an indication of possible delamination of the coating layer due to the cutting process.
The TC properties were identified with the same identification approaches used to estimate the BC properties. Tables 9.11 and 9.12 present the single- and multi-orientation results of the first identification approach, while figure 9.9 provides a graphical representation. The average difference between the properties obtained with single- and multi-orientation routine is 6.2 % for the elastic modulus, and 1.5 % for the shear modulus. Note that the TC was found to have a Poisson's ratio of zero, therefore it is not meaningful to compute the relative difference between the Poisson's ratios obtained with the single- and multi-orientation routine. Like for the bond coat, there is no significant variation in the properties as a function of the material orientation, which indicated that the ceramic top coat was also isotropic. In contrast to the bond coat, the properties of the TC did not vary in function of the coating thickness.
Figure 9.2 shows the microstructure of the TC, revealing the presence of a huge amount of internal microcracks. Due to these microcracks, the material is more or less segmented, so that a deformation in one direction does not cause a deformation in an orthogonal direction, which means that there is no Poisson effect. The properties identified with the MNET routine thus agree with the results of the microstructural characterisation of the TC by SEM.

Table 9.11: *The averages of the single-orientation results, approach 1.*

	250 µm coating			500 µm coating		
Dir. [°]	E [GPa]	G [GPa]	ν [–]	E [GPa]	G [GPa]	ν [–]
0.0	22.80	11.72	−0.021	24.49	12.39	−0.012
45.0	25.85	12.38	0.049	26.17	12.09	0.083
90.0	22.90	12.19	−0.054	22.45	11.87	−0.054

Note that the properties of sample ATC-14, which was probably damaged, and

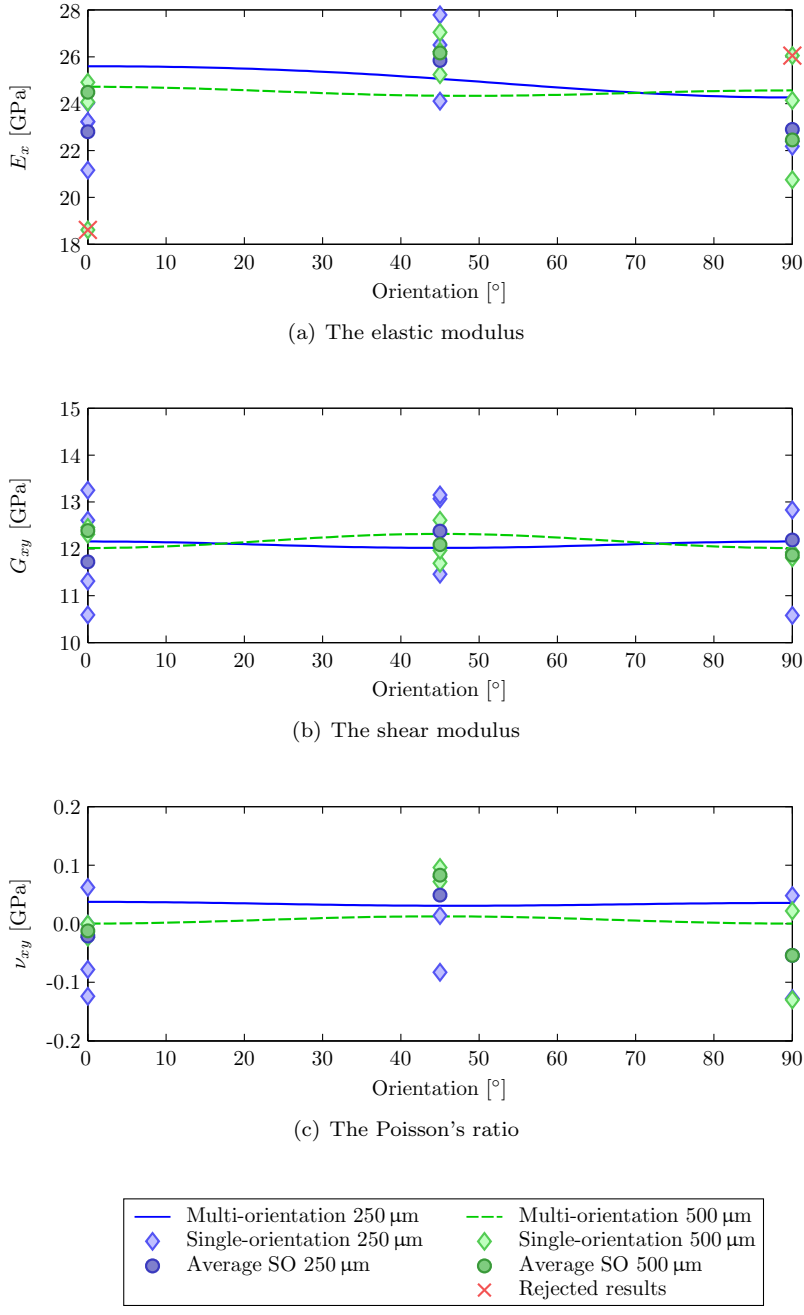

(a) The elastic modulus

(b) The shear modulus

(c) The Poisson's ratio

Figure 9.9: *The properties of the 8YSZ TC, approach 1.*

Table 9.12: *The multi-orientation results, approach 1.*

	E_1 [GPa]	E_2 [GPa]	G_{12} [GPa]	ν_{12} [–]
250 µm coating	24.72	24.57	12.018	0.000
500 µm coating	25.60	24.27	12.157	0.037

sample ATC-18, which had a suspension hole, were rejected. Also note that the multi-orientation routine used a weighted least-square cost-function. The weighting coefficients were chosen in such a way that every material direction had the same importance. Table 9.13 gives an overview of the used weighting coefficients (w_i). Appendix E presents all the results in detail.

Table 9.13: *The weighting coefficients of the multi-orientation routines.*

Dir. [°]	250 µm coating			500 µm coating		
	n_s	w_i	$\sum n_s w_i$	n_s	w_i	$\sum n_s w_i$
0.0	4	0.75	3.00	2	1.50	3.00
45.0	3	1.00	3.00	3	1.00	3.00
90.0	2	1.50	3.00	2	1.50	3.00

Since the properties of the TC did not vary with the coating thickness, the properties of both substrate and coating could be identified by means of a sample set that comprised specimens with both a 250 µm and a 500 µm coating layer. Table 9.14 and 9.15 present the results of the second identification approach for the single- and multi-orientation routine, respectively. The plots of figures 9.10 and 9.11 present these results in a graphical form.
With the single-orientation routine, the properties were identified from a sample set that comprised all the coated samples representing the same material orientation. The response weights in the MNET's cost-function were chosen in such a way that the layer configurations, i.e. the 250 µm and 500 µm thick coatings, always had the same importance, i.e. the response weights of table 9.13. The single-orientation routine provided acceptable results. The average difference between the identified and reference[5] substrate properties was about 1.4 %, while the average difference between the identified and reference[6] coating properties was estimated at about 10 %.
With the multi-orientation routine, the elastic properties were identified from the resonant frequencies of a sample set that comprised all the coated samples, using the response weights of table 9.13. Table 9.15 presents the results of the multi-orientation routine. For the substrate properties, there was an average difference of only 0.4 % between the identified and reference properties. For the

[5]The properties obtained with the multi-orientation routine on the pure substrate samples are used as reference data for the substrate.

[6]The average of the properties obtained with the first identification approach using the multi-orientation routine are used as reference data for the coating.

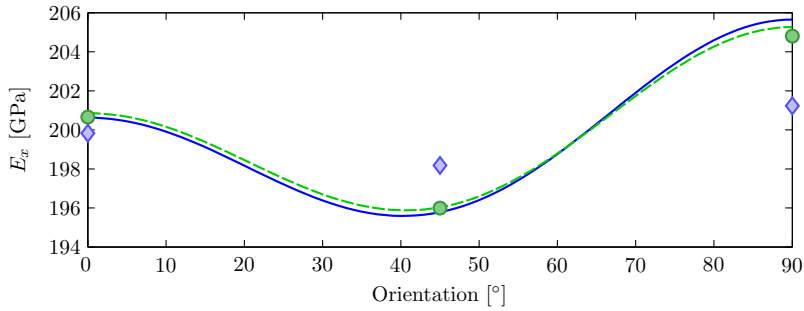

(a) The elastic modulus

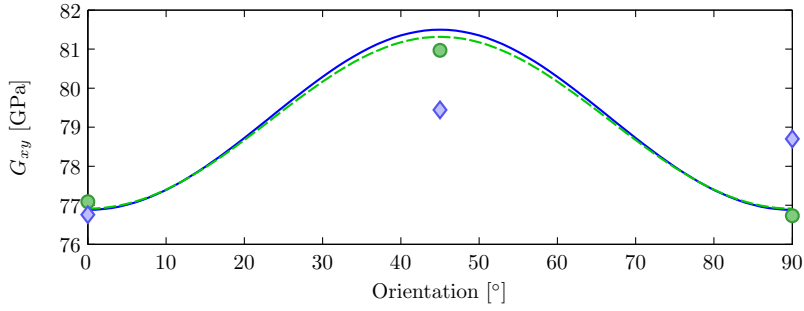

(b) The shear modulus

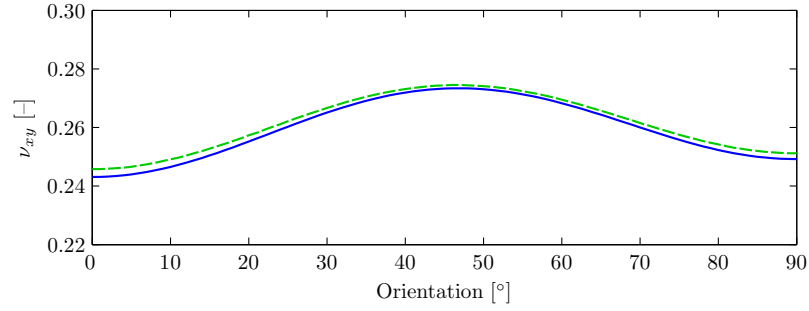

(c) The Poisson's ratio

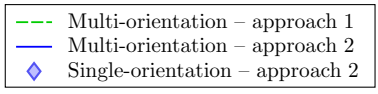

Figure 9.10: *The properties of the steel substrate, approach 2.*

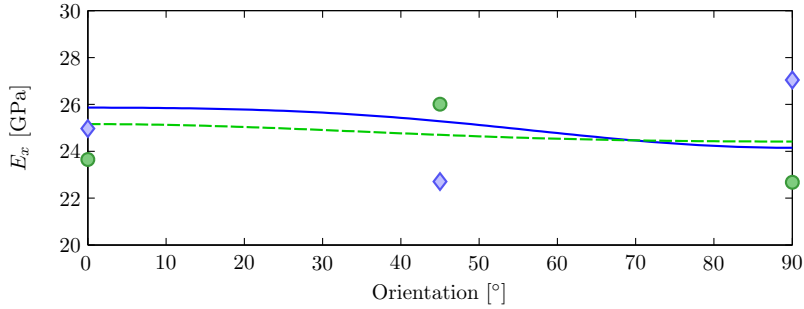

(a) The elastic modulus

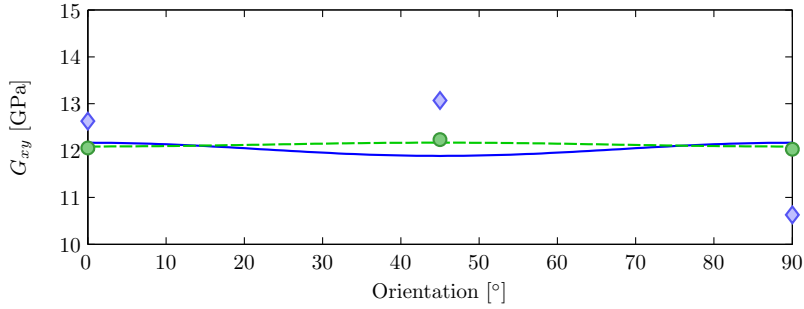

(b) The shear modulus

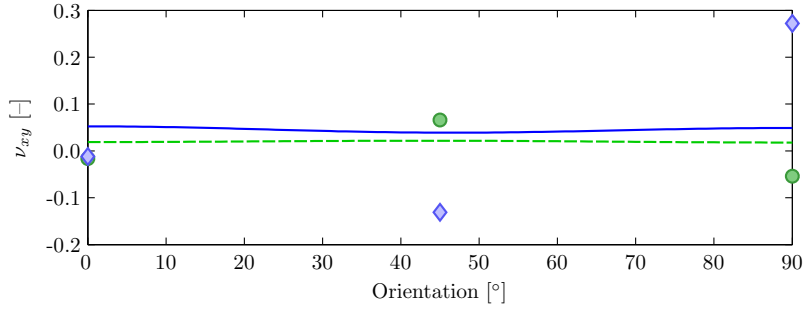

(c) The Poisson's ratio

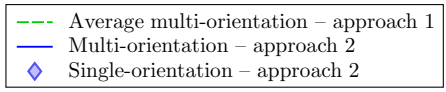

Figure 9.11: *The properties of the 8YSZ TC, approach 2.*

Table 9.14: *The single-orientation results, approach 2.*

	Substrate properties		TC properties		
Dir. [°]	E [GPa]	G [GPa]	E [GPa]	G [GPa]	ν [–]
0.0	199.83	76.76	24.97	12.63	−0.012
45.0	198.18	79.44	22.71	13.07	−0.131
90.0	201.23	78.70	27.04	10.63	0.272

coating properties, there was an average difference of 1.5 % from the reference properties[7].

Table 9.15: *The multi-orientation results, approach 2.*

	E_1 [GPa]	E_2 [GPa]	G_{12} [GPa]	ν_{12} [–]
Substrate	200.63	205.65	76.88	0.243
TBC	25.86	24.14	12.17	0.052

Discussion

Unlike the plate shaped specimens, the beam-shaped specimens provided meaningful results. Using the beam-shaped specimens, the elastic parameters of the substrate and coatings could be identified. Both coatings proved to be elastically isotropic[8]. For the bond coat, the elastic and shear moduli of the 500 µm thick layer were found to be about 20 % higher than the respective moduli of the 250 µm thick layer. An uncertainty analysis revealed that this difference could not be attributed to the uncertainty of the identified properties. The bond coat properties thus varied in function of the thickness of the coating layer. This implies that the bond coat properties could not be identified from a sample set that comprised specimens with different coating thicknesses. The properties of the top coat did not vary in function of the thickness. The TC properties were identified in two different ways: using a combination of coated and uncoated samples, and using a combination of coated samples with different coating thicknesses. Both identification approaches provided similar results. Note that the TC was found to have a zero Poisson's ratio, and that this observation was supported by the microstrucural characterisation.

9.2.4. Conclusions

A few interesting conclusions concerning the performance of the MNET routines can be drawn from the test case presented in this section.

[7]The Poisson's ratio of the TBC is very low, a small difference in absolute terms easily results in a large relative difference. Therefore, the difference on the Poisson's ratio values were not taken into account for the calculation of the average difference with the reference properties.

[8]The considered identification methods only provide information about the in-plane behaviour. The coatings are isotropic in the plane of the samples, however, the elastic properties in the transverse direction may vary from the in-plane properties.

The experiments confirmed the conclusions of the theoretical study of appendix C. The influence of the sample curvature on resonant frequencies of plate-shaped specimens was indeed too large for material identification purposes. As predicted, the identification of the layer properties from the resonant frequencies of beams-shaped specimens did not pose any problems. It is thus advisable to use a set of beam-shaped samples to identify the properties of coatings.
In case the substrate properties can be measured from a set of pure substrate samples, the identification of the coating properties functions well for both the single- and multi-orientation routines. If the coating is isotropic, the single-orientation routine can provide an acceptable estimation of the coating's Poisson's ratio, even with an anisotropic substrate.
In case the substrate properties cannot be measured from a set of pure substrate samples, the coating properties can be identified from two layer configurations with the same substrate but with a different coating thickness. In this situation, the multi-orientation routine is clearly superior to the single-orientation routine, i.e. the single-orientation routine provides a rough estimation of the properties, while the multi-orientation routine identifies the properties.

9.3. Electron Beam – Physical Vapour Deposited Coatings

9.3.1. Introduction

The NiCoCrAlY and the yttria-stabilised zirconia coatings studied in the previous test case can also be produced with the electron beam – physical vapour deposition (EB-PVD) technique. With this technique, the ceramic material is vaporised into a gas phase and ionised by a high-power electron beam. The substrate is heated to improve adhesion and electrically loaded to attract the ceramic ions. Eventually, the ceramic vapour condenses onto the substrate forming the coating layer. Note that the whole process takes place in a vacuum chamber to prevent the contamination of the coating with foreign molecules.

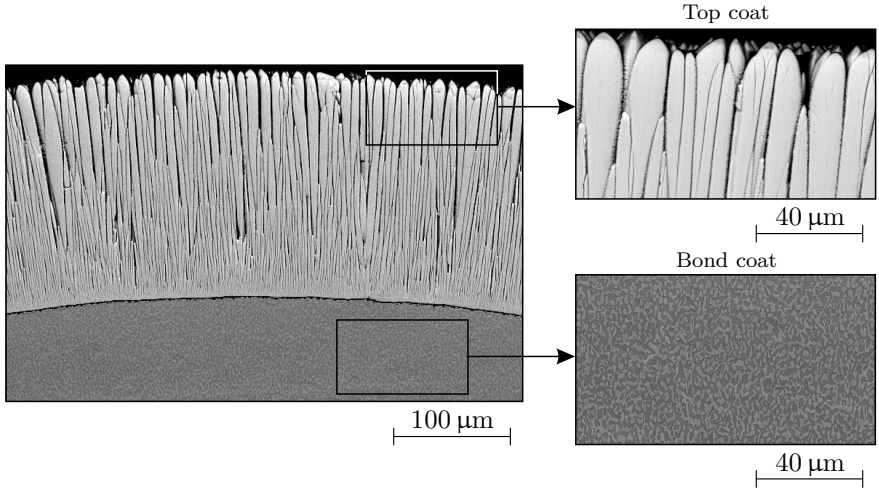

Figure 9.12: *The microstructure of the EB-PVD TBCs.* *(SEM pictures used with kind permission of K. Lambrinou.)*

The EB-PVD coatings had a fundamentally different microstructure[9] than the APS coatings. The EB-PVD bond coat was a dense material without cracks or pores. The EB-PVD top coat had a columnar structure. Figure 9.12 displays the microstructure of both BC and TC.

9.3.2. The Test Samples

The EB-PVD test samples were cylinders with a nominal length of 67 mm and a substrate diameter of about 2 mm. The substrate material was the Ni-based super-alloy Inconel 625. Ten substrates were produced by machining cylinders from a monolithic block of Inconel. Nine substrates were coated with a layer of bond coat. Seven of the coated samples also received a layer of TC. Figure 9.13 presents the layer configurations of the ten test samples. Note that between every intermediate step of the coating process, the diameter of the test specimens was measured with a microscope.

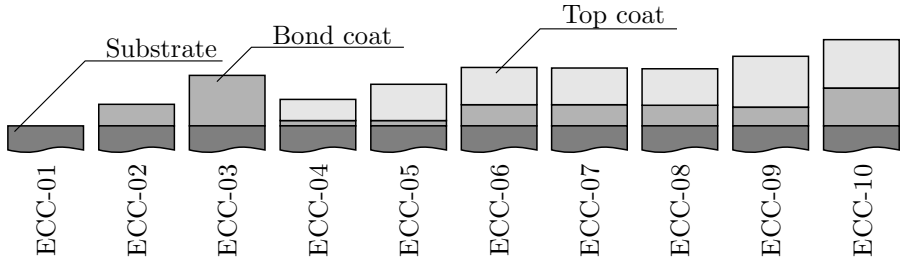

Figure 9.13: *The layer configurations of the ten test samples.*

For every test sample, the length, layer thicknesses, mass, and resonant frequency of the first flexural mode were determined. Table E.66 of appendix E presents the measured sample properties. For identification purposes, the ten test samples were grouped into five different sample sets; table 9.16 gives an overview.

Table 9.16: *The considered sample sets of EB-PVD cylinders.*

	Set 1	Set 2	Set 3	Set 4	Set 5
ECC-01	✓	✓	—	✓	—
ECC-02	—	✓	✓	✓	—
ECC-03	—	✓	✓	✓	—
ECC-04	—	—	—	✓	✓
ECC-05	—	—	—	✓	✓
ECC-06	—	—	—	✓	✓
ECC-07	—	—	—	✓	✓
ECC-08	—	—	—	✓	✓
ECC-09	—	—	—	✓	✓
ECC-10	—	—	—	✓	✓

[9]The microstructural characterisation of the EB-PVD coatings presented in this thesis was performed by Dr. K. Lambrinou of the department of metallurgy and material engineering of the Katholieke Universiteit Leuven.

9.3.3. The Identification Routine

Chapter 6 does not present any routines to identify elastic properties using cylindrical specimens. However, cylindrical specimens behave basically the same as beam-shaped specimens. There is only one important difference: it is practically impossible to measure torsional frequencies of cylindrical specimens. As a result, the measured frequencies only provide information about the elastic moduli.

The single-orientation routine for beam-shaped specimens can be modified to identify the properties of cylindrical specimens. Layered cylindrical specimens can easily be modelled with the finite element method. Figure 9.14 shows a close-up of the mesh of an EB-PVD sample with both BC and TC. Note that the coating layers are partially removed for visualisation purposes. In the MNET, the fundamental flexural frequencies of the FE-models were updated by fine-tuning the elastic moduli of the substrate and coating layers. Once the solution has converged, the procedure was aborted, and the elastic moduli could be extracted from the material database of the FE-models.

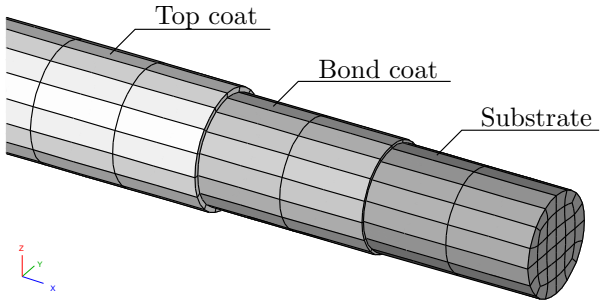

Figure 9.14: *Close-up of the FE-model, a part of the coating was removed for visualisation purposes.*

9.3.4. The Identified Properties

The Substrate

The first sample was a pure, uncoated substrate. The Inconel 625 properties can be derived from the resonant frequency of the fundamental flexural mode of this sample, i.e. sample set 1. The identification resulted in an elastic modulus of 203.86 GPa. Because of the simplicity of the identification procedure, this value is assumed to be reliable. Therefore, it was used as a reference value to estimate the accuracy of the properties identified from the coated specimen.

The Bond Coat

The second and third sample were only coated with a bond coat. The identification of a uniform coating requires two different layer configurations. Useful sample sets were: a set comprising coated and uncoated substrates, or a set comprising coated samples with different coating thicknesses.

Sample set 2 comprises the substrate sample and the two samples with bond coat. To balance the importance of the resonant frequencies of the two layer configurations, the frequency of the uncoated sample was given a weighting coefficient of 2, while the frequencies of the bond coat samples were given a weighting coefficient of 1. Table 9.17 presents the results obtained from set 2.

Table 9.17: *The results obtained using sample set 2.*

	E [GPa]
Sub	204.74
BC	194.90

Sample	f_{exp} [Hz]	f_{num} [Hz]	Diff. [%]	w_i [–]
ECC-1	3860.72	3869.02	−0.21	2
ECC-2	4038.85	4003.74	0.87	1
ECC-3	4370.02	4389.21	−0.44	1

Since the coating of sample ECC-3 was about two times as thick as the coating of sample ECC-2, the bond coat properties could also be identified from a sample set comprising the two bond coated samples, i.e. sample set 3. Table 9.18 presents the results obtained from this sample set.

Table 9.18: *The results obtained using sample set 3.*

	E [GPa]
Sub	213.85
BC	176.35

Sample	f_{exp} [Hz]	f_{num} [Hz]	Diff. [%]	w_i [–]
ECC-2	4038.85	4038.85	0.00	1
ECC-3	4370.02	4370.02	0.00	1

Note that the zero residuals associated with sample set 3 do not imply a high reliability of the results. The identification problem linked to sample set 3 identifies two unknown parameters from two experimental quantities, so mathematically, there has to be an exact solution. Therefore, the zero residuals just indicate that the problem was not overdetermined, they do not provide any information about the reliability of the identified elastic properties.

The Top Coat

The identification of the properties of the ceramic top coat required three different layer configurations. The full sample set, i.e. set 4, comprised one pure substrate, two samples coated only with BC, and seven samples coated with both BC and TC. To have a balanced weighting between the three layer configurations of this sample set, the response of the pure substrate was weighted with a factor 7, the responses of the two bond coat samples were weighted with a factor 3.5, and the responses of the other samples were weighted with a unit weight. Table 9.19 presents the results obtained from sample set 4.
Sample set 5 comprised only the cylinders that were coated with both BC and TC. The thicknesses of the BC and TC were not constant but varied from sample to sample; only samples ECC-6, ECC-7, and ECC-8 had the same nominal thickness for the two coating layers. Since the sample set comprised

Table 9.19: *The results obtained using sample set 4.*

	E [GPa]
Sub	204.84
BC	193.73
TC	35.74

Sample	f_{exp} [Hz]	f_{num} [Hz]	Diff. [%]	w_i [–]
ECC-1	3860.72	3869.97	−0.2	7
ECC-2	4038.85	4002.21	0.9	3.5
ECC-3	4370.02	4384.84	−0.3	3.5
ECC-4	3844.40	3838.15	0.2	1
ECC-5	3803.14	3794.66	0.2	1
ECC-6	4004.45	4008.36	−0.1	1
ECC-7	4002.17	3984.70	0.4	1
ECC-8	4008.97	4041.03	−0.8	1
ECC-9	4305.94	4335.76	−0.7	1
ECC-10	4307.72	4288.02	0.5	1

more than three layer thickness sets with a significant difference, it could be used to identify the properties of the three considered materials. Table 9.20 provides the results obtained from sample set 5.

Table 9.20: *The results obtained using sample set 5.*

	E [GPa]
Sub	202.68
BC	189.18
TC	42.61

Sample	f_{exp} [Hz]	f_{num} [Hz]	Diff. [%]	w_i [–]
ECC-4	3844.40	3832.51	0.3	1
ECC-5	3803.14	3800.92	0.1	1
ECC-6	4004.45	4011.23	−0.2	1
ECC-7	4002.17	3987.37	0.4	1
ECC-8	4008.97	4043.24	−0.9	1
ECC-9	4305.94	4316.44	−0.2	1
ECC-10	4307.72	4284.85	0.5	1

Discussion

The elastic moduli of the substrate and coating layers were identified using five different sample sets. Table 9.21 gives an overview of the results and compares the obtained elastic moduli with the reference values.

Note that there were two different types of sample sets: the first type comprised a number of layer configurations with a varying number of layers, while the second type comprised layer configurations with a constant number of layers. In both types of sample sets, the thickness of the individual layers varied from one configuration to another. Sample sets 2 and 4 belonged to the first type, while sample sets 3 and 5 belonged to the second.

Table 9.21 reveals that the results obtained with sample sets 2 and 4 corresponded better to the reference values than the results obtained with sample sets 3 and 5. This means that, the results obtained with a sample set of the

Table 9.21: *Summary of the obtained results. The results that are used as reference values are printed in boldface.*

	E_{Sub}		E_{BC}		E_{TC}	
Set 1	**203.9**	—	—	—	—	—
Set 2	204.7	0.4 %	**194.9**	—	—	—
Set 3	213.9	4.9 %	176.4	−9.5 %	—	—
Set 4	204.8	0.5 %	193.7	−0.6 %	**35.7**	—
Set 5	202.7	−0.6 %	189.2	−2.9 %	42.6	19.2 %
	[GPa]		[GPa]		[GPa]	

first type appeared to be more reliable than the results obtained with a sample set of the second type. In the considered case, the sample sets of the second type provided only a rough estimation of the layer properties.
The comparison of the microstructure of APS and EB-PVD bond coats suggested that the EB-PVD coating should be stiffer than the APS coating. The MNET routines showed that the EB-PVD bond coat has an elastic modulus that is about eight times higher than the APS one. The difference between the two top coats is less severe, since the EB-PVD top coat was only about 20 % stiffer than the APS top coat. This smaller difference is most probably related to the microstructure of the EB-PVD top coat. Unlike the bond coat, the EB-PVD top coat does not have a flawless microstructure. The columnar structure of the top coat introduces a vast amount of interface which, most likely, has a negative effect on the bending stiffness of the material.

9.3.5. Analytical Identification Approach

The properties of the EB-PVD coatings can also be identified with an extended version[10] of the analytical approach presented in [6]. Table 9.22 presents the obtained properties and compares them with the reference properties of table 9.21. The analytical approach provides coating properties that are about 1 % higher than the properties identified with the MNET approach. Appendix D shows that analytical approach overestimates the coating properties due to the homogenisation of the stiffness properties during the idetification of the overall stiffness of the layered samples. Note that the magnitude of this overestimation varies with the difference in stiffness and thickness of the coating layers.

Table 9.22: *The results of the analytical identification approach.*

	Value	Difference
E_{Sub}	204.1	0.1 %
E_{BC}	196.2	0.7 %
E_{TC}	36.3	1.2 %
	[GPa]	

[10]The extended identification equations are provided in appendix D.

9.3.6. Conclusion

This test case illustrated the flexibility of the MNET routines; the single-orientation routine of chapter 6 was easily modified to identify the elastic moduli from the resonant frequencies of cylindrical specimens. The obtained results indicated that the optimal sample set to identify the properties of coatings should comprise layer configurations with an increasing number of layers.

9.4. Summary

This chapter presented two applications of layered material identification using the vibration-based MNET procedures presented in chapter 6. In the first application, the elastic properties of two plasma sprayed coatings were successfully identified. Due to the curvature of the material samples, the elastic properties could only be correctly identified using a set of beam-shaped samples that were cut out of the initial material samples. In the second application, the Young's modulus of electron beam – physical vapour deposited coating were identified from a set of ten cylindrical specimens using the single-orientation routine.

10
Conclusions

This chapter presents the general conclusions of the work performed in the framework of this thesis, and provides suggestions for future research.

10.1. Conclusions

10.1.1. The MNET Identification Routines

The main goal of this thesis was to develop an identification routine for the determination of the elastic material properties of the constituent layers of layered materials.

Based on the classical lamination theory, it has been shown that the bending stiffness of layered materials is controlled by the overall material stiffness, and not by the stiffness of the individual layers. Consequently, it is impossible to identify the elastic properties of the constituent layers from the bending stiffness of a single test specimen. The bending stiffness of the material can only be decomposed into layer stiffnesses by using a number of samples with different layer configurations; a different layer configuration is obtained by changing the layer thickness or the stacking sequence. It was proven that the minimum number of required layer configurations equals the number of independent layer materials that must be characterised.

This work proposes a vibration-based mixed numerical-experimental technique (MNET) for the identification of the elastic properties of layered materials. The experimental part of the MNET consists of measuring a number of resonant frequencies on freely vibrating test samples. The numerical part of the MNET uses finite element models to compute the resonant frequencies of the test samples. The elastic properties of the constituent layers are identified by fine-tuning the corresponding model parameters until a match between the experimental and numerical resonant frequencies is obtained.

Three identification routines, all based on the same MNET approach, have been introduced in this text. The first routine determines the elastic properties of isotropic layers from the fundamental flexural and torsional resonant frequencies of a number of beam-shaped samples, all cut in the same material direction. The second routine identifies the elastic properties of orthotropic layers from the fundamental flexural and torsional resonant frequencies of a number of beam-shaped specimens, all cut in a different material direction. Note that this routine is based on the new concept of using samples in different material orientations, which enables the identification of the properties of orthotropic materials using beam-shaped samples. The third identification routine determines the elastic properties of orthotropic layers from the resonant frequencies of the first five vibration modes of plate-shaped specimens.

This thesis also introduces an uncertainty analysis procedure for vibration-based MNET routines. The developed uncertainty analysis routine estimates the uncertainty of the identified material properties from the uncertainties of the input parameters in a computationally efficient way. The routine is available in both a probabilistic and a non-probabilistic form and can be applied to all three identification routines.

The presented identification techniques are not only provided with a sound theoretical foundation, they have also been thoroughly evaluated in an experimental way. After being successfully validated on two different purpose-built layered materials, the vibration-based MNET technique was used to identify the elastic properties of a number of ceramic coatings.

10.1.2. Comparison to the State-of-the-Art

The most advanced identification techniques for layered materials found in literature are the techniques described in [6, 10]. These two techniques were discussed in the introduction, and were found to have a number of shortcomings. This section compares the developed MNET-based routines with the techniques of [6, 10] in order to evaluate the contribution of this thesis to the state-of-the-art.

Orthotropic Materials — The techniques of [6, 10] are limited to materials with isotropic layers. The MNET-based techniques developed in this thesis can determine the elastic properties of materials with isotropic, orthotropic, or a mixture of isotropic and orthotropic layers.

Sample Shape — The vibration-based technique of [6] is restricted to prismatic bars with a circular or rectangular cross-section and a symmetric layer sequence. The quasi-static technique of [10] is limited to beam- and plate-shaped samples. The MNET-based approach does not pose any significant restriction on the sample geometry. The MNET-based techniques can be applied using sample with both a symmetric or a non-symmetric layer stacking and having any possible regular shape[1]. Also note that the quasi-static technique [10] identifies E from beam-shaped specimens and ν from plate-shaped specimens, while the MNET techniques are able to identify both E and ν on beam- and plate-shaped specimens.

Sample Set — The techniques of [6,10] require a particular set of test samples, i.e. a set with specimens that have an increasing number of layers, without justifying why this is necessary. Chapter 5 shows that this problem is related to the physics of the mechanical behaviour of layered materials: the bending stiffness only provides information about the overall stiffness, it does not provide any information about the stiffness of the constituent layers. Any technique that uses the overall bending stiffness to determine the layer properties will require a set of test samples with different layer configurations.
Unlike the technique of [6, 10], the MNET-based techniques proposed in this thesis are capable of identifying the layer properties from a set of samples with the same number of layers, but different layer thicknesses. This is however not an advisable approach since uncertainty analyses have shown that optimal results are obtained with a sample set that comprises specimens with an increasing number of layers.

Partially Coated Samples — Partially coated samples are useful to investigate the strain-dependent behaviour of ceramic coatings [109]. The techniques of [6, 10] are incapable of identifying the layer properties using partially coated specimens. With the MNET-based technique suggested here, partially coated samples do not pose any problem, as long as the coated area is large enough to yield a measurable influence on the sample stiffness.

Contactless — The quasi-static technique [10] is not contactless. On the other hand, the MNET-based identification of the layer properties can easily be performed in a contactless way, i.e. by exciting the specimen acoustically and

[1] Beam-shaped, plate-shaped, disk-shaped, cylindrical rods, tubes, rings, etc.

measuring its response with a laser vibrometer. The MNET-based techniques can thus be applied to measure the properties of porous or thin brittle materials.

Layer Thicknesses — The first test configuration of the quasi-static technique [10] does not derive the layer stiffness from the overall bending stiffness of the test specimen. Because of this, the first configuration of the quasi-static technique [10] is less sensitive to errors related to layer thicknesses than the vibration-based identification techniques, a fact that can be considered as an advantage of the quasi-static technique [10].

Uncertainty — The uncertainty analysis routines that were developed for the MNET-based techniques are more powerful that the error propagation approach that is suggested in [10]. Unlike the approach of [10], the MNET uncertainty analysis routines can provide the worst-case values of the estimated parameters, the uncertainty contributions of the various input parameters, or the distributions of the identified elastic parameters.

10.1.3. Using of the MNET Techniques

The vibration-based MNETs that were introduced in this thesis require a sample set that comprises samples with different layer configurations. Different layer configurations are obtained by changing the layer thickness or layer stacking. The MNET techniques can be applied to any material with homogeneous linear elastic layers as long as the required layer configurations can be produced. Unfortunately, the production of the required layer configurations can be very complicated or even impossible.

At this moment, the identification of the elastic properties of coatings is expected to be the most important field of application of the presented routines. First of all, in the case of coatings it is very straightforward to produce the required layer configurations. Furthermore, an identification technique for layered materials is a necesity to identify the propterties of a coating. Alternative approaches, such as identifying the properties of the coating in a non-layered form, are rarely meaningful. Separating the coating layer from its substrate will, most probably, damage the material so that it is no longer useful for identification purposes. Another option, producing the material in a bulk form, is usually not possible. Even if the coating material can be produced in bulk form, it is not certain if the material will have the same properties as when it is produced under the form of a thin layer. The identification of the properties from coated substrates using a layered material identification technique is thus the only viable option.

In general, it is advisable to take the following considerations into account, when using the MNET-based techniques for the identification of the elastic properties of layered materials.

Layer Thicknesses — Uncertainty analyses have shown that an accurate measurement of the layer thicknesses is of utmost importance to obtain reliable elastic properties. Unfortunately, the layer thicknesses are rather difficult to measure accurately. In fact, the determination of the layer thickness needs to be integrated in the test procedure; in case of coated specimens for example, it is advisable to measure the sample thicknesses before and after the coating

process. The sample and/or layer thicknesses are preferably determined with a digital micrometer screw, a scanning electron microscope (SEM), or both. Measuring the thicknesses with a calliper is not advisable.

Additional Layer Configurations — In some cases, the required layer configurations have to be produced by adding a glass layer to the material. In this situation, beam-shaped samples are preferred, since plate-shaped samples are more prone to creating problems related to non-uniform glue films, especially when the additional glass layer is relatively thin.

Coatings — A thermal coating process will usually result in sample that has a residual out-of-plane deformation due to the thermal expansion coefficient mismatch between coating and substrate material. The resonant frequencies of plate-shaped specimens are very sensitive to out-of-plane sample deformation, while the resonant frequencies of beam-shaped specimens are practically insensitive to it. Therefore, it is advisable to identify the properties of these coatings from the resonant frequencies of beam-shaped samples.

Thin Layers — There is no lower limit to the thickness of a layer, below which the determination of its elastic properties using the MNET routines would be impossible. In general, a layer should be thick enough to provide a significant contribution to the overall sample stiffness. In case of thin coating layers, the coating should be deposited on a rather flexible substrate, i.e. a material that has low elastic properties or is sufficiently thin.

Starting Values — The MNET-based routines need a set of trail values for the unknown elastic properties that have to be identified. The MNET routines do not require very accurate starting values for the unknown elastic properties; a correct order of magnitude is more than accurate enough. Note that the trial values do not have any influence on the values of the identified parameters, they will only influence the number of required iteration steps.

Optimal Routine — It is hard to say which one of the three suggested identification routines is the optimal technique, since this depends on the investigated material. However, the multi-orientation routine has shown to be the most robust and reliable routine for a wide range of applications. Therefore, if there is no a priori information or experience indicating otherwise, it is advisable to use the multi-orientation routine to identify the layer properties.

10.2. Recommendations for Future Research

The performance of the vibration-based MNET routines developed in this thesis could be extended in one or more of the following ways:

Functionally Graded Materials — This thesis only considered layered materials made of layers with uniform properties and sharp interfaces with the adjacent layers. However, in functionally graded materials (FGMs), the material properties vary in a continuous way. The application of the presented techniques for the identification of the property gradient of FGMs is not straightforward. The current MNET techniques require a discretisation of the property gradient, so that the material can be segmented in a number of layers with uniform properties. The properties of these layers have to be identified from the

resonant frequencies of a number of sample configurations.
Unfortunately, an accurate approximation of the gradient requires a fine discretisation with large number of layers and layer configurations, which would eventually lead to a huge computation time. It would be much more elegant to create an element formulation for a FGM material, i.e. an element with a gradient in material properties. The identification of the FGM properties then reduces to the identification of the parameters used in the element formulation to model the property gradient. This approach should be computationally faster, and will most probably use the experimental data more efficiently, so that fewer layer configurations are needed to identify the gradient parameters.

High Temperature Properties — Although this thesis only considered measurements at room temperature, the single- and multi-orientation routines are designed in such a way that all the required input data can also be measured at high temperatures. In theory, the presented identification routines should thus be able to identify the layer properties of orthotropic materials as a function of temperature. So far, such a test has not been executed, and it thus not known whether there will be experimental difficulties related to it.

Damping Properties — The presented MNET routines provided only the elastic properties of the layers, they did not consider their damping properties. It has been shown that it is possible to identify the damping properties of homogeneous orthotropic materials from the modal damping ratios [19]. It is expected that it is possible to identify the damping properties of the layer materials from the modal damping ratios of the vibration modes of the used layer configurations; however, this has not yet been attempted.

Complex Sample Shapes — Although only test samples with very simple shapes, like rectangular plates or cylinders, were used in this thesis, the MNET routine can in principle identify the layer properties from samples with an arbitrary shape. However, a number of practical limitations are expected; these limitations are caused by the limited accuracy of the FE-models, the sensitivity of the resonant frequencies with respect to the material parameters, the fabrication of samples with a modified layer configuration, etc.

Interpretation of Uncertainties — This thesis introduced a probabilistic and a non-probabilistic technique to handle uncertainties, however this does not imply that the whole uncertainty problem was solved. The presented techniques only dealt with the mathematics of the uncertainty problem, i.e. the estimation of the uncertainties of the identified properties from the uncertainties of the input parameters. The problem of estimating the input parameter uncertainties was not addressed in this text.

A

The ASTM Standard on Resonant Beam Testing

This appendix provides the basis of the ASTM standard on resonant beam testing.

A.1. Introduction

The ASTM standard C 1259-01 [4] presents a number of analytical formulas to derive the elastic properties of homogeneous isotropic materials from the resonant frequencies of a beam-shaped specimen with a rectangular cross-section. This standard is based on the work of Spinner and Teft [3].

A.2. Calculating the Elastic Properties

The elastic modulus of an isotropic material can be derived from the resonant frequency of the fundamental out-of-plane flexural vibration mode of a beam-shaped specimen as

$$E = 0.9465 \, \frac{m \, f_f^2 \, l^3}{w \, t^3} T_1 \tag{A.1}$$

where T_1 is a correction factor defined as

$$T_1 = 1 + 6.585 \left(1 + 0.0752\nu + 0.8109\nu^2\right) \left(\frac{t}{l}\right)^2 - 0.868 \left(\frac{t}{l}\right)^4 - \left(\frac{8.340 \left(1 + 0.2023\nu + 2.173\nu^2\right) \left(\frac{t}{l}\right)^4}{1.000 + 6.338 \left(1 + 0.1408\nu + 1.536\nu^2\right) \left(\frac{t}{l}\right)^2} \right) \tag{A.2}$$

The shear modulus of an isotropic material can be derived from the fundamental torsional frequency of a beam-shaped specimen as

$$G = 4 \, \frac{m \, f_t^2 \, l}{w \, t} \left(\frac{B}{1 + A} \right) \tag{A.3}$$

where

$$B = \frac{\frac{w}{t} + \frac{t}{w}}{4 \left(\frac{t}{w}\right) - 2.52 \left(\frac{t}{w}\right)^2 + 0.21 \left(\frac{t}{w}\right)^6} \tag{A.4}$$

The coefficient A is an empirical correction factor given by

$$A = \frac{0.5062 - 0.8776 \left(\frac{w}{t}\right) + 0.3504 \left(\frac{w}{t}\right)^2 - 0.0078 \left(\frac{w}{t}\right)^3}{12.03 \left(\frac{w}{t}\right) + 9.892 \left(\frac{w}{t}\right)^2} \tag{A.5}$$

If the materials Poisson's ratio is unknown, it can be obtained from the E and G modulus as

$$\nu = \frac{E}{2\,G} - 1 \tag{A.6}$$

Note that in this case, the E-modulus has to be calculated with an estimation of Poisson's ratio. The Poisson's ratio obtained with (A.6) has to be inserted into (A.2) to compute an improved value of the E-modulus. The ASTM standard advises to repeat this iterative calculation until the difference between the Poisson's ratios of two successive iteration steps becomes smaller than 2 %.

B

Experimental Set-up & Measurement Procedures

This appendix presents the experimental test set-ups and measurement procedures used for the test cases of chapter 8.

B.1. Measuring the Resonant Frequencies

The resonant frequencies of the test specimens were measured by exciting the test specimens with a computer-controlled loudspeaker, and capturing the vibration response with a laser vibrometer[1]. The vibration signal was digitised with a data acquisition card[2] and stored into the computer. The resonant frequencies were estimated from the time signals with the RFDA[3] software. Every frequency was measured five times and the average value was used as input data for the MNET procedure.

B.1.1. The Measurement Set-up

The resonant frequencies of the beam- and plate-shaped specimens were measured with a slightly different test set-up. Figures B.1 and B.2 present the two test set-ups, while figure B.3 provides the legend to these plots.

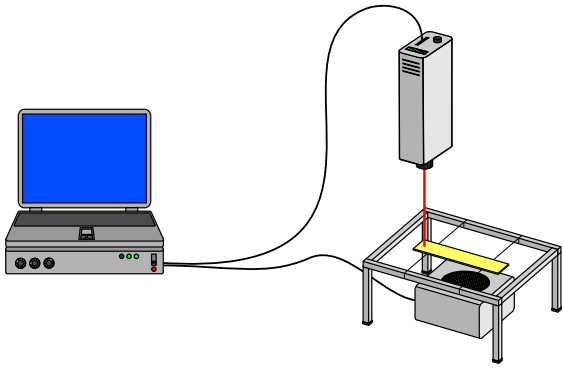

Figure B.1: *The test set-up for beam-shaped specimens.*

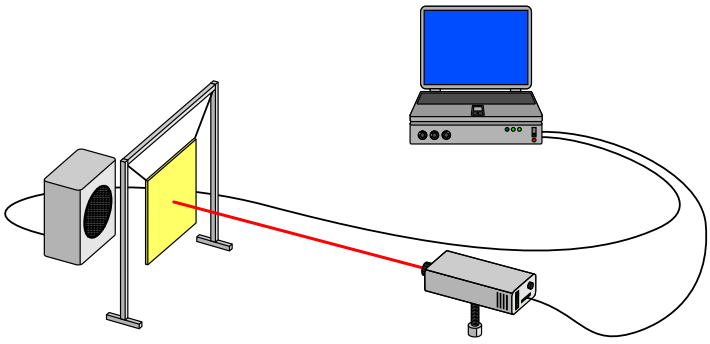

Figure B.2: *The test set-up for plate-shaped specimens.*

[1]Polytec OFV 303
[2]National Instruments DAQCard-6062E
[3]IMCE RFDA MF v6.2

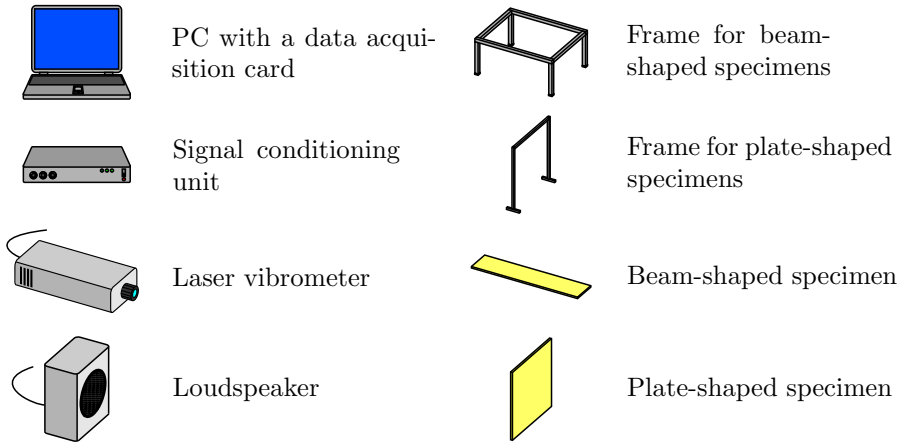

Figure B.3: *Legend of the test set-up drawings.*

B.1.2. Sample Suspension

The sample suspension should imitate the free-free boundary conditions of the FE-models as good as possible. In the test set-up, the beam-shaped samples were supported by two horizontal wires. To minimise the influence of the supporting wires, the wires were positioned at the locations of the nodes of the considered vibration mode. To measure the resonant frequency of the fundamental out-of-plane flexural vibration mode, the sample was supported by two parallel wires positioned at a distance of 0.224×length from the sample edges. The resonant frequency of the fundamental torsional mode was measured, while the sample was supported by two crossed wires. Both types of sample suspension are shown in figure B.4.

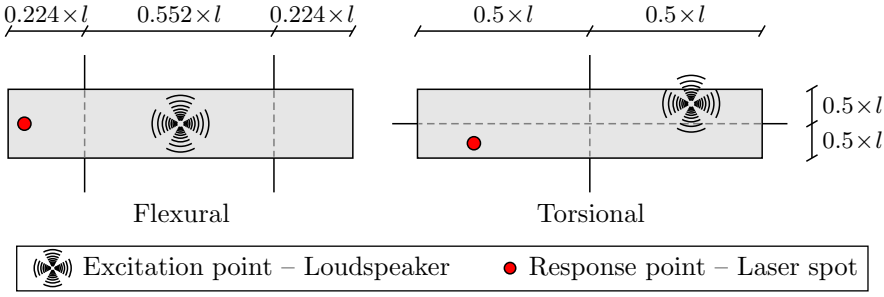

Figure B.4: *The position of the supporting wires for beam-shaped samples.*

The plate-shaped specimens were suspended using two vertical wires as shown on figure B.2. An experimental verification revealed that the position of the suspension wires did not influence the resonant frequencies of the plate-shaped samples. All the resonant frequencies could, therefore, be measured with the same suspension configuration. However, every vibration mode required a par-

ticular excitation and response location. Figure B.5 presents the optimal configurations to measure the resonant frequencies of the first five vibration modes of a Poisson plate.

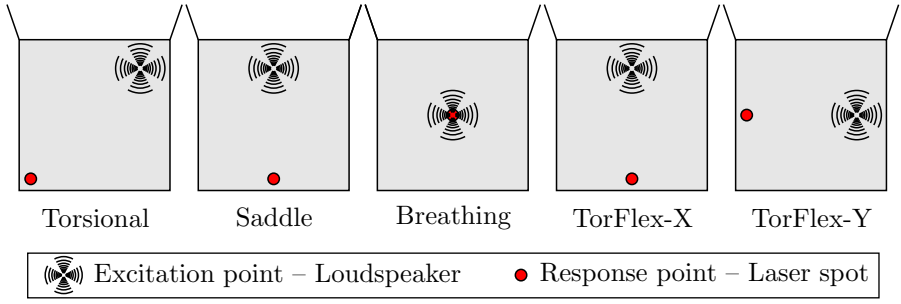

Figure B.5: *The excitation and response locations for the first five vibration modes of a plate-shaped specimen.*

B.2. Measuring the Sample Properties

The MNET routines also required the length, width, thickness, mass, and orientation of the test specimens. For the experiments described in chapter 8, the length and width were measured with a digital calliper[4]. For the beam-shaped specimens, the length and width were the average values of three and five measurements, respectively, as shown in figure B.6. For the plate-shaped specimens, the length and width were measured in five points as shown on figure B.8. The samples thickness was measured with a digital micrometer screw[5] according to the schemes of figures B.7 and B.8. The sample thickness was the average value of thickness measured in these five, ten or sixteen locations. The mass was measured with a digital balance[6]. The specimen orientations were not measured. All the test specimens were cut out of a material sample with a computer controlled laser or high pressure water jet cutting device. The orientations used for the identification were the orientations that were programmed into the cutting device to produce the test specimens.

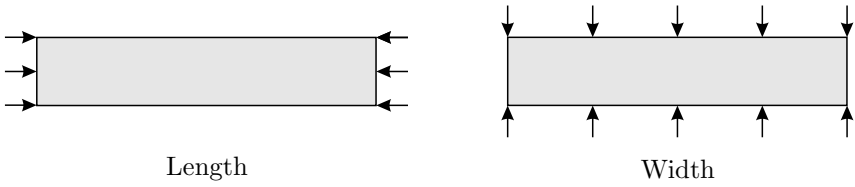

Figure B.6: *Measuring the dimensions of a beam-shaped specimen.*

[4]Mitutoyo Digimatic 500
[5]Mitutoyo Digimatic 293
[6]Mettler AE240

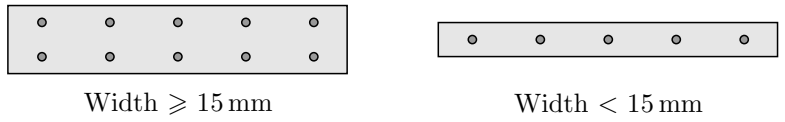

Figure B.7: *Measuring the thickness of a beam-shaped specimen.*

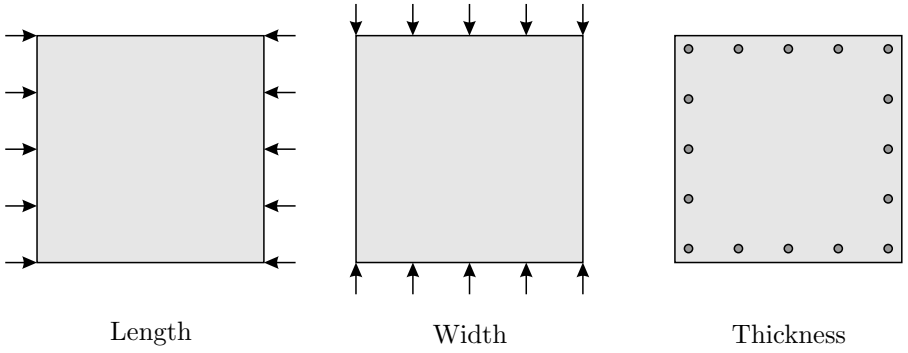

Figure B.8: *Measuring the dimensions of a plate-shaped specimen.*

C

The Influence of an Out-of-Plane Sample Deformation

Not every test material is available in a perfectly flat form. This appendix investigates the influence of an out-of-plane deformation of the test specimen on the resonant frequencies used for the identification of the elastic material properties.

C.1. Introduction

Layered material identification requires a number of test samples with a varying layer configuration. Coated materials are a class of materials where the required layer configurations can easily be produced, e.g. by changing the thickness of the coating layer. The identification of the elastic properties of coated materials is thus an important area, where the presented vibration-based MNETs could be applied.

Adding a layer of coating to a substrate will usually result in an out-of-plane deformation of the substrate. Since this deformation might have an effect on the resonant frequencies, it should be measured and incorporated in the FE-model of the MNET. Unfortunately, this is a very elaborate process that will complicate both the experimental and the modelling phase. It would be much easier to use samples, where the deformation does not affect the resonant frequencies. In this way, the deformation does not have to be measured and modelled.

This appendix addresses two types of deformation patterns: curvature and twisting. The influence of the sample deformation on the resonant frequencies was evaluated with a number of FE-models of an aluminium test beam and plate. The properties of the considered aluminium are shown in table C.1. Table C.2 presents the geometry of the considered test specimens.

Table C.1: *The material properties of the considered aluminium.*

E_1 [GPa]	E_2 [GPa]	G_{12} [GPa]	ν_{12} [–]	ρ [kg/m^3]
70.00	70.00	26.00	0.340	2700

Table C.2: *The geometry of the test specimens.*

	Length [mm]	Width [mm]	Thickness [mm]
Beam	100.00	20.00	1.000
Plate	100.00	95.00	1.000

The influence of the deformation on the resonant frequencies is estimated by comparing the frequencies of a perfectly flat sample with the frequencies of a deformed sample. The deformation amplitude is gradually increased to study its influence on the resonant frequencies of the test samples.

For beam-shaped samples, two types of deformation patterns are investigated:

- beams curved in the long direction
- twisted beams

For plate-shaped samples, three deformation patterns are investigated:

- plates curved in one direction
- plates curved in both directions
- twisted plates

For the beam-shaped specimens, only the fundamental flexural and torsional

resonant frequencies are considered; for the plate-shaped specimens, the resonant frequencies of the first five vibration modes are investigated.

C.2. Beam-Shaped Specimens

C.2.1. Curved Beams

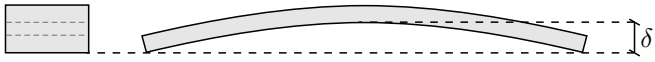

Figure C.1: *A curved beam-shaped specimen.*

Table C.3: *The fundamental resonant frequencies in function of the deformation amplitude δ.*

δ [mm]	f_f [Hz]	f_t [Hz]
0.00	524.872	1545.773
0.10	524.869	1545.766
0.20	524.859	1545.746
0.30	524.844	1545.712
0.40	524.822	1545.664
0.50	524.794	1545.602
0.60	524.759	1545.527
0.70	524.719	1545.439
0.80	524.672	1545.336
0.90	524.619	1545.220
1.00	524.560	1545.090

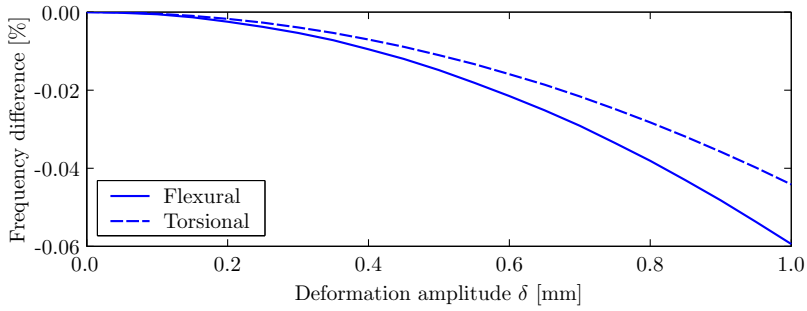

Figure C.2: *The frequency shift in function of the deformation amplitude δ.*

The curvature in the long direction of a beam-shaped specimen does not seem to have a significant influence on the fundamental flexural and torsional frequencies of the sample. The maximal considered deflection amplitude, a deflection that equals the sample thickness, caused a frequency shift of only 0.06 %.

C.2.2. Twisted Beams

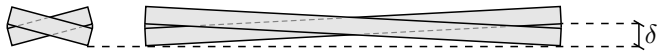

Figure C.3: *A twisted beam-shaped sample.*

Table C.4: *The fundamental resonant frequencies in function of the deformation amplitude δ.*

δ [mm]	f_f [Hz]	f_t [Hz]
0.00	524.872	1545.773
0.10	524.871	1545.813
0.20	524.869	1545.934
0.30	524.866	1546.135
0.40	524.862	1546.416
0.50	524.856	1546.778
0.60	524.849	1547.219
0.70	524.840	1547.741
0.80	524.831	1548.342
0.90	524.820	1549.022
1.00	524.807	1549.782

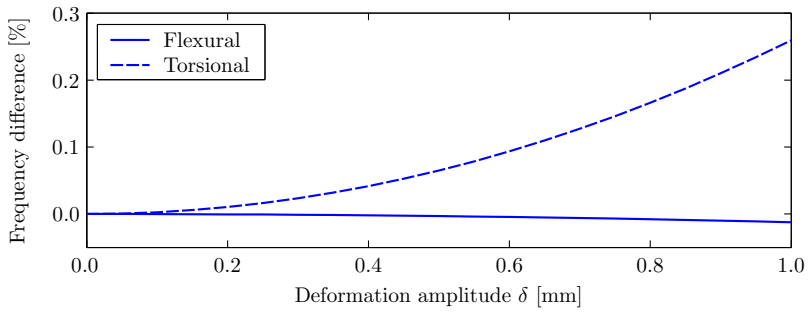

Figure C.4: *The frequency shift in function of the deformation amplitude δ.*

Twisting a beam-shaped sample appears to have practically no influence on its fundamental flexural frequency. However, the influence of twisting on the fundamental torsional frequency seems to be important. For the maximum considered deformation amplitude, the observed frequency difference is about twice the uncertainty of the experimental frequencies. This means that for twisted specimens, it is advisable to examine whether the influence of the deformation must be taken into account or not. Note that the influence on the resonant frequencies is proportional to the deformation amplitude to thickness ratio. This means that the influence of the twisting deformation can be reduced by using smaller samples.

C.3. Plate-Shaped Samples

C.3.1. Curved in One Direction

Figure C.5: *A plate-shaped specimen curved in one direction.*

Table C.5: *The frequencies in function of the deformation amplitude δ.*

δ [mm]	f_{tors} [Hz]	f_{sadd} [Hz]	f_{brea} [Hz]	f_{tf-x} [Hz]	f_{tf-y} [Hz]
0.00	341.641	495.971	647.173	873.797	907.597
0.10	341.640	496.363	647.822	873.795	907.724
0.20	341.639	497.514	649.782	873.788	908.106
0.30	341.636	499.350	653.085	873.775	908.742
0.40	341.633	501.754	657.780	873.758	909.631
0.50	341.628	504.584	663.922	873.735	910.772
0.60	341.623	507.685	671.560	873.705	912.164
0.70	341.616	510.902	680.725	873.669	913.805
0.80	341.609	514.104	691.421	873.626	915.694
0.90	341.600	517.184	703.615	873.576	917.826
1.00	341.590	520.068	717.243	873.517	920.202

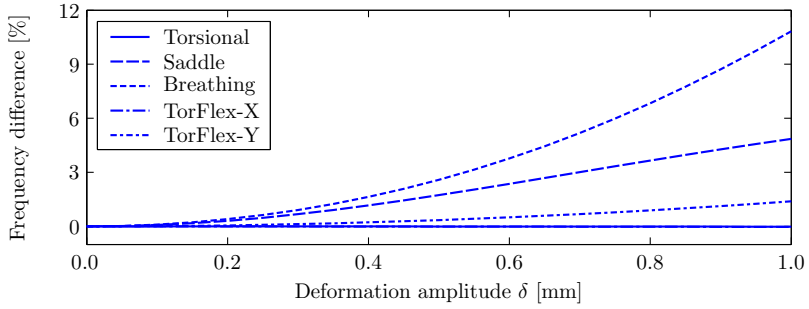

Figure C.6: *The frequency shift in function of the deformation amplitude δ.*

This type of curvature has a severe impact on the resonant frequency of the second and third vibration modes of a plate-shaped specimen, i.e. the saddle and breathing modes. The maximal considered deformation increases the third resonant frequency by about 11 %, and the second frequency with by 5 %. Since these two frequencies are very important for the estimation of the E-moduli and Poisson's ratio, it is useless to perform an identification using the frequencies of a curved plate-shaped specimen without taking the curvature into account. Note that the influence on the torsional frequeny is essensially non-existing. This implies that the torsional frequency of a plate-shaped specimen, curved in one direction, will provide a correct estimation of the in-plane shear modulus.

C.3.2. Curved in Both Directions

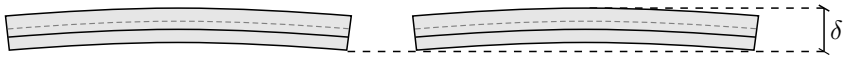

Figure C.7: *A plate-shaped specimen curved in both directions.*

Table C.6: *The frequencies in function of the deformation amplitude δ.*

δ [mm]	f_{tors} [Hz]	f_{sadd} [Hz]	f_{brea} [Hz]	f_{tf-x} [Hz]	f_{tf-y} [Hz]
0.000	341.641	495.971	647.173	873.797	907.597
0.100	341.641	495.996	647.606	873.816	907.612
0.200	341.641	496.071	648.902	873.872	907.658
0.300	341.642	496.193	651.054	873.965	907.734
0.400	341.644	496.357	654.050	874.095	907.841
0.500	341.645	496.557	657.874	874.260	907.976
0.600	341.647	496.788	662.505	874.462	908.140
0.700	341.649	497.041	667.915	874.698	908.332
0.800	341.652	497.312	674.074	874.967	908.550
0.900	341.654	497.593	680.946	875.269	908.793
1.000	341.657	497.880	688.492	875.603	909.059

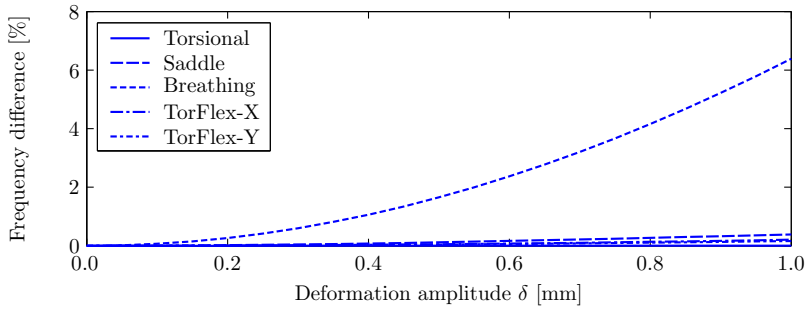

Figure C.8: *The frequency shift in function of the deformation amplitude δ.*

This type of curvature has a major impact on the resonant frequency of the third vibration mode of a plate-shaped specimen, i.e. the breathing mode. The maximal considered deformation results in an increase of the third resonant frequency by about 6.5 %. The influence on the other frequencies is limited to 0.4 %. Since the frequency of the third mode is essential for the estimation of the E-moduli and Poisson's ratio, it is useless to perform an identification using the frequencies of a curved plate-shaped specimen without taking the curvature into account. Note that the influence on the torsional frequeny is practically non-existing. This implies that the torsional frequeny of a plate-shaped specimen, curved in both directions, will provide a correct estimation of the in-plane shear modulus.

C.3.3. Twisted Plates

Figure C.9: *A twisted plate-shaped specimen.*

Table C.7: *The frequency in function of the deformation amplitude δ.*

δ [mm]	f_{tors} [Hz]	f_{sadd} [Hz]	f_{brea} [Hz]	f_{tf-x} [Hz]	f_{tf-y} [Hz]
0.000	341.641	495.971	647.173	873.797	907.597
0.100	341.742	495.971	647.172	873.835	907.628
0.200	342.045	495.970	647.170	873.947	907.722
0.300	342.549	495.968	647.167	874.133	907.878
0.400	343.254	495.966	647.163	874.394	908.097
0.500	344.158	495.964	647.157	874.730	908.378
0.600	345.260	495.960	647.150	875.140	908.721
0.700	346.557	495.957	647.142	875.624	909.127
0.800	348.047	495.952	647.132	876.182	909.595
0.900	349.727	495.947	647.122	876.814	910.124
1.000	351.595	495.942	647.110	877.519	910.716

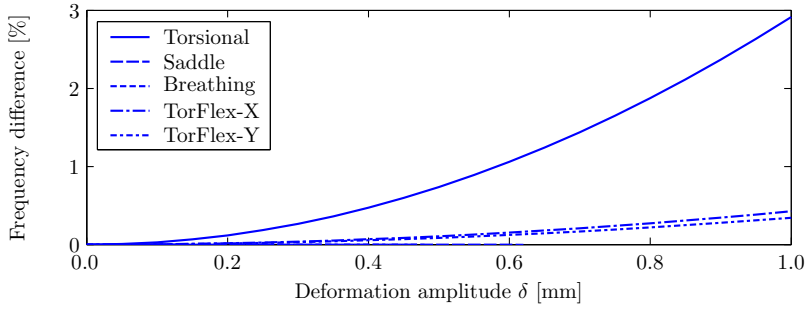

Figure C.10: *The frequency shift in function of the deformation amplitude δ.*

The maximal considered deformation results in an increase of the torsional frequency by about 3 %. The influence on the other frequencies is less significant, and is limited to about 0.45 %. Note that the frequencies of the saddle and breathing modes are not affected, implying that a twisted plate-shaped specimen can provide a correct estimate of the Poisson's ratio.

C.4. Conclusions

The resonant frequencies of beam-shaped specimens are hardly affected by a curvature of the test sample. Moreover, the influence of a twisting deformation

is more pronounced but acceptable. In general, the influence of the deformation is sufficiently small, so that the resonant frequencies of slightly deformed beam-shaped specimens can be used for identification purposes without having to take into account the deformation in the FE-models of the MNET.
On the other hand, the resonant frequencies of plate-shaped specimens proved to be much more sensitive to the deformation of the test sample. The influence of the sample deformation on the resonant frequencies is significant. Consequently, even slightly deformed plate-shaped specimens cannot be used for identification purposes without taking into account the deformation in the FE-models of the MNET. With plate-shaped specimens, it is advisable to cut a series of beam-shaped specimens out of the initial test plate, instead of measuring the deformation and taking it into account in the identification procedure. An application of this approach is presented in section 9.2.

D

The Analytical Approach for Layered Cylinders

D.1. Identification Formulas for Cylindrical Specimens

D.1.1. Homogenenous Specimens

The elastic modulus of cylindrical bars can be derived from the resonant frequency of the fundamental flexural mode [4] as

$$E = 1.6067 \, \frac{m \, f_f^2 \, l^3}{d^4} T_1 \tag{D.1}$$

in which d is the diameter of the cross-section and T_1 is a correction factor defined as

$$\begin{aligned} T_1 = 1 + 4.939 \left(1 + 0.0752\nu + 0.8109\nu^2\right) \left(\frac{d}{l}\right)^2 - 0.4883 \left(\frac{t}{l}\right)^4 \\ - \left(\frac{4.691 \left(1 + 0.2023\nu + 2.173\nu^2\right) \left(\frac{d}{l}\right)^4}{1.000 + 1.754 \left(1 + 0.1408\nu + 1.536\nu^2\right) \left(\frac{d}{l}\right)^2} \right) \end{aligned} \tag{D.2}$$

D.1.2. Layered Specimens

Figure D.1 presents the three layer configurations of the EB-PVD cylinders.

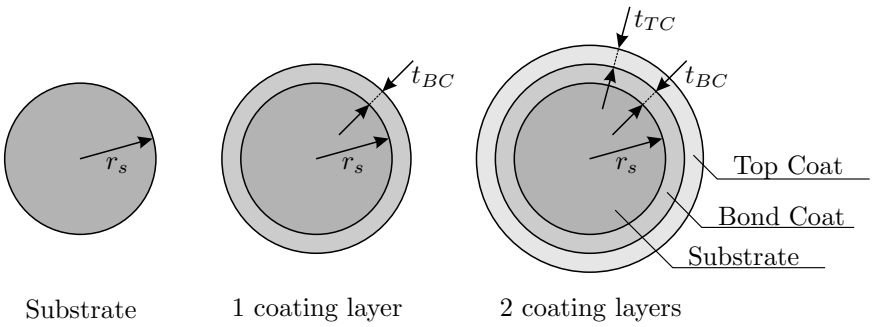

Figure D.1: *A cross-section of the coated cylinders.*

The elastic modulus of the substrate can be identified with (D.1) from the resonant frequency of the pure substrate. According to [6], the elastic modulus of the bond coat can be identified as

$$E_{BC} = \frac{E_{tot_1}(r_s + t_{BC})^4 - E_s \, r_s^4}{(r_s + t_{BC})^4 - r_s^4} \tag{D.3}$$

in which E_{tot_1} is the elastic modulus identified with (D.1) from the resonant frequency of the test samples with one coating layer. Using the same reasoning as in [6], it can be shown that the top coat properties of the considered specimens can be identified with

$$E_{TC} = \frac{E_{tot_2}(r_s + t_{BC} + t_{TC})^4 - E_s\, r_s^4 - E_{BC}\big((r_s + t_{BC})^4 - r_s^4\big)}{(r_s + t_{BC} + t_{TC})^4 - (r_s + t_{BC})^4} \tag{D.4}$$

in which E_{tot_2} is the elastic modulus identified with (D.1) from the resonant frequency of the test samples with two coating layer.

D.2. Evaluation of the Identification Approach

D.2.1. Comparison of the ASTM Formula with FEM

The ASTM formula can be rewritten into a from that allows to compute the resonant frequency of the fundamental flexural mode of a homogeneous, isotropic cylindrical sample. Consider a test sample with a length of 70 mm and a diameter of 4 mm made of an isotropic material with an elastic modulus of 205 GPa, a Poisson's ratio of 0.25 and a mass density of 8400 kg/m^3. For this sample equation (D.1) provides a resonant frequency f_f of 3559.6. A 3D finite element model of this sample provides a resonant frequency f_f of 3561.5. The difference between the ASTM formula and the FE-model is thus 0.05%, which is lower than the assumed accuracy of both the FE-model and the ASTM formula[1]. The ASTM formula and the FE-model thus provide the same resonant frequency, within the limits of their accuracy.

D.2.2. Verification of the Identification Approach of [6]

The identification approach of [6] makes two important simplifications: a) the identification formula (D.1) only uses the overall mass of the test sample, therefore it ignores the differences in mass density between the various layers, and b) the identification formula (D.1) uses a uniform Young's modulus for the whole sample, therefore it ignores the difference in stiffness of the various layers. The classical lamination theory (CLT) shows that the influence of these two assumptions is minimal in the case of plate-shaped samples. However, the CLT assumes that the layers of the material are parallel with the neutral plane of the considered bending deformation, which is not the case for a cylindrical specimen. It is thus not so obvious that these two simplifications are also correct here.

To evaluate the validity of the two assumptions, consider the nine test specimens of tables D.1 and D.2. The resonant frequencies of the fundamental flexural mode of these nine test samples were computed with a finite element model. The elastic properties of the layer materials can be identified from these resonant frequencies using equations (D.1), (D.3), and (D.4). The accuracy of the identified parameter can be evaluated by comparing the obtained results with the elastic properties that were used in the FE-models to compute the frequencies.

The sample set comprising sample 1, 2, and 3 represents the situation where there is (virtually) no variation in E-modulus and mass density between the three layers. Table D.3 presents the identified properties. The first sample set

[1] The accuracy of the ASTM formulas and the converged FE-models is estimated at 0.1%.

Table D.1: *The geometry and resonant frequencies of the test samples.*

Id.	l	r_s	t_{BC}	t_{TC}	m	f_f
Sample-1	70	2	—	—	7.3887	3561.50
Sample-2	70	2	0.25	—	9.3513	3993.95
Sample-3	70	2	0.25	0.25	11.5448	4420.77
Sample-4	70	2	0.25	—	9.0475	4061.11
Sample-5	70	2	0.25	0.25	10.4054	4659.19
Sample-6	70	2	0.25	—	9.3513	3942.52
Sample-7	70	2	0.25	0.25	11.5448	3701.82
Sample-8	70	2	0.25	—	9.0475	4008.81
Sample-9	70	2	0.25	0.25	10.4054	3901.57
	[mm]	[mm]	[mm]	[mm]	[g]	[Hz]

Table D.2: *The material properties used to model the test samples.*

Id.	E			Mass Density		
	Sub	BC	TC	Sub	BC	TC
Sample-1	205	—	—	8400	—	—
Sample-2	205	204	—	8400	8400	—
Sample-3	205	204	203	8400	8400	8400
Sample-4	205	204	—	8400	7100	—
Sample-5	205	204	203	8400	7100	5200
Sample-6	205	190	—	8400	8400	—
Sample-7	205	190	35	8400	8400	8400
Sample-8	205	190	—	8400	7100	—
Sample-9	205	190	35	8400	7100	5200
	[GPa]	[GPa]	[GPa]	[kg/m^3]	[kg/m^3]	[kg/m^3]

Table D.3: *The material properties obtained from the various sample sets.*

Samples	Substrate		Bond Coat		Top Coat	
	Value	Error	Value	Error	Value	Error
1-2-3	205.2	0.11%	204.2	0.09%	203.2	0.10%
1-4-5	205.2	0.11%	204.4	0.18%	203.8	0.38%
1-6-7	205.2	0.11%	190.2	0.12%	35.7	2.08%
1-8-9	205.2	0.11%	190.4	0.21%	36.1	3.14%
	[GPa]	[%]	[GPa]	[%]	[GPa]	[%]

results in an error of about 0.1 % on the elastic moduli of the three layers. This difference is the due to the difference between the results of the ASTM formula and the FE-models as discribed in the previous section.
The second sample set, i.e. samples 1, 4, and 5, represents the situation where there is a variation in mass density between the layers, while there is no significant variation of the E-modulus. The obtained results show that the homogenisation of the mass density results in an small but observable increase of the error on the identified properties.
The third sample set, i.e. samples 1, 6, and 7, represents the situation where there is a variation in the stiffness between the different layers, while there is no variation in mass density. The results show that the homogenisation of the elastic properties leads to a important increase of the error on the identified properties of the top coat.
The fourth sample set, i.e. samples 1, 8, and 9, represents the real situation where there is a variation in the both the stiffness and mass density of the layer materials. The results of table D.3 show that the identification approach of [6] leads to an significant error on the identified properties of the top coat.

D.3. Conclusions

In the case of the EB-PVD coatings, the homogenisation of the mass density in the approach of [6] leads to a small but observable error on the identified properties of the top coat. However, the homogenisation of the elastic properties in (D.1) leads to a significant overestimation of the stiffness of the top coat. In general, this overestimation is function of the relative difference in stiffness and thickness between the various layers. Due to the signification difference in stiffness between the substrate and top coat, it is advisable to use the MNET-based approach to identify the Young's moduli of the EB-PVD coatings.

E

Experimental Results

The appendix presents all the experimental values that were measured for the experiments that are described in chapter 8

E.1. Brass-Steel Bi-metal

E.1.1. The Homogeneous Brass Samples

Sample Description

Table E.1: *The properties of the beam-shaped brass samples.*

Id.	Dir.	Length	Width	Thickness				Mass	f_f	f_t
				Total	Top	Bottom	Glue			
	[°]	[mm]	[mm]	[mm]	[mm]	[mm]	[mm]	[g]	[Hz]	[Hz]
Bra-01	0.0	103.507	19.684	1.6306	0.8123	0.8119	0.0064	27.7515	562.111	1652.695
Bra-02	0.0	103.553	19.530	1.6299	0.8114	0.8115	0.0070	27.5412	560.012	1651.384
Bra-03	0.0	102.277	18.242	1.6375	0.8101	0.8193	0.0081	25.5204	577.489	1799.568
Bra-04	0.0	103.667	19.666	1.6410	0.8179	0.8188	0.0043	28.0085	562.133	1653.425
Bra-05	22.5	102.703	19.682	1.6290	0.8145	0.8135	0.0010	27.5979	565.495	1682.493
Bra-06	22.5	102.527	19.564	1.6324	0.8152	0.8165	0.0007	27.4793	566.563	1699.779
Bra-07	22.5	102.730	19.638	1.6351	0.8161	0.8170	0.0020	27.6295	566.239	1687.559
Bra-08	22.5	102.710	19.754	1.6371	0.8167	0.8175	0.0029	27.7914	567.159	1672.556
Bra-09	45.0	101.723	19.574	1.6294	0.8109	0.8162	0.0023	27.1416	567.043	1726.608
Bra-10	45.0	101.440	19.554	1.6427	0.8179	0.8177	0.0071	27.2324	574.936	1737.224
Bra-11	45.0	101.783	19.594	1.6442	0.8177	0.8175	0.0090	27.2326	573.372	1731.084
Bra-12	45.0	101.667	19.680	1.6515	0.8204	0.8204	0.0107	27.4837	576.416	1736.676
Bra-13	67.5	100.637	19.750	1.6312	0.8129	0.8149	0.0034	27.0751	578.413	1722.239
Bra-14	67.5	100.723	19.700	1.6277	0.8122	0.8108	0.0047	27.0250	574.940	1702.428
Bra-15	67.5	100.713	19.574	1.6324	0.8124	0.8129	0.0071	26.9394	577.191	1727.645
Bra-16	67.5	100.650	19.658	1.6385	0.8139	0.8134	0.0112	27.0463	580.246	1733.610
Bra-17	90.0	99.663	19.666	1.6493	0.8185	0.8180	0.0128	26.9093	596.510	1739.785
Bra-18	90.0	99.660	19.614	1.6390	0.8122	0.8127	0.0141	26.6898	593.204	1741.448
Bra-19	90.0	99.340	19.496	1.6307	0.8127	0.8123	0.0057	26.4390	593.061	1736.456
Bra-20	90.0	99.607	19.656	1.6275	0.8121	0.8116	0.0038	26.7154	588.981	1721.195

Table E.2: *The properties of the plate-shaped brass samples.*

Id.	Dir.	Length	Width	Thickness	Mass
Bra-21	0-90	104.700	99.710	1.6288	142.3716
Bra-22	0-90	104.724	99.620	1.6284	141.8954
Bra-23	0-90	104.380	99.710	1.6444	143.1856
Bra-24	0-90	103.962	99.200	1.6444	141.4260
	[°]	[mm]	[mm]	[mm]	[g]

Table E.3: *The layer thicknesses of the plate-shaped brass samples.*

Id.	Total	Top	Bottom	Glue
Bra-21	1.6288	0.8111	0.8105	0.0072
Bra-22	1.6284	0.8100	0.8127	0.0057
Bra-23	1.6444	0.8179	0.8180	0.0086
Bra-24	1.6444	0.8160	0.8159	0.0125
	[mm]	[mm]	[mm]	[mm]

Table E.4: *The resonant frequencies of the plate-shaped brass samples.*

Id.	f_{tors}	f_{sadd}	f_{brea}	f_{tf-x}	f_{tf-y}
Bra-21	343.460	509.847	662.912	889.568	915.469
Bra-22	344.787	512.235	663.559	891.518	917.276
Bra-23	347.646	519.744	670.407	900.096	924.031
Bra-24	350.077	524.002	674.082	906.139	928.355
	[Hz]	[Hz]	[Hz]	[Hz]	[Hz]

Table E.5: *The size of the converged FE-models in terms of elements.*

	Length	Width	Thickness		
			Top	Bottom	Glue
Beam	19	14	1	1	1
Plate	23	23	1	1	1

Elastic Properties

Table E.6: *The elastic properties of the beam-shaped brass samples.*

Id.	Dir.	E	G	ν
Bra-01	0.0	107.17	37.33	0.435
Bra-02	0.0	106.64	36.80	0.449
Bra-03	0.0	107.02	37.17	0.439
Bra-04	0.0	106.68	36.96	0.443
Bra-05	22.5	105.78	38.10	0.388
Bra-06	22.5	105.19	38.21	0.377
Bra-07	22.5	105.33	37.93	0.388
Bra-08	22.5	105.18	37.56	0.400
Bra-09	45.0	102.33	38.97	0.313
Bra-10	45.0	102.27	38.68	0.322
Bra-11	45.0	102.26	38.58	0.325
Bra-12	45.0	102.16	38.86	0.315
Bra-13	67.5	101.57	38.47	0.320
Bra-14	67.5	101.29	37.74	0.342
Bra-15	67.5	101.57	38.30	0.326
Bra-16	67.5	101.34	38.57	0.314
Bra-17	90.0	101.32	37.56	0.349
Bra-18	90.0	101.65	38.01	0.337
Bra-19	90.0	101.62	37.34	0.361
Bra-20	90.0	101.85	37.59	0.355
	[°]	[GPa]	[GPa]	[–]

Table E.7: *The averages of the elastic properties of the beam-shaped brass samples.*

Dir.	E	G	ν
0.0	106.88	37.07	0.442
22.5	105.37	37.95	0.388
45.0	102.26	38.77	0.318
67.5	101.44	38.27	0.326
90.0	101.61	37.51	0.350
[°]	[GPa]	[GPa]	[–]

Table E.8: *The elastic properties of the multi-orientation routine and the plate-shaped brass samples.*

Id.	E_1	E_2	G_{12}	ν_{12}
Multi-orientation	107.38	101.75	37.41	0.358
Bra-21	106.30	101.88	37.36	0.355
Bra-22	106.99	101.87	37.44	0.352
Bra-23	107.09	102.31	37.16	0.349
Bra-24	107.12	100.78	36.88	0.350
Average PS	106.88	101.71	37.21	0.351
	[GPa]	[GPa]	[GPa]	[–]

Frequency residuals

Table E.9: *The numerical frequencies and frequency residuals of the multi-orientation routine, brass beams.*

	Flexural		Torsional	
Id.	f_{num}	Resid.	f_{num}	Resid.
Bra-01	561.994	0.02 %	1653.984	−0.08 %
Bra-02	561.159	−0.20 %	1664.220	−0.78 %
Bra-03	577.817	−0.06 %	1804.746	−0.29 %
Bra-04	563.232	−0.20 %	1662.794	−0.57 %
Bra-05	563.783	0.30 %	1681.681	0.05 %
Bra-06	566.511	0.01 %	1696.793	0.18 %
Bra-07	565.735	0.09 %	1690.495	−0.17 %
Bra-08	566.944	0.04 %	1683.514	−0.66 %
Bra-09	566.631	0.07 %	1721.509	0.30 %
Bra-10	574.612	0.06 %	1738.320	−0.06 %
Bra-11	573.042	0.06 %	1734.516	−0.20 %
Bra-12	576.438	0.00 %	1734.115	0.15 %
Bra-13	577.998	0.07 %	1713.183	0.53 %
Bra-14	575.173	−0.04 %	1709.471	−0.41 %
Bra-15	576.746	0.08 %	1722.466	0.30 %
Bra-16	580.549	−0.05 %	1722.557	0.64 %
Bra-17	597.723	−0.20 %	1736.577	0.18 %
Bra-18	593.514	−0.05 %	1728.147	0.76 %
Bra-19	593.292	−0.04 %	1738.178	−0.10 %
Bra-20	588.576	0.07 %	1717.139	0.24 %
	[Hz]	[–]	[Hz]	[–]

E.1.2. The Homogeneous Steel Samples

Sample Description

Table E.10: *The properties of the beam-shaped steel samples.*

Id.	Dir.	Length	Width	Thickness				Mass	f_f	f_t
				Total	Top	Bottom	Glue			
	[°]	[mm]	[mm]	[mm]	[mm]	[mm]	[mm]	[g]	[Hz]	[Hz]
Ste-01	0.0	103.590	19.646	0.9798	0.4845	0.4863	0.0090	15.5327	478.214	1452.023
Ste-02	0.0	103.407	19.638	0.9747	0.4836	0.4824	0.0087	15.4512	477.940	1445.170
Ste-03	0.0	103.353	19.472	0.9785	0.4840	0.4830	0.0115	15.3011	480.293	1462.464
Ste-04	0.0	102.140	18.298	0.9743	0.4809	0.4843	0.0091	14.1783	490.446	1565.873
Ste-05	22.5	102.617	19.566	0.9825	0.4883	0.4882	0.0060	15.4009	482.717	1497.122
Ste-06	22.5	102.493	19.516	0.9743	0.4838	0.4837	0.0068	15.2494	479.701	1489.181
Ste-07	22.5	102.533	19.554	0.9729	0.4835	0.4847	0.0047	15.2633	479.398	1486.240
Ste-08	22.5	102.593	19.538	0.9763	0.4846	0.4844	0.0073	15.2277	479.579	1493.960
Ste-09	45.0	101.587	19.556	0.9742	0.4818	0.4822	0.0102	15.0994	482.850	1535.984
Ste-10	45.0	101.500	19.602	0.9845	0.4826	0.4831	0.0188	15.1474	490.457	1554.488
Ste-11	45.0	101.560	19.620	0.9898	0.4845	0.4843	0.0210	15.2068	492.819	1561.397
Ste-12	45.0	101.533	19.556	0.9708	0.4831	0.4838	0.0039	15.0948	479.802	1526.819
Ste-13	67.5	100.427	19.704	0.9768	0.4857	0.4870	0.0041	15.1161	501.306	1533.916
Ste-14	67.5	100.640	19.646	0.9804	0.4867	0.4854	0.0083	15.1506	500.075	1523.233
Ste-15	67.5	100.610	19.634	0.9794	0.4865	0.4861	0.0068	15.1392	499.264	1519.792
Ste-16	67.5	100.690	19.660	0.9798	0.4857	0.4857	0.0084	15.1262	499.274	1520.545
Ste-17	90.0	99.417	19.546	0.9768	0.4841	0.4877	0.0050	14.8288	516.487	1511.824
Ste-18	90.0	99.597	19.572	0.9857	0.4874	0.4871	0.0112	14.8921	522.670	1523.734
Ste-19	90.0	99.577	19.520	0.9853	0.4899	0.4860	0.0094	14.8243	522.085	1533.581
Ste-20	90.0	99.613	19.632	0.9958	0.4859	0.4871	0.0228	14.9534	528.307	1538.095

Table E.11: *The properties of the plate-shaped steel samples.*

Id.	Dir.	Length	Width	Thickness	Mass
Ste-21	0-90	104.534	99.486	0.9814	79.6138
Ste-22	0-90	104.322	99.312	0.9799	78.9813
Ste-23	0-90	104.398	99.356	0.9793	78.9116
Ste-24	0-90	104.484	99.452	0.9769	79.1744
	[°]	[mm]	[mm]	[mm]	[g]

Table E.12: *The layer thicknesses of the plate-shaped steel samples.*

Id.	Total	Top	Bottom	Glue
Ste-21	0.9814	0.4854	0.4861	0.0099
Ste-22	0.9799	0.4841	0.4832	0.0126
Ste-23	0.9793	0.4833	0.4837	0.0123
Ste-24	0.9769	0.4847	0.4824	0.0098
	[mm]	[mm]	[mm]	[mm]

Table E.13: *The resonant frequencies of the plate-shaped steel samples.*

Id.	f_{tors}	f_{sadd}	f_{brea}	f_{tf-x}	f_{tf-y}
Ste-21	300.2370	449.4820	559.0890	770.1840	799.3570
Ste-22	297.2700	447.9140	562.3480	768.2300	797.8210
Ste-23	300.9090	450.6130	556.4430	771.3450	800.9190
Ste-24	299.5370	447.8440	564.3280	768.5160	797.9280
	[Hz]	[Hz]	[Hz]	[Hz]	[Hz]

Table E.14: *The size of the converged FE-models in terms of elements.*

	Length	Width	Thickness		
			Top	Bottom	Glue
Beam	21	16	1	1	1
Plate	23	23	1	1	1

Elastic Properties

Table E.15: *The elastic properties of the beam-shaped steel samples.*

Id.	Dir.	E	G	ν
Ste-01	0.0	201.03	72.96	0.378
Ste-02	0.0	201.85	72.81	0.386
Ste-03	0.0	200.99	72.65	0.383
Ste-04	0.0	201.88	72.69	0.389
Ste-05	22.5	196.89	75.06	0.312
Ste-06	22.5	197.23	75.20	0.311
Ste-07	22.5	197.80	75.21	0.315
Ste-08	22.5	196.05	75.35	0.301
Ste-09	45.0	192.76	79.25	0.216
Ste-10	45.0	192.52	79.90	0.205
Ste-11	45.0	192.22	79.97	0.202
Ste-12	45.0	191.84	78.28	0.225
Ste-13	67.5	197.50	77.29	0.278
Ste-14	67.5	196.65	75.98	0.294
Ste-15	67.5	196.36	75.56	0.299
Ste-16	67.5	196.22	75.82	0.294
Ste-17	90.0	200.55	72.25	0.388
Ste-18	90.0	201.68	72.61	0.389
Ste-19	90.0	201.01	72.96	0.378
Ste-20	90.0	200.45	73.28	0.368
	[°]	[GPa]	[GPa]	[–]

Table E.16: *The averages of the elastic properties of the beam-shaped steel samples.*

Dir.	E	G	ν
0.0	201.44	72.78	0.384
22.5	196.99	75.20	0.310
45.0	192.33	79.35	0.212
67.5	196.68	76.16	0.291
90.0	200.92	72.78	0.380
[°]	[GPa]	[GPa]	[–]

Table E.17: *The elastic properties of the multi-orientation routine and the plate-shaped steel samples.*

Id.	E_1	E_2	G_{12}	ν_{12}
Multi-orientation	202.28	201.82	72.82	0.279
Ste-21	201.43	200.68	72.55	0.276
Ste-22	199.68	199.80	70.87	0.288
Ste-23	200.42	200.24	72.73	0.264
Ste-24	202.72	202.30	72.49	0.294
Average PS	201.06	200.75	72.16	0.280
	[GPa]	[GPa]	[GPa]	[–]

Frequency residuals

Table E.18: *The numerical frequencies and frequency residuals of the multi-orientation routine, steel beams.*

	Flexural		Torsional	
Id.	f_{num}	Resid.	f_{num}	Resid.
Ste-01	479.041	−0.17 %	1450.252	0.12 %
Ste-02	477.735	0.04 %	1444.761	0.03 %
Ste-03	481.149	−0.18 %	1463.646	−0.08 %
Ste-04	490.254	0.04 %	1566.699	−0.05 %
Ste-05	482.563	0.03 %	1504.680	−0.50 %
Ste-06	479.137	0.12 %	1495.306	−0.41 %
Ste-07	478.125	0.27 %	1492.225	−0.40 %
Ste-08	480.512	−0.19 %	1498.842	−0.33 %
Ste-09	481.996	0.18 %	1533.665	0.15 %
Ste-10	489.933	0.11 %	1546.181	0.53 %
Ste-11	492.679	0.03 %	1552.459	0.57 %
Ste-12	480.077	−0.06 %	1533.619	−0.45 %
Ste-13	500.180	0.22 %	1519.854	0.92 %
Ste-14	499.932	0.03 %	1521.986	0.08 %
Ste-15	499.460	−0.04 %	1522.551	−0.18 %
Ste-16	499.682	−0.08 %	1520.846	−0.02 %
Ste-17	517.272	−0.15 %	1517.004	−0.34 %
Ste-18	522.025	0.12 %	1525.279	−0.10 %
Ste-19	522.395	−0.06 %	1531.639	0.13 %
Ste-20	529.452	−0.22 %	1533.086	0.33 %
	[Hz]	[–]	[Hz]	[–]

E.1.3. The Brass-Steel Bi-Metal Samples

Sample Description

Table E.19: *The properties of the beam-shaped brass-steel samples.*

Id.	Dir.	Length	Width	Thickness				Mass	f_f	f_t
				Total	Brass	Steel	Glue			
	[°]	[mm]	[mm]	[mm]	[mm]	[mm]	[mm]	[g]	[Hz]	[Hz]
BSB-01	0.0	103.697	19.516	1.3044	0.8144	0.4850	0.0050	21.5481	525.131	1576.642
BSB-02	0.0	103.520	19.574	1.2973	0.8079	0.4844	0.0050	21.4415	523.930	1574.362
BSB-03	0.0	103.713	19.648	1.3059	0.8149	0.4863	0.0047	21.6924	525.901	1575.496
BSB-04	0.0	103.540	19.418	1.3048	0.8134	0.4841	0.0073	21.3990	527.115	1579.752
BSB-05	0.0	102.273	18.270	1.3236	0.8111	0.4847	0.0278	19.8902	548.560	1733.792
BSB-06	0.0	103.367	19.600	1.3100	0.8201	0.4877	0.0022	21.6497	529.016	1585.511
BSB-07	22.5	102.650	19.688	1.3066	0.8162	0.4854	0.0050	21.5853	532.138	1599.005
BSB-08	22.5	102.683	19.600	1.3147	0.8137	0.4853	0.0157	21.5113	534.897	1617.108
BSB-09	22.5	102.750	19.540	1.3151	0.8169	0.4869	0.0113	21.5097	535.901	1630.203
BSB-10	22.5	102.593	19.674	1.3085	0.8161	0.4862	0.0062	21.5418	531.791	1605.267
BSB-11	22.5	102.583	19.512	1.3049	0.8190	0.4838	0.0021	21.3680	530.558	1598.476
BSB-12	22.5	102.510	19.544	1.3108	0.8200	0.4848	0.0060	21.3669	533.316	1621.539
BSB-13	45.0	101.773	19.656	1.3244	0.8157	0.4838	0.0249	21.3421	540.782	1658.251
BSB-14	45.0	101.360	19.516	1.3118	0.8200	0.4857	0.0061	21.1708	537.924	1666.932
BSB-15	45.0	101.667	19.678	1.3158	0.8164	0.4833	0.0161	21.3711	536.225	1642.362
BSB-16	45.0	101.560	19.592	1.3106	0.8212	0.4852	0.0042	21.2770	536.707	1659.175
BSB-17	45.0	101.577	19.662	1.3143	0.8182	0.4827	0.0134	21.3244	536.332	1588.111
BSB-18	45.0	101.450	19.574	1.3123	0.8204	0.4861	0.0058	21.2823	537.104	1616.725

...

Table E.20: *The properties of the beam-shaped brass-steel samples.*

Id.	Dir.	Length	Width	Thickness				Mass	f_f	f_t
				Total	Brass	Steel	Glue			
...										
BSB-19	67.5	100.613	19.666	1.3043	0.8133	0.4831	0.0079	21.0540	543.401	1634.874
BSB-20	67.5	100.690	19.684	1.3038	0.8120	0.4835	0.0083	21.0541	543.747	1636.061
BSB-21	67.5	100.660	19.630	1.3115	0.8132	0.4865	0.0118	21.0454	548.588	1649.278
BSB-22	67.5	100.500	19.602	1.3078	0.8120	0.4837	0.0120	20.9615	546.187	1646.031
BSB-23	67.5	100.657	19.658	1.3150	0.8135	0.4859	0.0156	21.1017	548.913	1646.959
BSB-24	67.5	100.560	19.634	1.3074	0.8142	0.4854	0.0078	21.0574	546.333	1639.586
BSB-25	90.0	99.630	19.516	1.3133	0.8187	0.4841	0.0105	20.7667	563.015	1653.064
BSB-26	90.0	99.607	19.610	1.3073	0.8175	0.4831	0.0067	20.8488	560.559	1640.486
BSB-27	90.0	99.580	19.466	1.3121	0.8182	0.4842	0.0097	20.7830	563.549	1657.501
BSB-28	90.0	99.680	19.584	1.3084	0.8166	0.4841	0.0077	20.8468	560.688	1630.196
BSB-29	90.0	99.730	19.558	1.3134	0.8200	0.4864	0.0070	20.9033	561.543	1582.156
BSB-30	90.0	99.523	19.576	1.3019	0.8087	0.4836	0.0095	21.6328	547.123	1598.419
	[°]	[mm]	[mm]	[mm]	[mm]	[mm]	[mm]	[g]	[Hz]	[Hz]

Table E.21: *The properties of the modified beam-shaped brass-steel samples.*

Id.	Dir.	Length	Width	Thickness				Mass	f_f	f_t	Glass Id.
				Total	BSB	Glue	Glass				
BSB-01a	0.0	103.527	19.438	2.0054	1.3044	0.0166	0.6844	24.8822	826.576	2538.239	Gla-0.7-01
BSB-02a	0.0	102.527	19.492	2.0043	1.2973	0.0261	0.6809	24.5904	837.900	2499.660	Gla-0.7-02
BSB-03a	0.0	103.517	19.552	2.0062	1.3059	0.0172	0.6831	25.0508	738.340	2244.460	Gla-0.7-03
BSB-04a	0.0	103.543	19.346	2.0065	1.3048	0.0152	0.6865	24.7467	736.872	2254.517	Gla-0.7-04
BSB-05a	0.0	102.213	18.248	1.8938	1.3236	0.0169	0.5533	22.4204	793.615	2564.465	Gla-0.6-01
BSB-06a	0.0	103.357	19.518	1.8797	1.3100	0.0163	0.5534	23.3783	700.104	2099.796	Gla-0.6-02
BSB-07a	22.5	102.673	19.630	2.0141	1.3066	0.0220	0.6855	24.9979	840.780	2557.124	Gla-0.7-05
BSB-08a	22.5	102.560	19.510	2.0212	1.3147	0.0241	0.6824	24.8380	845.212	2589.257	Gla-0.7-06
BSB-09a	22.5	102.507	19.490	2.0129	1.3151	0.0153	0.6824	24.7705	752.312	2299.708	Gla-0.7-07
BSB-10a	22.5	102.520	19.620	2.0005	1.3085	0.0084	0.6835	24.8903	744.562	2265.997	Gla-0.7-08
BSB-11a	22.5	102.467	19.462	1.8783	1.3049	0.0188	0.5547	24.0849	775.062	2348.662	Gla-0.6-03
BSB-12a	22.5	102.467	19.476	1.8780	1.3108	0.0141	0.5532	24.0650	697.823	2111.229	Gla-0.6-04
BSB-13a	45.0	101.650	19.616	2.0350	1.3244	0.0278	0.6827	24.6953	859.634	2627.496	Gla-0.7-09
BSB-14a	45.0	101.317	19.444	2.0159	1.3118	0.0279	0.6811	24.5011	859.872	2658.106	Gla-0.7-10
BSB-15a	45.0	101.650	19.618	2.0181	1.3158	0.0187	0.6836	24.6966	760.355	2312.636	Gla-0.7-11
BSB-16a	45.0	101.493	19.484	2.0152	1.3106	0.0247	0.6798	24.5856	760.853	2304.267	Gla-0.7-12
BSB-17a	45.0	101.510	19.570	1.9016	1.3143	0.0335	0.5538	24.0070	794.533	2369.800	Gla-0.6-05
BSB-18a	45.0	101.383	19.550	1.8793	1.3123	0.0136	0.5534	23.9883	704.438	2100.390	Gla-0.6-06
...											
	[°]	[mm]	[mm]	[mm]	[mm]	[mm]	[mm]	[g]	[Hz]	[Hz]	

Table E.22: *The properties of the modified beam-shaped brass-steel samples.*

Id.	Dir.	Length	Width	Thickness				Mass	f_f	f_t	Glass Id.
				Total	BSB	Glue	Glass				
...											
BSB-19a	67.5	100.643	19.508	2.0118	1.3043	0.0245	0.6830	24.2758	871.448	2638.384	Gla-0.7-13
BSB-20a	67.5	100.643	19.588	2.0145	1.3038	0.0308	0.6800	24.3851	872.740	2611.505	Gla-0.7-14
BSB-21a	67.5	100.507	19.552	2.0182	1.3115	0.0254	0.6813	24.3456	774.556	2330.772	Gla-0.7-15
BSB-22a	67.5	100.480	19.554	2.0219	1.3078	0.0309	0.6832	24.2413	777.277	2338.122	Gla-0.7-16
BSB-23a	67.5	100.617	19.548	1.8844	1.3150	0.0160	0.5534	23.7254	806.813	2439.687	Gla-0.6-07
BSB-24a	67.5	100.480	19.554	1.8807	1.3074	0.0193	0.5539	23.7140	717.599	2160.422	Gla-0.6-08
BSB-25a	90.0	99.513	19.476	2.0232	1.3133	0.0246	0.6853	24.0514	900.798	2660.286	Gla-0.7-17
BSB-26a	90.0	99.430	19.546	2.0208	1.3073	0.0317	0.6818	24.1105	897.166	2644.695	Gla-0.7-18
BSB-27a	90.0	99.567	19.488	2.0036	1.3121	0.0066	0.6849	24.0584	786.351	2344.537	Gla-0.7-19
BSB-28a	90.0	99.430	19.534	2.0127	1.3084	0.0217	0.6827	24.1185	788.204	2325.638	Gla-0.7-20
BSB-29a	90.0	99.617	19.456	1.8878	1.3134	0.0200	0.5544	23.4777	826.979	2369.521	Gla-0.6-09
BSB-30a	90.0	99.433	19.470	1.8685	1.3019	0.0103	0.5564	23.2092	729.429	2177.080	Gla-0.6-10
	[°]	[mm]	[mm]	[mm]	[mm]	[mm]	[mm]	[g]	[Hz]	[Hz]	

Table E.23: *The properties of the plate-shaped brass-steel samples.*

Id.	Dir.	Length	Width	Thickness	Mass
BSB-31	0-90	104.508	99.534	1.3129	110.9973
BSB-32	0-90	104.500	99.534	1.3133	111.2240
BSB-33	0-90	104.530	99.610	1.3111	111.1373
BSB-34	0-90	104.598	99.506	1.3076	110.8261
BSB-35	0-90	104.584	99.458	1.3206	111.4791
BSB-36	0-90	104.284	99.564	1.3112	110.7103
	[°]	[mm]	[mm]	[mm]	[g]

Table E.24: *The layer thicknesses of the plate-shaped brass-steel samples.*

Id.	Total	Brass	Steel	Glue
BSB-31	1.3129	0.8178	0.4837	0.0114
BSB-32	1.3133	0.8187	0.4861	0.0085
BSB-33	1.3111	0.8168	0.4862	0.0081
BSB-34	1.3076	0.8163	0.4834	0.0078
BSB-35	1.3206	0.8220	0.4844	0.0143
BSB-36	1.3112	0.8156	0.4850	0.0106
	[mm]	[mm]	[mm]	[mm]

Table E.25: *The resonant frequencies of the plate-shaped brass-steel samples.*

Id.	f_{tors}	f_{sadd}	f_{brea}	f_{tf-x}	f_{tf-y}
BSB-31	328.078	490.103	622.872	846.960	872.926
BSB-32	327.550	488.722	624.085	847.083	874.330
BSB-33	326.528	488.206	623.448	845.138	870.869
BSB-34	326.742	488.359	621.502	841.226	869.563
BSB-35	330.199	492.561	627.461	851.222	878.882
BSB-36	328.326	490.712	621.602	845.669	871.959
	[Hz]	[Hz]	[Hz]	[Hz]	[Hz]

Table E.26: *The size of the converged FE-models in terms of elements, brass-steel samples.*

	Length	Width	Thickness		
			Brass	Steel	Glue
Beam	19	15	1	1	1
Plate	23	23	2	1	1

Table E.27: *The properties of the modified plate-shaped brass-steel samples.*

Id.	Dir.	Length	Width	Thickness	Mass	Glass id.
BSB-31a	0-90	104.488	99.468	2.0447	129.1790	Gla-0.7-43
BSB-32a	0-90	104.426	99.440	2.0412	129.3863	Gla-0.7-45
BSB-33a	0-90	104.378	99.466	2.0308	129.0584	Gla-0.7-44
BSB-34a	0-90	104.472	99.436	2.0321	128.9519	Gla-0.7-46
BSB-35a	0-90	104.480	99.356	1.9121	126.3886	Gla-0.6-1
BSB-36a	0-90	104.178	99.444	1.9098	125.4250	Gla-0.6-2
	[°]	[mm]	[mm]	[mm]	[g]	

Table E.28: *The layer thicknesses of the modified plate-shaped brass-steel samples.*

Id.	Total	BSB	Glass	Glue
BSB-31a	2.0447	1.3129	0.6828	0.0491
BSB-32a	2.0412	1.3133	0.6799	0.0480
BSB-33a	2.0308	1.3111	0.6816	0.0380
BSB-34a	2.0321	1.3076	0.6852	0.0394
BSB-35a	1.9121	1.3206	0.5542	0.0372
BSB-36a	1.9098	1.3112	0.5526	0.0460
	[mm]	[mm]	[mm]	[mm]

Table E.29: *The resonant frequencies of the modified plate-shaped brass-steel samples.*

Id.	f_{tors}	f_{sadd}	f_{brea}	f_{tf-x}	f_{tf-y}
BSB-31a	542.023	800.541	978.339	1373.869	1421.772
BSB-32a	547.426	808.329	989.379	1379.367	1427.491
BSB-33a	477.700	702.003	877.726	1213.998	1251.972
BSB-34a	479.115	702.776	879.790	1214.798	1255.850
BSB-35a	507.295	747.138	920.974	1276.620	1323.231
BSB-36a	445.863	655.762	816.301	1133.727	1168.103
	[Hz]	[Hz]	[Hz]	[Hz]	[Hz]

Table E.30: *The size of the converged FE-models in terms of elements, modified brass-steel samples.*

	Length	Width	Thickness				
			Brass	Steel	Glass	E-32	B-682
Beam	17	12	1	1	1	1	1
Plate	23	23	1	1	1	1	1

Elastic Properties

Table E.31: *The elastic properties of the beam-shaped brass-steel samples, identification with the properties of one layer fixed to the reference properties.*

Id.	Dir.	Brass			Steel		
		E	G	ν	E	G	ν
BSB-01	0.0	107.82	37.32	0.444	203.88	73.49	0.387
BSB-02	0.0	107.67	37.93	0.419	203.27	75.18	0.352
BSB-03	0.0	107.86	37.83	0.425	203.81	74.92	0.360
BSB-04	0.0	107.81	36.84	0.463	204.02	72.15	0.414
BSB-05	0.0	106.30	38.46	0.382	199.35	76.67	0.300
BSB-06	0.0	106.48	37.36	0.425	200.27	73.61	0.360
BSB-07	22.5	106.79	37.97	0.406	200.81	75.25	0.334
BSB-08	22.5	106.00	38.55	0.375	198.42	76.91	0.290
BSB-09	22.5	107.39	39.14	0.372	201.93	78.58	0.285
BSB-10	22.5	105.34	38.09	0.383	196.84	75.61	0.302
BSB-11	22.5	105.60	36.71	0.438	198.09	71.75	0.380
BSB-12	22.5	104.75	38.09	0.375	195.27	75.60	0.291
BSB-13	45.0	101.44	38.71	0.310	190.16	79.15	0.201
BSB-14	45.0	102.02	38.78	0.315	191.69	79.38	0.207
BSB-15	45.0	101.21	38.25	0.323	189.75	77.81	0.219
BSB-16	45.0	102.88	38.88	0.323	194.00	79.68	0.217
BSB-17	45.0	100.06	33.86	0.478	188.37	65.47	0.439
BSB-18	45.0	101.40	35.33	0.435	191.47	69.49	0.378
BSB-19	67.5	100.71	38.12	0.321	194.71	75.74	0.285
BSB-20	67.5	101.38	38.42	0.319	196.48	76.60	0.283
BSB-21	67.5	101.68	38.37	0.325	197.32	76.45	0.291
BSB-22	67.5	100.43	38.24	0.313	193.93	76.09	0.274
BSB-23	67.5	100.77	38.18	0.320	194.86	75.91	0.283
BSB-24	67.5	101.33	37.89	0.337	196.42	75.11	0.307
BSB-25	90.0	101.54	37.57	0.351	200.71	72.62	0.382
BSB-26	90.0	102.06	37.70	0.353	202.14	72.99	0.385
BSB-27	90.0	102.66	37.90	0.354	203.80	73.53	0.386
BSB-28	90.0	102.22	36.74	0.391	202.31	70.40	0.437
BSB-29	90.0	99.37	33.12	0.500	188.83	62.94	0.500
BSB-30	90.0	102.12	37.56	0.359	202.29	72.60	0.393
	[°]	[GPa]	[GPa]	[–]	[GPa]	[GPa]	[–]

Table E.32: *The elastic properties of the beam-shaped brass-steel samples, identification using the initial and modified layer configurations.*

Id.	Dir.	Brass			Steel		
		E	G	ν	E	G	ν
BSB-01	0.0	107.49	37.10	0.449	202.23	73.39	0.378
BSB-02	0.0	109.88	41.06	0.338	195.12	65.47	0.490
BSB-03	0.0	107.65	37.31	0.443	201.42	71.61	0.406
BSB-04	0.0	106.37	37.17	0.431	205.38	71.87	0.429
BSB-05	0.0	105.99	36.60	0.448	201.45	78.08	0.290
BSB-06	0.0	102.75	34.25	0.500	210.44	82.57	0.274
BSB-07	22.5	104.95	37.65	0.394	201.87	76.10	0.326
BSB-08	22.5	104.74	37.67	0.390	200.03	77.71	0.287
BSB-09	22.5	106.68	39.23	0.360	198.85	74.97	0.326
BSB-10	22.5	105.55	38.43	0.373	196.54	74.29	0.323
BSB-11	22.5	105.97	39.59	0.338	196.14	67.76	0.447
BSB-12	22.5	105.75	36.39	0.453	192.65	80.37	0.198
BSB-13	45.0	102.13	38.73	0.319	190.46	79.29	0.201
BSB-14	45.0	100.58	37.98	0.324	195.98	81.81	0.198
BSB-15	45.0	104.36	39.93	0.307	184.81	74.66	0.238
BSB-16	45.0	103.56	37.57	0.378	189.29	83.46	0.134
BSB-17	45.0	101.13	37.12	0.362	191.66	69.39	0.381
BSB-18	45.0	101.21	34.76	0.456	192.01	81.34	0.180
BSB-19	67.5	98.82	37.03	0.334	201.90	79.41	0.271
BSB-20	67.5	100.04	38.57	0.297	200.37	75.75	0.323
BSB-21	67.5	101.80	38.79	0.312	196.40	74.99	0.310
BSB-22	67.5	102.02	39.19	0.302	192.51	73.60	0.308
BSB-23	67.5	100.00	37.64	0.328	198.74	77.72	0.279
BSB-24	67.5	102.08	38.21	0.336	194.68	75.27	0.293
BSB-25	90.0	100.28	36.40	0.377	204.48	76.12	0.343
BSB-26	90.0	102.25	37.04	0.380	200.39	74.61	0.343
BSB-27	90.0	102.84	38.24	0.345	200.36	71.88	0.394
BSB-28	90.0	100.99	37.08	0.362	204.20	71.84	0.421
BSB-29	90.0	104.86	35.46	0.478	191.91	63.97	0.500
BSB-30	90.0	102.75	38.42	0.337	199.04	70.54	0.411
	[°]	[GPa]	[GPa]	[–]	[GPa]	[GPa]	[–]

Table E.33: *The average elastic properties of the beam-shaped brass-steel samples, identification with the properties of one layer fixed to the reference properties.*

Dir.	Brass			Steel		
	E	G	ν	E	G	ν
0.0	107.32	37.62	0.427	202.43	74.34	0.362
22.5	105.98	38.09	0.391	198.56	75.62	0.314
45.0	101.50	38.65	0.318	190.91	79.01	0.211
67.5	101.05	38.20	0.323	195.62	75.98	0.287
90.0	101.66	37.50	0.362	202.25	72.43	0.397
[°]	[GPa]	[GPa]	[–]	[GPa]	[GPa]	[–]

Table E.34: *The elastic properties of the beam-shaped brass-steel samples, identification using the initial and modified layer configurations.*

Dir.	Brass			Steel		
	E	G	ν	E	G	ν
0.0	107.48	37.05	0.422	202.67	72.29	0.378
22.5	105.60	38.16	0.385	197.68	76.69	0.318
45.0	102.16	38.27	0.358	190.70	80.11	0.222
67.5	100.79	38.24	0.318	197.43	76.12	0.297
90.0	102.33	37.11	0.380	201.69	73.00	0.382
[°]	[GPa]	[GPa]	[–]	[GPa]	[GPa]	[–]

Table E.35: *The elastic properties of the multi-orientation routines.*

	Brass			
Id.	E_1	E_2	G_{12}	ν_{12}
Steel props. fixed	107.68	101.59	37.53	0.359
All frequencies	107.20	101.31	37.51	0.372
Selected frequencies	107.52	101.62	37.36	0.366
	[GPa]	[GPa]	[GPa]	[–]
	Steel			
Id.	E_1	E_2	G_{12}	ν_{12}
Brass props. fixed	203.04	201.36	73.14	0.280
All frequencies	202.71	202.11	72.00	0.300
Selected frequencies	203.22	202.78	73.18	0.270
	[GPa]	[GPa]	[GPa]	[–]

Table E.36: *The elastic properties of the plate-shaped samples, identification with the properties of one layer fixed to the reference properties.*

	Brass			
Id.	E_1	E_2	G_{12}	ν_{12}
BSB-31	107.37	101.01	37.40	0.352
BSB-32	106.40	101.68	37.34	0.357
BSB-33	107.49	101.38	37.17	0.363
BSB-34	107.42	102.69	37.35	0.347
BSB-35	106.80	101.08	37.41	0.353
BSB-36	106.23	101.85	37.32	0.341
	[GPa]	[GPa]	[GPa]	[–]
	Steel			
Id.	E_1	E_2	G_{12}	ν_{12}
BSB-31	202.33	198.82	72.67	0.281
BSB-32	199.94	200.72	72.50	0.289
BSB-33	202.77	199.92	72.06	0.297
BSB-34	202.40	203.44	72.54	0.274
BSB-35	200.91	199.02	72.68	0.283
BSB-36	199.29	201.07	72.45	0.266
	[GPa]	[GPa]	[GPa]	[–]

Table E.37: *The elastic properties of the plate-shaped samples, identification using the initial and modified layer configurations.*

	Brass			
Id.	E_1	E_2	G_{12}	ν_{12}
BSB-31	102.14	97.26	35.96	0.348
BSB-32	97.00	94.84	34.78	0.343
BSB-33	112.45	105.89	38.95	0.384
BSB-34	112.73	108.75	39.55	0.367
BSB-35	95.97	92.39	35.24	0.331
BSB-36	111.38	105.01	38.52	0.357
	[GPa]	[GPa]	[GPa]	[–]
	Steel			
Id.	E_1	E_2	G_{12}	ν_{12}
BSB-31	215.60	211.94	76.28	0.284
BSB-32	230.00	222.30	79.96	0.297
BSB-33	189.11	188.92	67.76	0.256
BSB-34	188.41	185.67	66.83	0.256
BSB-35	235.07	229.46	78.60	0.309
BSB-36	188.67	192.46	69.10	0.262
	[GPa]	[GPa]	[GPa]	[–]

Frequency residuals

Table E.38: *The frequency residuals and the new weighting coefficients of the multi-orientation routine.*

Id.	Dir.	Frequency residuals				New w_i coefficients			
		Initial		Modified		Initial		Modified	
		f_f	f_t	f_f	f_t	f_f	f_t	f_f	f_t
BSB-01	0.0	0.15	0.11	0.21	0.34	1.0	1.0	1.0	2.0
BSB-02	0.0	0.09	0.57	−0.30	−1.45	1.0	1.0	1.0	0.0
BSB-03	0.0	0.14	0.50	0.47	0.23	1.0	1.0	1.0	2.0
BSB-04	0.0	0.18	−0.26	0.13	−0.21	1.0	1.0	1.0	2.0
BSB-05	0.0	−0.33	0.92	−0.03	1.41	1.0	1.0	1.0	0.0
BSB-06	0.0	−0.23	0.14	−0.39	−1.96	1.0	1.0	1.0	0.0
BSB-07	22.5	0.35	0.16	0.46	0.30	1.0	1.0	1.0	1.2
BSB-08	22.5	0.09	0.58	0.23	0.69	1.0	1.0	1.0	1.2
BSB-09	22.5	0.46	1.01	0.27	0.85	1.0	1.0	1.0	1.2
BSB-10	22.5	−0.08	0.24	0.00	0.34	1.0	1.0	1.0	1.2
BSB-11	22.5	0.08	−0.81	0.10	−1.70	1.0	1.0	1.0	0.0
BSB-12	22.5	−0.25	0.24	0.07	−0.73	1.0	1.0	1.0	1.2
BSB-13	45.0	−0.43	0.68	−0.35	0.39	1.0	1.5	1.0	1.5
BSB-14	45.0	−0.27	0.75	0.17	0.91	1.0	1.5	1.0	1.5
BSB-15	45.0	−0.49	0.34	0.13	0.92	1.0	1.5	1.0	1.5
BSB-16	45.0	−0.02	0.83	0.15	−0.32	1.0	1.5	1.0	1.5
BSB-17	45.0	−0.51	−3.22	−0.09	−2.39	1.0	0.0	1.0	0.0
BSB-18	45.0	−0.23	−1.95	−0.27	−2.28	1.0	0.0	1.0	0.0
BSB-19	67.5	−0.29	0.52	0.32	1.02	1.0	1.0	1.0	1.0
BSB-20	67.5	−0.10	0.75	0.24	0.31	1.0	1.0	1.0	1.0
BSB-21	67.5	−0.01	0.71	−0.01	0.58	1.0	1.0	1.0	1.0
BSB-22	67.5	−0.38	0.61	−0.02	0.76	1.0	1.0	1.0	1.0
BSB-23	67.5	−0.27	0.56	0.02	0.69	1.0	1.0	1.0	1.0
BSB-24	67.5	−0.10	0.36	0.05	0.25	1.0	1.0	1.0	1.0
BSB-25	90.0	−0.02	0.27	0.27	0.94	1.0	1.2	1.0	1.2
BSB-26	90.0	0.14	0.38	−0.05	0.63	1.0	1.2	1.0	1.2
BSB-27	90.0	0.31	0.53	0.41	0.47	1.0	1.2	1.0	1.2
BSB-28	90.0	0.21	−0.34	0.08	−0.28	1.0	1.2	1.0	1.2
BSB-29	90.0	0.06	−3.91	0.16	−2.99	1.0	0.0	1.0	0.0
BSB-30	90.0	0.16	0.27	0.41	0.53	1.0	1.2	1.0	1.2
	[°]	[%]	[%]	[%]	[%]	[–]	[–]	[–]	[–]

E.1.4. The Glass Samples

Sample Description

Table E.39: *The properties of the beam-shaped glass samples.*

Id	Length	Width	Thick.	Mass	f_f	f_t
Gla-0.6-01	102.660	18.768	0.5533	2.6599	288.914	981.361
Gla-0.6-02	103.900	19.984	0.5534	2.8615	282.718	913.552
Gla-0.6-03	103.220	20.242	0.5547	2.8800	286.643	911.515
Gla-0.6-04	103.345	20.114	0.5532	2.8659	285.913	913.270
Gla-0.6-05	102.085	19.746	0.5538	2.7819	293.054	940.368
Gla-0.6-06	102.085	19.748	0.5534	2.8136	291.051	933.248
Gla-0.6-07	101.370	20.056	0.5534	2.8031	297.428	932.852
Gla-0.6-08	101.100	19.920	0.5539	2.7742	299.235	944.464
Gla-0.6-09	100.245	20.296	0.5544	2.8050	304.047	931.703
Gla-0.6-10	99.920	19.996	0.5564	2.7548	307.304	957.090
	[mm]	[mm]	[mm]	[g]	[Hz]	[Hz]

Table E.40: *The properties of the beam-shaped glass samples.*

Id	Length	Width	Thick.	Mass	f_f	f_t
Gla-0.7-01	104.055	19.958	0.6844	3.5204	348.208	1125.291
Gla-0.7-02	102.865	19.404	0.6809	3.3666	354.170	1165.906
Gla-0.7-03	104.025	20.376	0.6831	3.5810	347.449	1105.188
Gla-0.7-04	104.295	19.940	0.6865	3.5311	348.091	1127.851
Gla-0.7-05	102.980	19.810	0.6855	3.4589	356.177	1145.837
Gla-0.7-06	103.055	20.418	0.6824	3.5529	355.094	1113.375
Gla-0.7-07	102.790	20.820	0.6824	3.6123	356.422	1093.550
Gla-0.7-08	102.875	20.084	0.6835	3.5038	355.636	1129.024
Gla-0.7-09	101.925	20.060	0.6827	3.4620	363.771	1146.705
Gla-0.7-10	101.865	20.674	0.6811	3.5627	362.638	1108.119
Gla-0.7-11	102.105	20.148	0.6836	3.4790	361.013	1135.560
Gla-0.7-12	102.040	20.644	0.6798	3.5537	360.390	1108.105
Gla-0.7-13	101.170	20.352	0.6830	3.4860	367.538	1133.340
Gla-0.7-14	101.260	20.432	0.6800	3.4875	366.303	1128.086
Gla-0.7-15	100.995	20.562	0.6813	3.5071	368.360	1124.724
Gla-0.7-16	101.085	20.030	0.6832	3.4292	368.459	1154.211
Gla-0.7-17	100.210	20.020	0.6843	3.3920	375.972	1164.219
Gla-0.7-18	100.515	19.958	0.6818	3.3895	371.663	1165.414
Gla-0.7-19	100.010	20.290	0.6849	3.4457	377.289	1150.750
Gla-0.7-20	100.295	20.608	0.6827	3.4968	374.123	1131.992
	[mm]	[mm]	[mm]	[g]	[Hz]	[Hz]

Table E.41: *The properties of the plate-shaped glass samples.*

Id.	Dir.	Length	Width	Thickness	Mass
Gla-0.6-11	0-90	104.697	99.845	0.5542	14.4091
Gla-0.6-12	0-90	104.963	99.755	0.5526	14.4259
Gla-0.7-21	0-90	105.750	100.150	0.6828	17.9866
Gla-0.7-22	0-90	105.723	100.365	0.6799	17.9159
Gla-0.7-23	0-90	105.670	100.025	0.6816	17.9179
Gla-0.7-24	0-90	105.263	100.247	0.6852	17.9711
	[°]	[mm]	[mm]	[mm]	[g]

Table E.42: *The resonant frequencies of the plate-shaped glass samples.*

Id.	f_{tors}	f_{sadd}	f_{brea}	f_{tf-x}	f_{tf-y}
Gla-0.6-11	189.787	268.800	322.340	474.020	490.541
Gla-0.6-12	187.812	266.836	321.034	470.906	488.801
Gla-0.7-21	228.436	325.690	393.055	571.094	593.442
Gla-0.7-22	227.187	325.144	391.827	568.731	590.638
Gla-0.7-23	228.458	326.386	392.158	571.099	594.621
Gla-0.7-24	229.362	328.391	393.741	575.912	596.080
	[Hz]	[Hz]	[Hz]	[Hz]	[Hz]

Table E.43: *The size of the converged FE-model in terms of elements.*

	Length	Width	Thickness
Beam 0.6 mm	23	22	3
Beam 0.7 mm	22	21	3
Plate 0.6 mm	21	21	1
Plate 0.7 mm	21	22	1

Elastic Properties

Table E.44: *The elastic properties of the beam-shaped glass samples.*

Id.	E	G	ν
Gla-0.6-01	71.26	29.26	0.218
Gla-0.6-02	71.41	29.30	0.218
Gla-0.6-03	71.02	29.32	0.211
Gla-0.6-04	71.59	29.38	0.218
Gla-0.6-05	71.45	29.24	0.222
Gla-0.6-06	71.67	29.30	0.223
Gla-0.6-07	71.63	29.28	0.223
Gla-0.6-08	71.49	29.36	0.218
Gla-0.6-09	71.19	29.07	0.225
Gla-0.6-10	71.04	29.29	0.213
	[GPa]	[GPa]	[–]

Table E.45: *The elastic properties of the beam-shaped glass samples.*

Id.	E	G	ν
Gla-0.7-01	70.87	29.06	0.219
Gla-0.7-02	70.76	29.15	0.214
Gla-0.7-03	70.66	29.26	0.208
Gla-0.7-04	70.94	29.06	0.221
Gla-0.7-05	70.80	28.95	0.223
Gla-0.7-06	71.25	29.31	0.216
Gla-0.7-07	71.02	29.20	0.216
Gla-0.7-08	70.93	29.06	0.220
Gla-0.7-09	71.65	29.41	0.218
Gla-0.7-10	71.47	29.27	0.221
Gla-0.7-11	70.70	29.05	0.217
Gla-0.7-12	71.29	29.38	0.213
Gla-0.7-13	70.89	29.07	0.219
Gla-0.7-14	71.30	29.33	0.216
Gla-0.7-15	71.08	29.25	0.215
Gla-0.7-16	70.98	29.16	0.217
Gla-0.7-17	70.90	28.93	0.225
Gla-0.7-18	70.88	29.30	0.210
Gla-0.7-19	71.13	29.02	0.226
Gla-0.7-20	70.99	29.22	0.215
	[GPa]	[GPa]	[–]

Table E.46: *The elastic properties of the plate-shaped glass samples.*

Id.	E_1	E_2	G_{12}	ν_{12}
Gla-0.6-11	70.70	70.88	29.40	0.218
Gla-0.6-12	70.72	71.09	29.25	0.216
Gla-0.7-21	70.88	70.55	28.76	0.220
Gla-0.7-22	71.11	71.17	28.73	0.219
Gla-0.7-23	70.75	71.01	28.80	0.207
Gla-0.7-24	70.58	70.28	28.64	0.220
	[GPa]	[GPa]	[GPa]	[–]

E.2. Carbon-Epoxy Composite

E.2.1. The Carbon-Epoxy Specimens

Sample Description

Table E.47: *The properties of the carbon-epoxy samples.*

Id.	Dir.	Length	Width	Thickness	Mass
PCE-01	0–90	157.945	104.035	1.8419	43.5439
PCE-02	0–90	151.020	104.035	1.8419	41.6458
PCE-03	0–90	—	—	1.8541	—
PCE-03a	0–90	156.417	149.463	3.9371	183.8965
	[°]	[mm]	[mm]	[mm]	[mm]

Table E.48: *The layer thicknesses, after correction for the peel ply imprint.*

Id.	Total	Skin	Core	Skin	Glue	Glass
PCE-01	1.7676	—	—	—	—	—
PCE-02	1.7676	0.4419	0.8838	0.4419	—	—
PCE-03	1.7799	0.4450	0.8899	0.4450	—	—
PCE-03a	3.9000	0.4450	0.8899	0.4450	0.0454	2.0747
	[mm]	[mm]	[mm]	[mm]	[mm]	[mm]

Table E.49: *The resonant frequencies of the first five vibration modes.*

Id.	f_{tors}	f_{sadd}	f_{brea}	f_{tf-x}	f_{tf-y}
PCE-01	188.49	572.07	626.76	689.12	730.01
PCE-02	196.63	614.06	638.36	738.72	743.81
PCE-03	—	—	—	—	—
PCE-03a	388.83	917.89	1010.04	1224.54	1251.06
	[Hz]	[Hz]	[Hz]	[Hz]	[Hz]

Table E.50: *The size of the converged FE-models in terms of elements.*

Id.	Length	Width	Thickness				
			Skin	Core	Skin	Glue	Glass
PCE-01	20	17	1	1	1	—	—
PCE-02	20	17	1	1	1	—	—
PCE-03a	19	18	1	1	1	1	1

Elastic Properties

Table E.51: *The elastic properties of the carbon-epoxy samples.*

Id.	E_1	E_2	G_{12}	ν_{12}	Remarks
PCE-01	82.85	18.31	3.53	0.129	Homogeneous
PCE-02	103.76	9.30	3.99	0.260	Layered
PCE-03a	67.22	60.25	9.82	0.136	Homogeneous
PCE-02/03a	103.68	9.36	3.99	0.259	Layered – Skin
	9.92	103.38	3.97	0.024	Layered – Core
	[GPa]	[GPa]	[GPa]	[–]	

E.2.2. Glass Specimens

Sample Description

Table E.52: *The properties of the glass sample.*

Id.	Dir.	Length	Width	Thickness	Mass
Gla-2.0-01	0–90	156.227	149.670	2.0747	121.1915
	[°]	[mm]	[mm]	[mm]	[mm]

Table E.53: *The resonant frequencies of the first five vibration modes.*

Id.	f_{tors}	f_{sadd}	f_{brea}	f_{tf-x}	f_{tf-y}
Gla-2.0-01	315.40	452.95	540.89	791.13	815.65
	[Hz]	[Hz]	[Hz]	[Hz]	[Hz]

Table E.54: *The size of the converged FE-model in terms of elements.*

Id.	Length	Width	Thickness
Gla-2.0-01	23	23	3

Elastic Properties

Table E.55: *The elastic properties of the glass sample.*

Id.	E_1	E_2	G_{12}	ν_{12}
Gla-2.0-01	71.96	71.81	29.24	0.222
	[GPa]	[GPa]	[GPa]	[–]

E.3. Air Plasma Sprayed Coatings

E.3.1. The Initial Plate-Shaped Specimens

Sample Description

Table E.56: *The properties of the initial plate-shaped samples.*

Id.	Length	Width	Thickness			Mass
			Total	Substr.	Coating	
ACS-01	145.424	150.264	1.9350	1.9350	—	331.121
ACB-01	145.340	150.438	2.1999	1.9350	0.2649	357.429
ACB-11	145.878	150.636	2.5236	1.9350	0.5886	401.881
ACT-01	145.394	150.160	2.1649	1.9350	0.2299	351.079
ACT-11	145.732	150.734	2.5829	1.9350	0.6479	400.066
	[mm]	[mm]	[mm]	[mm]	[mm]	[g]

Table E.57: *The resonant frequencies of the initial plate-shaped samples.*

Id.	f_{tors}	f_{sadd}	f_{brea}	f_{tf-x}	f_{tf-y}
ACS-01	291.503	434.380	515.805	742.459	757.604
ACB-01	285.275	421.653	528.246	730.406	745.609
ACB-11	292.497	433.015	510.626	738.091	757.723
ACT-01	291.482	431.601	526.759	738.784	755.042
ACT-11	295.048	432.387	524.971	744.073	761.861
	[Hz]	[Hz]	[Hz]	[Hz]	[Hz]

Table E.58: *The mesh sizes of the converged FE-models in terms of elements.*

Id.	Length	Width	Thickness	
			Substrate	Coating
ACS-01	23	23	3	—
ACB-01	23	23	3	1
ACB-11	23	23	3	1
ACT-01	23	23	3	1
ACT-11	23	23	3	1

Elastic Properties

Table E.59: *The elastic properties of the substrate.*

	E_1 [GPa]	E_2 [GPa]	G_{12} [GPa]	ν_{12} [–]
ACS-01	203.75	208.66	77.86	0.229
ACS-01/ACB-01	203.79	208.68	77.85	0.229
ACS-01/ACB-11	203.75	208.66	77.85	0.229
ACB-01/ACB-11	193.31	204.00	71.55	0.353
ACS-01/ACT-01	203.75	208.66	77.85	0.229
ACS-01/ACT-11	203.75	208.66	77.85	0.229
ACB-01/ACT-11	206.19	209.95	76.56	0.271

Table E.60: *The elastic properties of the bond coat.*

	E_1 [GPa]	E_2 [GPa]	G_{12} [GPa]	ν_{12} [–]
ACS-01/ACB-01	Err.	Err.	Err.	Err.
ACS-01/ACB-11	30.92	25.27	11.81	0.121
ACB-01/ACB-11	28.38	17.26	16.29	0.043

Table E.61: *The elastic properties of the top coat.*

	E_1 [GPa]	E_2 [GPa]	G_{12} [GPa]	ν_{12} [–]
ACS-01/ACT-01	20.77	19.05	8.30	0.757
ACS-01/ACT-11	26.05	24.69	10.49	0.391
ACB-01/ACT-11	25.07	24.17	11.27	0.187

E.3.2. The Beam-Shaped Specimens

E.3.3. Sample Description

Table E.62: *The mesh sizes of the converged FE-models in terms of elements.*

Id.	Length	Width	Thickness	
			Substrate	Coating
ASC-beams	14	11	3	—
ACB-Beams, 250µm	14	11	3	1
ACB-Beams, 500µm	14	11	3	1
ACT-Beams, 250µm	14	11	3	1
ACT-Beams, 500µm	14	11	3	1

Table E.63: *The properties of the beam-shaped APS substrate samples.*

Id	Dir.	Length	Width	Thick.	Mass	f_f	f_t
ACS-02	0.0	41.633	11.718	1.9370	7.3967	5800.81	11825.05
ACS-03	0.0	41.627	11.798	1.9362	7.4363	5783.44	11685.08
ACS-04	0.0	41.653	11.662	1.9326	7.3437	5770.40	11798.50
ACS-05	45.0	40.597	11.764	1.9368	7.2298	6017.40	12350.00
ACS-06	45.0	40.570	11.770	1.9358	7.2328	6017.27	12331.91
ACS-07	45.0	40.530	11.788	1.9362	7.2266	6024.48	12324.37
ACS-08	90.0	39.637	11.714	1.9370	7.0279	6453.50	12376.26
ACS-09	90.0	39.697	11.676	1.9342	7.0114	6432.14	12383.23
ACS-10	90.0	39.650	11.678	1.9358	7.0110	6445.04	12390.17
	[°]	[mm]	[mm]	[mm]	[g]	[Hz]	[Hz]

Table E.64: *The properties of the beam-shaped APS bond coat samples.*

Id.	Dir.	Length	Width	Thickness			Mass	f_f	f_t
				Total	Substr.	Coating			
ACB-02	0.0	41.610	11.622	2.2006	1.9357	0.2649	7.9242	5720.49	11690.72
ACB-03	0.0	41.573	11.684	2.2048	1.9357	0.2691	7.9560	5752.51	11671.22
ACB-04	0.0	41.550	11.730	2.2014	1.9357	0.2657	7.9796	5732.52	11606.59
ACB-05	45.0	40.530	11.706	2.2000	1.9357	0.2643	7.7737	5969.58	12221.59
ACB-06	45.0	40.487	11.740	2.2016	1.9357	0.2659	7.7872	5981.01	12197.85
ACB-07	45.0	40.493	11.680	2.2030	1.9357	0.2673	7.7789	5959.10	12192.82
ACB-08	90.0	39.583	11.632	2.2084	1.9357	0.2727	7.5642	6367.91	12272.88
ACB-09	90.0	39.573	11.622	2.2122	1.9357	0.2765	7.5813	6383.01	12265.32
ACB-10	90.0	39.613	11.616	2.2058	1.9357	0.2701	7.5617	6386.77	12281.50
ACB-12	0.0	41.697	11.778	2.5094	1.9357	0.5737	8.9745	5716.80	11554.13
ACB-13	0.0	41.680	11.742	2.5306	1.9357	0.5949	9.0240	5740.58	11610.73
ACB-14	0.0	41.693	11.762	2.5454	1.9357	0.6097	9.0742	5758.42	11628.30
ACB-15	45.0	40.690	11.692	2.5198	1.9357	0.5841	8.7644	5965.60	12159.52
ACB-16	45.0	40.693	11.700	2.5168	1.9357	0.5811	8.7495	5970.15	12158.02
ACB-17	45.0	40.740	11.696	2.5186	1.9357	0.5829	8.7540	5958.88	12144.11
ACB-18	90.0	39.723	11.748	2.4982	1.9357	0.5625	8.5374	6374.60	12175.96
ACB-19	90.0	39.700	11.718	2.5232	1.9357	0.5875	8.5464	6369.04	12217.27
ACB-20	90.0	39.713	11.712	2.5102	1.9357	0.5745	8.5261	6379.58	12224.29
	[°]	[mm]	[mm]	[mm]	[mm]	[mm]	[g]	[Hz]	[Hz]

Table E.65: *The properties of the beam-shaped APS top coat samples.*

Id.	Dir.	Length	Width	Thickness			Mass	f_f	f_t
				Total	Substr.	Coating			
ACT-02	0.0	41.617	11.708	2.1658	1.9357	0.2301	7.8053	5787.14	11832.68
ACT-03	0.0	41.623	11.760	2.1552	1.9357	0.2195	7.8255	5760.22	11702.97
ACT-04	0.0	41.697	11.624	2.1506	1.9357	0.2149	7.7469	5750.30	11817.77
ACT-05	0.0	41.657	11.704	2.1560	1.9357	0.2203	7.7749	5777.26	11815.54
ACT-06	45.0	40.603	11.688	2.1574	1.9357	0.2217	7.6058	6000.92	12350.11
ACT-07	45.0	40.603	11.756	2.1452	1.9357	0.2095	7.6087	6003.86	12342.05
ACT-08	45.0	40.563	11.778	2.1522	1.9357	0.2165	7.6223	6010.25	12342.46
ACT-09	90.0	39.667	11.780	2.1470	1.9357	0.2113	7.4740	6418.68	12294.09
ACT-10	90.0	39.590	11.652	2.1586	1.9357	0.2229	7.3899	6430.06	12383.01
ACT-12	0.0	41.647	11.748	2.5464	1.9357	0.6107	8.8070	5810.85	11892.40
ACT-13	0.0	41.583	11.670	2.5758	1.9357	0.6401	8.7887	5831.83	12003.39
ACT-14	0.0	41.607	11.718	2.6008	1.9357	0.6651	8.8861	5855.25	12777.40
ACT-15	45.0	40.650	11.628	2.5884	1.9357	0.6527	8.5639	6043.89	12524.66
ACT-16	45.0	40.667	11.648	2.5378	1.9357	0.6021	8.4582	6057.41	12551.93
ACT-17	45.0	40.670	11.620	2.5966	1.9357	0.6609	8.6091	6051.69	12540.23
ACT-18	90.0	39.623	11.586	2.5198	1.9357	0.5841	8.1101	6377.55	12460.37
ACT-19	90.0	39.620	11.590	2.5916	1.9357	0.6559	8.3413	6444.54	12641.50
ACT-20	90.0	39.657	11.566	2.6046	1.9357	0.6689	8.3662	6475.31	12651.64
	[°]	[mm]	[mm]	[mm]	[mm]	[mm]	[g]	[Hz]	[Hz]

Elastic Properties

Table E.66: *The elastic properties of the beam-shaped substrate samples.*

Id.	Dir.	E	G	ν
ACS-02	0.0	201.45	77.63	0.297
ACS-03	0.0	200.05	76.68	0.304
ACS-04	0.0	200.47	76.96	0.302
ACS-05	45.0	196.30	81.11	0.210
ACS-06	45.0	196.18	81.00	0.211
ACS-07	45.0	195.49	80.81	0.210
ACS-08	90.0	204.53	76.70	0.333
ACS-09	90.0	205.15	76.84	0.335
ACS-10	90.0	204.70	76.66	0.335
	[°]	[GPa]	[GPa]	[–]

Table E.67: *The averages of the elastic properties of the beam-shaped substrate samples.*

Dir.	E	G	ν
0.0	200.66	77.09	0.301
45.0	195.99	80.97	0.210
90.0	204.80	76.73	0.335
[°]	[GPa]	[GPa]	[–]

Table E.68: *The multi-orientation results obtained from the beam-shaped substrate samples.*

E_1	E_2	G_{12}	ν_{12}
200.85	205.26	76.91	0.246
[GPa]	[GPa]	[GPa]	[–]

Table E.69: *The elastic properties of the beam-shaped samples coated with 250 µm bond coat, approach 1.*

Id.	Dir.	E	G	ν
ACB-02	0.0	22.19	8.77	0.266
ACB-03	0.0	24.62	9.22	0.336
ACB-04	0.0	21.10	8.44	0.250
ACB-05	45.0	24.26	9.49	0.278
ACB-06	45.0	23.83	9.25	0.288
ACB-07	45.0	22.20	8.21	0.352
ACB-08	90.0	21.79	9.15	0.191
ACB-09	90.0	23.32	9.01	0.295
ACB-10	90.0	24.85	9.34	0.330
	[°]	[GPa]	[GPa]	[–]

Table E.70: *The averages of the elastic properties of the beam-shaped samples coated with 250 µm bond coat, approach 1.*

Dir.	E	G	ν
0.0	22.64	8.81	0.284
45.0	23.43	8.98	0.306
90.0	23.32	9.17	0.272
[°]	[GPa]	[GPa]	[–]

Table E.71: *The elastic properties of the beam-shaped samples coated with 500 µm bond coat, approach 1.*

Id.	Dir.	E	G	ν
ACB-12	0.0	26.53	10.96	0.210
ACB-13	0.0	27.78	11.27	0.233
ACB-14	0.0	28.57	11.56	0.236
ACB-15	45.0	28.86	11.29	0.278
ACB-16	45.0	28.94	11.27	0.284
ACB-17	45.0	28.86	11.16	0.293
ACB-18	90.0	28.79	11.74	0.226
ACB-19	90.0	26.85	11.45	0.172
ACB-20	90.0	28.33	11.70	0.210
	[°]	[GPa]	[GPa]	[–]

Table E.72: *The averages of the elastic properties of the beam-shaped sample coated with 500 µm bond coat, approach 1.*

Dir.	E	G	ν
0.0	27.63	11.27	0.226
45.0	28.89	11.24	0.285
90.0	27.99	11.63	0.203
[°]	[GPa]	[GPa]	[–]

Table E.73: *The elastic properties of the beam-shaped bond coat samples, approach 2.*

Dir.	Substrate			Bond coat		
	E	G	ν	E	G	ν
0.0	196.45	75.18	0.307	30.48	12.70	0.200
45.0	191.65	79.22	0.210	32.01	12.55	0.275
90.0	200.58	74.66	0.343	30.64	13.19	0.161
[°]	[GPa]	[GPa]	[–]	[GPa]	[GPa]	[–]

Table E.74: *The multi-orientation results obtained from the beam-shaped bond coat samples, approach 1.*

	E_1	E_2	G_{12}	ν_{12}
All 250 µmBC Beams	22.83	23.59	9.04	0.287
All 500 µmBC Beams	27.94	28.47	11.50	0.256
	[GPa]	[GPa]	[GPa]	[–]

Table E.75: *The multi-orientation results obtained from the beam-shaped bond coat samples, approach 2.*

	E_1	E_2	G_{12}	ν_{12}
Substrate	196.77	201.24	74.95	0.248
Bond coat	30.79	31.38	12.96	0.240
	[GPa]	[GPa]	[GPa]	[–]

Table E.76: *The elastic properties of the beam-shaped samples coated with 250 µm top coat, approach 1.*

Id.	Dir.	E	G	ν
ACT-02	0.0	23.22	13.25	−0.124
ACT-03	0.0	21.16	10.59	−0.001
ACT-04	0.0	24.04	11.31	0.062
ACT-05	0.0	23.24	12.61	−0.078
ACT-06	45.0	27.79	11.46	0.213
ACT-07	45.0	26.51	13.07	0.014
ACT-08	45.0	24.11	13.15	−0.083
ACT-09	90.0	22.39	12.83	−0.128
ACT-10	90.0	22.18	10.58	0.048
	[°]	[GPa]	[GPa]	[–]

Table E.77: *The averages of the elastic properties of the beam-shaped samples coated with 250 µm top coat, approach 1.*

Dir.	E	G	ν
0.0	22.80	11.72	−0.021
45.0	25.85	12.38	0.049
90.0	22.90	12.19	−0.054
[°]	[GPa]	[GPa]	[–]

Table E.78: *The elastic properties of the beam-shaped samples coated with 500 µm top coat, approach 1.*

Id.	Dir.	E	G	ν
ACT-12	0.0	24.91	12.46	−0.001
ACT-13	0.0	24.07	12.31	−0.023
ACT-14	0.0	18.61	19.74	−0.529
ACT-15	45.0	25.24	11.69	0.080
ACT-16	45.0	27.05	12.61	0.072
ACT-17	45.0	26.23	11.97	0.096
ACT-18	90.0	26.05	8.68	0.500
ACT-19	90.0	20.75	11.93	−0.130
ACT-20	90.0	24.14	11.81	0.022
	[°]	[GPa]	[GPa]	[–]

Table E.79: *The averages of the elastic properties of the beam-shaped samples coated with 500 µm top coat, approach 1.*

Dir.	E	G	ν
0.0	24.49	12.39	−0.012
45.0	26.17	12.09	0.083
90.0	22.45	11.87	−0.054
[°]	[GPa]	[GPa]	[–]

Table E.80: *The elastic properties of the beam-shaped top coat samples, approach 2.*

Dir.	Substrate			TC		
	E	G	ν	E	G	ν
0.0	199.83	76.76	0.302	24.97	12.63	−0.012
45.0	198.18	79.44	0.247	22.71	13.07	−0.131
90.0	201.23	78.70	0.278	27.04	10.63	0.272
[°]	[GPa]	[GPa]	[–]	[GPa]	[GPa]	[–]

Table E.81: *The multi-orientation results obtained from the beam-shaped samples coated with top coat, approach 1.*

	E_1	E_2	G_{12}	ν_{12}
All 250 µmTC Beams	24.72	24.57	12.02	0.000
All 500 µmTC Beams	25.60	24.27	12.16	0.037
	[GPa]	[GPa]	[GPa]	[–]

Table E.82: *The multi-orientation results obtained from the beam-shaped samples coated with top coat, approach 2.*

	E_1	E_2	G_{12}	ν_{12}
Substrate	200.63	205.65	76.88	0.243
TC	25.86	24.15	12.17	0.052
	[GPa]	[GPa]	[GPa]	[–]

E.4. Electron Beam – Physical Vapour Deposited Coatings

Sample Description

Table E.83: *The properties of the EB-PVD cylinders.*

Id.	Length	Diameter substrate	Coating thickness BC	Coating thickness TC	Mass	f_f
ECC-01	67.082	3.997	—	—	7.073	3860.72
ECC-02	67.152	3.948	0.114	—	7.634	4038.85
ECC-03	67.176	3.994	0.267	—	8.802	4370.02
ECC-04	67.016	3.951	0.028	0.112	7.564	3844.40
ECC-05	67.104	3.955	0.029	0.192	8.005	3803.14
ECC-06	67.042	3.992	0.112	0.197	8.669	4004.45
ECC-07	67.028	3.963	0.110	0.194	8.505	4002.17
ECC-08	67.088	4.025	0.109	0.193	8.715	4008.97
ECC-09	67.106	3.977	0.270	0.098	9.227	4305.94
ECC-10	67.064	3.994	0.257	0.199	9.726	4307.72
	[mm]	[mm]	[mm]	[mm]	[g]	[Hz]

Table E.84: *The considered sample sets of EB-PVD cylinders.*

	Set 1	Set 2	Set 3	Set 4	Set 5
ECC-01	✓	✓	—	✓	—
ECC-02	—	✓	✓	✓	—
ECC-03	—	✓	✓	✓	—
ECC-04	—	—	—	✓	✓
ECC-05	—	—	—	✓	✓
ECC-06	—	—	—	✓	✓
ECC-07	—	—	—	✓	✓
ECC-08	—	—	—	✓	✓
ECC-09	—	—	—	✓	✓
ECC-10	—	—	—	✓	✓

Table E.85: *The size of the converged FE-models in terms of elements.*

Samples	Length	Radius		
		Sub.	BC	TC
ECC-01	14	3	—	—
ECC-01 – ECC-02	14	3	1	—
ECC-03 – ECC-10	14	3	1	1

Elastic Properties

Table E.86: *The elastic properties identified with the various sample sets.*

	E_{Sub}	E_{BC}	E_{TC}
Set 1	203.86	—	—
Set 2	204.74	194.90	—
Set 3	213.85	176.35	—
Set 4	204.84	193.73	35.74
Set 5	202.68	189.18	42.61
	[GPa]	[GPa]	[GPa]

Bibliography

[1] F. Förster. *Ein neues Messverfahren zur Bestimmung des Elastizitätsmoduls und der Dämpfung.* Z. Metallkd., Vol. 29:109–115, 1937.

[2] G. Pickett. *Equations for computing elastic constants from flexural and torsional resonant frequencies of vibrating prisms and cylinders.* Proceedings ASTM, Vol. 45:846–865, 1945.

[3] S. Spinner and W. E. Teft. *A method for determining mechanical resonance frequencies and for calculating elastic moduli from these frequencies.* Proceedings ASTM, Vol. 61:1209–1221, 1961.

[4] ASTM Standard C 1259-01. *Standard Test Method for Dynamic Young's Modulus, Shear Modulus, and Poisson's Ratio for Advanced Ceramics by Impulse Excitation of Vibration.* April, 2001.

[5] H. Sol. *Identification of anisotropic plate rigidities using free vibration data.* PhD thesis, Vrije Universiteit Brussel, Brussels, Belgium, 1986.

[6] J. Schrooten, G. Roebben, and J.A. Helsen. *Young's modulus of bioactive glass coated oral implants: porosity corrected bulk modulus versus resonance frequency analysis.* Scripta Materialia, Vol. 41:10471053, 1999.

[7] E. Goens. *Über die Bestimmung des Elastizitätsmodulus von Stäben met Hilfe von Biegungsschwingungen.* Annalen der Physik, Band 11:649–678, 1931.

[8] S. Timoshenko. *Vibration problems is engineering.* Wiley, New York, USA, 4th edition, 1974. ISBN 0-471-87315-2.

[9] W. Wang, H. Ishikawa, and H. Yuki. *An inverse method for determining material parameters of a multi-layer medium by boundary element method.* International journal of solids and structures, Vol. 38:8907–8920, 2001.

[10] M. Beghini, L. Bertini, and F. Frendo. *Measurement of coatings' elastic properties by mechanical methods: part 1. Consideration on experimental errors.* Experimental mechanics, Vol. 41, No. 4:293–304, 2001.

[11] M. Beghini, L. Bertini, and F. Frendo. *Measurement of coatings' elastic properties by mechanical methods: part 2. Application to thermal barrier coatings.* Experimental mechanics, Vol. 41, No. 4:305–311, 2001.

[12] A. Javadi, R. Farmani, V. Toropov, and M. Snee. *Identification of parameters for air permeability of shotcrete tunnel lining using a genetic algorithm.* Computers and Geotechnics, Vol. 25:1–24, 1999.

[13] A. Hikawa, M. Kawahara, and N. Kaneko. *Parameter identification of ground elastic modulus at tunnel excavation site.* Annual report of the Kawahara Laboratory, Chuo University, Japan, 2004.

[14] G. Férin, D. Certon, J. Guyonvarch, and N. Félix. *Inverse calculation method for piezocomposite materials characterization.* In Proceedings of IEEE International Ultrasonics, Ferroelectrics, and Frequency Control Conference, Montréal, Canada, August 24-27, 2004.

[15] Z. Fellah, F. Mitri, C. Depollier, S. Berger, W. Lauriks, and J. Chapelon. *Characterization of porous materials with a rigid frame via reflected waves.* Journal of Applied Physics, Vol. 94, Number 12:7914–7922, 2003.

[16] K. Hoes, D. Dinescu, H. Sol, R. Parnas, and S. Lomov. *Study of nesting induced scatter of permeability values in layered reinforcement fabrics.* Composites Part A, Vol. 35:1407–1418, 2004.

[17] D. Trujillo and H. Busby. *Practical Inverse Analysis in Engineering.* CRC Press, Boca Raton, Florida, USA, 1th edition, 1997. ISBN 0-8493965-9-X.

[18] R. Panneton, Y. Atalla, D. Blanchet, and Bloor M. *Validation of the inverse method of acoustic material characterization.* In Proceedings of the 2003 SAE Noise & Vibration conference, Traverse City, Michigan, USA, May 5-8, 2003.

[19] J. De Visscher. *Identification of the complex stiffness matrix of orthotropic materials by a mixed numerical experimental method.* PhD thesis, Vrije Universiteit Brussel, Brussels, Belgium, 1995.

[20] J. Tudor. *Determination of dynamic properties and modelling of extensional damping materials.* In Proceedings of the 2003 SAE Noise & Vibration conference, Traverse City, Michigan, USA, May 5-8, 2003.

[21] T. Furukwaw and G. Yagawa. *Implicit constitutive modelling for viscoplasticity using neural networks.* International Journal for Numerical Methods in Engineering, Vol. 43:195–219, 1998.

[22] F. Yoshida, M. Urabe, R. Hino, and V. Toropov. *Inverse approach to identification of material parameters of cyclic elasto-plasticity for component layers of a bimetallic sheet.* International Journal of Plasticity, Vol. 19:2149–2170, 2003.

[23] F. Hendriks, D. Brokken, J. van Eemeren, C. Oomens, F. Baaijens, and J. Horsten. *A numerical-experimental method to characterize the non-linear mechanical behaviour of human skin.* Skin research and technology, Vol. 9:274–283, 2003.

[24] M. Kauer. *Inverse finite element characterization of soft tissues with aspiration experiments.* PhD thesis, Swiss Federal Institute of Technology, Zürich, Switzerland, 2001.

[25] G. Schiltges. *Continuum mechanical investigations on microstructures.* PhD thesis, Swiss Federal Institute of Technology, Zürich, Switzerland, 1999.

[26] R. Ardito, P. Bartalotta, L. Ceriani, and G. Maier. *Diagnostic inverse analysis of concrete dams with statical excitation.* In Proceedings of the 5$^{\text{th}}$ Euromech Solid Mechanics Conference ESMC, Thessaloniki, Greece, August 17-22, 2003.

[27] D. Lecompte, H. Sol, J. Vantomme, and A. M. Habraken. *Identification of elastic orthotropic material parameters based on ESPI measurements.* In Proceedings of the 2005 SEM Annual Conference on Experimental and Applied Mechanics, Portland, Oregon, USA, June 7-9, 2005.

[28] E. Lucchinetti and E. Stüssi. *Measuring the flexural rigidity in non-uniform beams using an inverse problem approach.* Inverse problems, Vol. 18:837–857, 2002.

[29] F. Pierron and M. Greédiac. *Identification of the through-thickness moduli of thick composites from whole-field measurements using the Iosipescu fixture: theory and simulations.* Composites Part A, Vol. 31:309–318, 2000.

[30] F. Pierron, S. Zhavoronokb, and M. Grédiac. *Identification of the through-thickness properties of thick laminated tubes using the virtual fields method.* International journal of solids and structures, Vol. 37:4437–4453, 2000.

[31] M. Bocciarelli, G. Bolzon, and G. Maier. *Parameter identification in anisotropic elastoplasticity by indentation and imprint mapping.* Mechanics of materials, Vol. 37:855–868, 2005.

[32] D. Gsell and J. Dual. *Non-destructive evaluation of elastic material properties in anisotropic circular cylindrical structures.* Ultrasonics, Vol. 43, Issue 2:123–132, 2004.

[33] G. R. Liu, W. B. Ma, and X. Han. *An inverse procedure for determination of material constants of composite laminates using elastic waves.* Computational. Methods in Applied Mechanics and Engineering, Vol. 191:3543–3554, 2002.

[34] G. R. Liu, X. Han, and Lam K. Y. *Stress waves in functionally gradient materials and its use for material characterization.* Composites Part B, Vol. 30:383–294, 1999.

[35] H. Sol, J. De Vissher, H. Hua, J. Vantomme, and W.P. De Wilde. *La procédure résonalyser.* La revue des Laboratoires d'essais, Vol. 46:10–12, 1996.

[36] M. Carne, Th. adn Nielsen and E. Stasiunas. *Experimental and analytical validation of a computationally developed orthotropic constitutive model.* In Proceedings of the 21th International Modal Analysis Conference, Kissimmee, February 3-6, 2003.

[37] M. F. Teixeira Silva, L. M. S. Alves Borges, F. Alves Rochinha, and L. A. Vidal de Carvalho. *Genetic algorithms for identification of elastic constants of composite materials.* In 4th International Conference on Inverse Problems in Engineering (ICIPE), Rio de Janeiro, Brazil, May 26-31, 2002.

[38] L.R. Deobald and R.F. Gibson. *Determination of elastic constants of orthotropic plates by a modal analysis/Rayleigh Ritz technique.* Journal of sound and vibration, Vol. 124:269–283, 1988.

[39] M. Grediac and A. Vautrin. *Mechanical characterization of anisotropic plates: experiments and results.* Eur. J. Mech. A/Solids, Vol. 12, No. 6:819–838, 1993.

[40] F. Moussu and M. Nivoit. *Determination of the elastic constants of orthotropic plates by a modal analysis method of superposition.* Journal of sound and vibration, Vol. 165:149–163, 1993.

[41] D. Larsson. *In-plane modal testing of a free isotropic rectangular plate.* Experimental-Mechanics, Vol. 37:339–343, 1997.

[42] D. Larsson. *Mechanical characterization of engineering materials by modal testing.* PhD thesis, Chalmer university of technology, G oteborg, Sweden, 1997.

[43] P. S. Frederiksen. *Estimation of elastic moduli in thick composite plates by inversion of vibrational data.* In Proceedings of the second international symposium on inverse problems, Paris, 1994.

[44] E. O. Ayorinde. *Elastic constants of thick orthotropic composite plates.* Journal of composite materials, Vol. 29:1025–1039, 1995.

[45] M. C. M. Soares, M. Moreira de Freitas, and A. L. Araújo. *Identification of material properties of composite plate specimens.* Composite Structures, Vol. 25:277285, 2003.

[46] J. Cunha. *Application des techniques de recalage en dynamique a lidentification des constantes elastiques des matériaux composites.* PhD thesis, Université de Franche-Compte, Besançon, France, 1997.

[47] J. Cunha, S. Cogan, and C. Berthod. *Application of genetic algorithms for the identification of elastic constants of composite materials from dynamic tests.* International journal for numerical methods in engineering, Vol. 45:891–900, 1999.

[48] J. Cugnoni, Th. Gmür, and A. Schorderet. *Identification by modal analysis of composite structures modelled with FSDT and HSDT laminated shell finite elements.* Composites Part A, Vol. 35:977–987, 2004.

[49] J. Cugnoni. *Identification par recalage modal et fréquentiel des propriétés constitutives de coques en matériaux composites.* PhD thesis, École Polytechnique Fédérale de Lausanne, Lausanne, Switzerland, 2005.

[50] R. Rikards. *Identification of mechanical properties of laminates.* www.bf.rtu.lv/ icas/files/R62.pdf, 2002.

[51] W. Heylen. *Twenty years of optimisation of model matrices by means of experimentally obtained dynamic data.* In Proceedings of the 20$^{\text{th}}$ International Modal Analysis Conference (IMAC), Los Angeles, California, USA, Feb 4-7, 2002.

[52] R. M. Jones. *Mechanics of composite materials.* MacGraw-Hill, New York, USA, 1st edition, 1975. ISBN 0-07-032790-4.

[53] S. W. Tsai. *Composite design.* Think Composites, Ohio, USA, 4th edition, 1988. ISBN 0-9618090-2-7.

[54] R. C. Reuter. *Concise property transformation relations for an anisotropic lamina.* Journal of composite materials, Vol. 4:270–272, 1971.

[55] S. G. Lekhnitski. *Theory of elasticity of an anisotropic elastic body.* Holden-Day, San Fransico, USA, 1st edition, 1963.

[56] B. M. Lempriere. *Poisson's ratio in orthotropic materials.* AAIA Journal, Vol. 11:2226–2227, 1968.

[57] P. Van Houtte. *Continuum Modelling of Material Properties.* Lecture notes H0G12D, Katholieke Universiteit Leuven.

[58] K. J. Bathe and E. L. Wilson. *Numerical methods in finite element analysis.* Printice-Hall, Inc., Englewoods Cliffs, New Jersey, USA, 1st edition, 1976. ISBN 0-13-627190-1.

[59] O. C. Zienkiewicz and R. L. Taylor. *The finite element method. 2: Solid and fluid mechanics, dynamics and non-linearity.* MacGraw-Hill, London, UK, 4th edition, 1989. ISBN 0-07-084175-6.

[60] C. Felippa. *Introduction to Finite Element Methods.* http://caswww.colorado.edu/courses.d/IFEM.d/Home.html, 2004.

[61] Y. Sun. *The filter algorithm for solving large-scale eigenproblems from accelerator simulations.* PhD thesis, Stanford University, Stanford, California, USA, March, 2003.

[62] M. Morris. *Input screening: finding the important inputs on a budget.* In Proceedings of the International Conference on Sensitivity Analysis (SAMO), Santa Fé, New Mexico, USA, March 8-11, 2004.

[63] Saltelli A. *Global sensitivity analysis, an introduction.* In Proceedings of the International Conference on Sensitivity Analysis (SAMO), Santa Fé, New Mexico, March 8-11, 2004.

[64] A. Saltelli, S. Tarantola, F. Campolongo, and M. Ratto. *Sensitivity analysis in practice: A guide to assessing scientific models.* John Wiley & Sons, New York, USA, 1st edition, 2004. ISBN 0-470-87093-1.

[65] W. Heylen, S. Lammens, and P. Sas. *Modal analysis theory and testing.* Department of Mechanical Engineering, Katholieke Universiteit Leuven, Leuven, Belgium, 1st edition, 1995. ISBN 90-73802-46-6.

[66] J.-P. Kleinermann. *Identification paramétrique et optimation des procédés de mis à forme par problème inverse.* PhD thesis, Université de Liège, Liège, Belgium, 2000.

[67] I. Grešovnik. *A general purpose computational shell for solving inverse and optimisation problems: Applications to metal forming processes.* PhD thesis, University of Wales, Swansea, UK, 2000.

[68] F. Van Keulen, J. J. M. Rijpkema, and L. F. P. Etman. *Engineering optimisation.* Lecture notes, Graduate School Engineering Mechanics, Eindhoven University of Technology, 2003.

[69] R. T. Haftka and Z. Gürdal. *Elements of structural optimization.* Kluwer Academic Publishers, Dordrecht, The Netherlands, 3th revised and expanded edition, 1993. ISBN 0-7923-1505-7.

[70] R. Fox and M. Kapoor. *Rate of change of eigenvalues and eigenvectors.* AIAA Journal, Vol. 6:2426–2429, 1968.

[71] J. E. Dennis and R. B. Schnabel. *Numerical methods for unconstrained optimization and nonlinear equations.* Prentice-hall, New Jersey, USA, 1st edition, 1983.

[72] R. J. Allemang and D. L. Brown. *A correlation coefficient for modal vector analysis.* In Proceedings of the 1st International Modal Analysis Conference (IMAC), Orlando, Florida, 1982, 1982.

[73] S. Boyd and L. Vandenberghe. *Convex optimization.* Cambridge University Press, Cambridge, UK, 1th edition, 2004. ISBN 0-521-83378-7.

[74] R. T. Rockafellar. *Lagrange multipliers and optimality.* SIAM Review, Vol. 35:183–283, 1993.

[75] J. V. Beck and K. J. Arnold. *Parameter estimation in engineering and science.* Wiley and Sons, New York, USA, 1st edition, 1977. ISBN 0-471-06118-2.

[76] P. Hooke and T. A. Jeeves. *Direct search solution of numerical and statistical problems.* Journal of the Association for Computing Machinery, Vol. 8:212–229, 1961.

[77] F. H. Walters, L. R. Jr. Parker, S. L. Morgan, and S. N. Deming. *Sequential simplex optimization: a technique for improving quality and productivity in research, development and manufacturing.* Chemometrics Series, CRC Press Inc., Boca Raton, Florida, USA, 1st edition, 1991. ISBN 0-849-35894-9.

[78] W. Spendley, G. R. Hext, and F. R. Himsworth. *Sequential application of simplex designs in optimization and evolutionary operation.* Technometrics, Vol. 4(4):441–461, 1962.

[79] J. A. Nelder and R. Mead. *A simplex method for function minimazation.* Computer J., Vol. 7:308–313, 1965.

[80] R. M. Lewis, V. Torczon, and M. W. Trosset. *Direct search methods: then and now.* NASA Langley Research Center, NASA/CR-2000-210125, ICASE Report No. 2000-26, 2000.

[81] V. Toropov and F. Yoshida. *Applications of advanced optimization techniques to parameter and damage identification problems.* In Proceedings of the advance course on Parameter Identification of Materials and Structures, Centre International des Sciences Méchanique, Udine, Italy, October 6-10, 2003.

[82] Z. Waszczyszyn. *Neural Networks in the Analysis and Design of Structures.* Courses and Lectures No. 404, Centre Interational des Science Méchaniques (CISM), Udine, Italy, 1st edition, 2000. ISBN 3-211-83322-6.

[83] Z. Waszczyszyn and L. Ziemiański. *Neural networks in mechanics of structures and materials – new results and prospects of applications.* Computers and Structures, Vol. 79:2261–2276, 2001.

[84] L. Hillström, U. Valdek, and B. Lundberg. *Estimation of the state vector and identification of the complex modulus of a beam.* Journal of Sound and Vibration, Vol. 261:653673, 2003.

[85] W. Beluch, W. Kuś, and T. Burczyński. *Evolutionary identification of material constants in composites.* In Proceedings of the conference on Artificial Intelligence Methods (IA-METH), Gliwice, Poland, November 5-7, 2003.

[86] L. Roseiro, U. Ramos, and R. Leal. *Determination of material constants of composite laminates using neural networks and genetic algorithms.* In Proceeding of the European congress on computational methods in applied sciences and engineering (ECCOMAS), Jyväslylä, Finland, July 24-28, 2004.

[87] G. R. Liu, X. Han, Y. G. Xu, and Lam K. Y. *Material characterization of functionally graded material by means of elastic waves and a progressive-learning neural network.* Composites Science and Technology, Vol. 61:1401–1411, 2001.

[88] A. L. Araújo, C. M. Mota Soares, J. Herskovits, and P. Pedersen. *Parameter estimation in active plate structures using gradient optimization and neural networks.* In Proceedings of the Inverse Problems, Design and Optimization Symposium (IPDO), Rio de Janeiro, Brazil, March 17-19, 2004.

[89] J. C. Lagarias, J. A. Reeds, M. H. Wright, and P. E. Wright. *Convergence properties of the nelder-mead simplex method in low dimensions.* SIAM Journal of Optimization, Vol. 9:112–147, 1998.

[90] A. N. Tikhonov, V. Y. Arsenin, and F. John. *Solutions of ill posed problems.* Wiley, New York, USA, 1st edition, 1977. ISBN 0-470-99124-0.

[91] A. J. Morris. *Foundations of structural optimization: A unified approach.* John Wiley & Sons Ltd., New York, USA, 1st edition, 1982. ISBN 0-471-10200-8.

[92] A. Teughels. *Inverse modelling of civil engineering structures based on operational modal data.* PhD thesis, Katholieke Universiteit Leuven, Leuven, Belgium, December, 2003.

[93] C. R. Vogel. *Computational methods for inverse problems.* Frontiers in Applied Mathematics. SIAM, Philadelphia, USA, 1st edition, 2002. ISBN 0-898-71507-5.

[94] C. C. Chamis. *Structural design and analysis, Part 1, Composite materials, Vol. 7.* Academic Press, New York, USA, 1st edition, 1975. ISBN 0-12-136507-7.

[95] R. D. Blevins. *Formulas for natural frequency and mode shape.* Litton Educational Publishing Inc., New York, USA, 1th edition, 1979. ISBN 0-442-20710-7.

[96] N. Imamovic. *Validation of large structural dynamics models using modal test data.* PhD thesis, Imperial College of Science, Technology & Medicine, London, UK, 1998.

[97] International Organisation for Standardisation (ISO), Geneva, Switzerland. *Guide to the expression of uncertainty in measurement.* First edition, 1993. ISBN 92-67-10188-9.

[98] National Institute of Standards and Technology (NIST). *Essentials of expressing measurement uncertainty.* http://physics.nist.gov/cuu/Uncertainty/index.html.

[99] E. W. Weisstein. *Mathworld.* http://mathworld.wolfram.com.

[100] EURACHEM/CITAC. *Quantifying Uncertainty in Analytical Measurement.* Second English edition, 2000. ISBN 0-948926-15.

[101] T. Lauwagie. *Error estimation in material identification.* Second annex of the fifth GRAMATIC report, Katholieke Universiteit Leuven, Belgium, 2003.

[102] C. K. Bullough. *The determination of uncertainties in dynamic young's modulus. Manual of codes of practice for the determination of uncertainties in mechanical tests on metallic materials.* Project UNCERT, EU Contract SMT4-CT97-2165, Standards, Measurement and Testing Programme, Issue 1, September, 2000. ISBN 0-946754-41-1.

[103] M. Cox and P. Harris. *Up a GUM tree? Try the full monte!* Centre for Mathematics & Scientific Computing National Physical Laboratory, http://www.npl.co.uk/scientific software/tutorials/uncertainties/up a gum tree.pdf.

[104] R. E. Moore. *Methods and applications of interval analysis.* SIAM, Philadelphia, USA, 1966. ISBN 0-89871-161-4.

[105] D. Moens. *A non-probabilistic finite element approach for structural dynamic analysis with uncertain parameters.* PhD thesis, Katholieke Universiteit Leuven, Leuven, Belgium, 2002.

[106] M. Hanss. *The transformation method for the simulation and analysis of systems with uncertain parameters.* Fuzzy Sets and Systems, Vol. 130:277–289, 2002.

[107] M. Hanss, S. Oexl, and L. Gaul. *Simulation and analysis of structural joint models with uncertainties.* In Proceedings of the Structural Dynamics Modelling conference (SDM), Madeira, Portugal, June 3-5, 2002.

[108] F. Kroupa and J. Plešek. *Nonlinear elastic behaviour in compression of thermally sprayed materials.* Materials Science and Engineering A, Vol. 328:1–7, 2002.

[109] N. Tassini, K. Lambrinou, I. Mircea, M. Bartsch, S. Patsias, and O. Van Der Biest. *Study of the amplitude dependent behaviour of Yttria-stabilised Zirconia thermal barrier coatings.* In Proceedings of the IX conference & Exhibition of the European Ceramic Society, Portorož, Slovenia, June 19-23, 2005.

Curriculum Vitae

Tom Lauwagie
° 7 November 1975, Brugge, Belgium

Education

2000 – 2005
PhD. student at the department of mechanical engineering (PMA), Katholieke Universiteit Leuven, Leuven, Belgium.

1998 – 1999
MSc. in Civil Engineering (Ir. Burgerlijke Bouwkunde), Vrije Universiteit Brussel, Brussel, Belgium.

1993 – 1998
MSc. in Construction Engineering, Polytechnic division, Koninklijke Militaire School, Brussel, Belgium.

1987 – 1993
Secondary education, Wetenschappelijke A, St.-Leo College, Brugge, Belgium.

Work Experience

April 2000 – November 2000
Project Engineer, Harbour & Engineering Consultants HEACON N.V., Gent, Belgium.

September 1999 – March 2000
Project Engineer, Dredging International N.V., Antwerpen, Belgium.

Publications

Publications in Conference Proceedings

T. Lauwagie, E. Dascotte. *Layered material identification using multi-model updating*, Proceedings of the Structural Dynamics Modelling Conference, Madeira, Portugal, 2002, pp. 483-490.

H. Sol, T. Lauwagie, P. Guillaume. *Identification of distributed material properties using measured modal data*, Proceedings of ISMA 2002, International Conference on Noise and Vibration Engineering, Leuven, 16-18 Sept. 2002, pp. 695-704.

T. Lauwagie, H. Sol, E. Dascotte. *Damage identification in beams using inverse methods*, Proceedings of ISMA 2002, International Conference on Noise and Vibration Engineering, Leuven, 16-18 Sept. 2002, pp. 715-722.

T. Lauwagie, H. Sol, G. Roebben, W. Heylen and Y. Shi. *Validation of the resonalyser method: an inverse method for material identification*, Proceedings of ISMA 2002, International Conference on Noise and Vibration Engineering, Leuven, 16-18 Sept. 2002, pp. 687-694.

T. Lauwagie, W. Heylen. *A Multi-Model Updating Routine For Layered Material Identification*, Proceedings of the International Modal Analysis Conference, IMAC XXI, Kissimmee, 3-6 Feb. 2003.

H. Sol, T. Lauwagie, W. Heylen, G. Roebben. *Simultaneous identification of the elastic and damping properties of composite materials as a function of temperature.*, Second International workshop on damping technologies, Materials and devices for the next decade, Stellenbosch, South Africa, 24-26 mar. 2003.

T. Lauwagie and W. Heylen. *Identifying the elastic properties of the individual layers of layered materials from vibration data*, Proceeding of the 6th National Congress on Theoretical and Applied Mechanics, Gent, May 26-27, 2003.

T. Lauwagie, K. Lambrinou, I. Mircea, M. Bartsch, W. Heylen, O. Van der Biest. *Determination of the elastic moduli of the material components of the cylindrical thermal barrier coatings systems by means of a mixed numerical-experimental techniques*, Proceeding of the 8$^{\text{th}}$ International Symposium on multifunctional and functionally graded materials FGM2004, Leuven, Belgium 11-14 July 2004, pp. 653-658.

T. Lauwagie, W. Heylen, H. Sol, O. Van der Biest. *Validation of a vibration based identification procedure for layered materials.*, Proceedings of ISMA 2004, International conference on Noise and Vibration Engineering, Leuven, 20-22 Sept. 2004, pp. 1325-1336.

T. Lauwagie, G. Roebben, H. Sol, W. Heylen, O. Van der Biest. *The uncertainty budget of Mixed-Numerical-Experimental-Techniques for the identification of elastic material properties from resonance vibrations*, Proceedings of ISMA 2004, International conference on Noise and Vibration Engineering, Leuven, 20-22 Sept. 2004, pp. 1313-1324.

K. Lambrinou, T. Lauwagie, F. Chalvet, G. de Portu, N. Tassini, S. Patsias, T. Lube, O. Van der Biest. *Elastic properties and damping behaviour of alumnia - alumina/zirconia laminates*, Proceedings of the IX Conference & Exhibition of the European Ceramic Society, 19-23 June, 2005, Portorož, Slovenia.

D. Lecompte, T. Lauwagie, H. Sol, W. Heylen, J. Vantomme. *A comparison between static and dynamic inverse modelling for the identification of orthotropic elastic material parameters.*, Proceedings of the Second International Conference on Computational Methods and Experiments in Material Characterisation, 2-4 Nov. 2005, Portland, Maine, USA.
Full paper submitted in June 2005.

Publications in Interntational Journals

T. Lauwagie, H. Sol, G. Roebben, W. Heylen, Y. Shi, O. Van Der Biest. *Mixed numerical-experimental identification of elastic properties of orthotropic metal plates*, NDT & E International, Volume 36, Issue 7, October 2003, Pages 487-495.

T. Lauwagie, W. Heylen, H. Sol, G. Roebben. *Determination of the in-plane elastic properties of the different layers of a laminated plates by means of vibration testing and model updating.*, Journal of Sound and Vibration, Volume 274, Issues 3-5, Pages 529-546.

T. Lauwagie, K. Lambrinou, I. Mircea, M. Bartsch, W. Heylen, O. Van der Biest. *Determination of the elastic moduli of the material components of the cylindrical thermal barrier coatings systems by means of a mixed numerical-experimental techniques.*, Materials Science Forum, Vols. 492-493 (2005), pp. 653-658.

G. Roebben, O. Van der Biest, D. Sciti, A. Bellosi, C. Sarbu, T. Lauwagie. *High temperature stiffness and damping measurements to monitor the glassy intergranular phase in liquid-phase-sintered silicon carbides*, Journal of the American Ceramic Society, Volume 88, Issue 8, Page 2152, August 2005.

T. Lauwagie, H. Sol, W. Heylen. *Handling uncertainties in mixed numerical-experimental techniques for vibration based material identification.*, Journal of Sound and Vibration.
Accepted for publication on June 23, 2005.

S. Gimnez, T. Lauwagie, G. Roebben, W. Heylen, O. Van der Biest. *Effects of microstructural heterogeneity on the mechanical properties of pressed soft magnetic composite bodies.*, Journal of Alloys and Compounds.
Accepted for publication on September 19, 2005.